



HAL
open science

Ionic irradiation of materials: real-time dynamics of electronic excitations

Ivan Maliyov

► **To cite this version:**

Ivan Maliyov. Ionic irradiation of materials: real-time dynamics of electronic excitations. Computational Physics [physics.comp-ph]. Université Paris Saclay (COmUE), 2019. English. NNT: 2019SACLS434 . tel-02495699

HAL Id: tel-02495699

<https://theses.hal.science/tel-02495699>

Submitted on 2 Mar 2020

HAL is a multi-disciplinary open access archive for the deposit and dissemination of scientific research documents, whether they are published or not. The documents may come from teaching and research institutions in France or abroad, or from public or private research centers.

L'archive ouverte pluridisciplinaire **HAL**, est destinée au dépôt et à la diffusion de documents scientifiques de niveau recherche, publiés ou non, émanant des établissements d'enseignement et de recherche français ou étrangers, des laboratoires publics ou privés.

Irradiation ionique des matériaux: dynamique des excitations électroniques en temps réel

Thèse de doctorat de l'Université Paris-Saclay
préparée à l'Université Paris-Sud

Ecole doctorale n°564 Physique en Île-de-France (EDPIF)
Spécialité de doctorat : Physique du solide

Thèse présentée et soutenue à Saclay, le 15 Novembre 2019, par

IVAN MALIYOV

Thèse de doctorat

Composition du Jury :

M. Frédérico Garrido Professeur, Université Paris-Sud (IN2P3-CSNSM)	Président
M ^{me} Mai Dinh Professeure, Université Paul Sabatier (Laboratoire de Physique Théorique)	Rapporteure
M ^{me} Eleonora Luppi Maître de Conférences, Université Pierre et Marie Curie (Laboratoire de Chimie Théorique)	Rapporteure
M. Emilio Artacho Professeur, Université de Cambridge (The Cavendish Laboratory)	Examineur
M ^{me} Lucia Reining Directrice de Recherche, École Polytechnique (Laboratoire des Solides Irradiés)	Examineure
M. Jean-Paul Crocombette Ingénieur-Chercheur, CEA Saclay (SRMP)	Directeur de thèse
M. Fabien Bruneval Ingénieur-Chercheur, CEA Saclay (SRMP)	Encadrant

Remerciements

Avant de plonger dans un monde merveilleux des électrons, protons et leurs confrères, j'estime nécessaire de remercier les gens sans lesquels ce travail n'aurait pas été possible.

Tout d'abord, je suis infiniment reconnaissant à mes encadrants Fabien Bruneval et Jean-Paul Crocombette. Le format conventionnel de remerciements ainsi que ma connaissance du français ne me permettent pas d'exprimer toute ma gratitude à vous. En commençant par des aspects techniques de calculs quantiques, programmation, GitHub, support et soutien au quotidien, jusqu'à la vision globale de la physique et de la recherche d'aujourd'hui... Je suis très heureux d'avoir eu la chance de travailler sous votre direction pendant ces trois ans !

Merci beaucoup à Mai Dinh et Eleonora Luppi d'avoir rapporté ce travail. Je remercie Frédéric Garrido pour l'honneur qui m'a été accordé de présider le jury. Un grand merci à Emilio Artacho et Lucia Reining pour avoir examiné la thèse. Merci beaucoup à tout le jury pour vos questions et remarques qui ont permis d'améliorer la qualité de ce travail.

Je remercie chaleureusement toute l'équipe du laboratoire dans lequel j'ai effectué ma thèse, SRMP, notamment le chef du laboratoire Jean-Luc Béchade. L'ambiance au SRMP favorise la recherche dans de meilleures conditions. Je tiens à remercier particulièrement ma co-bureau Marie Landeiro pour ton aide avec le français, pour les discussions scientifiques que l'on a eues, pour ton amitié.

Finalement, merci beaucoup à toi, Masha, de m'avoir soutenu pendant ma thèse tandis que tu avais la tienne bien en même temps.

Contents

Introduction	9
1 Theoretical background	17
1.1 Ground state density-functional theory (DFT)	17
1.1.1 The many-body framework	18
1.1.2 Hohenberg-Kohn theorem	21
1.1.3 Kohn-Sham scheme	23
1.1.4 Extension to spin-polarized DFT	32
1.2 Exchange-correlation functionals approximations	34
1.2.1 Local density approximation	34
1.2.2 Generalized-gradient approximations	35
1.2.3 Meta-generalized-gradient approximations	36
1.2.4 Hybrid exchange-correlation functionals	37
1.3 Time-Dependent DFT (TDDFT)	38
1.3.1 Many-body time-dependent problem	38
1.3.2 One-to-one correspondence: time-dependent case	39
1.3.3 Time-Dependent Kohn-Sham system	41
1.4 Real-time TDDFT (RT-TDDFT)	44
1.4.1 Propagator technique	44
1.5 Stopping power from RT-TDDFT	48
1.5.1 Single-trajectory stopping power	48
1.5.2 Random stopping power	52
1.5.3 Channeling stopping power	55
2 RT-TDDFT implementation in Gaussian basis	57
2.1 The backbone of the implementation	57
2.1.1 Implementation workflow	57
2.1.2 Gaussian basis set	58

2.1.3	Roothaan-Hall equations	62
2.1.4	Orthogonalization of the basis	64
2.1.5	Hamiltonian expression in Gaussian basis	68
2.2	Algorithm of the time propagation of Kohn-Sham equations	72
2.2.1	Standard propagator techniques	72
2.2.2	Predictor-corrector method	75
2.2.3	Propagators in orthogonal basis	76
2.2.4	Different bases	77
2.2.5	Occupations analysis	78
2.2.6	Implementation in the code	79
2.2.7	Frozen states propagation	84
2.3	Validation	86
2.3.1	Dipole coupling	86
2.3.2	Optical absorption	89
2.3.3	Choice of the propagator and the predictor-corrector scheme	92
3	Methodology of the stopping power calculation	95
3.1	Li as a model system	95
3.1.1	Single-trajectory stopping power	96
3.1.2	Cluster geometry	101
3.1.3	Random stopping power	103
3.2	Basis set influence on the stopping power	112
3.2.1	Mixed basis technique	113
3.2.2	Dunning basis series comparison	114
3.3	Basis set convergence in aluminum	118
3.3.1	Convergence of cc-pCVXZ basis sets: comparison with the frozen core dynamics	119
3.3.2	Most complete aug-cc-pCVXZ basis set family	120
3.3.3	Stopping power extrapolation	121
3.4	Basis set generation	124
3.4.1	Motivation	124
3.4.2	Basis set optimization algorithm	126
3.4.3	Stopping power calculated with the optimized basis	132
3.5	Validity of fixed trajectory approximation	136
3.5.1	Projectile slowing down	136
3.5.2	Deviation from straight path due to ballistic losses	138
3.6	Summary	144
4	Stopping power of light projectiles in Li and Al	147
4.1	RESP of proton	148
4.1.1	Lithium target	148
4.1.2	Aluminum target	149
4.2	Occupation analysis	154

4.2.1	Single-trajectory occupation dynamics	154
4.2.2	Weighted occupations: correlation with weighted stopping power . .	155
4.2.3	Valence electron occupations in frozen core dynamics	157
4.2.4	Core electron occupations velocity dependence	158
4.2.5	Channeling conditions	159
4.3	Centroid path approximation accuracy	162
4.4	RESP of α -particle	164
4.5	Penetration depth of \mathbf{H}^+ and \mathbf{He}^{2+} within CSDA	165
4.6	RESP of antiproton	168
4.7	Effective charge of projectile	169
4.8	Summary	171
	Conclusions and perspectives	173

Introduction

The problem of the interaction between an incident ion and a target material occupied the minds of scientists even before the birth of Quantum Mechanics: The celebrated Rutherford α -particles on gold scattering experiment [1], that largely contributed to the atomic physics theory, is one of the first experimental setups directed towards the projectile/matter studies.

Nowadays, one deals with ionic radiation in a large variety of scientific and technological fields. In some cases, this phenomenon is a valuable tool, in others, the damage caused by energetic ions is undesirable and one wants to avoid it. Even if the present work is mostly motivated by the nuclear energy domain (see below in the text), we will mention here some examples from different fields.

In medicine, the ionic (in particular, protonic) irradiation is widely used to treat the cancer tumors. It is named “proton therapy”. The profile of the ion energy loss as a function of the penetration depth is well adapted for this task: The maximum of the deposited irradiation dose, known as the Bragg peak, is quite sharp in space and is located at some depth in material (in this case, in tissue). This is a unique property of ion irradiation, which distinguishes it from, for example, electron or X-ray irradiations (see Fig. I.1). In addition, changing the energy of the proton beam and the beam collimation, one can change the depth of the peak and its width. In such a way, using the proton therapy of cancer in the cases where the tumor is deeply located in tissues (more than 1 cm), one kills the cancer cells, at the same time, keeping the normal tissues less exposed to radiation [4].

On the other hand, in the space industry, ion irradiation has a negative impact. While the Earth atmosphere protects us from cosmic radiation, the spacecrafts do not have such a privilege. There are various sources of cosmic radiations: solar winds, solar flares or radiations that have origins outside the Solar System. These radiations, in particular, protons and heavy ions, cause damage to the spacecrafts in different ways: the electronic circuit damages, the data corruption (memory errors), the degradation of the solar cells [5]. Hence, in this case, one would like to protect the electronics from the irradiation, to produce solar cells that better resist the ionic damage and to predict the duration of the normal operation of a spacecraft.

Furthermore, understanding the ion/matter interactions is highly important to fission

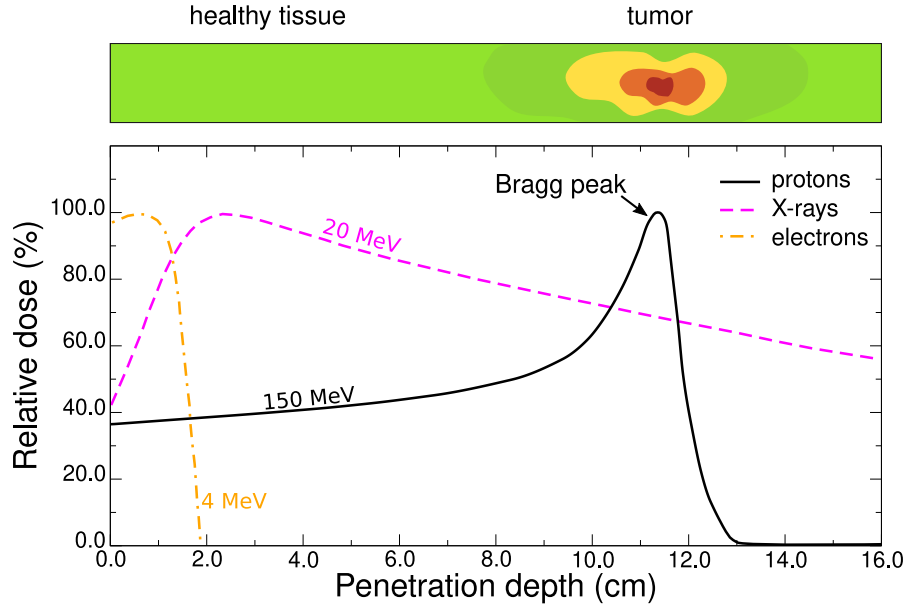


Figure I.1 : Irradiation dose as a function of the penetration depth in the case of proton, X-ray and electron irradiations. Data is taken from references [2, 3]. On the inset on the top of the image, an illustration of tissue with cancer is shown. In the presented case, the tumor is situated at a depth ≈ 12 cm. The maximum of the deposited dose in the case of the protonic irradiation coincides with the tumor location. The initial energies of protons, photons, and electrons are indicated next to the corresponding curves.

applications [6], imaging and processing of materials using the focused beam techniques [7, 8], helium ion microscopy [9], doping of semiconductors and more. The nuclear application will be described below.

The interaction between the irradiating ion and the target can be described by a stopping power, defined as the energy transfer from projectile to material per penetration distance

$$S = -\frac{dE_{proj}^{kin}}{dz}, \quad (1)$$

where E_{proj}^{kin} is the kinetic energy of the projectile and z is the path length. Dimensionally, the stopping power is a force and is usually presented in units of energy per distance. In this work, we present S in Ha/bohr (referred to atomic units, a.u.) or in keV/nm. Physically, the stopping power corresponds to a retarding (or drag) force due to the electrons and the nuclei of the target.

The mechanism of stopping depends on the ion velocity: At low velocities, the main projectile energy loss channel is the interaction with the nuclei of the target; At high velocities, the energy transfer is mediated through the electron excitations of the host material. In order to consider the stopping power velocity behavior in more details, we have taken an example of the α -particle irradiation in iron (Fig. I.2). One can see that the electronic

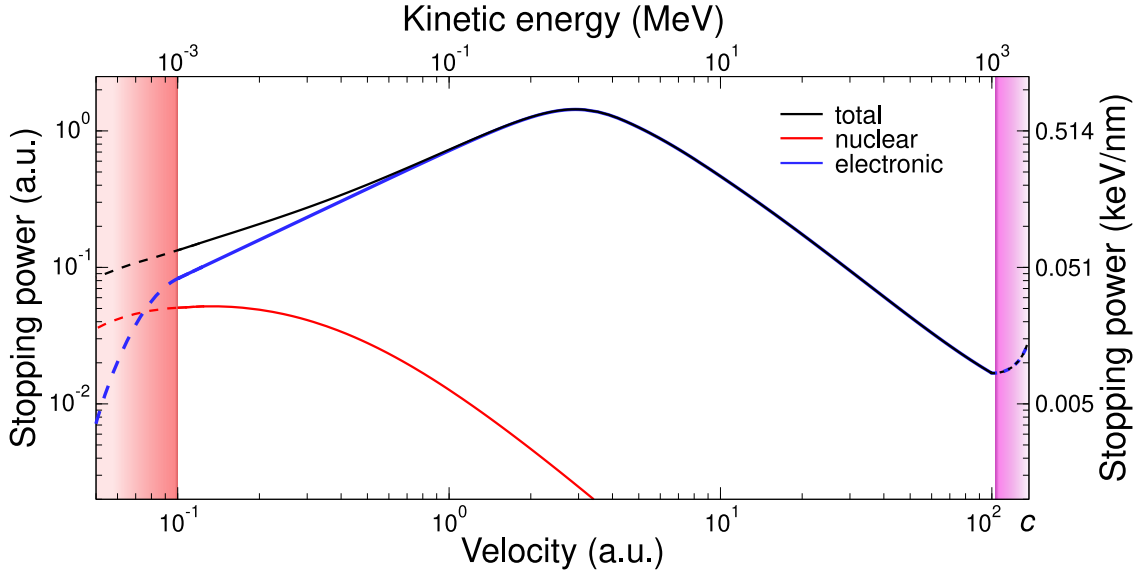


Figure I.2 : Stopping power of α -particle projectile in iron target. Stopping power is presented in atomic units (left y -axis) and in keV/nm (right y -axis). The bottom x -axis is the projectile velocity in atomic units and the top x -axis is the projectile kinetic energy in MeV. The red region on the left-hand side illustrates the nuclear stopping region, while the violet region on the right-hand side presents the region where the relativistic effects have a significant impact. The velocity scale on the graph is naturally limited by the speed of light, equal, in atomic units, to $c = 137.1$ a.u. The stopping power data (solid lines) are taken from the ASTAR database [10], while the dashed lines present a schematic continuation of curves in the “nuclear stopping” and the “relativistic” regions.

stopping is predominant for the projectile velocities starting from $v_{lim\ nuc} = 0.1$ a.u. There is a maximum of the stopping power. The projectile velocity corresponding to the stopping power peak is, typically, in the same order of magnitude as the Fermi velocity of the target material. For example, the Fermi velocity of iron is $v_F = 0.9$ a.u., whereas the peak velocity is $v = 2.9$ a.u.

In the limit of high projectile velocities, after the minimum (at $v \approx 100$ a.u.), the stopping power starts to increase due to the relativistic effects. One usually defines the projectile velocity, at which the relativistic effects become important as $v_{lim\ rel} \approx 0.87c$, where c is the speed of light [11, 12]. Numerically, this velocity is equal to $v_{lim\ rel} = 118.6$ a.u., which, for example, corresponds to the kinetic of proton $E^{H^+} = 12.9$ MeV and of α -particle $E^{He^{2+}} = 51.7$ MeV.

While the nuclear stopping power can be accurately modeled by the classical ion-ion interactions [13], the electronic excitations of the target material can be properly described only at the quantum-mechanical level. In addition, the electronic stopping power, being the major contribution to the ion/matter interactions, is central to all above-mentioned areas, including the nuclear domain.

In the nuclear material science, an accurate knowledge of the interaction between the

irradiating ion and the material is important for two reasons: First, such kind of interaction occurs directly during the nuclear reactor operation: Due to the nuclear reactions, the charged particles (for example, the fission products) interact with various materials (nuclear fuel, cladding, cables, etc.). Second, one often uses ionic beams in laboratory conditions in order to mimic the damage caused by neutrons. Indeed, the experiments related to neutrons are very expensive and difficult: To study the influence of neutron irradiation on some material, one needs to place a sample directly into the nuclear reactor. Such kind of experiments lasts for several years and requires extreme caution during the sample transportation and manipulation since the samples are activated then. On the other hand, the ionic beams are much less dangerous and easier to manipulate: Using the magnetic and electric fields, one can precisely select the ionic beam profile and energy, which is not possible in the case of neutrons. In addition, one can note the following advantages of the ionic beam approach: The experiments with ions are fast (a few hours), the samples do not have residual radioactivity, one can study the dose, flux or temperature effects on the irradiation damage, etc. Even if the interactions of neutrons and ions with matter are quite different, the experiments based on the ions can bring a lot of useful information at a lower cost and risk. From this perspective, the Joint Accelerators for Nano-science and Nuclear Simulation (JANNUS), one part of which is in CEA Saclay, were created [14, 15]. The main difference between the neutron and ion irradiations is the electronic stopping, which is completely absent for neutrons and which plays a major contribution to the stopping for ions. Therefore, the understanding and the description of the electronic excitations for various types of ionic projectiles and targets are indirectly necessary for the studies of the neutron-induced effects in nuclear materials using the ionic beams.

In the present work, we are thus interested in the modeling of the electronic stopping power (S_e) of the ionic projectiles. In particular, we will focus on the projectile velocity range $v_{lim\ nuc} \leq v \leq v_{lim\ rel}$.

Since the electronic stopping phenomenon was conceived, a large number of models has been elaborated. For a historical review of the problem, see, for example, references [16, 17]. Here we will mention only the most important stages. Using the binary collision model (BCA) between the target electrons (treated classically) and the projectile, Bethe, in 1930 [18], derived the electronic stopping power expression of the following form

$$S_e = \frac{B}{v^2} \ln(C \times v^2), \quad (2)$$

where B and C are some constants that depend on the projectile charge Z and the density of the target electrons n . It turns out that this approximation works very well for high projectile velocities while giving a wrong position of the stopping power peak and having even the divergent behavior for small v (see Fig. I.3).

Later, in 1947, Fermi and Teller [19] provided an expression for the low-velocity limit. The stopping power, within this model, is linear in v (which is correct for metals). Having these two models in mind, one can already note the general trends of the electronic stopping power velocity dependence (Fig. I.3): It linearly increases with v at small projectile velocities and decays approximatively as $1/v^2$ after the peak.

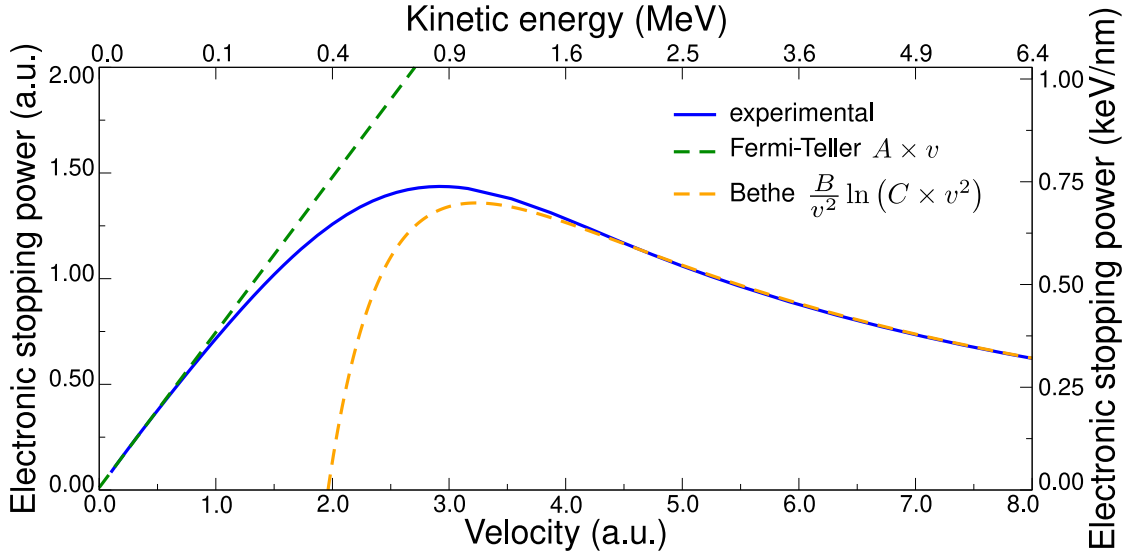


Figure I.3 : Electronic stopping power of α -particle in iron: Comparison between the experimental data (taken from [10]) and early theoretical models.

Subsequent efforts were aimed at improving the stopping power description at the whole velocity range, in particular, around the stopping power peak. There exist two main strategies to do so.

First, one can use the semi-empirical theories that incorporate a lot of parameters fitted from experiments. The most known example presenting this approach is the code SRIM [20], which is considered as a reference by experimentalists [21–23]. The SRIM code provides accurate stopping power values in the case when one has enough experimental points for a given projectile and target material and for a given projectile velocity. However, if the experimental data are absent, the SRIM extrapolation can be wrong and using this approach is then risky.

Another way is to improve the level of the theory, having as a goal, zero adjustable parameters. From this viewpoint, in 1963, Linhard proposed the first fully *ab initio* model of the stopping power in an electron gas within the linear response theory [24]. The first non-linear response model was developed by Echenique and coworkers in 1986 [25]. Nevertheless, these models do not take the atomic structure of a real material into account, therefore, they are able to produce acceptable results only for some special classes of systems. For example, these models failed to take into account the band structure effects [16].

The electronic structure calculations for a real material is a challenging and computationally hard task. The invention of density-functional theory (DFT) in 1964 by Hohenberg and Kohn [26] has opened access to the *ab initio* calculations of the ground state properties with a relatively low computational cost. However, the electronic stopping power phenomenon is related to a strongly excited state of matter. Therefore, DFT description could only bring some improvements to the existing models [27].

A proper description of the electronic excitations became possible only after the invention of the time-dependent DFT (TDDFT) [28] in 1984 by Runge and Gross. At that time the computational facilities did not allow the researchers to perform the all-response TDDFT and, in 1996, the linear-response approximation to TDDFT (LR-TDDFT) was elaborated by Petersilka, Gossman, and Gross [29].

The first linear response calculations of the electronic stopping power based on density-functional theory (LR-TDDFT) were performed by Pitarke and coworkers [30–32]. These calculations took into account explicitly the atomic structure of the target, but they were not fully converged. Then, recently, Shukri, Bruneval and Reining [33, 34] improved the LR-TDDFT stopping power calculations in terms of the converged cutoff energy, the number of empty states and the inclusion of the semi-core electrons [33, 34]. The calculated stopping power in this way compared well with experiment, in the case of proton irradiation, for a wide range of target materials and for the whole velocity range. This method had a significant limitation though: Being a perturbative approach, it failed in the case of the projectile charges larger than $Z = 1$.

With the continuously growing computational power, it has become possible to perform the all-response real-time TDDFT (RT-TDDFT) calculations. Nowadays, this approach presents the best compromise between the accuracy and the size of atomic systems one can deal with for the electronic stopping power simulations. In addition, within this method, one has direct access to the time-dependent properties, such as the total energy, electronic level occupations, electronic density, etc. Hence, this approach is expected to be the best tool to provide the electronic stopping power for any kind of projectile and any type of target material for the whole range of projectile velocities of interest. We should mention that while the target electrons are treated in a purely quantum-mechanical level, the projectile and the target nuclei are treated as classical charged particles.

Hence, in this work, our aim is to develop an *ab initio* code based on RT-TDDFT for the electronic stopping power calculations of ionic projectiles. Since simpler models (LR-TDDFT or even Bethe) work well for high projectile velocities (see, for example, Fig. I.3), we will mostly focus on this work on the projectile velocity range $0.1 \text{ a.u.} \leq v \leq 8.0 \text{ a.u.}$

Choosing the RT-TDDFT code implementation strategy, we were guided by the following considerations.

- First, in order to avoid the development from the scratch of the standard ground-state DFT part, we were looking at an open-source platform, which could provide not only the ground-state self-consistent calculations but also the Hamiltonian evaluation on the fly for the time propagation.

- Second, the ionic stopping power calculations are special in the sense that *all* the target electrons can be excited by an energetic projectile, including the core electrons. Usually, the valence electrons constitute the “interesting physics” of the system. For example, the chemical reactions - creation and breaking of the chemical bonds, charge transfer, optical absorption (in the weak field regime), etc. Therefore, most often the pseudopotential technique, which allows one to treat the core electrons implicitly, is quite accurate and an effective technique used in the real-space grid or plane-wave codes. However, for stopping power calculations, one needs to incorporate as many electrons as possible explicitly in the

simulations, which becomes computationally very expensive in the plane-wave and real-space grid codes [35]. Hence, we have decided to create our implementation based on an *all-electron localized basis* code. By the construction of the localized basis, the cost of the description of the core electrons is equal to (or, sometimes, even smaller than) the one of the valence electrons, which could be beneficial for the considered application.

- Third, though the electronic stopping power calculations from RT-TDDFT is an emergent topic, significant results have been already produced mostly using the plane-wave [35, 36] and the real-space grid [37, 38] codes (though, localized basis implementations also exist [39–41]). One of the difficulties of these approaches is an insufferable CPU time consumption and implementation difficulties related to the hybrid exchange-correlation functionals. That is why a great part of the stopping power calculations was performed using the standard LDA functional. Therefore, a possibility to use the modern hybrid functionals in the stopping power calculations could be a perspective direction for a new implementation.

- And finally, because of the complexity of the problem (long real-time trajectories, large simulation boxes, hybrid functionals, etc.), the overall computational cost is a non-negligible criterion for the choice of the development strategy.

Combining all the mentioned issues, we select the Gaussian localized basis set code MOLGW [42] as the development platform for a new RT-TDDFT implementation. A detailed argumentation for such choice is discussed in chapter 2. Thus, our goal is to develop a code based on RT-TDDFT and to use it for the electronic stopping power calculations of ions.

The present manuscript is organized as follows:

- In chapter 1 we will discuss the fundamental aspects of RT-TDDFT, starting from the basic DFT. As well, the general idea of the *ab initio* stopping power calculation will be discussed.
- Chapter 2 is dedicated to the details of RT-TDDFT development in the localized Gaussian basis code. The benchmarking of the code using the optical excitations will be also presented.
- In chapter 3 we describe the methodology of the electronic stopping power calculation with our code. In particular, we will consider the convergence of the different simulation parameters: The simulation box size, the time step, the Gaussian basis set problem, etc.
- The results of the electronic stopping power calculations using the converged parameters are presented in chapter 4.

CHAPTER 1

Theoretical background

This chapter is dedicated to the formulation of the fundamental concepts and practical issues of the Density-Functional Theory (DFT) and the Time-Dependent Density-Functional Theory (TDDFT). TDDFT has a lot of common points and ideas with the ground-state DFT on the fundamental level (one-to-one correspondence theorems, Kohn-Sham equations, exchange-correlation functionals, etc.). In addition, most often, the initial state of a TDDFT calculation is chosen as the ground-state obtained from DFT.

Therefore, in this chapter we will first consider the basic ground-state DFT: the celebrated Hohenberg and Kohn theorem, the Kohn-Sham approach as well as some particular problems and practical applications: spin-dependent DFT, exchange and correlation functionals approximations. Then we will use the concepts of the ground-state DFT in the time-dependent case. The similarities and principle differences between DFT and TDDFT will be also discussed.

Finally, we will discuss the general methodology of the electronic stopping power calculations from the RT-TDDFT simulations. We will, in particular, consider the fixed projectile trajectory technique. Then, the principal approaches to obtain the averaged stopping power will be discussed.

1.1 Ground state density-functional theory (DFT)

Atomic units

Throughout this work Hartree atomic units (a.u.) are employed. Therefore, we would like first to briefly discuss the conversions between SI and atomic units for the physical quantities used in this work. Atomic system of units is obtained by setting the reduced

Planck's constant, free-electron mass and charge to 1: $\hbar = m = e = 1$. Table 1.1 lists the conversion between SI and atomic unit systems. Detailed derivations and the complete list of constants can be found, for example, in [43].

Physical quantity	Interpretation	Atomic units	SI units
Angular momentum	Reduced Planck's constant	\hbar	1.05457×10^{-34} Js
Mass	Free-electron mass	m_e	9.10938×10^{-31} kg
Charge	Absolute value of free-electron charge	e	1.60218×10^{-19} C
Length	Bohr radius of the hydrogen atom	$a_0 = \frac{4\pi\epsilon_0\hbar^2}{me^2}$	5.29177×10^{-11} m
Velocity	Electron velocity in the first Bohr orbit	$v_0 = \frac{e^2}{4\pi\epsilon_0}$	2.18769×10^6 m/s
Time	Time of one revolution of an electron in the first Bohr orbit	$\tau_0 = \frac{a_0}{v_0}$	2.41888×10^{-17} s
Energy	2× ionization energy of the hydrogen atom	$E_H = \frac{e^2}{4\pi\epsilon_0 a_0}$	4.35974×10^{-18} J (27.21138 eV)
Electric field	Electric field of the charge e at the Bohr radius distance	$ \mathbf{E}_0 = \frac{e}{4\pi\epsilon_0 a_0^2}$	5.14221×10^{11} V/m
Electric dipole moment	Dipole moment of two charges e separated by a_0	$ \mathbf{d} = ea_0$	8.47837×10^{-30} Cm (2.54217 D)

Table 1.1 : Atomic system of units.

1.1.1 The many-body framework

The Born–Oppenheimer approximation

Let us consider an atomic system (atom, molecule or solid) with N electrons and M nuclei. The ground state of the system is given by the stationary Schrödinger equation

$$\hat{H}_{tot}(\mathbf{r}_1, \dots, \mathbf{r}_N, \mathbf{R}_1, \dots, \mathbf{R}_M)\Psi_{tot}(\mathbf{x}_1, \dots, \mathbf{x}_N, \mathbf{R}_1, \dots, \mathbf{R}_M) = E_{tot}\Psi_{tot}(\mathbf{x}_1, \dots, \mathbf{x}_N, \mathbf{R}_1, \dots, \mathbf{R}_M), \quad (1.1)$$

where \hat{H}_{tot} is the many-body Hamiltonian of the system, Ψ_{tot} is the wave function that includes both electrons and nuclei, \mathbf{R}_a is the coordinate of a nucleus a , $\mathbf{x}_i = (\mathbf{r}_i, \sigma_i)$ is an i space-spin electronic coordinate: $\mathbf{r}_i = (x_i, y_i, z_i)$, $\sigma_i = \uparrow$ or \downarrow and E_{tot} is the total energy of

the system. In the absence of external fields, the complete many-body Hamiltonian in the non-relativistic approximation reads, in atomic units,

$$\hat{H}_{tot} = -\frac{1}{2} \sum_{i=1}^N \nabla_i^2 - \frac{1}{2} \sum_{a=1}^M \frac{1}{M_a} \nabla_a^2 - \sum_{i=1}^N \sum_{a=1}^M \frac{Z_a}{|\mathbf{r}_i - \mathbf{R}_a|} + \sum_{i=1}^N \sum_{j>i}^N \frac{1}{|\mathbf{r}_i - \mathbf{r}_j|} + \sum_{a=1}^M \sum_{b>a}^M \frac{Z_a Z_b}{|\mathbf{R}_a - \mathbf{R}_b|}, \quad (1.2)$$

where M_a and Z_a are the mass and the atomic number of a nucleus a ; the Laplacian operators ∇_i^2 and ∇_a^2 are the differential operators with respect to the coordinates of an electron i and a nucleus a . The first two terms in the expression are the kinetic energies of the electrons and the nuclei respectively, the third term is the Coulomb attraction between electrons and nuclei, the fourth and fifth terms describe the electron-electron and nucleus-nucleus repulsions respectively.

The Born-Oppenheimer (BO) approximation is based on the fact that the nuclear mass is much larger than the electronic one, therefore the electronic and nuclear degrees of freedom can be decoupled. This means that we can factorize the total wave function as follows

$$\Psi_{tot} = \Phi_{nucl}(\mathbf{R}_1, \dots, \mathbf{R}_M) \Psi_{elec}(\mathbf{x}_1, \dots, \mathbf{x}_N; \{\mathbf{R}_a\}), \quad (1.3)$$

where Φ_{nucl} and Ψ_{elec} are the nuclear and electronic wave functions respectively. The electronic wave function depends *explicitly* on the electronic space-spin coordinates and *parametrically* on the nuclear coordinates.

The electronic problem

In this work, we are interested in the electronic problem and we consider the nuclei of the system to be *fixed*. Therefore, the nuclear kinetic energy term in equation 1.2 is zero. The nucleus-nucleus repulsion term is just a constant in the case of fixed nuclei, therefore it has to be taken into account only in the total energy expression, but not in the Hamiltonian expression. Hereafter we omit the index “*elec*” for the quantities related to the electronic degrees of freedom but we keep the “*nucl*” index for nuclear quantities which will be rarely mentioned in this chapter.

We can write the electronic Schrödinger equation

$$\hat{H}\Psi = E\Psi. \quad (1.4)$$

This equation can be rewritten in the representation independent Dirac formalism

$$\hat{H}|\Psi\rangle = E|\Psi\rangle. \quad (1.5)$$

The electronic Hamiltonian is

$$\hat{H} = -\frac{1}{2} \sum_{i=1}^N \nabla_i^2 + \sum_{i=1}^N \sum_{j>i}^N \frac{1}{|\mathbf{r}_i - \mathbf{r}_j|} - \sum_{i=1}^N \sum_{a=1}^M \frac{Z_a}{|\mathbf{r}_i - \mathbf{R}_a|} = \hat{T} + \hat{W}_{ee} + \hat{V}_{ne}, \quad (1.6)$$

where we have defined the kinetic energy operator \hat{T} , the electron-electron interaction operator \hat{W}_{ee} and the nuclei-electron interaction operator \hat{V}_{ne} .

One can note from the electronic Hamiltonian expression 1.6 that the only term which makes the difference between one system (solid, atom or molecule) and another is the nuclei-electron interaction operator \hat{V}_{ne} , which is a one-particle multiplicative operator. We denote the corresponding nuclear potential as $v_{ne}(\mathbf{r})$ as follows

$$v_{ne}(\mathbf{r}_i) = - \sum_{a=1}^M \frac{Z_a}{|\mathbf{r}_i - \mathbf{R}_a|}. \quad (1.7)$$

In this way, the nucleus-electron interaction operator reads

$$\hat{V}_{ne} = \sum_{i=1}^N v_{ne}(\mathbf{r}_i). \quad (1.8)$$

The total energy of the system can be found as the sum of the electronic and nuclear energy

$$E_{tot} = E + E_{nucl} = E + \sum_{a=1}^M \sum_{b>a}^M \frac{Z_a Z_b}{|\mathbf{R}_a - \mathbf{R}_b|}. \quad (1.9)$$

The principal quantity of interest in the electronic structure calculations is the ground-state energy E_0 . According to the variational theorem, this quantity can be found from the minimization of the expectation value $\langle \Psi | \hat{H} | \Psi \rangle$ over the normalized electronic wave functions Ψ

$$E_0 = \min_{\Psi} \langle \Psi | \hat{H} | \Psi \rangle, \quad \langle \Psi | \Psi \rangle = 1. \quad (1.10)$$

The electronic wave function $\Psi(\mathbf{x}_1, \mathbf{x}_2, \dots, \mathbf{x}_N)$ is a complex function in the $4N$ -dimensional configuration space (3 real-space degrees of freedom and one spin component per electron). In such a way, $|\Psi(\mathbf{x}_1, \mathbf{x}_2, \dots, \mathbf{x}_N)|^2 d\mathbf{x}_1, d\mathbf{x}_2, \dots, d\mathbf{x}_N$ is the probability to find the system in the $4N$ -dimensional volume $d\mathbf{x}_1, d\mathbf{x}_2, \dots, d\mathbf{x}_N$. Because electrons are fermions, the electronic wave function must be antisymmetric with respect to the exchange of two coordinates \mathbf{x}_i and \mathbf{x}_j

$$\Psi(\mathbf{x}_1, \dots, \mathbf{x}_i, \dots, \mathbf{x}_j, \dots, \mathbf{x}_N) = -\Psi(\mathbf{x}_1, \dots, \mathbf{x}_j, \dots, \mathbf{x}_i, \dots, \mathbf{x}_N). \quad (1.11)$$

In order to find the one-electron density from the wave function let us refer to the electronic density operator, which for the case of N particles is defined as

$$\hat{\rho}(\mathbf{r}) = \sum_i^N \hat{\rho}(\mathbf{r}_i) = \sum_i^N \delta(\mathbf{r}_i), \quad (1.12)$$

where $\delta(\mathbf{r})$ is the Dirac delta-function. Then the one-electron density can be found as

$$\begin{aligned} \rho(\mathbf{r}) &= \langle \Psi | \hat{\rho}(\mathbf{r}) | \Psi \rangle = \underbrace{\int \dots \int}_N \Psi^*(\mathbf{x}_1, \dots, \mathbf{x}_N) \sum_i^N \delta(\mathbf{r}_i - \mathbf{r}) \Psi(\mathbf{x}_1, \dots, \mathbf{x}_N) d\mathbf{x}_1 \dots \mathbf{x}_N \\ &= \sum_i^N \underbrace{\int \dots \int}_{N-1} |\Psi(\mathbf{x}_1, \dots, \mathbf{r}, \sigma_i, \dots, \mathbf{x}_N)|^2 d\sigma_1 \dots d\sigma_N d\mathbf{r}_1 \dots d\mathbf{r}_{i-1} d\mathbf{r}_{i+1} \dots d\mathbf{r}_N \end{aligned} \quad (1.13)$$

In this expression, the integration over spin degrees of freedom σ_i means just a summation over spin up σ_\uparrow and spin down σ_\downarrow . Due to the antisymmetric property of the wave function (equation 1.11) one can see that all the terms under the summation are identical. Therefore, the final expression of the one-electron density is the following

$$\rho(\mathbf{r}) = N \int \dots \int |\Psi(\mathbf{r}, \sigma_1, \mathbf{x}_2, \dots, \mathbf{x}_N)|^2 d\sigma_1 d\mathbf{x}_2 \dots d\mathbf{x}_N, \quad (1.14)$$

where the integration is performed over all space coordinates except \mathbf{r}_1 and over all spin coordinates σ_i . This density is normalized to the number of electrons

$$\int \rho(\mathbf{r}) d\mathbf{r} = N. \quad (1.15)$$

1.1.2 Hohenberg-Kohn theorem

One-to-one correspondence

In this section, we will consider an *arbitrary* external potential $v(\mathbf{r})$ instead of the specific electron-nuclei potential $v_{ne}(\mathbf{r})$. For example, this potential $v(\mathbf{r})$ can include $v_{ne}(\mathbf{r})$ and some additional external field. Let us call the corresponding operator to $v(\mathbf{r})$ - \hat{V} .

From the stationary Schrödinger equation 1.1 and from the one-electron density definition 1.14 it is seen that there is a direct mapping from the external potential to the ground-state electronic density $\hat{V} \rightarrow \rho(\mathbf{r})$: Having a given set of nuclei coordinates $\{\mathbf{R}_a\}$, the Schrödinger equation provides the ground-state wave function corresponding to this potential $\hat{V} \xrightarrow{1} \Psi$. Then, from the wave function, one can calculate the ground-state one-electron density $\Psi \xrightarrow{2} \rho(\mathbf{r})$. In other words, the map between \hat{V} and $\rho(\mathbf{r})$ is (at least) surjective: 1) each wave function Ψ corresponds to at least one potential \hat{V} and 2) each density $\rho(\mathbf{r})$ corresponds to at least one wave function Ψ . The Hohenberg-Kohn theorem (1964, [26]) shows that this mapping is *bijective*: two different potentials \hat{V} and \hat{V}' necessarily correspond to two different wave functions Ψ and Ψ' , which correspond to two different one-electron densities $\rho(\mathbf{r})$ and $\rho'(\mathbf{r})$ and *vice versa* (see Fig. 1.1). This theorem can be proven using the variational principle 1.10.

Since the observables are determined by the wave function, the ground-state expectation value of *any* observable \mathcal{O} is also a unique functional of the ground-state density

$$\langle \Psi[\rho] | \hat{\mathcal{O}} | \Psi[\rho] \rangle = \mathcal{O}[\rho]. \quad (1.16)$$

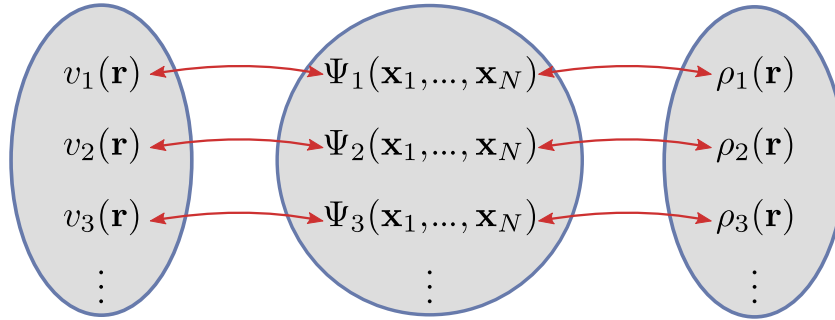


Figure 1.1 : Schematic representation of the bijective mapping between the set of external potentials $v(\mathbf{r})$, the set of wave functions $\Psi(\mathbf{x}_1, \dots, \mathbf{x}_N)$ and the set of one-electron densities $\rho(\mathbf{r})$.

In other words, the Hohenberg-Kohn theorem states that the potential $v(\mathbf{r})$ is a *unique* functional of the ground-state density. We consider that two potentials are equivalent if they differ not more than by an additive constant. Though the Hohenberg-Kohn theorem is valid for any form of potential $v(\mathbf{r})$, let us briefly demonstrate the fact that the potential is a functional of the ground-state density for the case of Coulombic potentials $v_{ne}(\mathbf{r})$ (which corresponds to the case of any material in the absence of external fields): It is seen from equation 1.7 that any Coulombic potential can be “reconstructed” having 1) the set of the nuclei coordinates $\{\mathbf{R}_a\}$ and 2) the nuclear charges Z_a . Around the nuclei, the wave function as well as the electronic density have a cusp behavior: a singularity at which the derivative over \mathbf{r} is not continuous and corresponds to the maximal value of the wave function (or of the electronic density). Therefore, the locations of the maxima of the density provide information about the nuclei positions. Moreover, it can be shown (Kato’s theorem [44],[45]) that the derivative of the spherical average of the density, $\bar{\rho}(\mathbf{r})$, around a nucleus a is

$$\left. \frac{\partial \bar{\rho}(r)}{\partial r} \right|_{r=R_a} = -2Z_a \bar{\rho}(R_a). \quad (1.17)$$

Due to this expression, the nuclear charges $\{Z_a\}$ can be found from the density cusps derivatives. In addition, one can find the number of electrons in the system from the integration of the electronic density (equation 1.15).

Universal functional

Since the electronic kinetic energy \hat{T} and the electron-electron repulsion term \hat{W}_{ee} (equation 1.6) are the same for any material, and since the wave function is a unique functional of the electronic density, one can define the universal density functional

$$F_{HK}[\rho] = \langle \Psi[\rho] | \hat{T} + \hat{W}_{ee} | \Psi[\rho] \rangle. \quad (1.18)$$

The F_{HK} functional is universal in the sense that it does not depend on the external potential \hat{V} . Then, adding the electron-nucleus contribution, we can express the total

energy of any electronic system (here we omit the ion-ion interaction energy)

$$E[\rho] = F_{HK}[\rho] + \int d\mathbf{r} v_{ne}(\mathbf{r})\rho(\mathbf{r}). \quad (1.19)$$

Since all the terms in this equation are functionals of the density, the ground-state energy E_0 of the system can be found from the minimization of the total electronic energy $E[\rho]$ over the electronic density (and not over the electronic wave function)

$$E_0 = \min_{\rho} \left\{ F_{HK}[\rho] + \int d\mathbf{r} v_{ne}(\mathbf{r})\rho(\mathbf{r}) \right\}. \quad (1.20)$$

This equation can be also rewritten in the following form

$$\left. \frac{\delta E[\rho]}{\delta \rho} \right|_{\rho_0} = 0, \quad (1.21)$$

where ρ_0 is the electronic density which minimizes the total electronic energy. It is called *the ground-state electronic density*.

These three statements - invertibility of the mapping, the existence of the universal density functional and the variational property constitute the Hohenberg-Kohn theorem.

1.1.3 Kohn-Sham scheme

Even if the $F_{HK}[\rho]$ functional exists, there is no procedure to find it and the direct approximations of the functional are complicated and not accurate enough. Therefore, in 1965 Walter Kohn and Lu Jeu Sham have proposed [46] to represent the problem of interacting N electrons as a problem of some fictitious independent electron system that yields *the same* ground-state density $\rho_0(\mathbf{r})$. In this case, all the ground-state properties of such a system would be similar to the interacting one. Replacing the many-body problem by a problem of non-interacting particles brings a tremendous simplification. The price to pay is to hide the complexity of the problem in the external potential. Let us consider this method in more detail. First, we will consider the non-interacting electron problem without detailing the expression of the external potential. And secondly, we will consider the way to represent the interacting problem via the non-interacting one.

Non-interacting electron system

Let us consider an auxiliary system of N electrons which *do not interact*. The Hamiltonian of this system, \hat{H}_s , reads

$$\hat{H}_s = \hat{T} + \hat{V}_s, \quad (1.22)$$

where \hat{T} is the kinetic energy operator as introduced before (equation 1.6) and \hat{V}_s is some external potential operator (we do not precise its expression for the moment). This Hamiltonian can be represented as a sum of one-particle Hamiltonians \hat{h}_s

$$\hat{H}_s = \sum_i^N \hat{h}_s = \sum_i^N \left(-\frac{1}{2} \nabla_i^2 \right) + \sum_i^N v_s(\mathbf{r}). \quad (1.23)$$

The ground-state electronic wave function of this system $\Phi_s(\mathbf{x}_1, \dots, \mathbf{x}_N)$ can be *exactly* represented as a single Slater determinant

$$\Phi_s(\mathbf{x}_1, \dots, \mathbf{x}_N) = \frac{1}{\sqrt{N!}} \det [\varphi_i(\mathbf{x}_j)] = \frac{1}{\sqrt{N!}} \begin{vmatrix} \varphi_1(\mathbf{x}_1) & \varphi_2(\mathbf{x}_1) & \dots & \varphi_N(\mathbf{x}_1) \\ \varphi_1(\mathbf{x}_2) & \varphi_2(\mathbf{x}_2) & \dots & \varphi_N(\mathbf{x}_2) \\ \vdots & \vdots & & \vdots \\ \varphi_1(\mathbf{x}_N) & \varphi_2(\mathbf{x}_N) & \dots & \varphi_N(\mathbf{x}_N) \end{vmatrix}, \quad (1.24)$$

where $\{\varphi_i(\mathbf{x}_k)\}_{i=1}^N$ is the set one-electron wave functions, which are orthonormal, namely,

$$\langle \varphi_i | \varphi_j \rangle = \int d\mathbf{x} \varphi_i^*(\mathbf{x}) \varphi_j(\mathbf{x}) = \delta_{ij}. \quad (1.25)$$

One should mention that in the interacting electron case the wave function $\Psi(\mathbf{x}_1, \dots, \mathbf{x}_N)$ is a linear combination of Slater determinants, also called multi-determinant.

In the spin-restricted case, the single electron wave functions can be factorized in the following way

$$\varphi_i(\mathbf{x}) = \varphi_i(\mathbf{r}) \chi_{\sigma_i}(\sigma), \quad (1.26)$$

where $\varphi_i(\mathbf{r})$ is a spatial orbital of i^{th} electron, $\chi_{\sigma_i}(\sigma) = \delta_{\sigma_i, \sigma}$ is the spin part and σ_i is the spin of an electron i . The case of spin-unrestricted calculations will be considered in section 1.1.4.

Due to the simple form of the non-interacting Hamiltonian (equation 1.23), the stationary Schrödinger equation

$$\hat{H}_s \Phi_s = E \Phi_s, \quad (1.27)$$

can be divided on N identical one-particle equations (we have integrated here over the spin variables)

$$\hat{h}_s \varphi_i(\mathbf{r}) = \left[-\frac{1}{2} \nabla^2 + v_s(\mathbf{r}) \right] \varphi_i(\mathbf{r}) = \varepsilon_i \varphi_i(\mathbf{r}), \quad (1.28)$$

where ε_i are the one-electron energies. Here we have omitted the index i in the Laplacian operator ∇^2 because there is only one space vector \mathbf{r} in an equation i (in contrast to the complete Schrödinger equation 1.23).

The one-electron density of the non-interacting system has a much simpler form than in the interacting case. To get this expression in a proper way, one can substitute the total non-interacting wave function 1.24 into the density expression 1.14, then one has

$$\rho_s(\mathbf{r}) = \sum_{i=1}^N |\varphi_i(\mathbf{r})|^2. \quad (1.29)$$

Then we can apply the Hohenberg-Kohn theorem for this case and write the unique energy functional

$$E_s[\rho] = T_s[\rho] + \int d\mathbf{r} v_s(\mathbf{r})\rho(\mathbf{r}). \quad (1.30)$$

$T_s[\rho]$ is the non-interacting kinetic energy functional

$$T_s[\rho] = \langle \Phi_s[\rho] | \hat{T} | \Phi_s[\rho] \rangle = \sum_i^N \int d\mathbf{r} \varphi_i^*(\mathbf{r}) \left(-\frac{1}{2} \nabla^2 \right) \varphi_i(\mathbf{r}). \quad (1.31)$$

The variational equation $\delta E_s[\rho] = 0$ will provide the ground-state density of this system $\rho_{s0}(\mathbf{r})$.

Connection to the interacting electron case

Unfortunately, in the real electronic system, the presence of the electron-electron interaction term \hat{W}_{ee} complicates the problem. The gist of the Kohn-Sham method is to find such external potential for the non-interacting system $v_s(\mathbf{r})$ which would lead to exactly the same ground-state electronic density as in the interacting system ($\rho_{s0}(\mathbf{r}) = \rho_0(\mathbf{r})$). So, here we assume the existence of such an external potential, then the uniqueness of this potential is guaranteed by the Hohenberg-Kohn theorem. In this way, one could treat the multi-electron problem in the single-electron fashion: The external potential $v_s(\mathbf{r})$ would correspond to the unique *single electron* wave function Ψ_s which provides the ground-state density $\rho_0(\mathbf{r})$.

In order to achieve this, the universal functional $F_{HK}[\rho]$ (equation 1.18) must be decomposed as follows

$$F_{HK}[\rho] = T_s[\rho] + E_{Hxc}[\rho], \quad (1.32)$$

where $T_s[\rho]$ is the universal kinetic energy functional of *non-interacting* particles as introduced before (equation 1.31) and the remaining $E_{Hxc}[\rho]$ part is called the Hartree-exchange-correlation functional.

Then, the minimization procedure to find the ground-state energy E_0 (equation 1.20) can be changed from the minimization over the density ρ to the minimization over the non-interacting wave function Φ_s

$$E_0 = \min_{\Phi_s} \left\{ \langle \Phi_s | \hat{T} + \hat{V}_{ne} | \Phi_s \rangle + E_{Hxc}[\rho] \right\}. \quad (1.33)$$

The Hartree-exchange-correlation functional consists of two parts

$$E_{Hxc}[\rho] = E_H[\rho] + E_{xc}[\rho], \quad (1.34)$$

where $E_H[\rho]$ is the Hartree functional, the classical density-density interaction energy,

$$E_H[\rho] = \frac{1}{2} \iint \frac{\rho(\mathbf{r}_1)\rho(\mathbf{r}_2)}{|\mathbf{r}_1 - \mathbf{r}_2|} d\mathbf{r}_1 d\mathbf{r}_2. \quad (1.35)$$

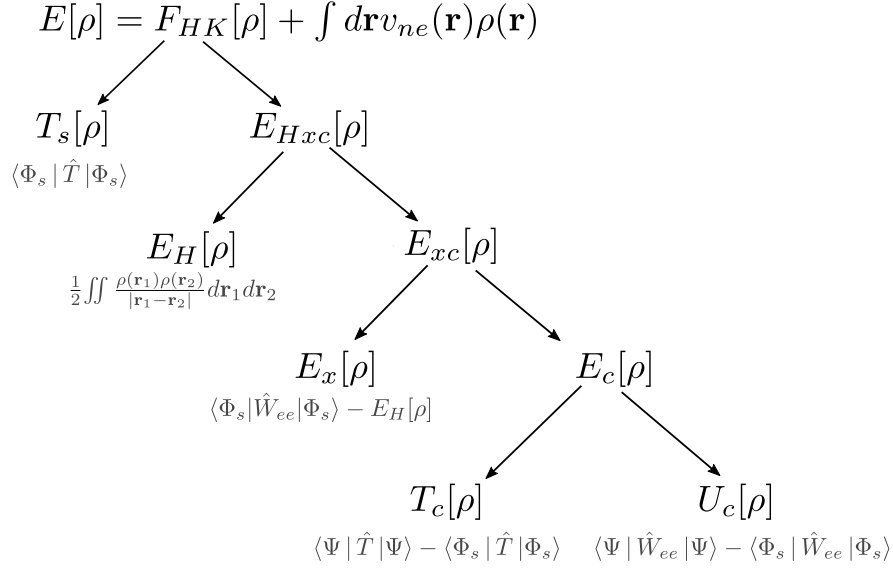


Figure 1.2 : The hierarchy of the Kohn-Sham approach functionals. All functionals definitions and expressions can be found in equations 1.19, 1.32 - 1.40.

$E_{xc}[\rho]$ is the exchange-correlation energy functional which one needs to approximate. This functional, in its turn, is usually represented as a sum of the exchange $E_x[\rho]$ and the correlation $E_c[\rho]$ functionals

$$E_{xc}[\rho] = E_x[\rho] + E_c[\rho]. \quad (1.36)$$

The exchange functional is defined as the difference between the electron-electron repulsion energy calculated with the non-interacting wave function Φ_s and the Hartree energy $E_H[\rho]$

$$E_x[\rho] = \langle \Phi_s | \hat{W}_{ee} | \Phi_s \rangle - E_H[\rho]. \quad (1.37)$$

The correlation functional then reads

$$E_c[\rho] = \langle \Psi[\rho] | \hat{T} + \hat{W}_{ee} | \Psi[\rho] \rangle - \langle \Phi_s[\rho] | \hat{T} + \hat{W}_{ee} | \Phi_s[\rho] \rangle, \quad (1.38)$$

where we have defined the kinetic energy contribution as the difference between the kinetic energy calculated with the complete interacting wave function $\Psi[\rho]$ and the non-interacting one $\Phi_s[\rho]$

$$T_c[\rho] = \langle \Psi[\rho] | \hat{T} | \Psi[\rho] \rangle - \langle \Phi_s[\rho] | \hat{T} | \Phi_s[\rho] \rangle. \quad (1.39)$$

In a similar manner, we have defined the potential contribution

$$U_c[\rho] = \langle \Psi[\rho] | \hat{W}_{ee} | \Psi[\rho] \rangle - \langle \Phi_s[\rho] | \hat{W}_{ee} | \Phi_s[\rho] \rangle. \quad (1.40)$$

Because of a large quantity of functionals definitions, we find it pertinent to present all the functionals definitions and their hierarchy in a schematic way (Fig. 1.2).

Quality of approximation - example

As seen from the scheme 1.2, the knowledge of the Hartree-exchange correlation functional $E_{Hxc}[\rho]$ allows one to find the total electronic energy *exactly*. However, as usually happens in science, the exact expression of this functional, as well as for $F_{HK}[\rho]$, is not known and the functionals approximations should be applied. Nevertheless, due to its accuracy and computational cost, DFT is one of the most used theories for the electronic structure calculations for solids as well as for molecules. In order to demonstrate the reason for the success of this theory, let us have a look at a numerical application of DFT. Let us take the Ne atom as an example. Since Ne (10 electrons) is a relatively simple system, higher accuracy calculations are also possible, namely, configuration-interaction [47], the method which is used as the reference for the quantum chemical calculations. Using this technique, we can calculate exactly the kinetic and the electron-electron interaction energies of *interacting* electrons and compare them to the Kohn-Sham quantities. Table 1.2 presents the energy contributions for the Ne atom.

Interacting system	T	W_{ee}	V	E_0	
	128.9	53.2	-311.1	-129.0	
Kohn-Sham system	T_s	E_H	E_{xc}	V	E_0
	128.6	66.1	-12.2	-311.1	-128.6

Table 1.2 : Energy contribution values (in Ha) for Ne atom. *Interacting system* section corresponds to a more precise and more time-consuming method - configuration-interaction [48]. *Kohn-Sham system* section corresponds to the DFT calculation using the PBE functional (in section 1.2.2 we detail this functional approximation).

The total ground-state energy is calculated in DFT within 0.3% of the error, which shows a very good quality of DFT calculations (at least for similar systems). It is seen that the non-interacting kinetic energy contribution T_s (which is calculated *exactly*) contains almost the total amount (99.8%) of the interacting kinetic energy T . This means that the kinetic contribution of the correlation energy T_c (equation 1.39) is very small. Concerning the electron-electron interaction energy, Hartree part E_H (which is also calculated *exactly*) has the same order of magnitude as the full Coulombic interaction energy W_{ee} , however, unlike the kinetic energy, the difference $W_{ee} - E_H$ is non-negligible. Finally, in the DFT calculation one approximates the E_{xc} contribution which is around 10% of the total energy. The approximations of a much smaller amount of energy (with respect to the total energy) make the DFT calculations accurate for a large number of different systems. In contrast to DFT, the semi-classical model of Thomas-Fermi [49], which is the precursor to DFT, approximates the full kinetic energy T and the electron-electron interaction energy W_{ee} , therefore it is less accurate.

Kohn-Sham equations

So far we have discussed the Kohn-Sham concept itself. In this section, we will derive the equations which allow one to find the total ground-state energy using the Kohn-Sham scheme.

So, we consider the system of N non-interacting electrons described by the single Slater determinant wave function $\Phi_s(\mathbf{x}_1, \dots, \mathbf{x}_N)$ (equation 1.24). We can rewrite the total energy (equation 1.33) in terms of spatial orbitals $\varphi_i(\mathbf{r})$

$$E[\{\varphi_i\}] = \sum_i^N \int d\mathbf{r} \varphi_i^*(\mathbf{r}) \left(-\frac{1}{2} \nabla^2 + v_{ne}(\mathbf{r}) \right) \varphi_i(\mathbf{r}) + E_{Hxc}[\rho], \quad (1.41)$$

where we have integrated over all spin variables. It is possible to switch from the minimization over the non-interacting N particles wave function Φ_s to the minimization over the spatial orbitals $\varphi_i(\mathbf{r})$. To do so, one needs to apply the Lagrange multipliers technique. We build the Lagrangian using the constraint of the orthonormalization of $\varphi_i(\mathbf{r})$ functions (equation 1.25)

$$\mathcal{L}[\{\varphi_i\}] = E[\{\varphi_i\}] - \sum_i^N \varepsilon_i \left(\int d\mathbf{r} \varphi_i^*(\mathbf{r}) \varphi_i(\mathbf{r}) - 1 \right), \quad (1.42)$$

where ε_i is the Lagrange multiplier corresponding to the spatial orbital $\varphi_i(\mathbf{r})$. To ensure the minimum of the energy $E[\{\varphi_i\}]$, the necessary conditions on the Lagrangian are

$$\frac{\delta \mathcal{L}}{\delta \varphi_i^*(\mathbf{r})} = 0, \quad \frac{\delta \mathcal{L}}{\delta \varphi_i(\mathbf{r})} = 0, \quad (1.43)$$

where $\delta \mathcal{L} / \delta \varphi_i(\mathbf{r})$ means the functional derivative of the Lagrangian over the spatial orbital $\varphi_i(\mathbf{r})$. In this case, the second equation of the functional derivative is just a complex conjugate of the first one, therefore we will consider only the first equation. Taking the functional derivative we obtain

$$\left(-\frac{1}{2} \nabla^2 + v_{ne}(\mathbf{r}) \right) \varphi_i(\mathbf{r}) + \frac{\delta E_{Hxc}[\rho]}{\delta \varphi_i^*(\mathbf{r})} = \varepsilon_i \varphi_i(\mathbf{r}). \quad (1.44)$$

Using the chain rule we can express the functional derivative of E_{Hxc} over $\varphi_i^*(\mathbf{r})$ through the derivative over the one-electron density $\rho(\mathbf{r})$

$$\frac{\delta E_{Hxc}[\rho]}{\delta \varphi_i^*(\mathbf{r})} = \int d\mathbf{r}' \frac{\delta E_{Hxc}[\rho]}{\delta \rho(\mathbf{r}')} \frac{\delta \rho(\mathbf{r}')}{\delta \varphi_i^*(\mathbf{r})}. \quad (1.45)$$

Using the expression 1.29 of the one-electron density, it is possible to show that

$$\frac{\delta \rho(\mathbf{r}')}{\delta \varphi_i^*(\mathbf{r})} = \varphi_i(\mathbf{r}) \delta(\mathbf{r} - \mathbf{r}'), \quad (1.46)$$

Then equation 1.45 becomes

$$\frac{\delta E_{Hxc}[\rho]}{\delta \varphi_i^*(\mathbf{r})} = \frac{\delta E_{Hxc}[\rho]}{\delta \rho(\mathbf{r})} \varphi_i(\mathbf{r}). \quad (1.47)$$

It is seen that the term $\delta E_{Hxc}[\rho]/\delta \rho(\mathbf{r})$ is itself a functional of the density, we define it as the Hartree-exchange-correlation potential

$$v_{Hxc}([\rho]; \mathbf{r}) = \frac{\delta E_{Hxc}[\rho]}{\delta \rho(\mathbf{r})}. \quad (1.48)$$

Similarly to the Hartree-exchange-correlation energy E_{Hxc} , we proceed the same separation for the potential v_{Hxc}

$$v_{Hxc}([\rho]; \mathbf{r}) = v_H([\rho]; \mathbf{r}) + v_{xc}([\rho]; \mathbf{r}), \quad (1.49)$$

where $v_H([\rho]; \mathbf{r})$ is the Hartree potential

$$v_H([\rho]; \mathbf{r}) = \frac{\delta E_H([\rho]; \mathbf{r})}{\delta \rho(\mathbf{r})} \quad (1.50)$$

and $v_{xc}([\rho]; \mathbf{r})$ is the exchange-correlation potential, which can be divided on the exchange potential $v_x([\rho]; \mathbf{r})$ and the correlation potential $v_c([\rho]; \mathbf{r})$

$$v_{xc}([\rho]; \mathbf{r}) = \frac{\delta E_{xc}([\rho]; \mathbf{r})}{\delta \rho(\mathbf{r})} = \frac{\delta E_x([\rho]; \mathbf{r})}{\delta \rho(\mathbf{r})} + \frac{\delta E_c([\rho]; \mathbf{r})}{\delta \rho(\mathbf{r})} = v_x([\rho]; \mathbf{r}) + v_c([\rho]; \mathbf{r}). \quad (1.51)$$

One does not have the exact analytic expressions neither for the exchange-correlation energy nor for the exchange-correlation potential. The approximations of E_{xc} and v_{xc} will be described in section 1.2.

In contrary, using the exact expression of the Hartree energy $E_H[\rho]$ (equation 1.35) and the definition of the Hartree potential (equation 1.50), we can find the analytical expression for the $v_H([\rho]; \mathbf{r})$ term

$$v_H([\rho]; \mathbf{r}) = \int d\mathbf{r}' \frac{\rho(\mathbf{r}')}{|\mathbf{r} - \mathbf{r}'|}. \quad (1.52)$$

Then the Hartree energy can be found from the Hartree potential in the following way

$$E_H = \frac{1}{2} \int d\mathbf{r} v_H([\rho]; \mathbf{r}) \rho(\mathbf{r}). \quad (1.53)$$

Finally, from equations 1.44 and 1.48, we obtain the Kohn-Sham equations

$$\left(-\frac{1}{2} \nabla_i^2 + v_s([\rho]; \mathbf{r}) \right) \varphi_i(\mathbf{r}) = \varepsilon_i \varphi_i(\mathbf{r}), \quad (1.54)$$

where $v_s([\rho]; \mathbf{r})$ is the so-called Kohn-Sham potential

$$v_s([\rho]; \mathbf{r}) = v_{ne}(\mathbf{r}) + v_{Hxc}([\rho]; \mathbf{r}). \quad (1.55)$$

Equation 1.54 is Schrödinger-like

$$\hat{h}_s([\rho]; \mathbf{r})\varphi_i(\mathbf{r}) = \varepsilon_i\varphi_i(\mathbf{r}), \quad (1.56)$$

where $\hat{h}_s([\rho]; \mathbf{r})$ is the *one-particle* Kohn-Sham Hamiltonian

$$\hat{h}_s([\rho]; \mathbf{r}) = \left(-\frac{1}{2}\nabla^2 + v_{ne}(\mathbf{r}) + v_{Hxc}([\rho]; \mathbf{r}) \right). \quad (1.57)$$

The eigenfunctions of \hat{h}_s , $\varphi_i(\mathbf{r})$, are the solutions of equation 1.54 and are called the Kohn-Sham orbitals. The eigenvalues ε_i are one-electron energies. One should note that $v_{Hxc}([\rho]; \mathbf{r})$ depends on the electronic density, therefore it depends on all the occupied orbitals $\varphi_i(\mathbf{r})$. This makes the system of equations 1.54 coupled through the density. One solves these equations in a self-consistent manner:

- (1) Start with some guess density $\rho^{(0)}(\mathbf{r})$.
- (2) Calculate the Kohn-Sham potential $v_s([\rho]; \mathbf{r})$ from the density $\rho(\mathbf{r})$ (equation 1.55).
- (3) Solve the Kohn-Sham equations (1.54).
- (4) Evaluate the density $\rho^{(i)}(\mathbf{r})$ from the Kohn-Sham orbitals $\varphi^{(i)}(\mathbf{r})$ (equation 1.29).
- (5) Repeat the steps (2)-(4) until the convergence of the density $\|\rho^{(i)}(\mathbf{r}) - \rho^{(i-1)}(\mathbf{r})\|$ is reached.

When the convergence of the self-consistent loop is achieved, one can calculate the *exact* (provided that v_{xc} is exact) ground-state energy E_0 by substituting the Kohn-Sham orbitals $\varphi_i(\mathbf{r})$ and the ground-state density $\rho_0(\mathbf{r})$ in equation 1.41. One should mention that, as in the Hartree-Fock approximation [50], in DFT the total ground-state energy E_0 is not the sum of the orbital energies ε_i . To demonstrate this, let us rewrite the total energy (equation 1.41) in the following way

$$E_0 = T_s + \int d\mathbf{r} v_{ne}(\mathbf{r})\rho_0(\mathbf{r}) + \frac{1}{2} \int d\mathbf{r} v_H([\rho_0]; \mathbf{r})\rho_0(\mathbf{r}) + E_{xc}([\rho_0]; \mathbf{r}). \quad (1.58)$$

The sum of the orbital energies has the following expression

$$\sum_i^N \varepsilon_i = \sum_i^N \langle \varphi_i | \hat{h}_s | \varphi_i \rangle = T_s + \int d\mathbf{r} v_{ne}(\mathbf{r})\rho_0(\mathbf{r}) + \int d\mathbf{r} v_H([\rho_0]; \mathbf{r})\rho_0(\mathbf{r}) + \int d\mathbf{r} v_{xc}([\rho_0]; \mathbf{r})\rho_0(\mathbf{r}). \quad (1.59)$$

Comparing equations 1.58 and 1.59 we can express the total energy through the sum of the orbital energies

$$E = \sum_i^N \varepsilon_i - E_H + E_{xc} - \int d\mathbf{r} v_{xc}\rho_0(\mathbf{r}), \quad (1.60)$$

where we have used the expression for the Hartree energy $E_H[\rho]$ (equation 1.53).

To summarize, in DFT the problem of N interacting electrons is recast as the problem of N non-interacting electrons in the effective external potential $v_s([\rho]; \mathbf{r})$. The non-interacting system is defined by the one-particle Hamiltonian $\hat{h}_s([\rho]; \mathbf{r})$ and the potential $v_s([\rho]; \mathbf{r})$. This system has the same ground-state density $\rho_0(\mathbf{r})$ as in the interacting case. This concept is illustrated in Fig. 1.3.

Similarly to the Hartree-Fock approximation [50] the Hamiltonian \hat{h}_s is one-particle, however the exchange potential $v_x([\rho]; \mathbf{r})$ in DFT is local in contrast to the Hartree-Fock approximation, which makes DFT calculations less computationally expensive. In addition, \hat{h}_s contains the correlation potential $v_c([\rho]; \mathbf{r})$ which is not present in the Hartree-Fock approximation.

1.1.4 Extension to spin-polarized DFT

Previously we have considered the case of paired electrons in double-occupied orbitals. This type of calculations is called spin-restricted in the sense that different spins are restricted to have the same spatial part

$$\varphi_i^\uparrow(\mathbf{x}) = \varphi_i(\mathbf{r})\chi_{\sigma\uparrow}(\sigma) \quad (1.61a)$$

$$\varphi_i^\downarrow(\mathbf{x}) = \varphi_i(\mathbf{r})\chi_{\sigma\downarrow}(\sigma). \quad (1.61b)$$

In the case of spin-unrestricted calculations, one may have different spatial orbitals for different spins

$$\varphi_i^\uparrow(\mathbf{x}) = \varphi_i^\uparrow(\mathbf{r})\chi_{\sigma\uparrow}(\sigma) \quad (1.62a)$$

$$\varphi_i^\downarrow(\mathbf{x}) = \varphi_i^\downarrow(\mathbf{r})\chi_{\sigma\downarrow}(\sigma). \quad (1.62b)$$

Therefore, the single-particle energies may be also different (see Fig. 1.4).

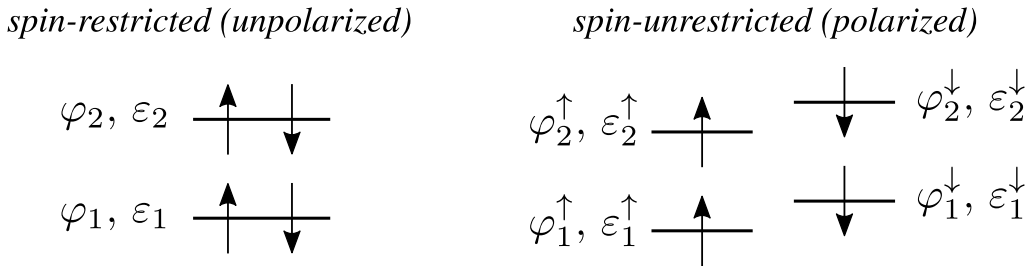


Figure 1.4 : Pictorial representation of the spin-restricted (on the left-hand side) and the spin-unrestricted (on the right-hand side) calculations. In the first case, the spatial orbitals $\varphi_i(\mathbf{r})$ are restricted to be the same for opposite spins, therefore the energies ε_i are also the same for both spins. In the second case, different spins are treated separately and have different spatial orbitals $\varphi_i^\sigma(\mathbf{r})$ and different energies ε_i^σ .

Even if the external magnetic field calculations are out of the scope of this work, the spin-unrestricted DFT calculations are necessary to treat the systems with unpaired electrons or magnetic systems (Fe, for example).

In order to establish the Kohn-Sham scheme for the spin-unrestricted case, we can generalize the universal functional expression (equation 1.18) as follows [51], [52]

$$F_{HK}[\rho_{\uparrow}, \rho_{\downarrow}] = \min_{\Psi \rightarrow \rho_{\uparrow}, \rho_{\downarrow}} \langle \Psi | \hat{T} + \hat{W}_{ee} | \Psi \rangle, \quad (1.63)$$

where the many-body wave function $\Psi(\mathbf{x}_1, \dots, \mathbf{x}_N)$ must yield the spin densities ρ_{\uparrow} and ρ_{\downarrow} defined as

$$\rho_{\uparrow}(\mathbf{r}) = N \int \dots \int |\Psi(\mathbf{r}, \uparrow, \mathbf{x}_2, \dots, \mathbf{x}_N)|^2 d\mathbf{x}_2 \dots d\mathbf{x}_N, \quad \int d\mathbf{r} \rho_{\uparrow}(\mathbf{r}) = N_{\uparrow} \quad (1.64a)$$

$$\rho_{\downarrow}(\mathbf{r}) = N \int \dots \int |\Psi(\mathbf{r}, \downarrow, \mathbf{x}_2, \dots, \mathbf{x}_N)|^2 d\mathbf{x}_2 \dots d\mathbf{x}_N, \quad \int d\mathbf{r} \rho_{\downarrow}(\mathbf{r}) = N_{\downarrow}, \quad (1.64b)$$

where N_{\uparrow} and N_{\downarrow} are the total numbers of spin-up and spin-down electrons respectively, $N_{\uparrow} + N_{\downarrow} = N$.

Then, one can reproduce the same functionals separation as it was done for the spin-restricted case (equations 1.32 - 1.40) using the spin-unrestricted densities $\rho_{\uparrow}(\mathbf{r})$ and $\rho_{\downarrow}(\mathbf{r})$. In this way, one obtains the following expression for the universal functional (analogous to equation 1.32)

$$F_{HK}[\rho_{\uparrow}, \rho_{\downarrow}] = T_s[\rho_{\uparrow}, \rho_{\downarrow}] + E_H[\rho] + E_{xc}[\rho_{\uparrow}, \rho_{\downarrow}]. \quad (1.65)$$

Since the Hartree term describes the classical density-density interaction (see equation 1.35), it depends only on the total electronic density $\rho(\mathbf{r})$

$$\rho(\mathbf{r}) = \rho_{\uparrow}(\mathbf{r}) + \rho_{\downarrow}(\mathbf{r}). \quad (1.66)$$

The non-interacting kinetic energy is defined in a similar manner as in the spin-restricted case (equation 1.31), but this time we require the single Slater determinant wave function $\Phi_s(\mathbf{x}_1, \dots, \mathbf{x}_N)$ to provide given $\rho_{\uparrow}(\mathbf{r})$ and $\rho_{\downarrow}(\mathbf{r})$ densities

$$T_s[\rho_{\uparrow}, \rho_{\downarrow}] = \min_{\Phi_s \rightarrow \rho_{\uparrow}, \rho_{\downarrow}} \langle \Phi_s | \hat{T} | \Phi_s \rangle. \quad (1.67)$$

The $E_{xc}[\rho_{\uparrow}, \rho_{\downarrow}]$ term in equation 1.65 is the spin-unrestricted exchange-correlation potential, which can be divided on the exchange $E_x[\rho_{\uparrow}, \rho_{\downarrow}]$ and correlation $E_c[\rho_{\uparrow}, \rho_{\downarrow}]$ parts. Since there is no exchange interaction between the spin-up and spin-down electrons, one can directly use the approximations of the exchange functional derived for the spin-restricted case [53]. However, there is no similar simplicity for the correlation functional and the spin-dependent expression $E_c[\rho_{\uparrow}, \rho_{\downarrow}]$ has to be derived specifically for the spin-unrestricted case.

Similarly to the spin-restricted calculations, in order to obtain the Kohn-Sham equations, we construct the Lagrangian (like equation 1.42), require the Lagrangian to be stationary over the orbitals $\varphi_i^{\uparrow}(\mathbf{r})$ and $\varphi_i^{\downarrow}(\mathbf{r})$ (like equation 1.43) and derive the Hartree-exchange-correlation potential $v_{Hxc}([\rho_{\uparrow}, \rho_{\downarrow}]; \mathbf{r})$ using the functional calculus (like equations

1.45-1.48). Finally, we obtain the Kohn-Sham spin-unrestricted equations

$$\left(-\frac{1}{2}\nabla^2 + v_{ne}(\mathbf{r}) + v_H([\rho]; \mathbf{r}) + v_{xc}^\uparrow([\rho_\uparrow, \rho_\downarrow]; \mathbf{r})\right) \varphi_i^\uparrow(\mathbf{r}) = \varepsilon_i^\uparrow \varphi_i^\uparrow(\mathbf{r}) \quad (1.68a)$$

$$\left(-\frac{1}{2}\nabla^2 + v_{ne}(\mathbf{r}) + v_H([\rho]; \mathbf{r}) + v_{xc}^\downarrow([\rho_\uparrow, \rho_\downarrow]; \mathbf{r})\right) \varphi_i^\downarrow(\mathbf{r}) = \varepsilon_i^\downarrow \varphi_i^\downarrow(\mathbf{r}). \quad (1.68b)$$

It is seen that the coupling between equations for different spins is performed through the total density $\rho(\mathbf{r})$ (equation 1.66). In equations 1.68 only the exchange-correlation potential expression, v_{xc}^σ , is spin-dependent. In the spin-unrestricted case, it is defined as follows

$$v_{xc}^\uparrow = \frac{\delta E_{xc}[\rho_\uparrow, \rho_\downarrow]}{\delta \rho_\uparrow(\mathbf{r})}, \quad v_{xc}^\downarrow = \frac{\delta E_{xc}[\rho_\uparrow, \rho_\downarrow]}{\delta \rho_\downarrow(\mathbf{r})}. \quad (1.69)$$

For the Hartree potential $v_H([\rho]; \mathbf{r})$ the same expression as in the spin-restricted case is applied (equation 1.52). The one-electron spin-densities $\rho^\sigma(\mathbf{r})$ can be obtained from the Kohn-Sham orbitals as

$$\rho_\uparrow(\mathbf{r}) = \sum_{i=1}^{N_\uparrow} |\varphi_i^\uparrow(\mathbf{r})|^2, \quad \rho_\downarrow(\mathbf{r}) = \sum_{i=1}^{N_\downarrow} |\varphi_i^\downarrow(\mathbf{r})|^2. \quad (1.70)$$

1.2 Exchange-correlation functionals approximations

As already mentioned, DFT is an exact theory under the condition that the exact exchange-correlation functional is known, which is, unfortunately, not the case. In this section, we will consider approximations to this quantity. Nowadays there is a very large number of exchange-correlation functionals accessible on the “market”. In this section, we will consider only some families of exchange-correlation functionals. In particular, we will consider those approximations that were used in this work.

It should be mentioned that for the time being there is no universal functional approximation which would be accurate enough for any class of electronic systems. Hence, for an unknown system, one needs to test different exchange-correlation functionals, compare the DFT results with experimental data and then choose the most appropriate one. This type of pragmatic approach questions the *ab initio* nature of DFT [54]. Therefore, new exchange-correlation functionals development is still a topic of interest at the present moment [55].

1.2.1 Local density approximation

In the local density approximation (LDA) the exchange-correlation functional is approximated in the following way [46]

$$E_{xc}^{LDA}[\rho] = \int d\mathbf{r} \rho(\mathbf{r}) \varepsilon_{xc}^{unif}(\rho(\mathbf{r})), \quad (1.71)$$

where $\varepsilon_{xc}^{unif}(\rho(\mathbf{r}))$ is the *function* of the exchange-correlation energy per electron of the infinite uniform electron gas with the density $\rho(\mathbf{r})$.

In order to illustrate this approximation, let us consider a volume element $d\mathbf{r}$, then $d\mathbf{r}\rho(\mathbf{r})$ is the average number of electrons in this volume. In LDA one assumes that the exchange-correlation energy for electrons in the volume $d\mathbf{r}$ is the same as it would be in a uniform gas with the *constant* density ρ at the point \mathbf{r} . Therefore, by definition, LDA is exact for any uniform density and it is accurate for slowly varying densities.

The function $\varepsilon_{xc}^{unif}(\rho(\mathbf{r}))$ can be divided into the exchange and correlation contributions

$$\varepsilon_{xc}^{unif}(\rho(\mathbf{r})) = \varepsilon_x^{unif}(\rho(\mathbf{r})) + \varepsilon_c^{unif}(\rho(\mathbf{r})). \quad (1.72)$$

The exchange contribution $\varepsilon_x^{unif}(\rho(\mathbf{r}))$ can be calculated exactly

$$\varepsilon_x^{unif}(\rho(\mathbf{r})) = -\frac{3}{4} \frac{3}{\pi^{1/3}} \rho(\mathbf{r})^{1/3}. \quad (1.73)$$

Then one can show that the LDA exchange potential is

$$v_x^{LDA}(\mathbf{r}) = -\frac{3}{\pi^{1/3}} \rho(\mathbf{r})^{1/3}. \quad (1.74)$$

For a finite system, the LDA exchange potential v_x^{LDA} decays exponentially for $r \rightarrow \infty$, whereas the exact exchange potential decays as $-1/r$.

The correlation contribution $\varepsilon_c^{unif}(\rho(\mathbf{r}))$ cannot be obtained analytically. The numerical values of $\varepsilon_c^{unif}(\rho(\mathbf{r}))$ are obtained using the quantum Monte Carlo calculations [56]. These values are then fitted to a parametrized function. The most used parametrizations are VWN (Vosko, Wilk and Nusair [57]) and PW92 (Perdew and Wang [58]). These parametrizations also include the spin-unrestricted case: $\varepsilon_c^{unif}(\rho_\uparrow, \rho_\downarrow)$. The spin-unrestricted LDA is called the local spin density approximation (LSD) [59].

1.2.2 Generalized-gradient approximations

One can consider the generalized gradient approximation (GGA) as a generalization of LDA. If in LDA the exchange-correlation energy was a functional of the density, in GGA it is a functional of the density and of the gradient of the density, i.e.,

$$E_{xc}^{GGA}[\rho] = \int d\mathbf{r} f(\rho(\mathbf{r}), \nabla\rho(\mathbf{r})). \quad (1.75)$$

In contrast to LDA, GGA is semi-local because the function f depends also on the gradient of the density. The spin-independent expression of the exchange-correlation potential has the following form

$$v_{xc}^{GGA}([\rho]; \mathbf{r}) = \frac{\delta E_{xc}^{GGA}[\rho]}{\delta\rho(\mathbf{r})} = \frac{\partial f}{\partial\rho}(\rho(\mathbf{r}), \nabla\rho(\mathbf{r})) - \nabla \cdot \frac{\partial f}{\partial\nabla\rho}(\rho(\mathbf{r}), \nabla\rho(\mathbf{r})). \quad (1.76)$$

It is also possible to deduce the analytical expression of the spin-dependent exchange-correlation potential $v_{xc}^{GGA}([\rho_\uparrow, \rho_\downarrow]; \mathbf{r})$.

B88 exchange functional

This functional developed by Becke in 1988 [60] is constructed as a correction to LDA

$$E_x^{B88} = E_x^{LDA} + \int d\mathbf{r} f(\rho(\mathbf{r}), s(\mathbf{r})), \quad (1.77)$$

where $s(\mathbf{r})$ is the reduced density gradient

$$s(\mathbf{r}) = \frac{|\nabla\rho(\mathbf{r})|}{\rho(\mathbf{r})^{4/3}}. \quad (1.78)$$

The function f is chosen in a way to satisfy the asymptotic behavior of the exact-exchange energy $\varepsilon_x(\mathbf{r})$ at large distance: $\varepsilon_x(\mathbf{r}) \xrightarrow{r \rightarrow \infty} -\frac{1}{2r}$. This functional contains one empirical parameter.

LYP correlation functional

This functional was developed by Lee, Yang, and Parr [61]. It has been constructed from the Colle-Salvetti correlation functional [62] (and not from LDA, which is rare for GGA functionals). It depends on the density $\rho(\mathbf{r})$, the density gradient $\nabla\rho(\mathbf{r})$ and the Laplacian of the density $\nabla^2\rho(\mathbf{r})$.

PBE exchange-correlation functional

The functional developed by Perdew, Burke, and Ernzerhof (PBE) [63] uses the functions of $\rho(\mathbf{r})$ and $|\nabla\rho(\mathbf{r})|$ to describe the exchange and correlation energies per particle. It does not contain any empirical parameter. These functions have been chosen to satisfy the small-gradient and high-gradient limits. The functional is a simplification of the Perdew Wang functional PW91 [64].

1.2.3 Meta-generalized-gradient approximations

This family of functionals, in its turn, is a generalization of GGA and has the following form

$$E_{xc}^{meta-GGA} = \int d\mathbf{r} f(\rho(\mathbf{r}), \nabla\rho(\mathbf{r}), \nabla^2\rho(\mathbf{r}), \tau(\mathbf{r})), \quad (1.79)$$

where $\tau(\mathbf{r})$ is the non-interacting kinetic energy density

$$\tau(\mathbf{r}) = \frac{1}{2} \sum_{i=1}^N |\nabla\varphi_i(\mathbf{r})|^2. \quad (1.80)$$

The most used exchange-correlation functionals from this family today are the Tao, Perdew, Staroverov, and Scuseria functional (TPSS) [65] and recently developed the so-called strongly constrained appropriately normed functional (SCAN) [55]. As a general

trend, one can mention that GGA functionals yield a significant gain in accuracy over LDA, whereas meta-GGAs do not make a large improvement on top of GGA.

1.2.4 Hybrid exchange-correlation functionals

The idea of the hybrid approximations is to include the exchange and correlation “ingredients” from different theories and approximations: exact Hartree-Fock exchange energy E_x^{HF} , LDA and GGA exchange energies E_x^{LDA} , E_x^{GGA} and LDA and GGA correlation energies E_c^{LDA} , E_c^{GGA} , namely,

$$E_{xc}^{hybrid} = aE_x^{HF} + bE_x^{GGA} + (1 - a - b)E_x^{LDA} + cE_c^{GGA} + (1 - c)E_c^{LDA}, \quad (1.81)$$

where a, b and c are the mixing parameters.

The Hartree-Fock exact-exchange energy is defined as

$$E_x^{HF} = -\frac{1}{2} \sum_{\sigma=\uparrow,\downarrow} \sum_{i=1}^{N_\sigma} \sum_{j=1}^{N_\sigma} \iint d\mathbf{r}_1 d\mathbf{r}_2 \frac{\varphi_i^{*\sigma}(\mathbf{r}_1)\varphi_j^\sigma(\mathbf{r}_1)\varphi_j^{*\sigma}(\mathbf{r}_2)\varphi_i^\sigma(\mathbf{r}_2)}{|\mathbf{r}_1 - \mathbf{r}_2|}. \quad (1.82)$$

This expression is the same as obtained in the Hartree-Fock approximation, but evaluated with the Kohn-Sham orbitals $\varphi_i^\sigma(\mathbf{r})$. The Hartree-Fock exchange potential can be found from the functional derivative of the Hartree-Fock energy E_x^{HF} over the Kohn-Sham orbitals $\varphi_i^*(\mathbf{r})$ (we cannot express this derivative through the derivative over the density, as it was done in equation 1.47 for the Kohn-Sham potentials)

$$\frac{\delta E_x^{HF}}{\delta \varphi_i^{*\sigma}(\mathbf{r})} = \int d\mathbf{r}' v_x^{\sigma HF}(\mathbf{r}, \mathbf{r}') \varphi_i^\sigma(\mathbf{r}'). \quad (1.83)$$

Finally, we get the following expression for the Hartree-Fock exchange potential

$$v_x^{\sigma HF}([\varphi]; \mathbf{r}, \mathbf{r}') = - \sum_{j=1}^{N_\sigma} \frac{\varphi_j^\sigma(\mathbf{r})\varphi_j^{*\sigma}(\mathbf{r}')}{|\mathbf{r} - \mathbf{r}'|}. \quad (1.84)$$

Since the exchange interaction occurs between the electrons of the same spin, the exchange potential is spin-dependent by definition. It is seen that this potential is *nonlocal*, which is the principal difference in comparison to the Kohn-Sham potential $v_s([\rho]; \mathbf{r})$. The calculations which include the Kohn-Sham potential and the nonlocal Hartree-Fock exchange potential are called the generalized Kohn-Sham (gKS) [66]. Adding the Hartree-Fock term, one decreases the electron self-interaction error which is completely absent in the Hartree-Fock calculations [50].

B3LYP functional

This functional [67] uses the same exchange energy functional as in the B88 approximation (hence the letter B in the name) and the same correlation functional as in the LYP approximation (from which the end of the functional name). It uses the parameters (in equation 1.81), which were fitted to experimental data: $a = 0.20$; $b = 0.72$; $c = 0.81$.

PBE0 functional

The name comes from the same abbreviation of names as in PBE. The PBE0 hybrid functional [68] uses only one parameter $a = 0.25$ ($b = c = 0$) and has the following form

$$E_{xc}^{PBE0} = aE_x^{HF} + (1 - a)E_x^{PBE} + E_c^{PBE}, \quad (1.85)$$

where E_x^{PBE} and E_c^{PBE} are the exchange and correlation functionals of the PBE approximation. The a parameter is usually considered as non-empirical (in contrast to B3LYP parameters) and its value has a physical explanation [69].

1.3 Time-Dependent DFT (TDDFT)

So far we were interested in the ground-state properties (ground-state density and energy). In order to go beyond the ground-state, one of the possible methods is the Time-Dependent DFT. Similarly to the DFT section, we will briefly consider the complete many-body problem, and then we will apply the Kohn-Sham method in the time-dependent case in order to make the problem numerically resolvable.

1.3.1 Many-body time-dependent problem

The evolution of the time-dependent many-body electronic wave function is governed by the time-dependent Schrödinger equation

$$i \frac{\partial \Psi(\mathbf{x}_1, \dots, \mathbf{x}_N, t)}{\partial t} = \hat{H}(\mathbf{r}_1, \dots, \mathbf{r}_N, \mathbf{R}_1, \dots, \mathbf{R}_N, t) \Psi(\mathbf{x}_1, \dots, \mathbf{x}_N, t). \quad (1.86)$$

This is a first-order differential equation, therefore the initial state condition $\Psi_0 = \Psi(t = 0)$ must be specified. The expression of the electronic Hamiltonian \hat{H} is similar to one considered in the stationary Schrödinger equation (1.6),

$$\hat{H}(t) = \hat{T} + \hat{W}_{ee} + \hat{V}_{ext}. \quad (1.87)$$

However, now we assume the time dependence of the external potential, which incorporates the electron-nucleus interaction \hat{V}_{ne} and some time-dependent external perturbation \hat{V}_{pert}

$$\hat{V}_{ext} = \sum_{i=1}^N v_{ext}(\mathbf{r}_i, t). \quad (1.88)$$

The expression of the one-particle density and its normalization condition are the same as in the stationary case (equations 1.29 and 1.15) but with the time-dependent wave function

$$\rho(\mathbf{r}, t) = N \int \dots \int |\Psi(\mathbf{r}, \sigma_1, \mathbf{x}_2, \dots, \mathbf{x}_N, t)|^2 d\sigma_1 d\mathbf{x}_2 \dots d\mathbf{x}_N, \quad (1.89)$$

$$\int \rho(\mathbf{r}, t) d\mathbf{r} = N. \quad (1.90)$$

As in the stationary case, the many-body problem is very complicated and one would like to density-functionalize it as well. In order to do so, let us first verify if one can express any observable through the density $\rho(\mathbf{r}, t)$ in the time domain as well.

1.3.2 One-to-one correspondence: time-dependent case

The analog of the Hohenberg-Kohn theorem in TDDFT is the Runge-Gross theorem [28]. This theorem states that the mapping between the external potential $v_{ext}(\mathbf{r}, t)$ and the time-dependent density $\rho(\mathbf{r}, t)$ is bijective. This means that a situation where two different potentials $v_{ext}(\mathbf{r}, t)$ and $v'_{ext}(\mathbf{r}, t)$ provide the same density $\rho(\mathbf{r}, t)$ is not possible. Here we assume that two time-dependent potentials $v_{ext}(\mathbf{r}, t)$ and $v'_{ext}(\mathbf{r}, t)$ are equivalent if they differ not more than by a purely time-dependent function $c(t)$. One should mention that we consider here *the same* initial state $\Psi_0 = \Psi(t = 0)$ for any density $\rho(\mathbf{r}, t)$ (Fig. 1.5).

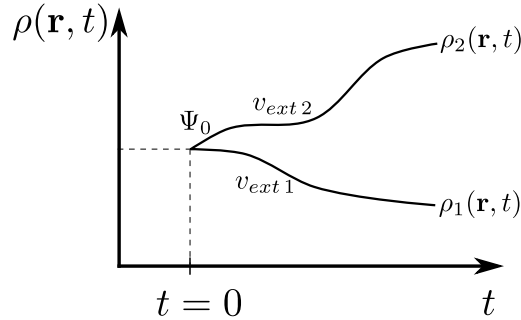


Figure 1.5 : Schematic illustration of the Runge-Gross theorem. Two densities $\rho(\mathbf{r}, t)$ and $\rho'(\mathbf{r}, t)$ which evolve from the same initial state $\Psi_0 = \Psi(t = 0)$ under two different potentials v_{ext1} and v_{ext2} start to deviate immediately after the moment $t = 0$ (at $t + \delta t$, $\delta t \rightarrow 0$). Adapted from [70].

In the ground-state DFT, the corresponding statement was proven using the variational principle (equation 1.10), however, in the time-dependent case, the variational principle is not valid [71]. Therefore, the proof of the Runge-Gross theorem is performed in a different way, through the time-dependent current density, which is defined as

$$\mathbf{j}(\mathbf{r}, t) = N \int \dots \int \text{Im}[\Psi(\mathbf{r}, \sigma_1, \mathbf{x}_2, \dots, \mathbf{x}_N, t) \nabla \Psi^*(\mathbf{r}, \sigma_1, \mathbf{x}_2, \dots, \mathbf{x}_N, t)] d\sigma_1 d\mathbf{x}_2 \dots d\mathbf{x}_N. \quad (1.91)$$

The link between the density $\rho(\mathbf{r}, t)$ and the current density $\mathbf{j}(\mathbf{r}, t)$ can be established through the continuity equation

$$\frac{\partial \rho(\mathbf{r}, t)}{\partial t} = -\nabla \cdot \mathbf{j}(\mathbf{r}, t). \quad (1.92)$$

To prove the theorem, one needs to prove consequently the following statements: 1) two different potentials necessarily lead to two different current densities; 2) two different current densities necessarily lead to two different densities:

$$v_{ext}(\mathbf{r}, t) \neq v'_{ext}(\mathbf{r}, t) + c(t) \iff \mathbf{j}(\mathbf{r}, t) \neq \mathbf{j}'(\mathbf{r}, t), \quad (1.93a)$$

$$\mathbf{j}(\mathbf{r}, t) \neq \mathbf{j}'(\mathbf{r}, t) \iff \rho(\mathbf{r}, t) \neq \rho'(\mathbf{r}, t). \quad (1.93b)$$

It is important to mention that in the Runge-Gross theorem the one-to-one correspondence is proven for $v_{ext}(\mathbf{r}, t)$, $\mathbf{j}(\mathbf{r}, t)$ and $\rho(\mathbf{r}, t)$, but there is no wave function in this chain. However, having an external potential $v_{ext}(\mathbf{r}, t)$ we can (in principle) solve the time-dependent Schrödinger equation 1.86 and in such way find the wave function $\Psi(t)$ (see Fig. 1.6) - here we omit for clarity the space-spin coordinates in the wave function expression \mathbf{x}_i .

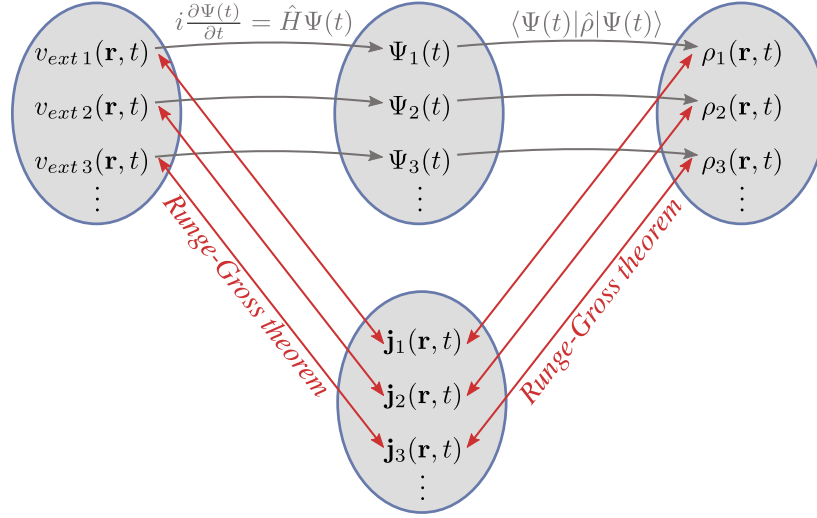


Figure 1.6 : Illustration of the mapping in TDDFT. According to the Runge-Gross theorem, there is a bijective mapping between the external potential $v_i(\mathbf{r}, t)$, current density $\mathbf{j}_i(\mathbf{r}, t)$ and the time-dependent density $\rho(\mathbf{r}, t)$ (red arrows). Using the time-dependent Schrödinger equation and the density expression through the wave function $\Psi_i(t)$, one can build a surjective mapping from $v_i(\mathbf{r}, t)$ to $\Psi_i(t)$ to $\rho(\mathbf{r}, t)$ (grey arrows). These two mappings are enough to prove that the time-dependent electronic density $\rho(\mathbf{r}, t)$ determines the external potential $v_i(\mathbf{r}, t)$ and the wave function $\Psi_i(t)$.

So, the electronic density $\rho(\mathbf{r}, t)$ determines the external potential $v_{ext}(\mathbf{r}, t)$ up to a purely time-dependent function $c(t)$. Then, the external potential determines, via the Schrödinger equation, the wave function $\Psi(t)$, this time up to a time-dependent phase $\theta(t)$

$$\Psi(t) = e^{i\theta(t)} \Psi([\rho, \Psi_0]; t). \quad (1.94)$$

One can also mention that the wave function is also a functional of the initial state Ψ_0 . The phase $\theta(t)$ cancels out for the expectation value of any operator

$$\langle \Psi(t) | \hat{\mathcal{O}} | \Psi(t) \rangle = \langle \Psi([\rho, \Psi_0]; t) | e^{-i\theta(t)} \hat{\mathcal{O}} e^{i\theta(t)} | \Psi([\rho, \Psi_0]; t) \rangle = \mathcal{O}([\rho, \Psi_0]; t). \quad (1.95)$$

1.3.3 Time-Dependent Kohn-Sham system

Van Leeuwen theorem

Let us consider an arbitrary time-dependent system with a density $\rho(\mathbf{r}, t)$, some two-particle interaction $\omega(|\mathbf{r} - \mathbf{r}'|)$ and an external potential $v_{ext}(\mathbf{r}, t)$. Suppose that at $t = 0$ the system is in a state Ψ_0 . The van Leeuwen theorem [72] stipulates that there exists a different many-body system with another two-particle interaction $\omega'(|\mathbf{r} - \mathbf{r}'|)$ and a unique external potential $v'_{ext}(\mathbf{r}, t)$ (up to a function $c(t)$) which reproduces exactly the time-dependent density of the first system $\rho(\mathbf{r}, t)$. The initial state of the second system Ψ'_0 must be chosen in the way to reproduce the density $\rho(\mathbf{r}, t = 0)$ and its time derivative $\left. \frac{\partial \rho(\mathbf{r}, t)}{\partial t} \right|_{t=0}$ at the initial time.

This theorem is very important in TDDFT. At first, choosing the two-particle interaction of the second system exactly the same as in the first system, one can identify the Runge-Gross theorem, which is just a special case of the van Leeuwen theorem. Second, selecting the second system as a system of non-interacting particles, namely $\omega'(|\mathbf{r} - \mathbf{r}'|) = 0$, one obtains the Kohn-Sham system in the time-dependent case. This theorem ensures the existence and the uniqueness (up to $c(t)$) of the external potential of the non-interacting system $v_s(\mathbf{r}, t)$. Therefore, we can apply the Kohn-Sham procedure for the time-dependent case.

Time-Dependent Kohn-Sham equations

Now, when we are sure about the existence of the time-dependent external potential of the Kohn-Sham system, we define a fictitious system of non-interacting electrons that satisfy the single-particle time-dependent Kohn-Sham (TDKS) equations

$$i \frac{\partial \varphi_i(\mathbf{r}, t)}{\partial t} = \hat{h}_s([\rho, \Psi_0]; \mathbf{r}, t) \varphi_i(\mathbf{r}, t) = [\hat{T} + v_s([\rho, \Psi_0]; \mathbf{r}, t)] \varphi_i(\mathbf{r}, t), \quad (1.96)$$

where $\hat{h}_s([\rho, \Psi_0]; \mathbf{r}, t)$ is the time-dependent single-particle Kohn-Sham Hamiltonian and $v_s([\rho, \Psi_0]; \mathbf{r}, t)$ is the time-dependent Kohn-Sham potential

$$v_s([\rho, \Psi_0]; \mathbf{r}, t) = v_{ext}(\mathbf{r}, t) + \int d\mathbf{r}' \frac{\rho(\mathbf{r}', t)}{|\mathbf{r} - \mathbf{r}'|} + v_{xc}([\rho, \Psi_0]; \mathbf{r}, t). \quad (1.97)$$

The definition and the separation of the time-dependent functionals is similar to the ground-state DFT case (equations 1.32 - 1.40). The case of spin-unrestricted Kohn-Sham equations in TDDFT can be obtained in a similar way as it was done in DFT (see section 1.1.4).

The one-particle density can be then found from the time-dependent Kohn-Sham orbitals

$$\rho(\mathbf{r}, t) = \sum_{i=1}^N |\varphi_i(\mathbf{r}, t)|^2. \quad (1.98)$$

Having the Kohn-Sham orbitals and the one-electron density at time t , one can calculate the total *electronic* energy (from equations 1.9 and 1.58)

$$E(t) = \sum_{i=1}^N \int d\mathbf{r} \varphi_i^*(\mathbf{r}, t) \left(-\frac{1}{2} \nabla^2 + \hat{V}_{ext} \right) \varphi_i(\mathbf{r}, t) + \frac{1}{2} \iint \frac{\rho(\mathbf{r}_1, t) \rho(\mathbf{r}_2, t)}{|\mathbf{r}_1 - \mathbf{r}_2|} d\mathbf{r}_1 d\mathbf{r}_2 + E_{xc}([\rho, \Psi_0]). \quad (1.99)$$

Constant occupation in time

The Kohn-Sham orbitals have the initial conditions

$$\varphi_i(\mathbf{r}, t = 0) = \varphi_i^{(0)}(\mathbf{r}). \quad (1.100)$$

Hence, it is seen that only initially occupied states are involved in the time propagation (in the TDKS equation 1.96). Therefore, we can restrict the index i in equation 1.96 to run only over the occupied Kohn-Sham states. We define N_{st} as a number of the highest occupied state. The system of equations 1.96 is coupled in the sense that the Kohn-Sham potential $v_s([\rho, \Psi_0]; \mathbf{r}, t)$ is a functional of the time-dependent density $\rho(\mathbf{r}, t)$ (and, depending on the exchange-correlation functional, possibly, of the density gradient $\nabla\rho(\mathbf{r}, t)$, Kohn-Sham orbitals $\varphi_i(\mathbf{r}, t)$, etc.). However, for a propagation from t to $t + dt$ each state evolves separately. This fact not only allows an efficient parallelization over the states, but also indicates a very important concept: in TDDFT one evolves the *states* while the *occupations* of the states remain constant.

To verify this, one can decompose the time-dependent wave function $\varphi_j(\mathbf{r}, t)$ in the basis of initial states $\varphi_i^{(0)}(\mathbf{r})$

$$\varphi_j(\mathbf{r}, t) = \sum_{i=1}^{\infty} Q_{ij}(t) \varphi_i^{(0)}(\mathbf{r}). \quad (1.101)$$

Because of the time-dependent potential $v_s([\rho, \Psi_0]; t)$, $Q_{ij}(t)$ elements for $i > N_{st}$ are different from zero. In such a way the time-dependent orbitals acquire admixtures of *initially* unoccupied orbitals.

This fact also emphasizes the importance of the initial state in the TDDFT calculations. One of the possible and the most standard TDDFT calculation procedures is to begin with a system in its ground-state, calculated in DFT and then add an external time-dependent perturbation.

Relation to the Ground State DFT

Even though the idea to represent the many-body system as a single-particle system in some external potential is the same in both DFT and TDDFT, these two theories have a number of differences. Let us clearly indicate them.

- In DFT the principal quantity is the ground-state density $\rho_0(\mathbf{r})$, whereas in TDDFT this principal quantity is the time-dependent density $\rho(\mathbf{r}, t)$ which gives access to excited states of atomic systems.
- In the time-dependent Kohn-Sham equations 1.96 one performs a *propagation* of the Kohn-Sham orbitals and not the self-consistent loop.
- In TDDFT the exchange-correlation functional is non-local in space (as in DFT), but also non-local in time. This means that the states of a system at $t < t'$ do influence the system at t' (because of the causality principle, we do not take into account $t > t'$).
- In addition to the exchange-correlation functional nonlocalities, TDDFT is an initial value problem in contrast to DFT.
- In TDDFT the variational principle does not apply.
- In DFT the one-electron density $\rho(\mathbf{r})$ determines the external potential $v_{ext}([\rho]; \mathbf{r})$ up to a constant, in TDDFT $\rho(\mathbf{r}, t)$ determines $v_{ext}([\rho]; \mathbf{r}, t)$ up to a pure time-dependent function.

Adiabatic exchange-correlation functionals

As well as DFT, the TDDFT theory is an exact theory provided that the exchange-correlation potential is exact. Even if in the general case the exchange-correlation functional should be non-local in time, the development of practical expressions for time-dependent exchange-correlation functionals is an open question [73],[74]. On the positive side, it was shown [75] that the memory dependence of the exchange-correlation functional becomes crucial for small systems (a few atoms) and it seems that the memory dependence is less important for systems with larger Hilbert space.

Therefore, the adiabatic approximation is currently used in TDDFT calculations. In this approximation, one assumes the exchange-correlation functional is time-dependent only through the time-dependent density $\rho(t)$, in such way one does not have the memory effect in adiabatic v_{xc}^A . Within this approximation, we can use *any* exchange-correlation functional from the ground-state DFT, plugging in the time-dependent density $\rho(\mathbf{r}, t)$

$$v_{xc}^A([\rho, \Psi_0]; \mathbf{r}, t) = v_{xc}^{DFT}([\rho(t)]; \mathbf{r}), \quad (1.102)$$

where v_x^{DFT} is the static exchange-correlation functional approximation. The advantage of such an approach is the possibility to use the extensive variety of the ground-state DFT exchange-correlation functionals in TDDFT calculations.

1.4 Real-time TDDFT (RT-TDDFT)

For the present moment, many TDDFT applications are performed within the linear response in the frequency domain [29]. However, in this work, we are interested in the Real-Time (RT) approach. In this approach, we propagate the Kohn-Sham occupied orbitals (using the TDKS equation 1.86) in real time. The time dependence of the problem comes from the time dependence of the Hamiltonian. The Hamiltonian, in its turn, is time-dependent for two reasons: because of a time-dependent perturbation \hat{V}_{pert} and, once the perturbation was applied, through the time-dependent charge density $\rho(\mathbf{r}, t)$.

1.4.1 Propagator technique

The most common and cost-effective algorithm to solve the time-dependent Schrödinger equation is the so-called propagator technique. It can be mentioned that we work in the Schrödinger picture. A propagator operator $\hat{U}(t, t_0)$, which propagates the wave function from t_0 to t is defined as

$$\varphi(t) = \hat{U}(t, t_0)\varphi(t_0). \quad (1.103)$$

Inserting the wave function in this form into the time-dependent Schrödinger equation 1.86, one obtains the differential equation for the propagator

$$i \frac{d\hat{U}(t, t_0)}{dt} = \hat{H}(t)\hat{U}(t, t_0) \quad (1.104)$$

with the initial condition

$$\hat{U}(t_0, t_0) = \hat{I}, \quad (1.105)$$

where \hat{I} is the identity operator. The equation 1.104 can be formally written as an integral equation (using the initial condition)

$$\hat{U}(t, t_0) = \hat{I} - i \int_{t_0}^t d\tau \hat{H}(\tau)\hat{U}(\tau, t_0). \quad (1.106)$$

One can solve this equation iteratively: we suppose that at 0^{th} order approximation the propagation operator is just equal to the identity

$$\hat{U}^{(0)}(t, t_0) = \hat{I}. \quad (1.107)$$

Then, we can find the approximation up to the 1^{st} order by inserting $\hat{U}^{(0)}(t, t_0)$ in equation 1.106

$$\hat{U}^{(1)}(t, t_0) = \hat{I} - i \int_{t_0}^t dt_1 \hat{H}(t_1)\hat{U}^{(0)}(t_1, t_0) = \hat{I} - i \int_{t_0}^t dt_1 \hat{H}(t_1) \quad (1.108)$$

Similarly, one finds the propagator expression up to the 2nd order correction as

$$\hat{U}^{(2)}(t, t_0) = \hat{I} - i \int_{t_0}^t dt_1 \hat{H}(t_1) \hat{U}^{(1)}(t_1, t_0) = \hat{I} - i \int_{t_0}^t dt_1 \hat{H}(t_1) + (-i)^2 \int_{t_0}^t dt_1 \int_{t_0}^{t_1} dt_2 \hat{H}(t_1) \hat{H}(t_2) \quad (1.109)$$

The full expression of the propagator $\hat{U}(t_0, t)$ is then obtained as $\hat{U}^{(n)}(t, t_0)$, $n \rightarrow \infty$. This construction is known as the so-called Dyson's series

$$\hat{U}(t, t_0) = \hat{I} + \sum_{n=1}^{\infty} (-i)^n \int_{t_0}^t dt_1 \int_{t_0}^{t_1} dt_2 \dots \int_{t_0}^{t_{n-1}} dt_n \hat{H}(t_1) \dots \hat{H}(t_n). \quad (1.110)$$

In equation 1.110 we have the summation of n -folded integrals, where the limits of the integral over t_n depend on t_{n-1} . In order to avoid this dependence and to bring the expression into a form of a normal Taylor series, one can use the time-ordering operator $\hat{\mathcal{T}}$ which orders the latest operator most left

$$\hat{\mathcal{T}} [\hat{A}(t_1) \hat{B}(t_2)] = \begin{cases} \hat{A}(t_1) \hat{B}(t_2), & \text{if } t_1 > t_2 \\ \hat{B}(t_2) \hat{A}(t_1), & \text{if } t_2 > t_1, \end{cases} \quad (1.111)$$

where \hat{A} and \hat{B} are arbitrary operators. Using the time-ordering operator expression, equation 1.110 becomes

$$\hat{U}(t, t_0) = \hat{I} + \sum_{n=1}^{\infty} \frac{(-i)^n}{n!} \int_{t_0}^t dt_1 \int_{t_0}^{t_1} dt_2 \dots \int_{t_0}^{t_{n-1}} dt_n \hat{\mathcal{T}} [\hat{H}(t_1) \dots \hat{H}(t_n)]. \quad (1.112)$$

This expression is the power series of the exponential

$$\hat{U}(t, t_0) = \hat{\mathcal{T}} \exp \left\{ -i \int_{t_0}^t d\tau \hat{H}(\tau) \right\}. \quad (1.113)$$

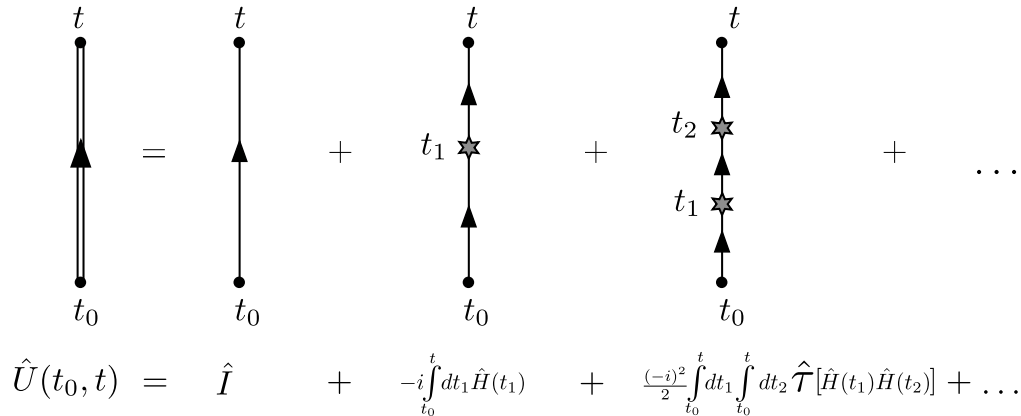


Figure 1.7 : Diagrammatic representation of the Dyson's series (equation 1.110).

These derivations are similar to those performed for the full interacting Green's function derivation in the many-body theory [76]. Therefore we can illustrate the Dyson series 1.112 using the Feynman diagrams in the same manner as it is done for the Green's function (Fig. 1.7).

One should mention that the derivations 1.112 and 1.113 do not simplify the calculation of the propagator $\hat{U}(t, t_0)$, but just bring its expression into a compact form. The numerical approximations of the propagator operator will be discussed in section 2.2.

If the Hamiltonian commutes with itself at different times, the time-ordering operator is unnecessary and this expression simplifies to $\hat{U}(t, t_0) = \exp\{-i \int_{t_0}^t d\tau \hat{H}(\tau)\}$ and, furthermore, if the Hamiltonian is time-independent, the integration can be performed $\hat{U}(t, t_0) = \exp\{-i(t - t_0)\hat{H}\}$. However, in a general case of RT-TDDFT simulation, none of these simplifications applies and one should consider the complete formula 1.113.

The propagator operator has three fundamental properties which can be derived from its definition 1.103. These properties should be satisfied by any decent propagator approximation.

- **Unitarity.** This property derives from the fact that the orthonormalization of the states $\varphi_i(t)$ must be constant

$$\langle \varphi_i(t_2) | \varphi_j(t_2) \rangle = \langle \varphi_i(t_1) | \varphi_j(t_1) \rangle = \delta_{ij}. \quad (1.114)$$

From equation 1.114 we can obtain the unitarity property of the propagator in the following way: One obtains the state at t_2 from the state at t_1 using the propagator operator

$$|\varphi_i(t_2)\rangle = \hat{U}(t_2, t_1) |\varphi_i(t_1)\rangle, \quad \langle \varphi_i(t_2) | = \langle \varphi_i(t_1) | \hat{U}^H(t_2, t_1). \quad (1.115)$$

Substituting these expressions into equation 1.114, one obtains

$$\langle \varphi_i(t_1) | \hat{U}^H(t_2, t_1) \hat{U}(t_2, t_1) | \varphi_i(t_1) \rangle = \langle \varphi_i(t_1) | \varphi_i(t_1) \rangle. \quad (1.116)$$

This equation is satisfied if the \hat{U} operator is unitary

$$\hat{U}^H(t_2, t_1) \hat{U}(t_2, t_1) = \hat{I}. \quad (1.117)$$

- **Time-reversal symmetry.** If one propagates a state from t_1 to t_2 and then, in reverse order, from t_2 to t_1 , one should obtain the same state. From the $t_1 \rightarrow t_2$ propagation, one can express (in the absence of the external magnetic field) the $\varphi_i(t_1)$ state

$$\varphi_i(t_2) = \hat{U}(t_2, t_1) \varphi_i(t_1), \quad \varphi_i(t_1) = \hat{U}^{-1}(t_2, t_1) \varphi_i(t_2). \quad (1.118)$$

On the other hand, the $\varphi_i(t_1)$ state can be obtained from $\varphi_i(t_2)$ as

$$\varphi_i(t_1) = \hat{U}(t_1, t_2) \varphi_i(t_2). \quad (1.119)$$

Equating the expressions of $\varphi_i(t_1)$ from 1.118 and 1.119, one gets the time-reversal property of the propagator operator

$$\hat{U}(t_1, t_2) = \hat{U}^{-1}(t_2, t_1). \quad (1.120)$$

- **Composition property.** For any three instants t_1 , t_2 and t_3 , one can write

$$\begin{aligned} \hat{U}(t_1, t_2)\hat{U}(t_2, t_3) &= \hat{\mathcal{T}} \left[\exp \left\{ -i \int_{t_1}^{t_2} d\tau \hat{H}(\tau) \right\} \right] \hat{\mathcal{T}} \left[\exp \left\{ -i \int_{t_2}^{t_3} d\tau' \hat{H}(\tau') \right\} \right] \\ &= \hat{\mathcal{T}} \left[\exp \left\{ -i \int_{t_1}^{t_2} d\tau \hat{H}(\tau) - i \int_{t_2}^{t_3} d\tau' \hat{H}(\tau') \right\} \right] \\ &= \hat{\mathcal{T}} \left[\exp \left\{ -i \int_{t_1}^{t_3} d\tau \hat{H}(\tau) \right\} \right]. \end{aligned} \quad (1.121)$$

And, finally, for this property we have

$$\hat{U}(t_1, t_3) = \hat{U}(t_1, t_2)\hat{U}(t_2, t_3). \quad (1.122)$$

It should be noted that it is possible to write the product of exponentials of operators as one exponential of a sum of these operators only due to the presence of the time-ordering operator, otherwise, the commutator of operators would have appeared.

The last property allows one to break the overall simulation time interval $[t_0, t_{sim}]$ into small intervals

$$\hat{U}(t_0, t) = \prod_{i=0}^{t < t_{sim}} \hat{U}(t_i + \Delta t_i, t_i), \quad (1.123)$$

where t_{sim} is the simulation time. There are two reasons for doing so: First, one is not usually interested in knowing only the initial and the final states, but rather the dynamics of the system, which implies a time step discretization. Second, such a scheme improves the quality of a propagator operator approximation, since an approximation error depends on the time step Δt : the smaller Δt , the better the propagation accuracy. So, as a final result, the propagation of the wave function from t to $t + \Delta t$ can be written as

$$\varphi_i(t + \Delta t) = \hat{\mathcal{T}} \exp \left\{ -i \int_t^{t+\Delta t} d\tau \hat{H}(\tau) \right\} \varphi_i(t). \quad (1.124)$$

RT-TDDFT typical simulation

To summarize, we present an outline of a typical RT-TDDFT simulation scenario, which was used in this work.

- Set up an atomic system: provide the set of atomic coordinates $\{\mathbf{R}_i\}$, number of electrons N in the system.

- Perform the ground-state DFT calculation: obtain the ground-state density $\rho_0(\mathbf{r})$ and energy E_0 as well as the set of the Kohn-Sham orbitals $\varphi_i^{(0)}(\mathbf{r})$.
- Add a time-dependent perturbation $\hat{V}_{pert}(\mathbf{r}, t_i)$.
- Evaluate the Kohn-Sham Hamiltonian at t_i , $\hat{h}_s([\rho(t_i)]; \mathbf{r}, t_i)$ using the adiabatic approximation for the Kohn-Sham potential $v_{xc}([\rho(t_i)]; \mathbf{r})$.
- Perform the time-propagation from t_i to $t_i + \Delta t$ using the propagator operator $\hat{U}(t_i, t_i + \Delta t)$.
- Evaluate the time-dependent quantities of interest at time $t = t_i + \Delta t$ (the total energy $E_{tot}(t)$, the dipole moment $\mathbf{d}(t)$, etc.).
- Continue the propagation until $t = t_{sim}$.

1.5 Stopping power from RT-TDDFT

In this section, we will discuss how to calculate the stopping power using the RT-TDDFT approach. First, we will briefly consider the most general case of the TDDFT-Ehrenfest dynamics. Then we will apply some approximations to simplify it and, therefore, to reduce the computational cost. Finally, we will discuss different techniques to reproduce the experimental results.

1.5.1 Single-trajectory stopping power

A straightforward approach to calculate the stopping power from atomistic simulations is to perform a non-equilibrium *ab initio* dynamics evolving the electrons as well as the nuclei positions of a system. One of the possibilities to do so is the coupled electron-nuclei TDDFT-Ehrenfest dynamics [70]. In this approach, the electron dynamics is covered by the time-dependent Kohn-Sham equations (1.96) and the nuclear motion is treated in a classical fashion and is given by the following equation

$$M_a \frac{\partial^2}{\partial t^2} \mathbf{R}_a(t) = - \sum_i \langle \varphi_i(t) | \nabla_{\mathbf{R}_a} \hat{H} | \varphi_i(t) \rangle - \nabla_{\mathbf{R}_a} \left[\sum_{b \neq a}^M \frac{Z_a Z_b}{|\mathbf{R}_a - \mathbf{R}_b|} \right], \quad (1.125)$$

where the expression of the electronic Hamiltonian H is presented in equation 1.6. The first term on the right-hand side represents the average time-dependent forces on a nucleus a from the electrons calculated using the Kohn-Sham time-dependent orbitals and the second term is the force exerted by all nuclei (except the nucleus a) on the nucleus a .

Within the TDDFT-Ehrenfest framework, the simulation procedure is, first, to perform the ground state DFT calculation, then assign an initial velocity to the projectile and after that perform a real-time simulation updating the projectile and atomic positions at each time step. One can mention that in this case the projectile is treated in the same manner

like all the other atoms of the system, therefore there is no need to introduce an external perturbation in the Hamiltonian: $\hat{V}_{pert}(\mathbf{r}, t) = 0$.

The total energy of the system E_{tot} will remain constant during the simulation. It is convenient to divide the total energy on the following contributions: 1) the electronic energy E , including the electrons of the projectile (its final expression within the TDDFT formalism is presented in equation 1.99); 2) the kinetic energy of the target nuclei E_{nucl}^{kin} and 3) the kinetic energy of the projectile nucleus E_{proj}^{kin}

$$E_{total} = E + E_{nucl}^{kin} + E_{proj}^{kin}. \quad (1.126)$$

Here we neglect the nucleus-nucleus interaction energy, which is usually done for this kind of problems [77].

Let us call l the coordinate along the projectile path. Then the total stopping power can be found directly from the energy transfer from the projectile to the target

$$S_{total} = -\frac{dE_{proj}^{kin}}{dl} = \frac{dE}{dl} + \frac{dE_{nucl}^{kin}}{dl}, \quad E_{total} = constant. \quad (1.127)$$

This is the expression of the *instantaneous* stopping power: it depends on the projectile path coordinate l and on a given projectile trajectory. This is not a quantity that one can measure experimentally. Below in this section, we will discuss how to deduce an experimentally measurable value from the instantaneous stopping power.

If the nuclear motion can be decoupled from the electronic one, the projectile energy dissipation can be split into two channels: projectile-nuclei and projectile-electrons interactions. Then, the first term on the right-hand side of equation 1.127 can be defined as the instantaneous *electronic* stopping power

$$S_e = \frac{dE}{dl} \quad (1.128)$$

and the second term as the instantaneous *nuclear* stopping power

$$S_n = \frac{dE_{nucl}^{kin}}{dl}. \quad (1.129)$$

Such separation is not valid when the nuclear motion is fast enough with respect to the projectile so the exchange between the electronic energy E and the nuclear kinetic energy E_{nucl}^{kin} takes place at time-scales comparable with those of the projectile passage. An example of such situations is the ionic irradiation of water at low projectile velocities [78]. In this work, we mostly consider the irradiation of light energetic projectiles (proton, antiproton, alpha-particle) in crystalline materials. Therefore the separation $S_{total} = S_e + S_n$ is valid. Such separation is sometimes called the adiabatic approximation [79, 80] (not to confuse with the adiabatic approximation of the exchange-correlation functional).

The stopping power for a single trajectory S^{traj} (total, nuclear or electronic) can be then found as an average over the projectile path of the instantaneous transfer rate [35, 81–87]

$$S_{total}^{traj} = -\left\langle \frac{dE_{proj}^{kin}}{dl} \right\rangle = -\frac{1}{L_{path}} \int_0^{L_{path}} dl \left(\frac{dE_{proj}^{kin}}{dl} \right), \quad (1.130)$$

where L_{path} is the length of the projectile path over which one calculates the average. The expressions for the nuclear and electronic stopping power averaged for a single trajectory can be obtained in the same manner.

On the other hand, the stopping power can be also found as a time average of the non-conservative drag force acting on the projectile [88–90]

$$S_{total}^{traj} = \left\langle \mathbf{F}(t) \cdot \frac{\mathbf{v}_{proj}(t)}{|\mathbf{v}_{proj}(t)|} \right\rangle, \quad (1.131)$$

where $\mathbf{v}_{proj}(t)$ is the time-dependent velocity of the projectile. These two methods are completely equivalent [16].

The TDDFT-Ehrenfest dynamics provides the most precise level of *ab initio* description of the ion-matter interaction. However, such a description has a large computational cost and one may want to apply several simplifications to this dynamics.

In this work, we are interested in the electronic stopping power, which is the prevailing contribution in the range of the projectile velocities, typically, $v_{proj} > 0.1$ a.u. ($E_{proj}^{kin} > 250$ eV). Therefore, first, assuming that the nuclear and electronic degrees of freedom can be decoupled, we then can fix the target nuclei positions. Doing so we restrict the energy deposition from the projectile to the material to be associated only with the electronic stopping power [91]. One cannot claim though that the *instantaneous* nuclear stopping power is zero in the case of the frozen target nuclei: the projectile does still interact with nuclei and its kinetic energy changes due to these interactions. However, in this work, we are interested in the stopping power calculations in periodic systems. In this case, the nuclear contribution *averaged* over the path length L_{path} vanishes due to the crystal periodicity if L_{path} is large enough. Hence, from now, we will consider only the average of the stopping power over the path length, S^{traj} . Then, the following equations are valid in the case of the frozen lattice dynamics

$$S_n^{traj} = \left\langle \frac{dE_{nucl}^{kin}}{dl} \right\rangle = 0, \quad S_e^{traj} = -\left\langle \frac{dE_{proj}^{kin}}{dl} \right\rangle = \left\langle \frac{dE}{dl} \right\rangle. \quad (1.132)$$

The second step of the simplification was proposed by Pruneda and coworkers [39]. One can fix the velocity of the projectile and thereby restrict the projectile to rectilinear motion. This approach corresponds to the experimental measurement of the stopping power as a *function of the projectile velocity*: for each projectile velocity, one needs to take a target thin enough to ensure that the velocity of the projectile remains (almost) constant during its propagation in the sample. That is why the stopping power measurements are complicated to perform for small projectile velocities: in this case, one needs to produce and to manipulate thin film samples and to precisely measure their thickness [92].

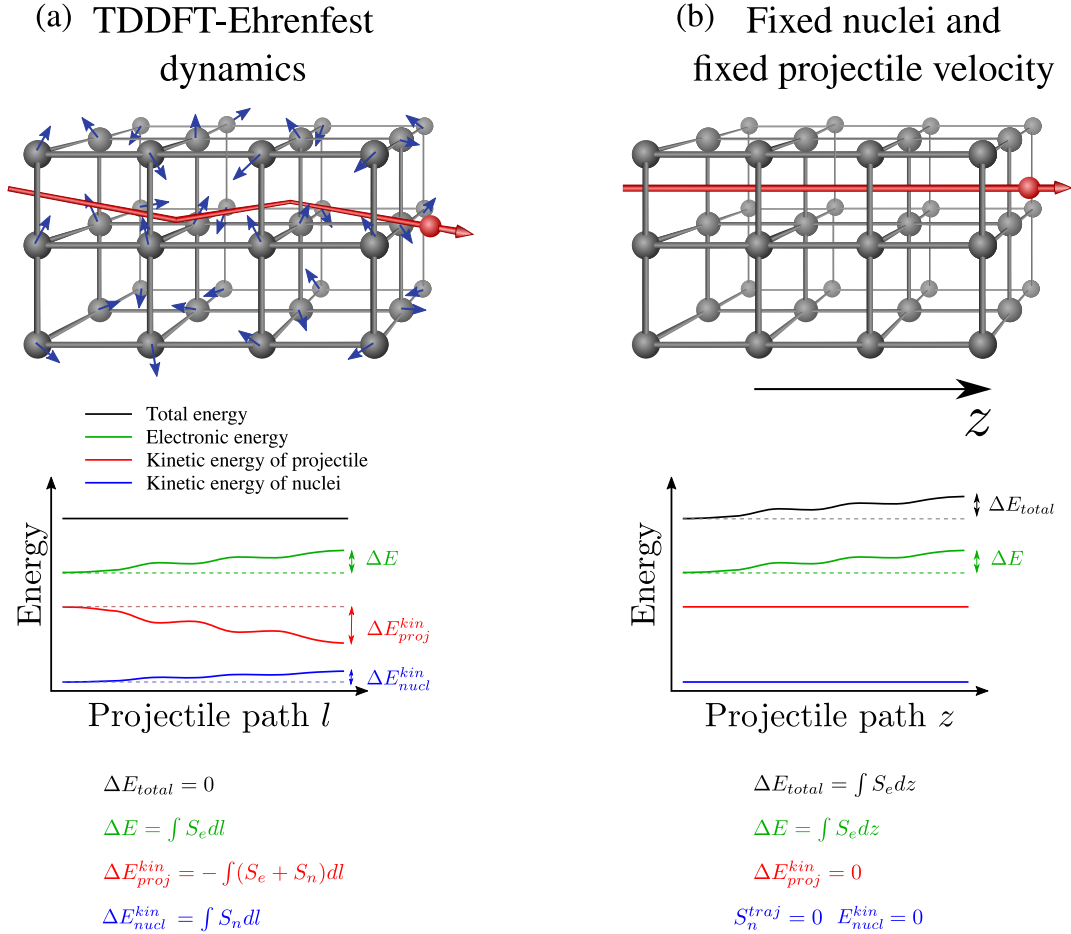


Figure 1.8 : Schematic illustration of different types of dynamics for the *ab initio* stopping power calculations. (a) TDDFT-Ehrenfest simulation: positions of the target nuclei (grey spheres) and of the projectile (red sphere) are updated at each time step, the projectile can undergo deflections (the projectile path is presented as the red line). Blue arrows represent small displacements of the nuclei. The stopping power can be calculated from the decay of the kinetic energy of the projectile. (b) The nuclei positions and the projectile velocity are fixed. The electronic stopping power can be found from the growth of the total energy of the complete system.

We select z -axis as the axis along the projectile track. Then the position of the projectile $\mathbf{r}_{proj}(t)$ is known for any time t

$$\mathbf{r}_{proj}(t) = (p_x; p_y; z_0 + vt), \quad (1.133)$$

where v is the absolute value of the projectile velocity, z_0 is the initial projectile position along z -axis, p_x and p_y are the components of the impact parameter vector ($\mathbf{p} = (p_x; p_y)$), which is the vector that designates the projectile position in the plane perpendicular to the projectile trajectory (XY plane). The impact vector \mathbf{p} remains constant during the projectile movement in this dynamics.

In this case, the atomic system is not closed and therefore the total energy is not

conserved. The electronic stopping power can be found from the increase of the total energy of the system (averaged over the path length)

$$S_e^{traj} = \left\langle \frac{dE}{dz} \right\rangle = \left\langle \frac{dE_{total}}{dz} \right\rangle, \quad E_{proj}^{kin} = constant, \quad E_{nucl}^{kin} = 0. \quad (1.134)$$

The conserved quantity in this case is the difference between the total energy and the work done by the “velocity constrain” force \mathbf{F}^{vc} [16]

$$E_{total}(t) - \int \mathbf{F}^{vc} \cdot d\mathbf{l} = constant. \quad (1.135)$$

This technique simplifies a lot the dynamics because one does not need to evaluate the forces neither on target nuclei nor on the projectile. Therefore, this dynamics can be seen as an RT-TDDFT simulation with an external perturbation in the form of the projectile moving with a constant velocity. The comparison between the TDDFT-Ehrenfest and the fixed projectile trajectory dynamics is illustrated in Fig. 1.8.

This dynamics is valid when the projectile deflection is small and the velocity change during the simulation is negligible. We will discuss in more detail these assumptions considering particular projectile/target systems (section 3.5).

1.5.2 Random stopping power

In the previous section we have discussed how to calculate the stopping power for a single trajectory $S^{traj}(v)$: one needs to specify the initial projectile position and velocity, then perform the real-time dynamics (any among the two mentioned, Fig. 1.8) and then deduce the stopping power as the time average of the instantaneous stopping power. In order to compare the *ab initio* simulations with the experimental results, one should take into account the following considerations: 1) most of the experiments are performed with polycrystalline materials (or intentionally tilted with respect to the projectile path monocrystals) [93]. 2) the beam of projectiles impinges the target with many different impact points (see Fig. 1.9 (a)). Therefore, the average over different trajectories $S^{traj}(v)$ should be calculated. The averaged quantity is then called the random stopping power $\langle S(v) \rangle$. There exist different methods to calculate this average from the atomistic simulations.

1. Random trajectory. This method implies a choice of one “quasi”-random *fixed* trajectory of the projectile [35]. The trajectory is not completely random because the choice is restricted to trajectories which are *incommensurate* with the crystal symmetries. Once the trajectory is chosen, one performs the fixed-trajectory (Fig. 1.8 (b)) simulation of the projectile passage for a given velocity v .

The random electronic stopping power, in this method, $\langle S_e \rangle_{rand.traj.}$ is found as the stopping power of the random trajectory under the conditions that the random trajectory is incommensurate with the crystal symmetries and the trajectory is long enough

$$\langle S_e(v) \rangle_{rand.traj.} = S_e^{traj}(v). \quad (1.136)$$

The simulation runs until the random electronic stopping power $\langle S_e(v) \rangle_{rand. traj.}$ is converged. Because of the random trajectory, the energy transfer rate is not periodic, therefore long trajectories (around 50 Å) are required. Since nowadays the RT-TDDFT simulations of atomic systems of such size are unrealizable, one is forced to perform these calculations in a simulation box of smaller size. Then, the projectile will re-enter the simulation box several times.

The advantage of this method is its similarity with the real experimental conditions. The disadvantage is the fact that since the projectile re-enters the periodic image of the simulation cell, it interacts with already perturbed electronic density (by the same projectile). Even if this effect was *a posteriori* shown to be negligible in the case of the proton projectile in aluminum target [35], the validity of such an approach has to be proven for different types of projectiles and materials.

2. Ensemble average. Another approach consists in selecting multiple short trajectories instead of one long. First, one selects a crystalline axis, along which the projectile will pass (we choose the direction of the passage as z -axis). Then, the impact parameter vector $\mathbf{p} = (p_x; p_y; 0)$ and the projectile velocity v must be specified. Since the propagation of the projectile along a crystalline symmetry axis has a periodic nature due to the crystal symmetry, one obtains a convergent stopping for a given trajectory $S_e^{traj}(v, \mathbf{p})$ for the trajectory lengths much lower than ones used in the previous method (around 10 Å). However, this time we have many short trajectories.

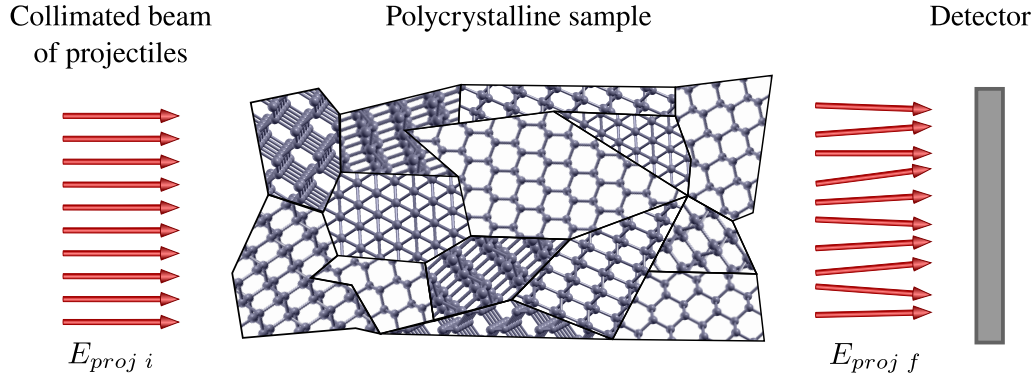
One obtains the random electronic stopping power corresponding to a given selected crystal orientation as an average over the impact parameter

$$\langle S_e(v) \rangle_{ens} = \frac{1}{\mathcal{A}} \int d\mathbf{p} S_e^{traj}(v, \mathbf{p}), \quad (1.137)$$

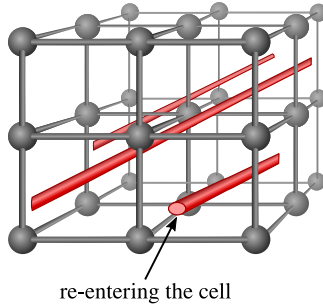
where \mathcal{A} designates a surface in the plane perpendicular to the projectile track (XY plane) in which the impact parameter \mathbf{p} is averaged out. Due to crystal symmetries, this surface can be restricted to an *elementary surface* which is not large (typically, it is in the order of $0.1 a_{lat}^2$, where a_{lat} is the lattice constant). Then, the average stopping power calculated for impact parameters within the elementary surface will completely represent the average for a given crystal orientation.

In linear-response calculations, one applies a similar approach where the impact parameter is explicitly averaged out in the equations for the random stopping power calculations [30, 33, 34]. In RT-TDDFT simulations this method was applied to the stopping power studies of several projectiles (H, He, Li, Ne, Na) in graphitic targets (which is the case of 2D materials) [86], of protons in Ge at low velocities [94], of protons and alpha-particles in SiC [87].

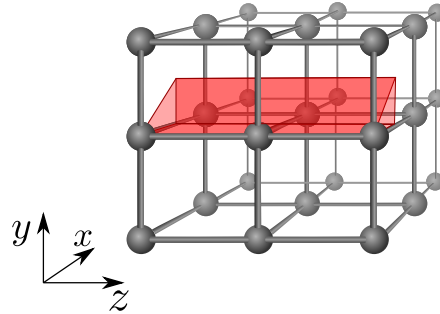
The advantage of this method is the systematic sampling of the impact parameter \mathbf{p} instead of the random behavior of sampling as in the previous method. In addition, since different short trajectories are independent, this allows one to run these calculations in parallel, thereby performing a dummy parallelization. The disadvantage consists in the fact that one should perform this procedure, in principle, for many different crystal orientations. We will consider this question in more detail in section 3.1.3.

(a) ExperimentAtomistic simulations

(b) Random trajectory



(c) Ensemble average



(d) Centroid path

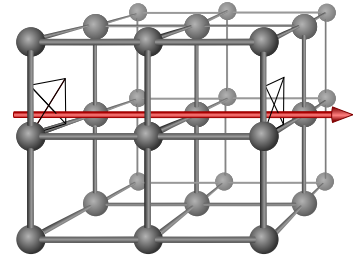


Figure 1.9 : (a) Simplified pictorial representation of the experimental conditions of the random stopping power measurement: A polycrystalline material is exposed to a parallel beam of fast projectiles, the difference between the initial ($E_{proj i}$) and the final ($E_{proj f}$) kinetic energies of projectiles is measured. (b), (c), (d) Schematic illustration of the *ab initio* methods of the random electronic stopping power calculations. (b) Random trajectory technique: Since the trajectory must be long enough the projectile re-enters the simulation box several times. Projectile's path is depicted as a red line. (c) Ensemble average method: One performs the calculations of multiple trajectories parallel to a crystalline axis. The elementary sampled region is depicted as a red prism (triangle in XY plane). (d) Centroid path approximation: One selects only one short trajectory along a crystalline axis. The impact parameter of this trajectory is selected as the geometric center of the elementary surface (the center of the triangle in XY plane).

3. Centroid path. This method is a simplification of the previous one. The idea is to select among the ensemble of trajectories, a single trajectory that would represent the real average value (equation 1.137). This trajectory is called the centroid path. The impact parameter corresponding to the centroid path trajectory, $\mathbf{p}_{centroid}$, is usually selected as the geometric center (hence the name of the method) of the elementary surface. It has been found that this approximation is satisfactory (up to 10%) for SiC [87] and graphitic

[86] targets. This method, of course, saves a lot of computational time, however, for new atomic systems, one should verify the validity of this approach.

All the three methods are schematically presented in Fig. 1.9.

1.5.3 Channeling stopping power

Another and much less common type of the stopping experiment is the channeling stopping power. By a definition, the channeling occurs when the projectiles travel along with the crystalline directions. This implies the conditions which are difficult to satisfy experimentally: the target must be correctly oriented with respect to the beam of projectiles and the target must not be polycrystalline. Such type of experiments can be performed with thin films [95, 96] or, with monocrystals [97].

In channeling conditions (also sometimes called the hyperchanneling [16, 81]), the projectiles that enter the crystal with an angle smaller than the critical angle continue the movement along the axis. The projectiles with the trajectory angles larger than the critical one quit the channel and do not reach the detector. Projectiles that undergo head-on collisions also quit the trajectory along the axis.

Because of the elastic interactions with the nuclei of the target, after some transient regime, the projectiles follow the channeling trajectories: the trajectories that are far from the target nuclei [98, 99].

One observes this behavior for a wide range of velocities (up to relativistic ones), though the critical angle decreases with the increase of the projectile velocity. One can explain this behavior in the following manner: when the projectile moves along a high-symmetry channel, it undergoes the deflections which are small at every time but systematic. Therefore, finally, the projectile will move with impact parameter $\mathbf{p}_{centroid}$ at which the interaction with the nuclei is the lowest. The penetration depth under channeling conditions is larger than in polycrystalline materials.

In the atomistic simulations of the channeling stopping power, one is not interested in the *transient* regime but rather by the passage of the projectiles in the *bulk*. Moreover, the transient regime occurs during, at least, hundreds of nm and therefore it is not possible to simulate this process in a straightforward manner on the *ab initio* level.

Finally, in order to simulate the channeling, one needs to choose one of the high symmetry crystalline directions and select the impact parameter $\mathbf{p}_{centroid}$ corresponding to the most distant projectile position with respect to the nuclei in *XY* plane (see Fig. 1.10).

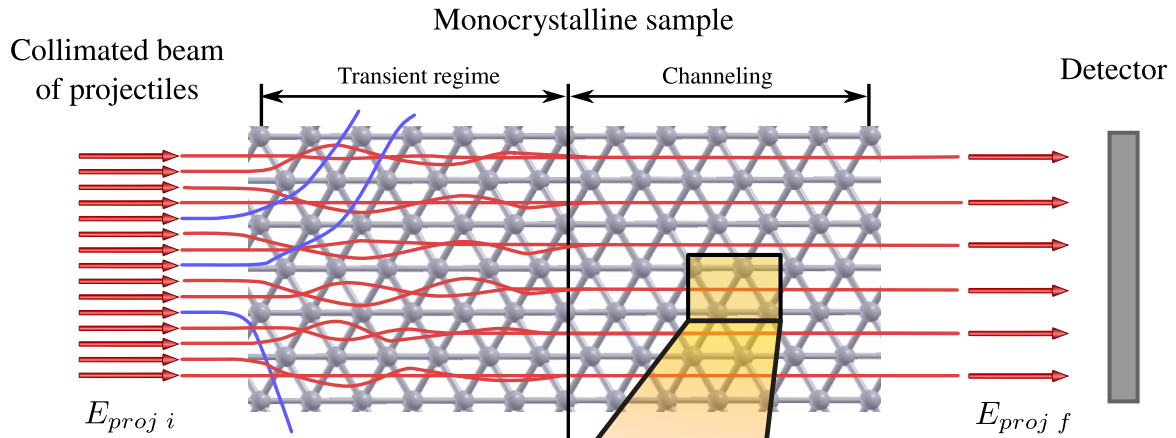
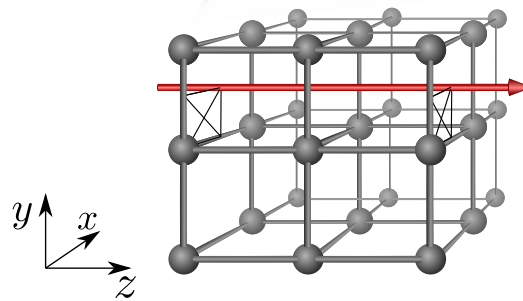
(a) Experiment(b) Atomistic simulation

Figure 1.10 : (a) Idealized representation of the channeling experiment. A collimated beam of projectiles enters along one of the high-symmetry crystalline axes. Due to collisions with the nuclei, the projectiles either continue their propagation in the *center* of the channel or quit the channel because of a head-on collision (depicted as blue lines). In order to demonstrate different behavior of the projectiles' motion, the beam of projectiles is presented as dense. In real experimental conditions, the distance between projectiles is large enough to neglect the interaction between them. Moreover, the projectiles do not enter the crystal at the same time as it is presented in the figure. For the sake of simplicity, we represent here only those projectiles that have initially ideally parallel trajectories to the crystalline axis. (b) Representation of the *ab initio* simulation of the irradiation under the channeling conditions. One simulates the projectile propagation *after* the transient regime. In the simulation, one uses only one trajectory parallel to the crystalline axis. The impact parameter of the trajectory is chosen in the way to have the maximal average distance between the projectile and the nuclei of the target. In the presented case, this impact parameter corresponds to the corner of the elementary sampling surface.

CHAPTER 2

RT-TDDFT implementation in Gaussian basis

In this chapter, we describe our implementation of the RT-TDDFT approach. This implementation is based on MOLGW code, therefore, first we will describe the main features of the DFT part of this code, then we will describe the implementation itself and finally, the validation of the implementation.

2.1 The backbone of the implementation

2.1.1 Implementation workflow

MOLGW is an *ab initio* code dedicated to the many-body perturbation theory (MBPT) calculations. In particular, it performs the calculations of the many-body self-energy within the GW approximation and of the solution of the Bethe-Salpeter equation (BSE) [42]. However, these methods are out of the scope of this work and the choice of MOLGW as the development platform is rather due to the basic generalized Kohn-Sham (gKS) framework which is also contained in the code. In general, the organization of the code is the following: 1) produce the wave functions and eigenvalues from the self-consistent gKS calculation; 2) use these quantities for the GW and the BSE calculations. In the present work, in a similar fashion, we obtain the ground-state wave function of a system using the self-consistent loop, but then we perform the propagation of the wave function in time. Hence, the ground-state DFT part of MOLGW code is used as a starting point for the time-dependent propagation (Fig. 2.1a).

However, the MOLGW subroutines intervene also all along the propagation (see Fig.

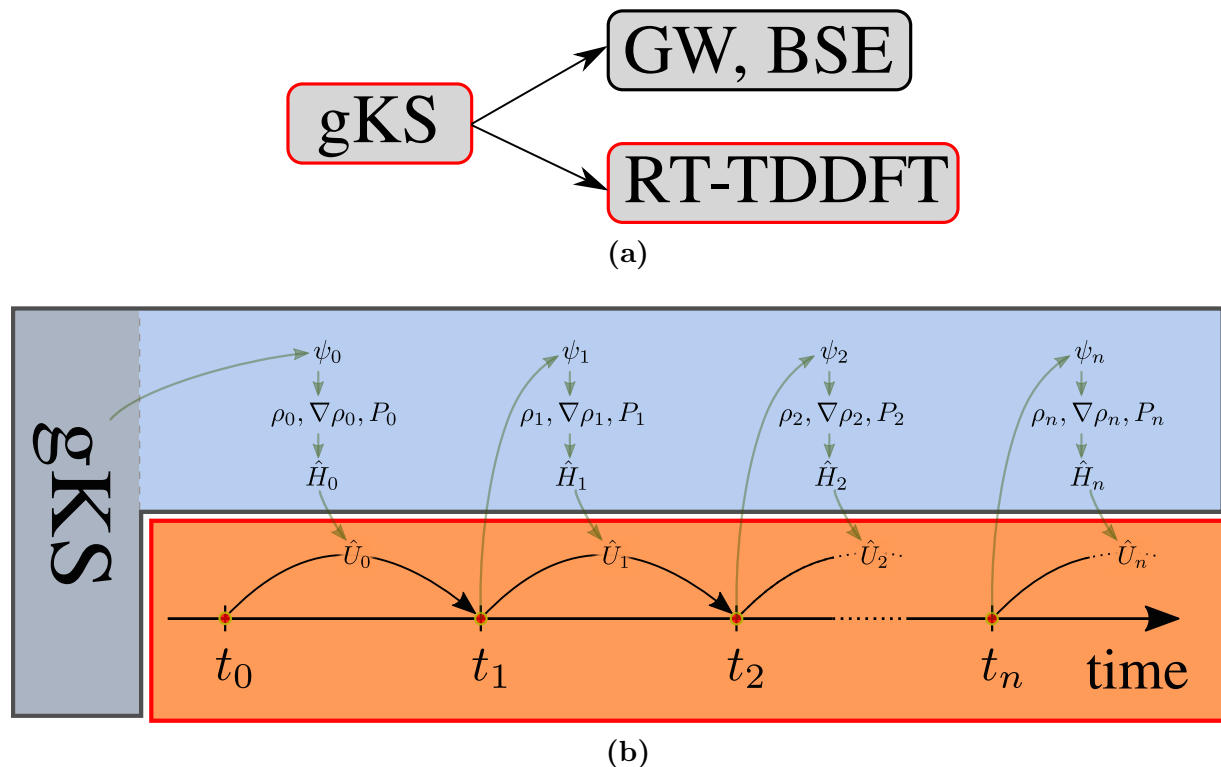


Figure 2.1 : (a) Workflow of MOLGW code: the RT-TDDFT part can be considered as a post-processing branch along with other possible post-processings (GW and BSE) ; (b) Schematic representation of the code organization. The grey area in the left-hand side represents the non-modified generalized Kohn-Sham part (gKS), the blue area represents slightly modified MOLGW subroutines because of the complex nature of the time-dependent wave function and the orange area depicts the RT-TDDFT part of the code developed in this work.

2.1b). As was discussed in the [previous chapter](#), for the RT-TDDFT propagation one needs to calculate the propagator operator on the fly, which depends on the Hamiltonian. The Hamiltonian, in its turn, is a functional of the electronic density $\rho(\mathbf{r})$, the electronic density gradient $\nabla\rho(\mathbf{r})$ and the density matrix P . The exact dependence is determined by the choice of the exchange-correlation functional. The procedure of the Hamiltonian calculation from $\rho(\mathbf{r})$, $\nabla\rho(\mathbf{r})$ and P for RT-TDDFT is similar to the ground-state DFT part. The only difference is that the wave function becomes complex for the RT-TDDFT. This leads to some modifications that will be discussed later in this chapter. Apart from that, numerical schemes and parallelization of the code are exactly the same.

2.1.2 Gaussian basis set

Expression

One of the main features which determines the niche of MOLGW code in *ab initio* codes classification is its implementation in the *localized Gaussian basis set*. The term *localized*

implies that one-electron wave functions are expanded as linear combinations of atom-centered orbitals ϕ_α :

$$\varphi_i^\sigma(\mathbf{r}) = \sum_{\alpha=1}^{N_{AO}} C_{\alpha i}^\sigma \phi_\alpha(\mathbf{r}), \quad (2.1)$$

where σ is the spin channel. The summation index α runs from 1 to the number of basis functions (or, in other words, the number of atomic orbitals, N_{AO}) in a set. Hereafter we reserve Greek indexes for the basis functions and Latin indexes for the electronic states.

The term *Gaussian* means that the radial components of the atom-centered orbitals are chosen to be linear combinations of Gaussian orbitals:

$$\phi_\alpha(\mathbf{r}) = Y_l^m(\hat{\mathbf{r}}) r^l \sum_b c_b e^{-\alpha_b r^2}, \quad (2.2)$$

where $Y_l^m(\hat{\mathbf{r}})$ are the real spherical harmonics, c_b are the decomposition coefficients which are *fixed* for a given basis set. Every function $\phi_\alpha(\mathbf{r})$ is centered around one of the atoms of a system.

In equation (2.2) the Gaussian exponents α_b determine the spatial extension of the basis functions. Basis functions with smaller α_b parameter are more diffused in space than those with larger α_b parameter. In such a way one can describe with a tunable accuracy both core and valence electrons. For example, let us consider one arbitrary atom and suppose that in a given basis set for this atom one has the lowest Gaussian exponent $\alpha_b = \alpha_{bmin}$ and the largest one $\alpha_b = \alpha_{bmax}$, we also assume that the basis contains enough exponents between the two limits. Then the electronic wave function will be correctly described within the interval $[1/\sqrt{\alpha_{bmax}}, 1/\sqrt{\alpha_{bmin}}]$. Usually, Gaussian basis functions contain exponents in the range of $10^{-2} \div 10^5 \text{ \AA}^{-2}$ which leads to a remarkable spatial range of $10^{-3} \div 10 \text{ \AA}$. Furthermore, for a specific application one could expand this range using an appropriate basis.

Benefits and drawbacks

The choice of Gaussian basis has several appealing advantages, in particular, for the electronic stopping power calculation.

- ⊕ The Gaussian basis set allows one to describe at the same level both the valence and the core electrons. This feature is very important since the ion irradiation is a high energy process that excites all the electrons of the target.
- ⊕ The calculation time is significantly lower (at least for the stopping power calculations) in comparison to, for example, plane-wave or real-space grid codes. This is possible because of the fact that Gaussian basis functions are located around atomic positions, somehow anticipating the electronic density distribution, therefore the number of Gaussian basis functions for a given system is normally ten to hundred times lower than in the case of plane-wave or real-space codes.

- ⊕ The Gaussian basis set enables the use of the hybrid functionals that include a part of exact-exchange, at a moderate cost.

On the minus side of the approach, one should mention the following points:

- ⊖ It has been reported that Gaussian basis may have difficulties to capture high-energy excitations for atomic systems [100, 101].
- ⊖ In some cases, the convergence of a physical quantity versus a basis set can be slow and not as systematic as in plane-wave or real-space codes.

Correlation-consistent basis sets

At the present time, there are a lot of available Gaussian basis sets. However, correlation-consistent (cc) basis set families developed by Dunning and coworkers [102, 103] are the most systematic and, will be used in this work. Therefore, we would like to focus on these basis sets. The cc-basis sets provide smooth and monotonic convergence for many physical quantities such as correlation energy [104], Hartree-Fock energy [105], harmonic frequencies [106], electric dipole moments [107].

The most standard cc family is the polarized valence (pV) set - cc-pVXZ. Here X stands for the number of Gaussian orbitals used to represent a valence shell orbital: X=D (double), T (triple), Q (quadruple), 5, 6; X=6 being usually the largest basis available in these series. The number of basis functions (N_{AO}) is a crucial parameter for the accuracy of calculations as well as for the calculation time, therefore, let us consider in more detail the construction of cc-pVXZ basis sets.

Let us consider an example of Al atom in the cc-pVDZ basis. Al electron configuration is: $1s^2 2s^2 2p^6 3s^2 3p^1$. DZ means that for the valence shell one has 2 Gaussian orbitals per atomic orbital. Then, for higher angular momenta one has a decreasing number of Gaussian orbitals: for the d orbitals, one has 1 Gaussian orbital and 0 orbitals starting from f . For core orbitals one has 1 Gaussian orbital per atomic orbital (by core orbitals we mean all orbitals which are below the valence shell). The idea behind is that for a given atom one can always select the parameters of Gaussian functions which will describe the core orbitals with high precision even with a few basis functions, because they are unaffected by the environment. Whereas for the valence and excited states one should have a more flexible basis, hence, larger number of basis functions. When counting the basis functions one should take into account that for a given orbital momentum l one has $2l + 1$ atomic orbitals. Finally, for Al in the cc-pVDZ basis one has 18 basis functions: 5 basis functions for the core shells ($1s \times 1, 2s \times 1, 2p \times 3$), 8 basis functions for the valence shell ($3s \times 2, 3p \times 6$) and 5 basis functions for the empty shells ($3d \times 5$).

Fig. 2.2 shows the order of the basis functions completion for the bases from cc-pVDZ to cc-pVQZ. It is seen that by switching from an X-1 to an X basis one increases the highest angular momentum, but as well the number of basis functions with the orbital momenta which were already included in the X-1 basis. As a consequence, the number of basis functions grows not linearly but as a square of X.

empty shells	{	g 9	 cc-pVDZ	N_{AO}	
		f 7 7			 cc-pVTZ
		d 5 5 5			
valence shell	{	sp 4 4 4 4			
core shells	{	2p 3			
		2s 1			
		1s 1			

Figure 2.2 : Illustration of the polarized valence basis sets $cc\text{-pVXZ}$ construction using an example of Al atom in $cc\text{-pVDZ}$ (green), $cc\text{-pVTZ}$ (blue) and $cc\text{-pVQZ}$ (red) basis sets. One square represents basis functions for a given orbital momentum, numbers inside the squares indicate the number of basis functions, which is nothing but $2l + 1$, where l is the orbital momentum. For the core shells, the number of Gaussians per atomic orbital is the same for all basis sets. On the right side of the picture, the color legend and the total number of basis functions (N_{AO}) for Al atom are indicated.

The polarized valence sets can be augmented with diffuse functions ($aug\text{-}cc\text{-pVXZ}$), which is frequently used for optical absorption spectra calculations and core functions ($cc\text{-pCVXZ}$), which was used in this work for the electronic stopping power calculations. This improvement of description of valence or core electrons leads to significant growth of the number of basis functions. For example, for Al atom, the number of basis functions in the $cc\text{-pV6Z}$ basis set is 144 whereas in the $cc\text{-pCV6Z}$ basis set it reaches 275.

Density matrix

For a single determinant wave function, the electronic charge density is given by

$$\rho^\sigma(\mathbf{r}) = \sum_{i=1}^{occ} f_i \varphi_i^\sigma(\mathbf{r}) \varphi_i^{\sigma*}(\mathbf{r}), \quad (2.3)$$

where f_i^σ is the occupation number for an electronic level i and occ is the highest occupied level number. By writing the electronic wave function $\varphi_i(\mathbf{r})$ decomposition in the basis set (equation 2.1), one gets

$$\rho^\sigma(\mathbf{r}) = \sum_{i=1}^{occ} f_i^\sigma \sum_{\alpha} C_{\alpha i}^\sigma \phi_{\alpha}(\mathbf{r}) \sum_{\beta} C_{\beta i}^{\sigma*} \phi_{\beta}^*(\mathbf{r}). \quad (2.4)$$

It should be noted that even if the C matrix can be complex, the Gaussian basis functions are always real in MOLGW ($\phi_{\beta}^*(\mathbf{r}) = \phi_{\beta}(\mathbf{r})$). One can reorder the terms in the expression

2.4 in the following way

$$\rho^\sigma(\mathbf{r}) = \sum_{\alpha\beta} \left[\sum_i f_i^\sigma C_{\alpha i}^\sigma C_{\beta i}^{\sigma*} \right] \phi_\alpha(\mathbf{r}) \phi_\beta(\mathbf{r}). \quad (2.5)$$

Then we define the expression in the square brackets as the density matrix

$$P_{\alpha\beta}^\sigma = \sum_i f_i^\sigma C_{\alpha i}^\sigma C_{\beta i}^{\sigma*}, \quad (2.6)$$

or, in a matrix form,

$$P^\sigma = C^\sigma F^\sigma C^{\sigma H}, \quad (2.7)$$

where F^σ is a diagonal matrix of occupations f_i^σ . The symbol $(^H)$ means the transpose(T)-conjugate(*) of a matrix. By a simple application of the transpose-conjugate operation to the 2.7 equation, one can show that the density matrix is Hermitian

$$P^{\sigma H} = (C^\sigma F^\sigma C^{\sigma H})^H = C^{\sigma H H} (C^\sigma F^\sigma)^H = C^\sigma F^\sigma C^{\sigma H} = P^\sigma. \quad (2.8)$$

Finally, using the definition of the density matrix, one can express the electronic density as

$$\rho^\sigma(\mathbf{r}) = \sum_{\alpha\beta} P_{\alpha\beta}^\sigma \phi_\alpha(\mathbf{r}) \phi_\beta(\mathbf{r}), \quad (2.9)$$

and similarly, the density gradient

$$\nabla \rho^\sigma(\mathbf{r}) = \sum_{\alpha\beta} P_{\alpha\beta}^\sigma \nabla_r [\phi_\alpha(\mathbf{r}) \phi_\beta(\mathbf{r})]. \quad (2.10)$$

To summarize, having the coefficient matrix C^σ one can deduce the density matrix P^σ , the electronic density $\rho^\sigma(\mathbf{r})$ and the electronic density gradient $\nabla \rho^\sigma(\mathbf{r})$.

2.1.3 Roothaan-Hall equations

For localized bases, the basis functions are normalized, but not orthogonal which leads to modifications of usual stationary and time-dependent Schrödinger equations. Here we derive basic equations which are necessary for the RT-TDDFT code implementation in the localized basis. In these sections, we will omit the spin channel index σ since the equations under discussion have exactly the same form for the spin up and spin down channels.

The overlap matrix is defined as

$$S_{\alpha\beta} = \langle \phi_\beta | \phi_\alpha \rangle = \int d\mathbf{r} \phi_\alpha(\mathbf{r}) \phi_\beta(\mathbf{r}), \quad (2.11)$$

where $|\phi_\alpha\rangle$ is the corresponding ket state to the basis function ϕ_α . The overlap matrix is symmetric ($S_{\alpha\beta} = S_{\beta\alpha}$).

When S is not the unitary matrix, the completeness relation reads

$$\sum_{\alpha\beta} |\phi_\alpha\rangle S_{\alpha\beta}^{-1} \langle\phi_\beta| = \hat{I}. \quad (2.12)$$

The expression of the Hamiltonian projected on the basis functions is given by

$$H_{\alpha\beta} = \iint d\mathbf{r}d\mathbf{r}' \phi_\alpha(\mathbf{r}) H(\mathbf{r}, \mathbf{r}') \phi_\beta(\mathbf{r}'). \quad (2.13)$$

The coefficients C allow one to describe a wave function $\varphi_i(\mathbf{r})$ as a linear combination of basis functions (equation 2.1). The construction of C matrix is such that the basis index comes first and the electronic state index - second, this means that one column of the C matrix corresponds to a state

$$C = \begin{pmatrix} \varphi_1 & \varphi_2 & \varphi_3 & \cdots & \varphi_{N_{AO}} \\ C_{11} & C_{12} & C_{13} & \cdots & C_{1N_{AO}} \\ C_{21} & C_{22} & C_{23} & \cdots & C_{2N_{AO}} \\ \vdots & \vdots & \vdots & \cdots & \vdots \\ C_{N_{AO}1} & C_{N_{AO}2} & C_{N_{AO}3} & \cdots & C_{N_{AO}N_{AO}} \end{pmatrix}. \quad (2.14)$$

In order to find the ground state wave functions, one needs to solve the stationary Schrödinger equation

$$\hat{H}\varphi_i(\mathbf{r}) = E_i\varphi_i(\mathbf{r}). \quad (2.15)$$

In general terms, this equation has the same form for both Hartree-Fock and gKS. Then, in order to write equation 2.15 in a matrix form, we can use the relation 2.1 to express $\varphi_i(\mathbf{r})$ in the basis set

$$\hat{H} \sum_{\alpha} \phi_\alpha(\mathbf{r}) C_{\alpha i} = E_i \sum_{\alpha} \phi_\alpha(\mathbf{r}) C_{\alpha i}. \quad (2.16)$$

Projecting this equation on a basis state $\langle\phi_\beta|$ one recovers the Hamiltonian expression in the basis set $H_{\beta\alpha} = \langle\phi_\beta|\hat{H}|\phi_\alpha\rangle$ on the left-hand side and the overlap matrix $S_{\beta\alpha} = \langle\phi_\beta|\phi_\alpha\rangle$ on the right-hand side, i.e.,

$$\sum_{\alpha} H_{\beta\alpha} C_{\alpha i} = E_i \sum_{\alpha} S_{\beta\alpha} C_{\alpha i}. \quad (2.17)$$

Writing this equation in the matrix form we obtain the Roothaan-Hall equation

$$HC = SCE, \quad (2.18)$$

where E is a diagonal matrix containing the orbital energies E_i

$$E = \begin{pmatrix} E_1 & & & 0 \\ & E_2 & & \\ 0 & & \ddots & \\ & & & E_{N_{AO}} \end{pmatrix}. \quad (2.19)$$

It is important to mention that the wave functions obtained as solutions of the Roothaan-Hall equation are orthonormal regardless of the basis representation or the Hamiltonian approximation. The orthonormality condition reads

$$\langle \varphi_j | \varphi_i \rangle = \delta_{ij}. \quad (2.20)$$

Using again the representation of $\varphi_i(\mathbf{r})$ in the localized basis 2.1, one obtains the orthonormalization of the coefficients $C_{\alpha i}$

$$\sum_{\alpha\beta} \langle \phi_\beta | C_{\beta j}^* C_{\alpha i} | \phi_\alpha \rangle = \sum_{\alpha\beta} S_{\beta\alpha} C_{\beta j}^* C_{\alpha i} = \delta_{ij}. \quad (2.21)$$

Writing this equation in the matrix form and applying some transformations (multiplication by C^{-1} , S^{-1} , etc.), one gets the set of orthonormalization equations

$$C^H S C = I \quad (2.22a)$$

$$S C C^H = I \quad (2.22b)$$

$$C C^H S = I, \quad (2.22c)$$

where I is the identity matrix.

Finally, multiplying equation 2.18 by the C^H matrix from the left and using the orthonormalization relation 2.22a, one obtains the eigenenergies matrix

$$E = C^H H C. \quad (2.23)$$

In a similar way, multiplying equation 2.18 by $C^H S$ from the right and using equation 2.22c, one gets the expression for the Hamiltonian

$$H = S C E C^H S. \quad (2.24)$$

2.1.4 Orthogonalization of the basis

Even though all the calculations (including the time-dependent part) can be performed in the non-orthogonal basis, switching to an orthogonal basis set at least for a part of calculations can be advantageous. There are essentially two reasons for doing so. First, this would put the Roothaan-Hall equation into the form of the usual matrix eigenvalue problem, which would allow one to use standard diagonalization packages. Second and more important, the S matrix is often ill-conditioned, it means that the calculation of the generalized eigenvalue problem can be unstable. To demonstrate this, let us multiply equation 2.18 by the S^{-1} matrix from the left, then we get

$$S^{-1} H C = C E. \quad (2.25)$$

It is seen now that in the non-orthogonal basis, one needs to diagonalize not H but $S^{-1} H$ matrix. When some basis functions have a large overlap (diffused functions, for example),

this leads to large values of S^{-1} and makes the solution procedure unstable. There is a classical transformation, *canonical orthogonalization* [50], which allows one to avoid the use of unstable S^{-1} matrix. Furthermore, using this transformation, one can eliminate small eigenvalues of S , thereby improving the stability of the problem.

The idea is to define a new set of orthogonal functions $\{\phi'_\alpha(\mathbf{r})\}$ which can be expressed through the non-orthogonal set $\{\phi_\alpha(\mathbf{r})\}$ via a transformation matrix X as follows

$$\phi'_\beta(\mathbf{r}) = \sum_{\alpha} X_{\alpha\beta} \phi_{\alpha}(\mathbf{r}). \quad (2.26)$$

This time, the orthonormality condition for the $\{\phi'_\alpha(\mathbf{r})\}$ set reads

$$\langle \phi'_\beta | \phi'_\alpha \rangle = \int d\mathbf{r} \phi'_\alpha(\mathbf{r}) \phi'_\beta(\mathbf{r}) = \delta_{\alpha\beta}. \quad (2.27)$$

Substituting $\phi'_\alpha(\mathbf{r})$ and $\phi'_\beta(\mathbf{r})$ with their expression 2.26 and using the definition of the overlap matrix 2.11 one finds a following property of the X matrix

$$X^H S X = I \quad (2.28)$$

The method of *canonical orthogonalization* consists in defining the transformation matrix as

$$X = U s^{-1/2}, \quad (2.29)$$

where s is a diagonal matrix, which contains the eigenvalues of the S matrix. Let U be a matrix of eigenstates of S since the overlap matrix is symmetric, U is a unitary matrix ($U^H U = U U^H = I$) and all eigenvalues of S are non-negative. Then, by a definition, one has

$$s = U^H S U, \quad (2.30a)$$

$$S = U s U^H. \quad (2.30b)$$

Thus, $s^{-1/2}$ is the matrix that contains inverses of square roots of diagonal elements of s in order to provide $(s^{-1/2} s^{-1/2})^{-1} = s$. With these definitions, it is seen that the expression of the X matrix 2.29 indeed satisfies the property of the transformation matrix 2.28, therefore it can be used for such transformation. This particular choice of the X matrix provides two additional properties of this matrix which will be used later

$$X X^H = U s^{-1/2} s^{-1/2} U^H = S^{-1} \quad (2.31a)$$

$$X^H X = s^{-1/2} U^H U s^{-1/2} = s^{-1}. \quad (2.31b)$$

Now it is explicitly seen that if there is a linear dependence between the basis set functions, this will lead to very small eigenvalues s_i (and, as a consequence, very large $s_i^{-1/2}$), which makes the orthogonalization procedure instable. In order to deal with this problem, one can eliminate too small s_i values. For sake of simplicity, let us order the eigenvalues s_i in a decreasing order ($s_1 > s_2 > s_3 > \dots$). Then, one can truncate the X

matrix keeping the s_i values larger than some threshold parameter. Suppose that N_{MO} eigenvalues are larger than the threshold, then for the X matrix we have

$$X = \left(\begin{array}{cccc|cccc} U_{11} s_1^{-1/2} & U_{12} s_2^{-1/2} & \cdots & U_{1 N_{MO}} s_{N_{MO}}^{-1/2} & U_{1 N_{MO}+1} s_{N_{MO}+1}^{-1/2} & \cdots & U_{1 N_{AO}} s_{N_{AO}}^{-1/2} & \\ U_{21} s_1^{-1/2} & U_{22} s_2^{-1/2} & \cdots & U_{2 N_{MO}} s_{N_{MO}}^{-1/2} & U_{2 N_{MO}+1} s_{N_{MO}+1}^{-1/2} & \cdots & U_{2 N_{AO}} s_{N_{AO}}^{-1/2} & \\ \vdots & \vdots & & \vdots & \vdots & & \vdots & \\ U_{N_{AO}1} s_1^{-1/2} & U_{N_{AO}2} s_2^{-1/2} & \cdots & U_{N_{AO} N_{MO}} s_{N_{MO}}^{-1/2} & U_{N_{AO} N_{MO}+1} s_{N_{MO}+1}^{-1/2} & \cdots & U_{N_{AO} N_{AO}} s_{N_{AO}}^{-1/2} & \end{array} \right), \quad (2.32)$$

where the right-hand part of the matrix is removed to ensure a stable solution. The threshold parameter depends on a given atomic system, but usually is in a range of $10^{-3} \div 10^{-5}$.

In this way, the X matrix is no more square and has dimensions $N_{AO} \times N_{MO}$. Therefore, according to equation 2.26, the orthogonal basis set $\{\phi'_\alpha(\mathbf{r})\}_{i=1}^{N_{MO}}$ contains now only N_{MO} basis functions. One can define a new coefficient matrix C' for the $\{\phi'_\alpha(\mathbf{r})\}$ basis in exactly the same manner as it was done for the C matrix (equation 2.1). Then, writing the decomposition of an electronic state φ_i both in the non-orthogonal and orthogonal bases

$$\varphi_i = \sum_{\alpha} C_{\alpha i} \phi_{\alpha} = \sum_{\beta} C'_{\beta i} \phi'_{\beta} \quad (2.33)$$

and using the expression 2.26 for ϕ'_{β} , one obtains a relation between C and C'

$$C = X C'. \quad (2.34)$$

Using the orthonormalization equations for the C matrix 2.22 as well as one of the properties of the X matrix 2.28, one can verify that the C' matrix is unitary

$$C' C'^H = C'^H C' = I. \quad (2.35)$$

In order to obtain the Schrödinger stationary equation 2.15 in the orthogonal basis, let us introduce the C' matrix in equation 2.18

$$H X C' = S X C' E. \quad (2.36)$$

Then, let us multiply this equation by X^H from the left

$$X^H H X C' = X^H S X C' E. \quad (2.37)$$

The term $X^H S X$ on the right-hand side of the equation, according to equation 2.28, is equal to the identity. Defining H' matrix as

$$H' = X^H H X, \quad (2.38)$$

one gets the usual eigenvalue problem in the orthogonal basis (without the overlap matrix)

$$H' C' = C' E. \quad (2.39)$$

The dimensions of the H' matrix are $N_{MO} \times N_{MO}$, whereas the dimensions of H are $N_{AO} \times N_{AO}$. It should be also noted that the C' matrix has dimensions $N_{MO} \times N_{MO}$ and the C matrix - $N_{AO} \times N_{MO}$. It is seen from the C matrix dimensions and from equation 2.1 that using this orthogonalization scheme we have reduced the number of electronic states from N_{AO} to N_{MO} (hence the name of the N_{MO} variable - number of molecular orbitals) while keeping the same number of basis functions in the $\{\phi_\alpha(\mathbf{r})\}_{\alpha=1}^{N_{AO}}$ basis set.

Since the Hamiltonian diagonalization is more stable in the orthogonal basis, in MOLGW this part is implemented in the orthogonal basis. However, the Hamiltonian calculation from $\rho(\mathbf{r})$, $\nabla\rho(\mathbf{r})$ and P is performed in the initial non-orthogonal atomic basis. Switching between the two bases during the self-consistent loop is presented in Figure 2.3. The loop starts with some initial C matrix guess. The C matrix allows one to calculate all input “ingredients” for the Hamiltonian H ($\rho(\mathbf{r})$, $\nabla\rho(\mathbf{r})$ and P). Once H is calculated, we calculate H' from H using equation 2.38. Then we perform the diagonalization of H' in order to find the eigenenergies E and eigenvalues C' . After that, we recover the coefficient matrix C in the non-orthogonal basis using equation 2.34. If the electronic density is not converged, we reiterate the loop, otherwise, we use the eigenenergies and wave functions for the post-processing (MBPT or RT-TDDFT). The self-consistent loop convergence is accelerated due to the method of Pulay mixing [108].

It should be noted that the properties of the X matrix (equations 2.28 and 2.31) allow one in principle to “go in reverse order” through some parts of the loop. More precisely, one can find the C' matrix from C , in the following way

$$C' = X^H S C \quad (2.40)$$

and the H matrix from H'

$$H = S X H' X^H S. \quad (2.41)$$

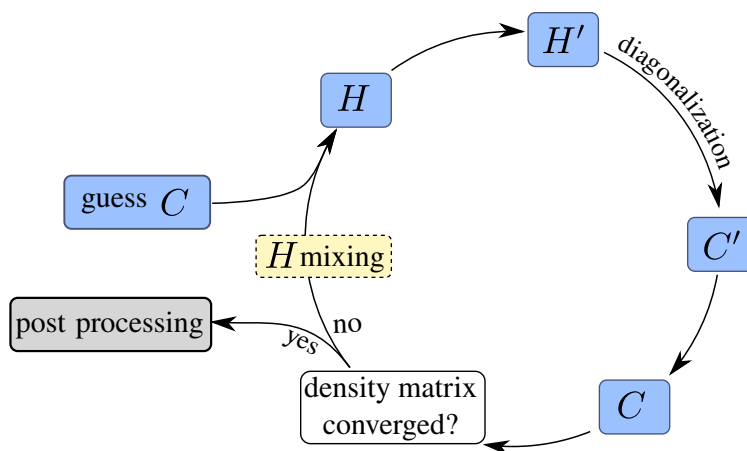


Figure 2.3 : Diagram of the generalized Kohn-Sham (gKS) self-consistent loop as implemented in MOLGW with a focus on the basis set representation of different parts of the loop.

2.1.5 Hamiltonian expression in Gaussian basis

In this section, we will discuss the Hamiltonian calculation in the localized basis. In the generalized Kohn-Sham part as well as in the GW and BSE parts a real wave function is used. However, in the RT-TDDFT part, a time-dependent wave function must be complex. Therefore, we will first consider the Hamiltonian implementation for the real wave function case and then we will discuss changes because of the complex nature of the wave function in the time-dependent part.

Real wave function case

The spin-dependent Hamiltonian, as implemented in MOLGW [42], reads in the localized basis as follows

$$H_{\mu\nu}^{\sigma} = T_{\mu\nu} + V_{ext\ \mu\nu} + J_{\mu\nu} - \alpha K_{\mu\nu}^{\sigma} - \beta K_{\mu\nu}^{\gamma\sigma} + (V_{xc}^{\sigma})_{\mu\nu}. \quad (2.42)$$

In this equation, α and β parameters govern the proportion of Fock exact-exchange $K_{\mu\nu}^{\sigma}$ and long-range Fock exchange $K_{\mu\nu}^{\gamma\sigma}$. Since long-range Fock exchange is not implemented in the RT-TDDFT part of the code, we will not consider this term further and we will set $\beta = 0$.

Let us detail equation 2.42. The first two terms are: the kinetic energy

$$T_{\mu\nu} = -\frac{1}{2} \int d\mathbf{r} \lim_{\mathbf{r}' \rightarrow \mathbf{r}} \phi_{\mu}(\mathbf{r}) \nabla_{\mathbf{r}'}^2 \phi_{\nu}(\mathbf{r}') \quad (2.43)$$

and the external potential energy

$$V_{ext\ \mu\nu} = -\sum_a \int d\mathbf{r} \phi_{\mu}(\mathbf{r}) \frac{Z_a}{|\mathbf{r} - \mathbf{R}_a|} \phi_{\nu}(\mathbf{r}), \quad (2.44)$$

where Z_a and \mathbf{R}_a are the charge and the positions of nuclei.

The Hartree term $J_{\mu\nu}$ describes the classical electron-electron interaction

$$J_{\mu\nu} = \sum_{\lambda\tau} (\mu\nu|\lambda\tau) \sum_{\sigma} P_{\lambda\tau}^{\sigma}, \quad (2.45)$$

where $P_{\lambda\tau}^{\sigma}$ is the density matrix defined in equation 2.6 and $(\mu\nu|\lambda\tau)$ is a two-electron integral term in Mulliken (chemists') notation

$$(\mu\nu|\lambda\tau) = \int \int d\mathbf{r} d\mathbf{r}' \phi_{\mu}(\mathbf{r}) \phi_{\nu}(\mathbf{r}) \frac{1}{|\mathbf{r} - \mathbf{r}'|} \phi_{\lambda}(\mathbf{r}') \phi_{\tau}(\mathbf{r}'). \quad (2.46)$$

It is seen from this expression that the pairs of indexes $(\mu\nu|$ and $|\lambda\tau)$ are interchangeable

$$(\mu\nu|\lambda\tau) = (\mu\nu|\tau\lambda) = (\nu\mu|\tau\lambda) = (\nu\mu|\lambda\tau) = \dots, \quad (2.47)$$

additional four expressions can be obtained by interchanging the parts $(\mu\nu|$ and $|\lambda\tau)$ themselves

$$\dots = (\lambda\tau|\mu\nu) = (\tau\lambda|\mu\nu) = (\tau\lambda|\nu\mu) = (\lambda\tau|\nu\mu). \quad (2.48)$$

The exact-exchange term is given by

$$K_{\mu\nu}^{\sigma} = \sum_{\lambda\tau} P_{\lambda\tau}^{\sigma} (\mu\lambda|\tau\nu). \quad (2.49)$$

The two-electron integrals can be calculated analytically with the so-called recursion formulas [109], which has a positive impact on the accuracy and on the computational time. In the code, these integrals are calculated using the external library LIBINT [110].

And, finally, the density-functional exchange-correlation potential V_{xc} in the GGA case is obtained as

$$\begin{aligned} (V_{xc}^{\uparrow})_{\mu\nu} &= \langle \mu | v_{xc} [\rho^{\sigma}(\mathbf{r}), \nabla_{\mathbf{r}} \rho^{\sigma}(\mathbf{r})] | \nu \rangle \\ &= \int d\mathbf{r} \left\{ \frac{\partial \epsilon_{xc}}{\partial \rho^{\uparrow}} \phi_{\mu}(\mathbf{r}) \phi_{\nu}(\mathbf{r}) + \left[2 \frac{\partial \epsilon_{xc}}{\partial \gamma_{\uparrow\uparrow}} \nabla_{\mathbf{r}} \rho^{\uparrow}(\mathbf{r}) + \frac{\partial \epsilon_{xc}}{\partial \gamma_{\uparrow\downarrow}} \nabla_{\mathbf{r}} \rho^{\downarrow}(\mathbf{r}) \right] \nabla_{\mathbf{r}} [\phi_{\mu}(\mathbf{r}) \phi_{\nu}(\mathbf{r})] \right\}, \end{aligned} \quad (2.50)$$

where ϵ_{xc} stands for the exchange-correlation energy density and $\gamma_{\sigma\sigma'}$ is defined as

$$\gamma_{\sigma\sigma'} = \nabla_{\mathbf{r}} \rho^{\sigma}(\mathbf{r}) \cdot \nabla_{\mathbf{r}} \rho^{\sigma'}(\mathbf{r}). \quad (2.51)$$

The expression for the $(V_{xc}^{\downarrow})_{\mu\nu}$ term can be written in an analogous way. In the code, the ϵ_{xc} values and its derivatives are obtained using the external library LIBXC [111]. The exchange-correlation potential, unlike other Hamiltonian terms, is evaluated on a real-space mesh.

The total energy of an atomic system can be found as

$$E = \sum_{\mu\nu} P_{\nu\mu} (T_{\mu\nu} + V_{ext\ \mu\nu}) + \frac{1}{2} \sum_{\mu\nu} P_{\nu\mu} J_{\mu\nu} + E_{xc}, \quad (2.52)$$

where E_{xc} is the exchange-correlation energy.

Resolution-of-identity approach

In order to accelerate the calculations, in MOLGW the two-electron integrals are evaluated using an auxiliary basis set [112]. This technique approximates the 4-center integrals in terms of 2- and 3-center integrals

$$(\mu\nu|\lambda\tau) \approx \sum_{RQ} (\mu\nu|R) (R|Q)^{-1} (Q|\lambda\tau), \quad (2.53)$$

where $(\mu\nu|R)$ and $(R|Q)$ are the 3- and 2- center integrals. This allows one to approximate the 4-center integrals as

$$(\mu\nu|\lambda\tau) \approx \sum_R M_{\mu\nu}^R M_{\lambda\tau}^R, \quad (2.54)$$

where

$$M_{\mu\nu}^R = \sum_Q (\mu\nu|Q) (Q|R)^{-1/2}. \quad (2.55)$$

It should be noted that due to the two-electron integral symmetry relations (equations 2.47), the $M_{\mu\nu}^R$ matrix is symmetric with respect to the μ and ν indexes ($M_{\mu\nu}^R = M_{\nu\mu}^R$).

The Hartree term $J_{\mu\nu}$, within the resolution-of-identity approach, writes

$$J_{\mu\nu} = \sum_{\lambda\tau} \sum_R M_{\mu\nu}^R M_{\lambda\tau}^R \sum_{\sigma} P_{\lambda\tau}^{\sigma}. \quad (2.56)$$

The expression of the exchange term $K_{\mu\nu}^{\sigma}$ in this approach will be given later in this section.

Complex wave function case

In this section, we will analyze the Hamiltonian expression (equation 2.42) term by term in order to determine whether the time-dependent complex wave function leads to complex terms in the Hamiltonian. Our derivations are similar to the one carried out by Lopata [113]. Conclusions made in this section are not dependent on the spin channel, therefore, for simplicity, we will omit the σ index in the derivations.

From the definition of the density matrix (equation 2.7), it is seen that a complex wave function (expressed in terms of $C(t)$) leads to a complex density matrix $P(t)$. Since the density matrix is used to calculate the charge density $\rho(\mathbf{r}, t)$, we should check how the complex density matrix influences the charge density calculations. In order to verify whether the imaginary part intervenes into the charge density, let us split the $P(t)$ matrix into the real and imaginary matrices

$$P(t) = \text{Re}[P(t)] + i \text{Im}[P(t)]. \quad (2.57)$$

Then, the charge density reads

$$\rho(\mathbf{r}, t) = \sum_{\mu\nu} \text{Re}[P_{\mu\nu}(t)] \phi_{\mu}(\mathbf{r}) \phi_{\nu}(\mathbf{r}) + i \sum_{\mu\nu} \text{Im}[P_{\mu\nu}(t)] \phi_{\mu}(\mathbf{r}) \phi_{\nu}(\mathbf{r}). \quad (2.58)$$

Since the $P(t)$ matrix is Hermitian (equation 2.8), its real part is symmetric and imaginary part is antisymmetric. Let us consider the second term in equation 2.58. We can divide the summation into two parts: $\mu > \nu$ and $\mu < \nu$ (for $\mu = \nu$ we have $\text{Im}[P_{\mu\mu}(t)] = 0$)

$$\sum_{\mu\nu} \text{Im}[P_{\mu\nu}(t)] \phi_{\mu}(\mathbf{r}) \phi_{\nu}(\mathbf{r}) = \sum_{\mu>\nu} \text{Im}[P_{\mu\nu}(t)] \phi_{\mu}(\mathbf{r}) \phi_{\nu}(\mathbf{r}) + \sum_{\mu<\nu} \text{Im}[P_{\mu\nu}(t)] \phi_{\mu}(\mathbf{r}) \phi_{\nu}(\mathbf{r}). \quad (2.59)$$

In the second term of the expression we use $\text{Im}[P(t)_{\mu\nu}] = -\text{Im}[P(t)_{\nu\mu}]$. In this way, we see that the expression 2.59 is equal to zero. Therefore, the charge density is determined only by the real part of the density matrix

$$\rho(\mathbf{r}, t) = \sum_{\mu\nu} \text{Re}[P_{\mu\nu}(t)] \phi_{\mu}(\mathbf{r}) \phi_{\nu}(\mathbf{r}). \quad (2.60)$$

The kinetic 2.43 and the external potential energy 2.44 terms do not depend on $P(t)$, $\rho(\mathbf{r}, t)$ or $\nabla\rho(\mathbf{r}, t)$, therefore these terms remain real.

The exchange and correlation DFT term (expression 2.50) depends only on the charge density $\rho(\mathbf{r}, t)$ and possibly on its gradient $\nabla\rho(\mathbf{r}, t)$. Therefore, we can directly conclude that this term is also real and depends only on the real part of the density matrix.

In order to analyze the Hartree term (equation 2.45) we will first proceed in a similar manner as for the $\text{Im}[P]$: we will split the summation

$$J_{\mu\nu}(t) = \sum_{\tau} \sum_{\lambda < \tau} P_{\lambda\tau}(t) (\mu\nu|\lambda\tau) + \sum_{\tau} P_{\tau\tau}(t) (\mu\nu|\tau\tau) + \sum_{\tau} \sum_{\lambda > \tau} P_{\lambda\tau}(t) (\mu\nu|\lambda\tau). \quad (2.61)$$

To group the first and the third terms of the expression, let us swap the indexes of summation for the third term

$$J_{\mu\nu}(t) = \sum_{\tau} \sum_{\lambda < \tau} P_{\lambda\tau}(t) (\mu\nu|\lambda\tau) + \sum_{\tau} P_{\tau\tau}(t) (\mu\nu|\tau\tau) + \sum_{\lambda} \sum_{\tau > \lambda} P_{\tau\lambda}(t) (\mu\nu|\tau\lambda). \quad (2.62)$$

Using the two-electronic integral symmetry relations 2.47 we exchange the τ and λ indexes in the third term, which simplifies the equation into

$$J_{\mu\nu}(t) = \sum_{\tau} \sum_{\lambda < \tau} [P_{\lambda\tau}(t) + P_{\tau\lambda}(t)] (\mu\nu|\lambda\tau) + \sum_{\tau} P_{\tau\tau}(t) (\mu\nu|\tau\tau). \quad (2.63)$$

Using the decomposition of the $P(t)$ matrix 2.57 and taking into account that the imaginary part of $P(t)$ is antisymmetric, we get $\text{Im}[P_{\lambda\tau}(t)] + \text{Im}[P_{\tau\lambda}(t)] = \text{Im}[P_{\tau\tau}] = 0$. So, the $J_{\mu\nu}(t)$ is real and depends only on the real part of the density matrix.

Concerning the exact-exchange term (equation 2.49), we, at first, split the summation into three parts, similarly to the Hartree term,

$$K_{\mu\nu}(t) = \sum_{\tau} \sum_{\lambda < \tau} P_{\lambda\tau}(t) (\mu\lambda|\tau\nu) + \sum_{\tau} P_{\tau\tau}(t) (\mu\tau|\tau\nu) + \sum_{\tau} \sum_{\lambda > \tau} P_{\lambda\tau}(t) (\mu\lambda|\tau\nu). \quad (2.64)$$

Then, we permute λ and τ in the third term and take the imaginary part of the equation

$$\text{Im}[K_{\mu\nu}(t)] = \sum_{\lambda < \tau} \text{Im}[P_{\lambda\tau}(t)] [(\mu\lambda|\tau\nu) - (\mu\tau|\lambda\nu)]. \quad (2.65)$$

In a general case, this expression is different from zero. Therefore, the exact-exchange term is complex and depends on the full density matrix.

Since in the RT-TDDFT part the exact-exchange term is different from that in the ground-state DFT, we will consider in more detail its implementation in the code. Using the resolution-of-identity approximation (equation 2.54), the exact-exchange term (equation 2.49) reads

$$K_{\mu\nu}(t) = \sum_{\lambda\tau} \sum_R P_{\lambda\tau}(t) M_{\mu\lambda}^R M_{\tau\nu}^R. \quad (2.66)$$

In order to improve the numerical efficiency, we switch from the density matrix to the coefficient matrix $C(t)$ using the expression 2.6

$$K_{\mu\nu}(t) = \sum_{\lambda\tau} \sum_R \sum_i f_i \left(M_{\mu\lambda}^R C_{\lambda i}(t) \right) \left(M_{\nu\tau}^R C_{\tau i}(t) \right)^* = \sum_i \sum_R \left(B_{\mu}^R(t) \right)_i \left(B_{\nu}^R(t) \right)_i^*, \quad (2.67)$$

where $\left(B_{\mu}^R(t) \right)_i = \sum_{\lambda} M_{\mu\lambda}^R C_{\lambda i}(t)$. We can write equation 2.67 in a following matrix form

$$K_{\mu\nu}(t) = \sum_i B_i^T(t) B_i^*(t). \quad (2.68)$$

Using this equation, we can show that the complex exact-exchange term is Hermitian

$$\left(K_{\mu\nu}(t) \right)^H = \left(\sum_i B_i^T(t) B_i^*(t) \right)^H = \sum_i \left(B_i^T(t) B_i^*(t) \right)^H = \sum_i B_i^T(t) B_i^*(t) = K_{\mu\nu}(t). \quad (2.69)$$

To summarize, in the case of an RT-TDDFT calculation without the exact Fock exchange, all the Hamiltonian terms are real and depend only on the real part of the density matrix (which does not exempt one from the complex wave function propagation and the complex density matrix calculation). However, in the case of the Hartree-Fock or a hybrid-functional DFT calculations, the exact-exchange term in the Hamiltonian is complex and depends on the full complex density matrix.

So, in order to adapt the MOLGW gKS subroutines for the RT-TDDFT part, represented as the blue area in Fig. 2.1b, we had to implement the complex density matrix calculation $P(t)$ from the complex wave functions $C(t)$ and the complex exact-exchange term. In the next section we will discuss the RT-TDDFT implementation itself, which is referred to the orange area in the figure.

2.2 Algorithm of the time propagation of Kohn-Sham equations

In this section, we will describe different propagator approximations that we implemented in the code. First, we will discuss the basic expressions of propagators written in the operator form, then, in section 2.2.6, we describe the implementation in the basis and precise algorithmic schemes.

2.2.1 Standard propagator techniques

Magnus propagator

As was previously discussed in section 1.4.1, the propagator operator $\hat{U}(t + \Delta t, t)$ can be expressed as a simple exponential $\exp\{-i\Delta t \hat{H}\}$ only in the case when the Hamiltonian is time-independent, which, unfortunately, does not apply in a general case of RT-TDDFT.

The idea of Magnus [114] was to find a series of operators $\hat{\Omega}_k$ for which we can express the propagator with a time-dependent Hamiltonian $\hat{H}(t)$ (equation 1.113) in the following way

$$\hat{U}(t + \Delta t, t) = \exp \left\{ \hat{\Omega}_1 + \hat{\Omega}_2 + \dots \right\}. \quad (2.70)$$

In this equation, $\hat{\Omega}_k$ is a k -dimensional integral of nested commutators of the Hamiltonian at different times. An approximation of order $2N$ is performed in two stages: 1) truncation of the Magnus series $\exp \left\{ \sum_k \hat{\Omega}_k \right\}$ to the N^{th} order and 2) approximation the time integrals with some N^{th} order quadrature formula. Blanes and coworkers [115] have shown that an efficient integral approximation for this problem can be done using the Gauss-Legendre quadrature. Since $\hat{\Omega}_2$ is usually the highest term used for practical applications, we will provide here the analytical expressions only for $\hat{\Omega}_1$ and $\hat{\Omega}_2$ terms.

The second order ($N = 1$) Magnus propagator reads

$$\hat{U}_{MAG2}(t + \Delta t, t) = \exp \left\{ \hat{\Omega}_1 \right\} + O(\Delta t^3) \quad (2.71a)$$

$$\hat{\Omega}_1 = -i\Delta t \hat{H}(t + \frac{\Delta t}{2}). \quad (2.71b)$$

In this expression, we have approximated the integration using only one point in the middle of the propagation interval $t + \Delta t/2$ and the Hamiltonian is approximated to a constant $\hat{H}(t + \Delta t/2)$ for the whole propagation interval. For this reason, this approximation is also called the exponential midpoint rule. In the set of Magnus propagators, the \hat{U}_{MAG2} is special in the sense that it does not contain any commutator.

The expression for the fourth order ($N = 2$) Magnus propagator can be written as

$$\hat{U}_{MAG4}(t + \Delta t, t) = \exp \left\{ \hat{\Omega}_1 + \hat{\Omega}_2 \right\} + O(\Delta t^5) \quad (2.72a)$$

$$\hat{\Omega}_1 = -i \left[\hat{H}(\tau_1) + \hat{H}(\tau_2) \right] \frac{\Delta t}{2} \quad (2.72b)$$

$$\hat{\Omega}_2 = \left[\hat{H}(\tau_1), \hat{H}(\tau_2) \right] \frac{\sqrt{3}\Delta t^2}{12} \quad (2.72c)$$

$$\tau_{1,2} = t + \left(\frac{1}{2} \mp \frac{\sqrt{3}}{6} \right) \Delta t, \quad (2.72d)$$

where $\tau_{1,2}$ are Gauss Legendre integration points. The expression for the \hat{U}_{MAG4} propagator is more complicated and requires two Hamiltonian evaluations per propagation from t to $t + \Delta t$. As an advantage of this method, one can use larger time steps than for the \hat{U}_{MAG2} propagator. However, it was reported [116] that, unless the Hamiltonian is *strongly* time dependent, second-order Magnus has a better quality/computational cost ratio. Therefore, \hat{U}_{MAG4} was not implemented in MOLGW.

Enforced time-reversal symmetry (ETRS) propagator

The idea of this method is that a backward propagation from $t + \Delta t$ to $t + \Delta t/2$ should lead to the same result as a forward propagation from t to $t + \Delta t/2$, i.e.,

$$\varphi(t + \frac{\Delta t}{2}) = \hat{U}(t + \frac{\Delta t}{2}, t + \Delta t)\varphi(t + \Delta t) = \hat{U}(t + \frac{\Delta t}{2}, t)\varphi(t). \quad (2.73)$$

We will approximate the Hamiltonian integration in the $\hat{U}(t + \frac{\Delta t}{2}, t + \Delta t)$ propagator by one point - $H(t + \Delta t)$, and, respectively, in the $\hat{U}(t + \frac{\Delta t}{2}, t)$ propagator - by $\hat{H}(t)$. The expression 2.73 then becomes

$$\varphi(t + \frac{\Delta t}{2}) = \exp \left\{ +i \frac{\Delta t}{2} \hat{H}(t + \Delta t) \right\} \varphi(t + \Delta t) = \exp \left\{ -i \frac{\Delta t}{2} \hat{H}(t) \right\} \varphi(t). \quad (2.74)$$

From this equation we get the expression for the ETRS propagator

$$\hat{U}_{ETRS} = \exp \left\{ -i \frac{\Delta t}{2} \hat{H}(t + \Delta t) \right\} \exp \left\{ -i \frac{\Delta t}{2} \hat{H}(t) \right\}. \quad (2.75)$$

It is seen, that the \hat{U}_{ETRS} propagator has a form of two subsequent propagations similar to \hat{U}_{MAG2} : $(t) \rightarrow (t + \Delta t/2)$ and $(t + \Delta t/2) \rightarrow (t + \Delta t)$, the difference is that for the \hat{U}_{MAG2} propagator the point for the integration is taken in the middle of the propagation interval (would be $t + \Delta t/4$ and $3\Delta t/4$ here), whereas for the \hat{U}_{ETRS} propagator these points are taken on the edges of each interval (t and $t + \Delta t$).

Crank-Nicolson propagator

For this method, similarly to the \hat{U}_{MAG2} propagator, we take only one point for the integral 1.124 approximation. Let us first consider a propagation from t to $t + \Delta t$ and let us approximate the integral by the leftmost Hamiltonian value in the interval: $\hat{H}(t)$. Then we develop the exponential $e^{-i\Delta t \hat{H}(t)}$ to the second order of Δt

$$\varphi(t + \Delta t) \approx e^{-i\Delta t \hat{H}(t)} \varphi(t) \approx \varphi(t) - i\Delta t \hat{H}(t) \varphi(t) - \frac{1}{2} \Delta t^2 \hat{H}^2(t) \varphi(t). \quad (2.76)$$

Now, let us perform the same expansion, but for the propagation from t to $t - \Delta t$ (applying the time-reversal property of the propagator operator, equation 1.118) and using the rightmost value of the Hamiltonian in this interval (which in absolute value is similar to equation 2.76: $\hat{H}(t)$)

$$\varphi(t - \Delta t) \approx e^{i\Delta t \hat{H}(t)} \varphi(t) \approx \varphi(t) + i\Delta t \hat{H}(t) \varphi(t) - \frac{1}{2} \Delta t^2 \hat{H}^2(t) \varphi(t). \quad (2.77)$$

Subtracting equation 2.77 from equation 2.76, we get

$$\varphi(t + \Delta t) = \varphi(t - \Delta t) - 2i\Delta t \hat{H}(t) \varphi(t). \quad (2.78)$$

This equation involves $t - \Delta t$, t and $t + \Delta t$ times. In order to have only two times in the equation, we approximate $\varphi(t)$ as follows

$$\varphi(t) \approx \frac{1}{2} (\varphi(t - \Delta t) + \varphi(t + \Delta t)). \quad (2.79)$$

Substituting this expression and switching from the interval $[t - \Delta t, t + \Delta t]$ to $[t, t + \Delta t]$, we get the final expression for the Crank-Nicolson propagator

$$\varphi(t + \Delta t) = \left(\hat{I} + i \frac{\Delta t}{2} \hat{H} \right)^{-1} \left(\hat{I} - i \frac{\Delta t}{2} \hat{H} \right) \varphi(t) + O(\Delta t^3). \quad (2.80)$$

As seen from these derivations, for the Crank-Nicolson propagator \hat{U}_{CN} (also called the implicit midpoint rule) we have used more approximations than for the equivalent in the computational cost second-order Magnus propagator \hat{U}_{MAG2} .

All the presented propagators are unitary and preserve the time-reversal symmetry (properties 1.117 and 1.120).

2.2.2 Predictor-corrector method

In order to solve the problem of the wave function propagation, choosing a propagator approximation is not enough: one needs also to approximate the Hamiltonian $\hat{H}(t)$ for the future times t . To demonstrate this problem, let us consider the expression of the second-order Magnus propagator (equations 2.71). To propagate the wave function $\varphi(t)$ from t to $t + \Delta t$ one needs to know the Hamiltonian at $t + \frac{\Delta t}{2}$, which, in its turn, depends on the wave function $\varphi(t + \frac{\Delta t}{2})$. The problem becomes self-consistent and to solve it one usually applies the so-called predictor-corrector method.

Let us assume that the evolution of the wave function is already calculated until a time t , then the next self-consistent propagation to $t + \Delta t$ can be described as follows [117]:

- (1) (Predictor) *Extrapolate* the Hamiltonian $\hat{H}(\tau)$ for $t < \tau \leq t + \Delta t$ using its values $\hat{H}(\tau \leq t)$.
- (2) (Predictor) Propagate the wave function φ from t to $t + \Delta t$.
- (3) (Corrector) Calculate $\hat{H}(t + \Delta t)$ from $\varphi(t + \Delta t)$.
- (4) (Corrector) *Interpolate* the Hamiltonian $\hat{H}(\tau)$ for $t < \tau \leq t + \Delta t$.
- (5) Repeat the steps (2)-(4) until the self-consistency is reached.

This algorithm is written in general terms. A precise predictor-corrector scheme should indicate a method for extrapolation/interpolation of the Hamiltonian as well as precise points in the propagation interval $[t, t + \Delta t]$ for the extrapolation/interpolation. Different propagators request the Hamiltonian at different times. For example, for the ETRS propagator one needs to provide the Hamiltonian values at t and $t + \Delta t$ (equation 2.75), whereas for the second-order Magnus and Crank-Nicolson propagators one needs to know the Hamiltonian at $t + \frac{\Delta t}{2}$ (equations 2.71 and 2.80). Therefore, a predictor-corrector scheme depends on the choice of the propagator technique. The final stability and accuracy of the propagation depend on both the propagator approximation and the predictor-corrector scheme.

2.2.3 Propagators in orthogonal basis

As detailed earlier, the localized Gaussian basis $\{\phi(\mathbf{r})\}_{i=1}^{N_{AO}}$ is non-orthogonal, however there exists the orthogonalization procedure (equations 2.26 to 2.34) which not only creates the orthogonal basis set $\{\phi'(\mathbf{r})\}_{i=1}^{N_{MO}}$, but also eliminates $N_{AO} - N_{MO}$ lowest eigenvalues of the overlap matrix in order to improve the stability of the Hamiltonian diagonalization procedure. Since in MOLGW in the gKS part both bases are used (see Fig. 2.3), for the time-dependent part we had a choice in which basis to represent the wave function $\varphi(t)$ and the propagator \hat{U} . Although the propagation can be performed in the non-orthogonal basis [118], to ensure the stability of the propagation, we have decided to work in the orthogonal basis.

In order to write the propagation equations in the matrix form, we use the wave function $\varphi_i(\mathbf{r}, t)$ decomposition in the orthogonal basis set

$$\varphi_i(\mathbf{r}, t) = \sum_{\alpha} C'_{\alpha i}(t) \phi'_{\alpha}(\mathbf{r}). \quad (2.81)$$

It is seen that the time dependence of the wave function is covered by the coefficient matrix $C'(t)$ and the spatial dependence by the basis functions $\phi'_{\alpha}(\mathbf{r})$. Then we substitute this expression into the time-dependent Schrödinger equation (1.86). Projecting this equation onto a state $\langle \phi'_{\beta} |$ and using the orthonormality condition 2.27, we get

$$i \frac{dC'(t)}{dt} = H'(t)C'(t). \quad (2.82)$$

We define the propagator matrix in a similar manner to the propagator operator definition (equation 1.103)

$$C'(t) = U'(t, t_0)C'(t_0) \quad (2.83)$$

with the initial condition

$$U'(t_0, t_0) = I. \quad (2.84)$$

Substituting the expression of C' 2.83 into equation 2.82 we get the differential equation for the propagator matrix

$$i \frac{dU'(t, t_0)}{dt} = H'(t)U'(t, t_0). \quad (2.85)$$

It is seen that the operator formulation of the propagator (equations 1.86, 1.103 and 1.104) corresponds exactly to the matrix formulation in the orthogonal basis (equations 2.82, 2.83 and 2.85). It means that one can use the results for the propagators obtained in the operator form just transforming an operator by a corresponding matrix. In the non-orthogonal basis case, the overlap matrix S would have appeared in the equations.

2.2.4 Different bases

We have several bases while performing the wave function propagation. First and the principal is the non-orthogonal basis of **atomic orbitals** $|\phi_\alpha\rangle$. Using the canonical orthogonalization technique, we obtain the orthogonal atomic basis $|\phi'_\beta\rangle$. The X matrix links these two bases (equation 2.26). Then, there are two bases of molecular orbitals: **propagated states** $|\varphi_i(t)\rangle$ and **instantaneous eigenstates** $|\chi_j(t)\rangle$ of the time-dependent Hamiltonian $\hat{H}'(t)$. The decomposition of the propagated molecular orbitals $|\varphi_i(t)\rangle$ in the orthogonal atomic basis $|\phi'_\beta\rangle$ is given by the $C'(t)$ matrix (equation 2.33) and the decomposition of the eigenstates $|\chi_j(t)\rangle$ is provided by an $A'(t)$ matrix

$$|\chi_j(t)\rangle = \sum_{\beta} A'_{\beta j}(t) |\phi'_\beta\rangle. \quad (2.86)$$

The bases $|\varphi_i(t)\rangle$ and $|\chi_j(t)\rangle$ change during the propagation while the bases $|\phi_\alpha\rangle$ and $|\phi'_\beta\rangle$ remain constant if the atomic coordinates are fixed. Usually, in an RT-TDDFT simulation, the initial state of a system is defined as the ground state obtained through the self-consistent gKS loop. We denote this moment as $t = t_0$. For this moment the $C'(t_0)$ and the $A'(t_0)$ matrices are the same since

$$|\varphi_i(t_0)\rangle = |\chi_i(t_0)\rangle. \quad (2.87)$$

Both matrices are the solution of the eigenstate problem 2.39 with the Hamiltonian $\hat{H}(t_0)$. Then, an external perturbation (a moving charge, an external electric field, etc.) leads to time dependence of the Hamiltonian and of the molecular states. The matrix of the propagated states $C'(t)$ evaluate according to the **time-dependent** Schrödinger equation 2.82 and for $t > t_0$ is no more a solution of the **stationary** Schrödinger equation. By defi-

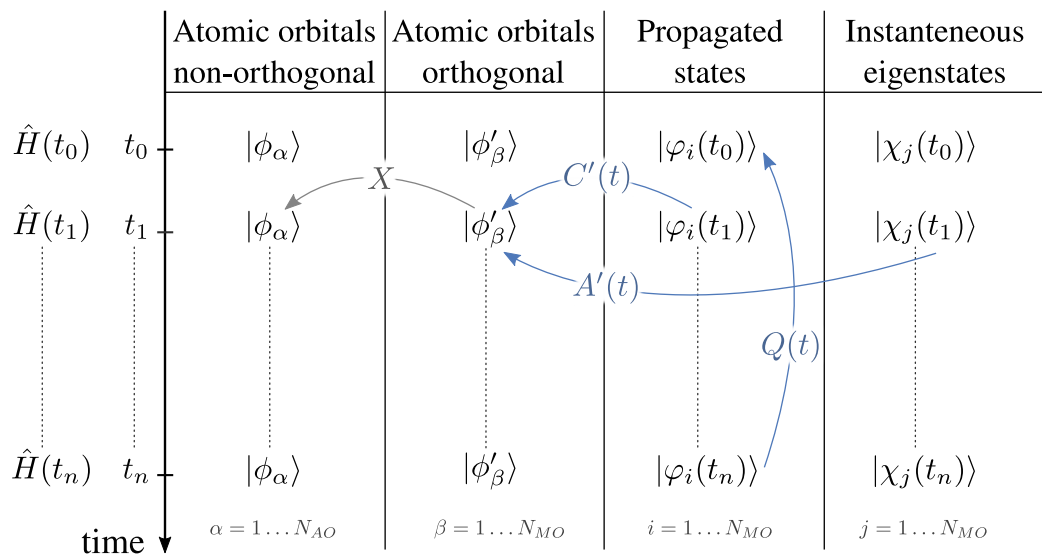


Figure 2.4 : Different bases used in the time-dependent propagation.

dition, the $A'(t)$ matrix is the solution of the stationary equation with the time-dependent Hamiltonian

$$H'(t)A'(t) = A'(t)E(t), \quad (2.88)$$

where $E(t)$ is the diagonal matrix of the instantaneous eigenvalues of the Hamiltonian $\hat{H}'(t)$. For the simulation analysis purposes, we also use a matrix $Q(t)$ which will be introduced in the next section. All the four bases and the links between them are schematically represented in Fig. 2.4.

2.2.5 Occupations analysis

Here we would like to establish an expression of an occupation matrix $Q(t)$, which characterizes occupations of the states during a simulation with respect to the **initial state** $|\varphi(t=0)\rangle$. As was discussed in section 1.4, in RT-TDDFT simulations the occupations of the electronic levels $|\varphi_j(t)\rangle$ do not change in time. Due to this fact, in the code, we propagate and keep in the memory *only* of the occupied states $|\varphi_j(t)\rangle$ (for j from 1 to *occ*).

However, the projections of $|\varphi_j(t)\rangle$ onto the initial states $|\varphi_i(t=0)\rangle$ do have non-zero components corresponding to initially unoccupied states. Let us consider this point in more detail. We define $Q(t)$ as a decomposition matrix of a propagated state $|\varphi_j(t)\rangle$ in the basis of initial states $|\varphi_i(0)\rangle$

$$|\varphi_j(t)\rangle = \sum_i Q_{ij}(t) |\varphi_i(0)\rangle. \quad (2.89)$$

Now we can decompose both $|\varphi_i(0)\rangle$ and $|\varphi_j(t)\rangle$ in the orthogonal atomic basis $|\phi'\rangle$

$$\sum_\alpha C'_{\alpha j}(t) |\phi'_\alpha\rangle = \sum_{i\beta} Q_{ij}(t) C'_{\beta i}(0) |\phi'_\beta\rangle. \quad (2.90)$$

Projecting this equation on $\langle\phi'_\gamma|$ and using the orthonormality condition 2.27, one gets the following expression

$$C'_{\gamma j}(t) = \sum_i C'_{\gamma i}(0) Q_{ij}(t), \quad (2.91)$$

which can be written in the matrix form as follows:

$$C'(t) = C'(0)Q(t). \quad (2.92)$$

Multiplying this equation by $C'^H(0)$ from the left and using equation 2.35, we obtain the expression for the $Q(t)$ matrix

$$Q(t) = C'^H(0)C'(t). \quad (2.93)$$

From equation 2.89 it is also seen that that the $Q_{ij}(t)$ matrix element is simply a projection of the state $|\varphi_j(t)\rangle$ onto the state $|\varphi_i(0)\rangle$

$$Q_{ij}(t) = \langle\varphi_i(0)|\varphi_j(t)\rangle. \quad (2.94)$$

Hence, the probability of the transition from the state j to the state i has the following expression

$$|\langle \varphi_i(0) | \varphi_j(t) \rangle|^2 = |Q_{ij}(t)|^2. \quad (2.95)$$

One can note the initial condition: $|Q_{ij}(0)|^2 = \delta_{ij}$. Then, the occupation of the level i , $q_i(t)$, can be found as a sum of transitions from all levels j to this level i multiplied by the initial occupations f_j

$$q_i(t) = \sum_j f_j |Q_{ij}(t)|^2. \quad (2.96)$$

To conclude, let us consider an example of an application of equation 2.96. Suppose, we want to calculate the occupation of all $1s$ levels of a system during the RT-TDDFT simulation. To do this, we need to sum $q_i(t)$ over all states i that belong to $1s$

$$q_{1s}(t) = \sum_{i \in \{1s\}} q_i(t). \quad (2.97)$$

2.2.6 Implementation in the code

Propagators implementation

Let us start with the second-order Magnus propagator. Its expression (equations 2.71) in the orthogonal basis reads

$$C'(t + \Delta t) = \exp \left\{ -i\Delta t H'(t + \frac{\Delta t}{2}) \right\} C'(t). \quad (2.98)$$

In order to calculate the exponential of the Hamiltonian $H'(t + \frac{\Delta t}{2})$, we need first to diagonalize it using the matrix $A'(t + \frac{\Delta t}{2})$. In the following derivations, we consider the time $t + \frac{\Delta t}{2}$ for the matrices H' and A' , we will skip the time argument for sake of clarity.

Multiplying equation 2.88 by A'^H from the right-hand side, and using the orthonormalization condition for the A' matrix (which is the same as for the C' matrix, equation 2.35), we get

$$H' = A'EA'^H. \quad (2.99)$$

The orthonormality of the A' matrix allows one to write any power n of the Hamiltonian H' as

$$(H')^n = (A'EA'^H)^n = A'E \underbrace{A'^H A'}_I EA'^H \dots A'E \underbrace{A'^H A'}_I EA'^H = A' \underbrace{E \dots E}_{n \text{ times}} A'^H = A'E^n A'^H, \quad (2.100)$$

where E^n is a diagonal matrix which contains the eigenenergies to the n^{th} power E_i^n . Using this expression, one can develop $e^{-i\Delta t H'}$ as follows

$$\begin{aligned} e^{-i\Delta t H'} &= I + (-i\Delta t)H' + \frac{(-i\Delta t)^2}{2}H'^2 + \dots \\ &= A'A'^H + (-i\Delta t)A'E A'^H + \frac{(-i\Delta t)^2}{2}A'E^2 A'^H + \dots \\ &= A'e^{-i\Delta t E} A'^H, \end{aligned} \quad (2.101)$$

where $e^{-i\Delta t E}$ matrix has the following form

$$e^{-i\Delta t E} = \begin{pmatrix} e^{-i\Delta t E_1} & & & \\ & e^{-i\Delta t E_2} & & \\ & & \ddots & \\ & & & e^{-i\Delta t E_{N_{MO}}} \end{pmatrix}. \quad (2.102)$$

Hence, the final expression for the second-order Magnus propagator in the orthogonal basis reads

$$C'(t + \Delta t) = A'(t + \frac{\Delta t}{2}) \exp \left\{ -i\Delta t E(t + \frac{\Delta t}{2}) \right\} A'^H(t + \frac{\Delta t}{2}) C'(t). \quad (2.103)$$

Due to the *exact* diagonalization of the exponentials, the propagated wave functions $\varphi_i(t + \Delta t)$ (expressed by $C'(t + \Delta t)$) are orthogonal ($C'^H(t + \Delta t)C'(t + \Delta t) = I$) and we do not need to perform an additional expensive procedure of the orthogonalization. One should also mention that the exact diagonalization is possible due to the choice of the localized basis for the implementation.

The fact that the $A'(t)$ matrix diagonalizes the Hamiltonian justifies the choice of the orthogonal basis for the propagation. In the case of the propagation in the non-orthogonal basis, one would need nonetheless switch to the orthogonal basis of $A'(t)$ to perform this diagonalization.

So, we can write the algorithm for the calculation of the propagation with the MAG2 method:

The **MAG2** propagator:

Given: $H'(t + \frac{\Delta t}{2})$, $C'(t)$

1. Diagonalization of $H'(t + \frac{\Delta t}{2}) \rightarrow A'(t + \frac{\Delta t}{2})$, $E(t + \frac{\Delta t}{2})$.
2. Calculation of $C'(t + \Delta t) = A'(t + \frac{\Delta t}{2}) e^{\left\{ -i\Delta t E(t + \frac{\Delta t}{2}) \right\}} A'^H(t + \frac{\Delta t}{2}) C'(t)$.
3. Calculation of $C(t + \Delta t) = XC'(t + \Delta t)$ for further Hamiltonian calculations.

For the ETRS propagator (equation 2.75) implementation, we perform the same procedure of the Hamiltonian diagonalization (equation 2.101). The implementation of the

ETRS propagator (equation 2.75) is analogous to the MAG2 with the difference that this time one needs to diagonalize two exponentials and one needs two evaluations of the Hamiltonian instead of one. Therefore, the algorithm for this method reads:

The **ETRS** propagator:

Given: $H'_1 \equiv H'(t)$, $H'_2 \equiv H'(t + \Delta t)$, $C'(t)$

1. Diagonalization of $H'_1 \rightarrow A'_1, E_1$.
2. Diagonalization of $H'_2 \rightarrow A'_2, E_2$.
3. Calculation of $C'(t + \Delta t) = A'_2 e^{-i \frac{\Delta t}{2} \hat{H}'_2} A_2'^H A'_1 e^{-i \frac{\Delta t}{2} \hat{H}'_1} A_1'^H C'(t)$.
4. Calculation of $C(t + \Delta t) = X C'(t + \Delta t)$ for further Hamiltonian calculations.

For the Crank-Nicolson propagator (equation 2.80) we define two matrices as follows

$$L' \equiv 1 + \frac{\Delta t}{2} H' \quad (2.104a)$$

$$B' \equiv 1 - \frac{\Delta t}{2} H'. \quad (2.104b)$$

Then, we can precise the algorithm for this method:

The **CN** propagator:

Given: $H'(t + \frac{\Delta t}{2})$, $C'(t)$

1. Inversion of $L'(t + \frac{\Delta t}{2}) \rightarrow L'^{-1}(t + \frac{\Delta t}{2})$.
2. Calculation of $C'(t + \Delta t) = L'^{-1} B' C'(t)$.
3. Calculation of $C(t + \Delta t) = X C'(t + \Delta t)$ for further Hamiltonian calculations.

Predictor-correctors implementation

Now we will detail the way in which the input blocks “Given:” for the propagators are obtained as well as in what way the output of the propagators is used. In fact, the described propagator algorithms simply determine how to find the wave function at a time $t + \Delta t$ from the wave function at t . However, due to the time dependence of the Hamiltonian, a direct propagation $\varphi(t_2) = \hat{U}(t_2, t_1) \varphi(t_1)$; $\varphi(t_3) = \hat{U}(t_3, t_2) \varphi(t_2) \dots$ (formula 1.123) would demand an unreasonably small time steps in order to ensure the accuracy of the propagation. On the other hand, a straightforward implementation of the iterative predictor-corrector, which is presented above, has also shown its inefficiency since it requires many (e.g., 4-5)

iterations to achieve an acceptable convergence. Therefore, an implementation of more complicated predictor-corrector schemes using a subdivision of the propagation intervals or an alternation of propagator techniques appeared to us a necessary measure in order to optimize the quality/computational cost ratio of the propagation.

As was discussed previously, the predictor-corrector scheme should take into account a given propagator method because different propagators use the Hamiltonian values at different times. Since \hat{U}_{MAG2} and \hat{U}_{CN} propagators require the value of the Hamiltonian at the same time ($t + \frac{\Delta t}{2}$), the predictor-corrector scheme can be developed for either of the two propagators. We have found the following predictor-corrector scheme (named PC1) optimal:

PC1:

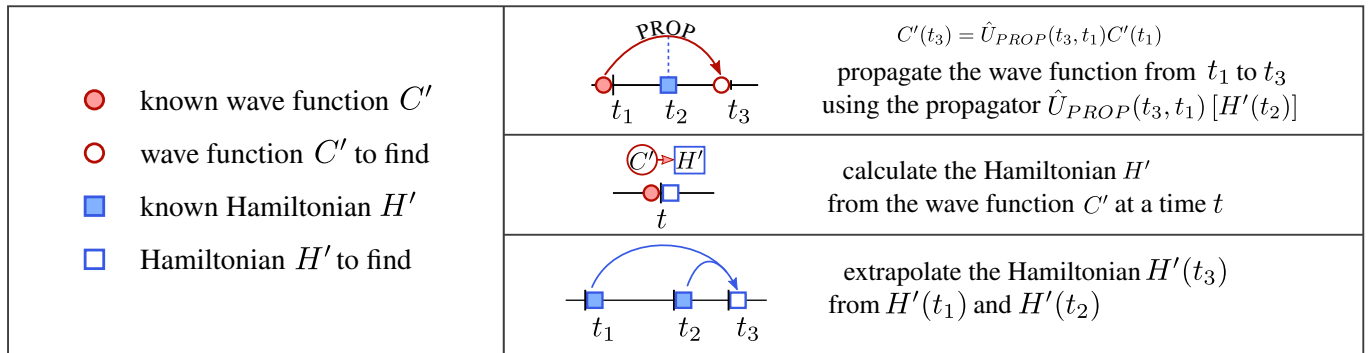
0. The Hamiltonian values H' are known at $t, t - \frac{\Delta t}{2}, \dots, t - (N - 1)\frac{\Delta t}{2}$; C' matrix is known only at t .
1. Using the Lagrange polynomial, extrapolate $H'(t + \frac{\Delta t}{4})$ from $H'(t), H'(t - \frac{\Delta t}{2}), \dots, H'(t - (N - 1)\frac{\Delta t}{2})$.
2. Propagate $C'(t) \xrightarrow{MAG2/CN} C'(t + \frac{\Delta t}{2})$ using MAG2 or CN with $H'(t + \frac{\Delta t}{4})$.
3. Calculate $H'(t + \frac{\Delta t}{2})$ using $C'(t + \frac{\Delta t}{2})$.
4. Propagate $C'(t) \xrightarrow{MAG2/CN} C'(t + \Delta t)$ with $H'(t + \frac{\Delta t}{2})$.
5. Calculate $H'(t + \Delta t)$ using $C'(t + \Delta t)$.
6. Update for the next step: H' and C' are shifted in time by Δt .

Since in MOLGW we calculate the Hamiltonian from the wave function written in the non-orthogonal atomic basis, each time when it is written “using C' calculate H' ” it actually means: first calculate C from C' (equation 2.34), then using C calculate H and then using the expression 2.38 calculate H' from H . So, schematically, $C' \rightarrow C \rightarrow H \rightarrow H'$.

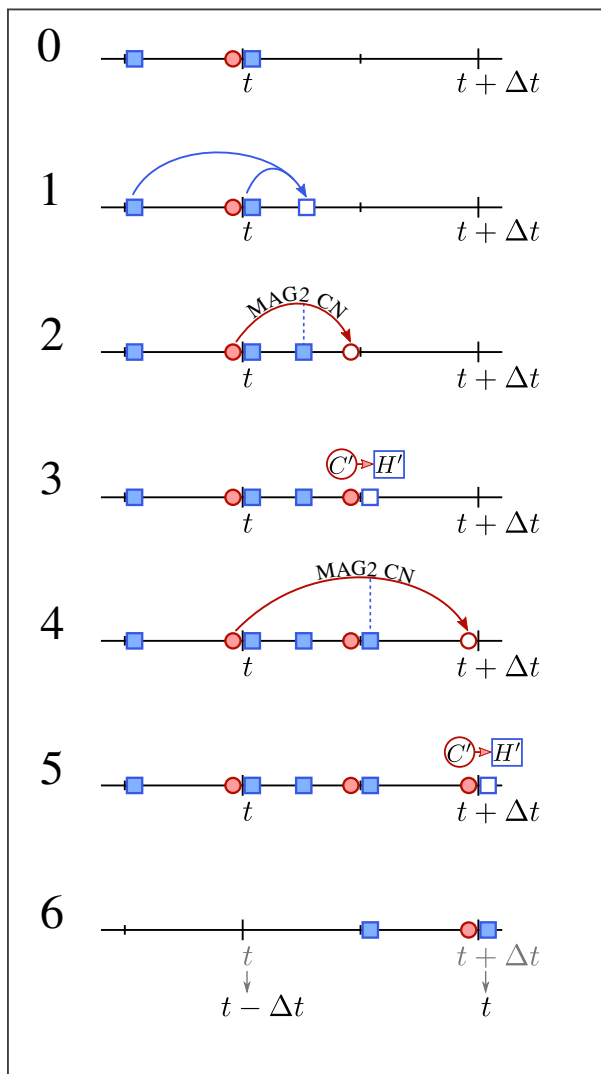
Concerning the Hamiltonian history from previous steps (governed by the parameter N), we have found that N in the range of 2-5 improves the stability of the propagation. However, larger N requires more memory for the Hamiltonian storage. Therefore, $N = 2$ is found to be the optimal history parameter, which means that in the step 1 the Hamiltonian at $t + \frac{\Delta t}{4}$ is approximated linearly from $H'(t)$ and $H'(t - \frac{\Delta t}{2})$.

One should also note that the most time consuming operations in the propagation are the diagonalization of the A' matrix for U'_{MAG2} (or the inverse of the L' matrix for U'_{CN}) and the Hamiltonian calculation from the coefficient matrix. The proposed scheme includes two diagonalizations (inversions) and two Hamiltonian evaluations per one total propagation. This predictor-corrector scheme is similar to one proposed by Cheng and coworkers [116]

2.2. ALGORITHM OF THE TIME PROPAGATION OF KOHN-SHAM EQUATIONS 83



PC1



PC2

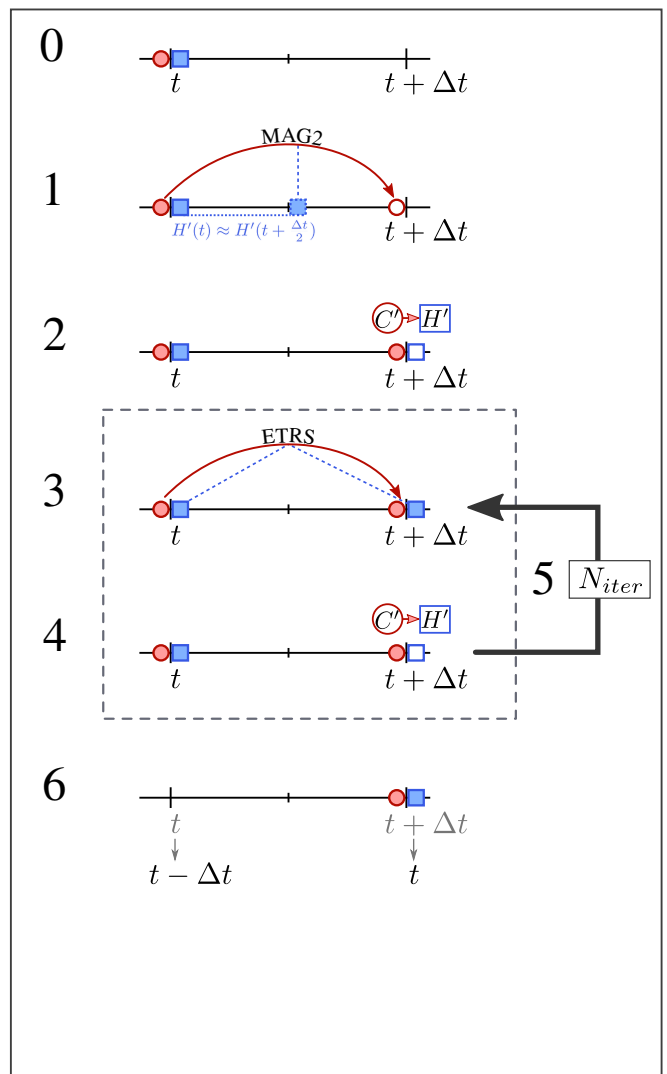


Figure 2.5 : Schematic representation of two selected predictor-corrector schemes used in the code. The legend is at the top of the figure. The enumeration of the predictor-corrector steps in the figure matches with those described in the text.

with the difference that in that work there is no step 5, namely, the Hamiltonian is not calculated after the final propagation. This means that the Hamiltonian grid is two times sparser than in our case.

For the ETRS propagator we have selected the following predictor-corrector scheme (named PC2):

PC2:

0. The Hamiltonian values H' and the coefficient matrix C' are known at t .
1. Propagate $C'(t) \xrightarrow{MAG2} C'(t + \Delta t)$ using MAG2 with $[H'(t + \frac{\Delta t}{2}) \approx H'(t)]$.
2. Calculate $H'(t + \Delta t)$ using $C'(t + \Delta t)$.
3. Propagate $C'(t) \xrightarrow{ETRS} C'(t + \Delta t)$ using ETRS with $H'(t)$ and $H'(t + \Delta t)$.
4. Calculate $H'(t + \Delta t)$ using $C'(t + \Delta t)$.
5. Repeat steps 3 and 4 N_{iter} times.
6. Update for the next step: H' and C' are shifted in time by Δt .

Though this scheme allows one in principle to perform several iterations, which could permit to use larger time steps, in practice, using $N_{iter} = 1$ and a moderate time step is found to be optimal. Hence, similarly to PC1, PC2 has two Hamiltonian evaluations, but three diagonalizations per one total propagation. The reason is that one ETRS propagation demands two diagonalizations. This scheme is similar to the one used in the real-space grid code OCTOPUS [119].

Both predictor-corrector schemes are represented in Fig. 2.5. The final choice of the propagation scheme will be performed later in this chapter. We will compare the efficiency of both schemes in the case of the light excitation of molecular systems.

2.2.7 Frozen states propagation

A possibility to prohibit the electronic excitations from some selected electronic levels could serve as a useful tool. For example, in order to evaluate the role of core electrons excitations for the stopping power calculations, one of the possible ways to do so is to “freeze” the core electrons in the simulation. Another example concerns the case when one wants to compare the results produced with an all-electron code with a plane-wave code in which normally the utilization of pseudopotentials is indispensable because of the computational cost reasons. One can directly use pseudopotentials in the localized basis codes as well, however, using the frozen core states, one does not need to develop a special pseudopotential for a given atom and for a given number of frozen electrons.

which we define as $\tilde{E}^{mod}(t)$. Then we transform back the modified Hamiltonian into the orthogonal atomic basis as follows

$$H'^{mod}(t) = A'(0)\tilde{E}^{mod}(t)A'^H(0). \quad (2.107)$$

We use the modified Hamiltonian $H'^{mod}(t)$ to perform the wave function propagation with any propagator described above. To summarize, for a standard propagation we proceed as follows: $C' \rightarrow H' \rightarrow U' \rightarrow C'$. Whereas for the frozen states propagation one has the following modification to the scheme: $C' \rightarrow H' \rightarrow \tilde{E} \rightarrow \tilde{E}^{mod} \rightarrow H'^{mod} \rightarrow U'^{mod} \rightarrow C'$. For the frozen core propagation, one select $k = 1$ and l equal to the number of core state to “freeze”.

2.3 Validation

In order to benchmark the RT-TDDFT propagation implementation, we have decided to test the RT-TDDFT results against the linear-response TDDFT (LR-TDDFT) for the optical absorption spectra calculations. The LR-TDDFT photoabsorption cross-section calculation is already implemented in MOLGW [120]. Therefore, in this section we will first describe an additional implementation in the code in order to calculate the optical absorption. Then we will compare the results of RT-TDDFT and LR-TDDFT and finally we will analyze the stability of different propagators and predictor-corrector schemes based on the optical excitation results.

2.3.1 Dipole coupling

Let us consider a finite charge distribution described by the charge density $\rho_{tot}(\mathbf{r}, t)$ in an external electric field $\mathbf{E}(\mathbf{r}, t)$. Here we consider that the charge density includes both the nuclear charges $\rho_n(\mathbf{r}) = \sum_a Z_a \delta(\mathbf{r} - \mathbf{R}_a)$ and the electron charge distribution $\rho(\mathbf{r}, t)$

$$\rho_{tot}(\mathbf{r}, t) = \rho_n(\mathbf{r}) + \rho(\mathbf{r}, t). \quad (2.108)$$

We assume that the nuclei are fixed, therefore the nuclear charge density $\rho_n(\mathbf{r})$ does not depend on time. In the *length gauge*, the electric field is given by a scalar potential $\Phi(\mathbf{r}, t)$ as follows

$$\mathbf{E}(\mathbf{r}, t) = -\nabla\Phi(\mathbf{r}, t). \quad (2.109)$$

The interaction energy $W(t)$ between this charge distribution and the scalar potential can be expressed as

$$W(t) = \int d\mathbf{r} \rho_{tot}(\mathbf{r}, t)\Phi(\mathbf{r}, t). \quad (2.110)$$

Suppose that the scalar potential varies slowly near the charge distribution $\rho_{tot}(\mathbf{r}, t)$: $\Phi(\mathbf{r}, t) \approx \Phi(\mathbf{r} = 0, t)$, where the origin $\mathbf{r} = 0$ is chosen in some point inside the charge

distribution. Then we can use the multipole expansion of the $\Phi(\mathbf{r}, t)$ around $\mathbf{r} = 0$ and we get the following expression for the interaction energy

$$W(t) = q\Phi(0, t) - \mathbf{d}(t) \cdot \mathbf{E}(0, t) - \frac{1}{6} \sum_{ij} q_{ij}(t) \frac{\partial E_i(\mathbf{r}, t)}{\partial r_j} \Big|_{\mathbf{r}=0} - \dots, \quad (2.111)$$

where $i, j = 1, 2, 3$; $r_1 = x, r_2 = y, r_3 = z$. q is the total charge of the system

$$q = \int d\mathbf{r} \rho_{tot}(\mathbf{r}, t), \quad (2.112)$$

the integration is performed over a sufficiently large volume to incorporate the whole system for any t . $\mathbf{d}(t)$ is the dipole moment

$$\mathbf{d}(t) = \int d\mathbf{r} \rho_{tot}(\mathbf{r}, t) \mathbf{r}. \quad (2.113)$$

And $q_{ij}(t)$ is the second-rank tensor of the quadruple moment

$$q_{ij}(t) = \int d\mathbf{r} (3r_i r_j - r^2 \delta_{ij}) \rho_{tot}(\mathbf{r}, t). \quad (2.114)$$

Since the expression of the dipole moment (equation 2.113) contains \mathbf{r} under the integral sign, one might wonder whether the dipole moment depends on the origin. To answer this question, let us displace the origin by \mathbf{r}_0 . The new dipole moment $\mathbf{d}'(t)$ will be given by

$$\mathbf{d}'(t) = \int d\mathbf{r} \rho_{tot}(\mathbf{r}, t) (\mathbf{r} - \mathbf{r}_0) = \int d\mathbf{r} \rho_{tot}(\mathbf{r}, t) \mathbf{r} - \mathbf{r}_0 \int d\mathbf{r} \rho_{tot}(\mathbf{r}, t) = \mathbf{d}(t) - \mathbf{r}_0 q. \quad (2.115)$$

Hereafter we will consider only neutral systems: $q = 0$. Only in this case, the dipole moment does not depend on the origin. One can generalize this conclusion (without the demonstration) in the following way: the lowest nonvanishing multipole moment of a charge distribution is independent on the origin.

Then we can divide the dipole moment into two contributions: 1) nuclear and 2) electronic. Substituting the expression of the total density (equation 2.108) into the expression of the dipole moment (equation 2.113), one gets

$$\mathbf{d}(t) = \int d\mathbf{r} \rho_n(\mathbf{r}, t) \mathbf{r} + \int d\mathbf{r} \rho(\mathbf{r}, t) \mathbf{r} = \mathbf{d}_0 + \int d\mathbf{r} \rho(\mathbf{r}, t) \mathbf{r}, \quad (2.116)$$

where \mathbf{d}_0 is a dipole moment provided by the nuclei. Since we consider fixed nuclei positions, \mathbf{d}_0 is not a function of time.

In this section, we *choose* the external electric field $\mathbf{E}(\mathbf{r}, t)$ to be homogeneous in space, but still time-dependent - $\mathbf{E}(t)$. Therefore, the quadruple term, as well as all other higher-order terms in the expansion 2.111, are *exactly* equal to zero. Therefore, in this regime, only dipole coupling is present. In an experimental setup, this would correspond to the regime when the wavelength of the laser field excitation is much larger than the size of the molecule.

Now we would like to express the dipole moment in the basis set. In the length form, the electron dipole operator is equal to the position operator (in atomic units): $\hat{\mathbf{d}} = \hat{\mathbf{r}}$. Therefore, the dipole moment can be written in the following form

$$\mathbf{d}(t) = \mathbf{d}_0 + \sum_i f_i \langle \varphi_i(t) | \hat{\mathbf{r}} | \varphi_i(t) \rangle. \quad (2.117)$$

Decomposing $\langle \varphi_i(t) |$ and $|\varphi_i(t)\rangle$ in the atomic basis set $\{\phi_\alpha\}$, one gets

$$\mathbf{d}(t) = \mathbf{d}_0 + \sum_i f_i \sum_{\alpha\beta} C_{\beta i}^*(t) C_{\alpha i}(t) \langle \phi_\beta | \hat{\mathbf{r}} | \phi_\alpha \rangle. \quad (2.118)$$

Using the definition of the density matrix P (equation 2.6), this expression becomes

$$\mathbf{d}(t) = \mathbf{d}_0 + \sum_{\alpha\beta} P_{\alpha\beta}(t) \langle \phi_\beta | \hat{\mathbf{r}} | \phi_\alpha \rangle, \quad (2.119)$$

or, in the integral form,

$$\mathbf{d}(t) = \mathbf{d}_0 + \sum_{\alpha\beta} P_{\alpha\beta}(t) \int d\mathbf{r} \phi_\beta(\mathbf{r}) \hat{\mathbf{r}} \phi_\alpha(\mathbf{r}). \quad (2.120)$$

We define the electron dipole matrix as follows

$$\mathbf{D}_{\alpha\beta} = \int d\mathbf{r} \phi_\alpha(\mathbf{r}) \mathbf{r} \phi_\beta(\mathbf{r}) = \langle \phi_\beta | \mathbf{r} | \phi_\alpha \rangle. \quad (2.121)$$

One can explicitly indicate an i component of the matrix

$$(D_{\alpha\beta})_i = \int d\mathbf{r} \phi_\alpha(\mathbf{r}) r_i \phi_\beta(\mathbf{r}) = \langle \phi_\beta | r_i | \phi_\alpha \rangle. \quad (2.122)$$

By construction, the \mathbf{D} matrix is symmetric. One can also note that the dipole matrix, unlike the dipole moment, does not depend on time, therefore it can be computed once for the whole simulation.

We can rewrite the expression of the dipole moment 2.120 using the dipole matrix in the following way

$$\mathbf{d}(t) = \mathbf{d}_0 + \sum_{\alpha\beta} P_{\alpha\beta}(t) \mathbf{D}_{\beta\alpha} = \mathbf{d}_0 + \sum_{\alpha} (P(t) \mathbf{D})_{\alpha\alpha} = \mathbf{d}_0 + \text{tr} [P(t) \mathbf{D}]. \quad (2.123)$$

The additional term to the Hamiltonian due the external electric field, $\hat{H}_1(t)$, writes

$$\hat{H}_1(t) = -\mathbf{r} \cdot \mathbf{E}(t). \quad (2.124)$$

Then in the atomic basis this term will be

$$\hat{H}_{1\alpha\beta}(t) = \int d\mathbf{r} \phi_\alpha(\mathbf{r}) \hat{H}_1(t) \phi_\beta(\mathbf{r}) = - \int d\mathbf{r} \phi_\alpha(\mathbf{r}) \mathbf{r} \phi_\beta(\mathbf{r}) \mathbf{E}(t) = -D_{\alpha\beta} \mathbf{E}(t). \quad (2.125)$$

2.3.2 Optical absorption

In the presence of the external field $\mathbf{E}(t)$, the time-dependent dipole moment has the following expansion

$$\begin{aligned}
 d_i(t) = & d_{i0} + \sum_j \int_{-\infty}^{\infty} dt_1 \alpha_{ij}(t-t_1) E_j(t_1) \\
 & + \sum_{jk} \int_{-\infty}^{\infty} \int_{-\infty}^{\infty} dt_1 dt_2 \beta_{ijk}(t-t_1, t-t_2) E_j(t_1) E_k(t_2) \\
 & + \sum_{jkl} \int_{-\infty}^{\infty} \int_{-\infty}^{\infty} \int_{-\infty}^{\infty} dt_1 dt_2 dt_3 \gamma_{ijkl}(t-t_1, t-t_2, t-t_3) E_j(t_1) E_k(t_2) E_l(t_3) \\
 & + \dots,
 \end{aligned} \tag{2.126}$$

where d_{i0} is the permanent dipole in direction i , α_{ij} is the linear polarizability tensor and β_{ijk} , γ_{ijkl} are higher order polarizabilities. In order to compare the RT-TDDFT results with the linear response theory, we will consider here the weak field limit. It means that we assume that the induced dipole moment $\mathbf{d}^{ind}(t)$ is dominated by the linear polarizability term

$$d_i^{ind}(t) \approx \sum_j \int_{-\infty}^{\infty} dt_1 \alpha_{ij}(t-t_1) E_j(t_1). \tag{2.127}$$

Rewriting this equation in the frequency domain, one gets the complex-valued frequency dependent polarizability tensor [113]

$$\alpha_{ij}(\omega) = \frac{d_i^{ind}(\omega)}{E_j(\omega)} = \frac{\int dt e^{i\omega t} d_i^{ind}(t) e^{-\gamma t}}{\int dt e^{i\omega t} E_j(t)}, \tag{2.128}$$

where γ is a numerically adjustable damping factor which leads to the artificial broadening of the absorption peaks. This factor emulates the coupling effect between electronic and nuclear degrees of freedom [121]. One can mention that the form of the damping factor determines the form of the broadening of the absorption peaks (Gaussian, Lorentzian, etc.). However, the integral over a peak corresponds to the oscillator strength and is a constant value.

There are different forms of the external electric field to excite the system [122, 123]. We have decided to use a nonphysical delta-function electric field perturbation

$$\mathbf{E}_\delta(t) = \kappa \delta(t) \hat{\mathbf{e}}, \tag{2.129}$$

where κ is the kick strength and $\hat{\mathbf{e}}$ is the unitary vector pointing in the direction of the field. In this way, we excite all electronic modes in the molecular system. And the quantity of energy transmitted to the system by the external field does not depend on the time discretization Δt : the electric field is non-zero only at one moment $t = 0$. In this case, the polarizability tensor has a simpler expression

$$\alpha_{ij}(\omega) = \frac{\hat{e}_j}{\kappa} \int dt e^{i\omega t} d_i^{ind}(t) e^{-\gamma t}. \tag{2.130}$$

The imaginary part of the linear polarizability is proportional to the absorption cross-section tensor

$$\sigma(\omega) = \frac{4\pi\omega}{c} \text{Im}\alpha(\omega). \quad (2.131)$$

Finally, the experimentally observed absorption spectrum (dipole strength function) can be found as

$$S(\omega) = \frac{1}{3} \text{tr}(\sigma(\omega)). \quad (2.132)$$

Because of a finite simulation time T and time step Δt , the Fourier transforms of time-dependent quantities are valid for frequencies less than $\omega_{max} = \pi/\Delta t$ and have the resolution $\Delta\omega = 2\pi/T$.

Hence, in order to calculate the optical response of a molecular system in the RT-TDDFT, one should proceed in the following way: 0) Perform the ground state DFT calculation. 1) Apply the electric field excitation $\mathbf{E}(t)$ in a direction j . 2) Calculate dipole moment during the simulation $\mathbf{d}(t)$. 3) Perform the calculation of *three* components of the polarizability tensor: $\alpha_{1j}(\omega)$, $\alpha_{2j}(\omega)$, $\alpha_{3j}(\omega)$. Repeat these steps for the other directions of the external electric field. Once the complete polarizability tensor is computed, one can calculate the dipole strength function $S(\omega)$ (equation 2.132). Using molecular symmetries, one can reduce the number of α_{ij} elements to calculate. Usually, in the absence of magnetic fields, the off-diagonal terms can be neglected.

It should be mentioned that due to the nonperturbative nature of the developed RT-TDDFT approach, one can calculate the optical response to any external field. However, for large values of the applied field one should take into account higher order polarizabilities [124].

Optical absorption spectra of benzene

In order to validate the RT-TDDFT approach we show the results of the absorption spectra calculation using RT-TDDFT and LR-TDDFT, both implemented in MOLGW. We have chosen benzene, C_6H_6 , as a model system. The advantage of benchmarking the RT-TDDFT versus the LR-TDDFT within the same code is that one can choose exactly the same basis set. For these calculations, the `cc-pVTZ` basis set was chosen.

For the real-time simulation we have used the following parameters: total simulation time $T = 5000$ a.u., time step $\Delta t = 0.1$ a.u., excitation kick strength $\kappa = 2 \times 10^{-4}$ a.u.. Large simulation time is chosen to have a good energy resolution of the spectrum: $\Delta E = 3.4 \times 10^{-2}$ eV. Whereas the time step is limited by the stability of the propagation rather than the energy range. The bandwidth corresponding to the $\Delta t = 0.1$ a.u. time step is equal to $E_{max} = 848.2$ eV. The dipole moment evolution, as well as the charge density difference, are presented in Fig. 2.6a and 2.6c. One can note that the initial kick ($t = t_1$) leads to the maximal dipole moment of the molecule. It is seen that the molecule presents multiple oscillation modes.

The absorption spectra obtained from RT-TDDFT and LR-TDDFT are normalized for clarity. Comparing the two approaches (Fig. 2.6b) one can see globally a good agreement

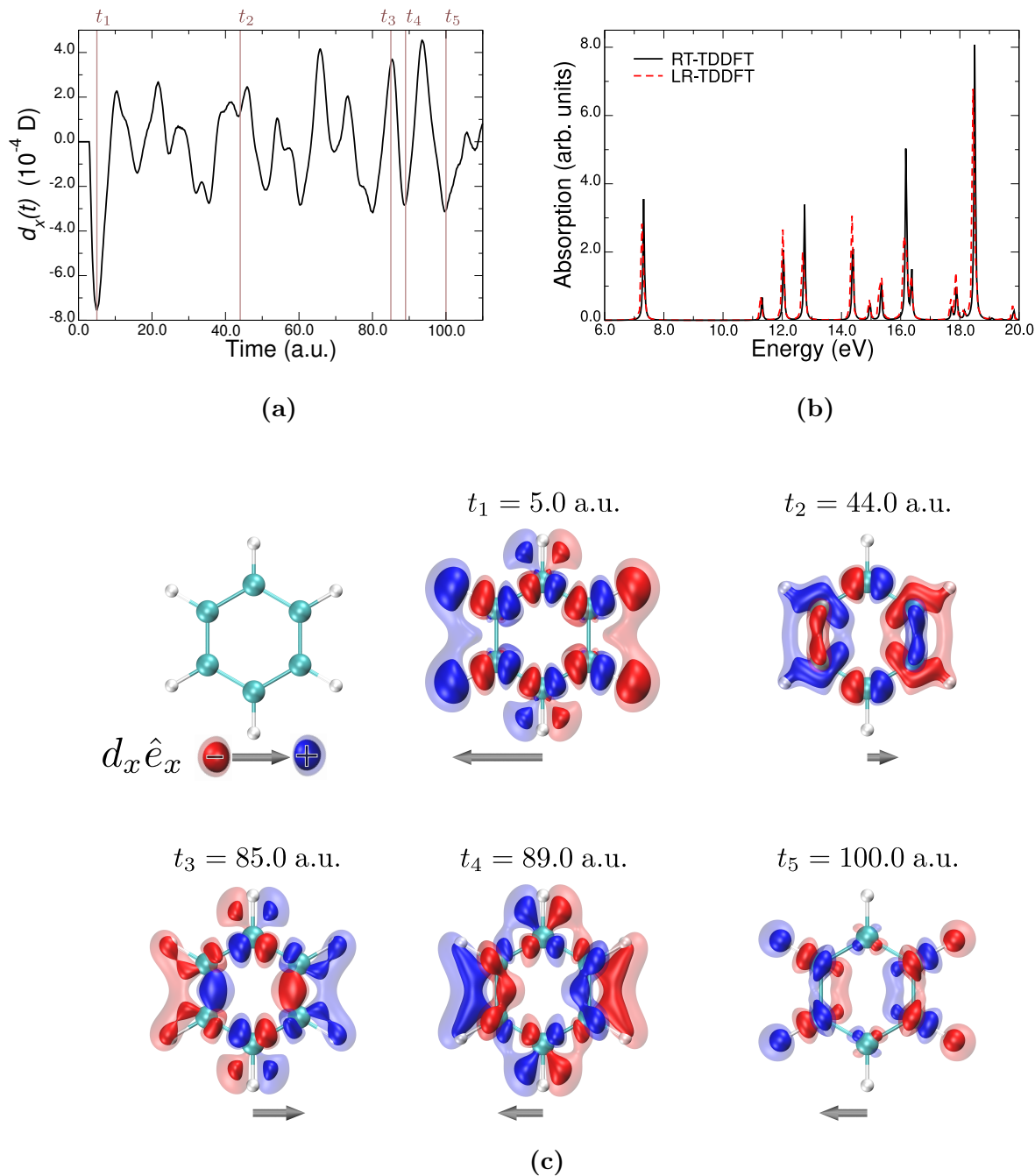


Figure 2.6 : (a) Temporal evolution of the x dipole moment after the delta-function excitation. (b) The resulting absorption spectrum obtained from the RT-TDDFT calculation (black) and LR-TDDFT (red). (c) Isosurface snapshots of the electronic density between the excited and the ground states for some selected times (these times are also indicated on the panel (a)). Red color corresponds to the accumulation of electrons: opaque red $\rho(\mathbf{r}, t) - \rho(\mathbf{r}, 0) = 1.0 \times 10^{-7} \text{ bohr}^{-3}$; transparent red $\rho(\mathbf{r}, t) - \rho(\mathbf{r}, 0) = 0.5 \times 10^{-7} \text{ bohr}^{-3}$. Blue color corresponds to the depletion of electrons, the color scheme is identical as for the red color, but with the opposite sign. The x -component of the dipole moment is presented under each snapshot.

between the linear-response theory and the time-dependent propagation. For each absorption peak the position and the amplitude match for both methods. There are some minor discrepancies though, perhaps because of the finite RT simulation time.

2.3.3 Choice of the propagator and the predictor-corrector scheme

Using the same model system and the same excitation type as in the previous section, we have made a choice of the propagator technique as well as for the predictor-corrector scheme. We have pre-selected the following methods: 1) predictor-corrector PC1 with the second order Magnus propagator \hat{U}_{MAG2} or with the Crank Nicolson propagator \hat{U}_{CN} ; 2) predictor-corrector PC2 with \hat{U}_{MAG2} for the first, predictor, step and the enforced time-reversal symmetry propagator \hat{U}_{ETRS} for the second, corrector, step.

We have used the density matrix error as a propagation quality criterion, which is defined as follows [116]

$$P^{Error}(t) = \frac{1}{N_{AO}} \sum_{ij} |P_{ij}^{exact}(t) - P_{ij}^{approx}(t)|, \quad (2.133)$$

where $P^{approx}(t)$ is the time-dependent density matrix obtained with a propagator scheme that one wants to evaluate and $P^{exact}(t)$ is the time-dependent density matrix computed with some propagation scheme with a very small time step. We have used the time step $\Delta t = 10^{-3}$ a.u. for the $P^{exact}(t)$ construction. At this time step, either of the preselected propagator schemes gives the same result.

First, we have compared the \hat{U}_{MAG2} and \hat{U}_{CN} propagators using the PC1 predictor-corrector scheme. We have used a relatively small time step $\Delta t = 0.1$ a.u.. In Fig. 2.7a it is seen that the \hat{U}_{CN} propagator leads to a nonphysical instability of the system, whereas the \hat{U}_{MAG2} propagator remains stable. Most certainly, this happens because, for the \hat{U}_{MAG2} propagator one performs the exact diagonalization of the Hamiltonian, whereas for the \hat{U}_{CN} some further approximations are made (equations 2.76, 2.79). Therefore, the choice of the propagator among these two is evident: \hat{U}_{MAG2} .

Second, we have performed a comparison between the predictor-corrector schemes: PC1 (using the chosen \hat{U}_{MAG2}) and PC2 (using \hat{U}_{MAG2} and then \hat{U}_{ETRS}). Fig. 2.7b represents this comparison. One can see that both predictor-corrector schemes show very similar behavior. Both propagations are stable during a long time with a larger time step than in Fig. 2.7a case. For this propagation $\Delta t = 0.5$ a.u.. Other things being equal, we should mention that for the \hat{U}_{ETRS} propagation one needs two diagonalizations of the Hamiltonian, whereas for the \hat{U}_{MAG2} - only one. Therefore, the propagation scheme provided by the PC2 is more expensive to calculate, which determines our choice of the predictor-corrector scheme.

Finally, based on these tests, we have selected the following propagation scheme for all further calculations: PC1 using the \hat{U}_{MAG2} propagator. This scheme is relatively cheap for the calculation and provides a stable propagation with time steps up to 1 a.u. The optimal time step, of course, depends on a given system and on the perturbation.

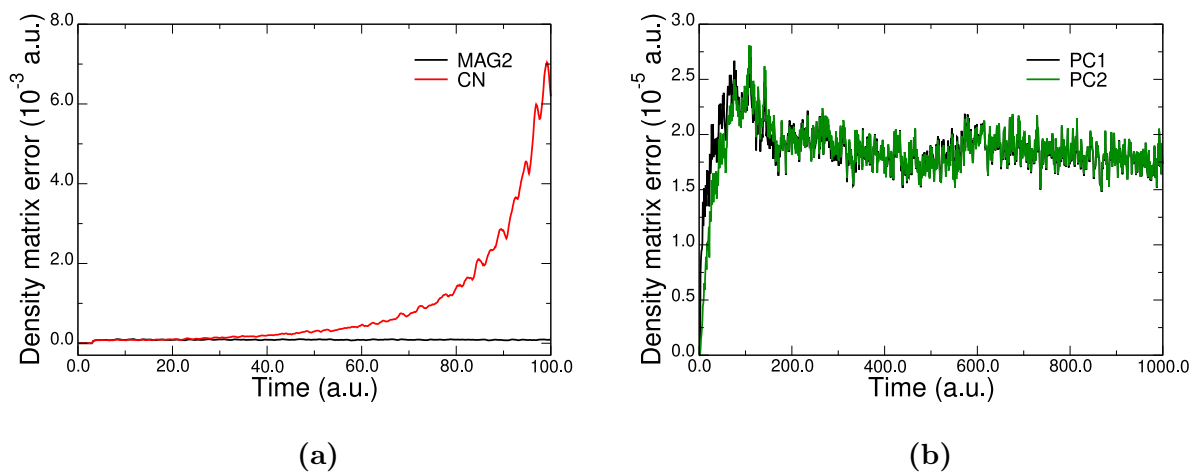


Figure 2.7 : Density matrix error evolution for the benzene electronic density propagation after the delta-function excitation. For the propagation the following schemes were used: (a) MAG2 and CN propagators within the PC1 predictor-corrector scheme, $\Delta t = 0.1$ a.u. . (b) PC1 and PC2 predictor-corrector schemes, $\Delta t = 0.5$ a.u.. In the PC1 the MAG2 propagator was used. In the PC2 we have used MAG2 for the predictor step and ETRS for the corrector step.

CHAPTER 3

Methodology of the stopping power calculation in the localized Gaussian basis

In this chapter, we will discuss the stopping power calculations in the localized Gaussian basis with particular emphasis on 3D crystalline materials. First, we will describe the method to deduce the stopping power from a single projectile trajectory in the localized basis. Then we will discuss our approach to deduce the random stopping power. After that, the Gaussian basis set specifics in the electronic stopping power calculations will be discussed. Finally, we will focus on the validity of the fixed projectile trajectory approximation, which is used in this work.

3.1 Li as a model system

Having developed the RT-TDDFT approach in the Gaussian basis and tested it using the light absorption spectra calculations (chapter 2), we have directed our efforts towards the electronic stopping power calculations in crystals. The MOLGW code does not contain periodic boundary conditions, therefore, in order to perform the stopping power calculations for crystalline materials, we use clusters that have a size large enough to mimic the bulk material (this point will be discussed in detail in section 3.1.2).

As a model system, we have selected the proton irradiation in a cluster of metallic body-centered cubic lithium. We have selected lithium for several reasons: it has few electrons per atom, it is metallic and therefore the surface truncation does not induce dangling bonds, there are experimental data for the proton in lithium system and finally

we have recent linear-response results to compare with [33].

3.1.1 Single-trajectory stopping power

We calculate the instantaneous stopping power using the fixed velocity technique introduced in section 1.5.1. We have selected this method because it corresponds to the electronic-only response of the system under the irradiation. In addition, since it does not require the calculation of the forces during the simulation, this method has a lower computational cost compared to the *ab initio* molecular dynamics.

To date, the basis functions moving along with the projectile are not implemented in the code, hence we confine ourselves to the electronic stopping power calculations of light projectiles. Therefore, the moving “naked” projectile in a cluster can be described simply as a bare Coulombic potential perturbation

$$\hat{V}_{pert}(\mathbf{r}, t) = \frac{Z_{proj}}{|\mathbf{r} - \mathbf{r}_{proj}|}, \quad (3.1)$$

where Z_{proj} is the charge of the projectile and \mathbf{r}_{proj} is the projectile position.

Simulation setup

In this section, we select the [001] orientation of the lithium cluster. RT-TDDFT calculations are performed using the LDA functional and cc-pVDZ basis set. In next section we will discuss the influence of these parameters on the stopping power.

A typical simulation of a projectile trajectory performed in this work, can be described as follows:

- The projectile initial position is $\mathbf{r}_{proj\ 0} = (p_x; p_y; -z_0)$, where z_0 is the initial separation between the projectile and the cluster. Typically, we take z_0 around 10 Å; p_x and p_y are the components of the impact parameter vector \mathbf{p} in the XY plane.
- First, the gKS DFT calculation is performed in order to calculate the ground-state density of the system.
- Once the convergence of the DFT loop is reached, the constant velocity is assigned to the projectile and the RT-TDDFT simulation starts.
- The real-time simulation is performed with a time step Δt which is inversely proportional to the projectile velocity in order to keep the spatial step Δz constant. For lithium, we have found $\Delta z = 0.1$ bohr (0.053 Å) to be an adequate spacing. For the projectile velocity $v = 1.0$ a.u. ($E_{proj}^{kin} \approx 25$ keV) the time step is $\Delta t = 0.1$ a.u. ≈ 2.42 as.
- The simulation runs until the projectile leaves the cluster. Typically, we have around 400 time steps per simulation (the simulation time is then about $t_{sim} = 40$ a.u. ≈ 1 fs for $v = 1.0$ a.u.).

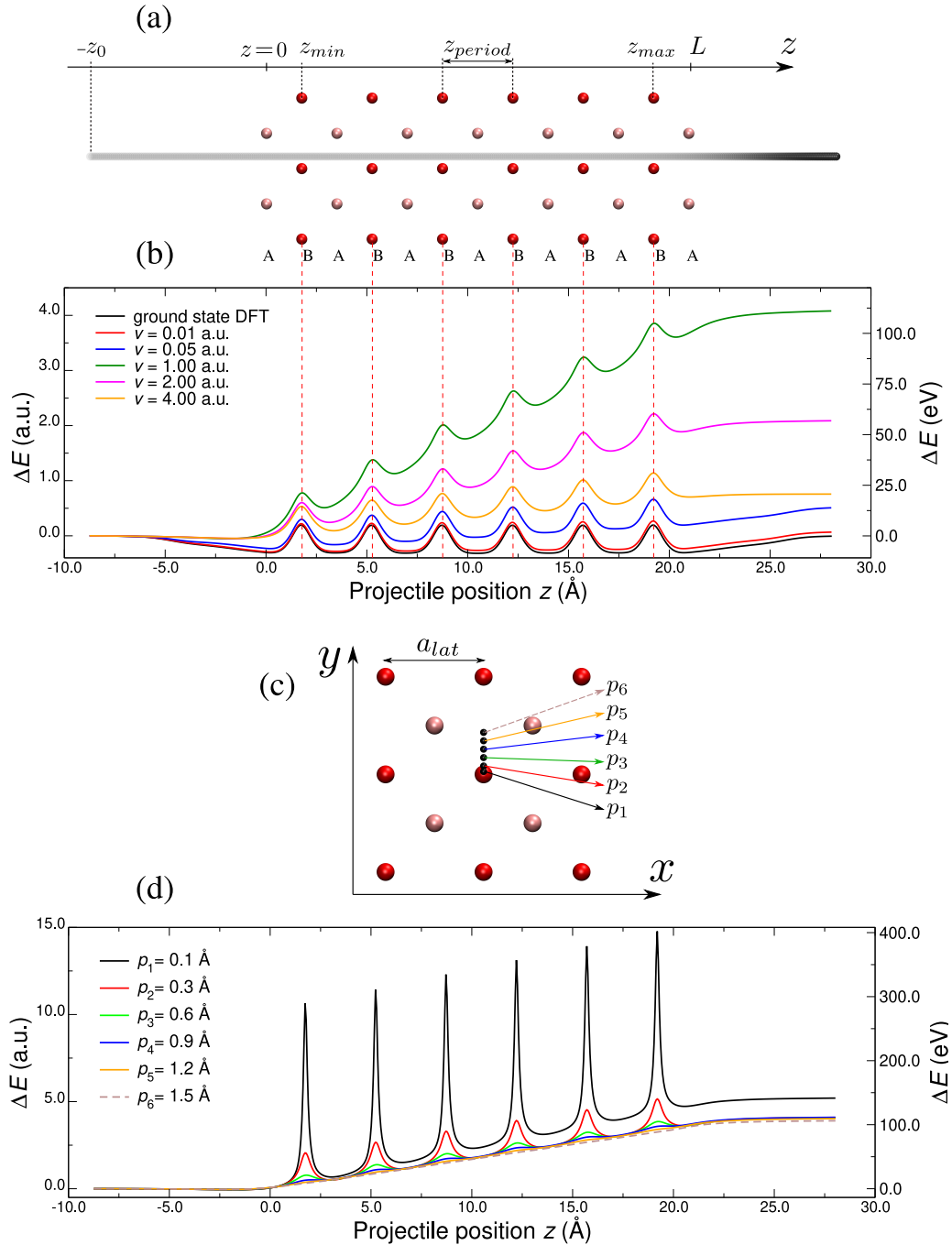


Figure 3.1 : Irradiation simulation of proton in the lithium cluster in the localized basis. (a) Profile view of the irradiation: The projectile (depicted as a black sphere) impinges on a metallic target (target atoms are in pink and red depending on the atomic plane). The projectile track is the grey line behind the projectile. The first atomic layer of the target has $z = 0$ coordinate. The initial projectile position is given by z_0 . L is the length of the cluster. (b) Total *electronic* energy as a function of the penetration depth z for different velocities (color online). All the trajectories presented on this graph have the impact parameter $p_y = 0.6$ Å, $p_x = 0.0$ Å. (c) Front view of the cluster. The black spheres correspond to six impact parameters for the panel (d). The p_x component is equal to zero for all impact points. (d) $E(z)$ curve for different impact parameters at the projectile velocity $v = 1.0$ a.u..

The total energy of the system then depends explicitly on the projectile position z (also called the penetration depth) and parametrically on the projectile velocity v and its impact parameter \mathbf{p} . For the sake of simplicity, in the expressions concerning the total energy, we will keep only z dependence and we will mention other arguments when necessary.

Figure 3.1 (b) shows the total electronic energy of the system E as a function of the penetration depth z for different projectile velocities. It is seen that the energy transfer rate varies as a function of the projectile velocity v , which demonstrates the electronic stopping power dependence on v . The peaks of the $E(z)$ curves correspond to the z positions where the projectile approaches the central atoms of even atomic layers (in red, denoted as B in Fig. 3.1 (a)). One can also mention that for small velocities ($v < 0.2$ a.u.) the energy dependence approaches the so-called adiabatic limit ($E(z, v = 0)$). In this limit, to get the $E(z)$ dependence, one performs the *time-independent* DFT calculation for every z point. Obviously, the electronic stopping power in this limit is zero (which is seen from Fig. 3.1 (b), black curve).

In Figure 3.1 (d) one can see the total energy dependence as a function of the penetration depth for several impact parameters \mathbf{p} . The origin $\mathbf{p} = 0$ is selected at the central atom in the XY plane (see Fig. 3.1 (c)). The peaks of $E(z)$ corresponding to the positions of B layers ($z = z_B$) become larger when the projectile impact parameter decreases. As well, it can be seen that the overall slope of the curves is larger for small impact parameters.

Electronic density excitations

We would like to illustrate the irradiation simulation by the use of the electronic density excitation. Fig 3.2 presents the deviation of the lithium electronic density due to a proton projectile penetration, $\rho(\mathbf{r}, t) - \rho(\mathbf{r}, t = 0)$, where $\rho(\mathbf{r}, t = 0)$ corresponds to the ground state electronic density. We present the results for different projectile velocities (that correspond to the rows of the figure). In order to visualize the excited density profile, the density snapshots for all velocities were taken when the proton nearly exists the cluster ($z \approx 22$ Å). The proton impact parameter was fixed to $p_x = 0.0$ Å and $p_y = 0.6$ Å. Red surfaces in Fig. 3.2 correspond to positive and blue to negative electronic density variations.

It is seen that even though there are no basis functions that are centered around the projectile, the target basis functions can describe the electronic states of the projectile (if the projectile is inside the cluster). For example, in the case of a very slow projectile velocity $v = 0.02$ a.u. (first row in Fig. 3.2), one can see the electronic density variation, which is almost spherical and centered around the proton. We expect that the capability of the target basis functions to capture the electronic density around the projectile is sufficient for the projectiles with a low charge Z_{proj} , that have the electronic states not very deep in energy and not very localized in space. Therefore, in this work, we will study the irradiation of protons, antiprotons, and alpha-particles.

Concerning the electronic density profile, one can see the accumulation of electrons behind the proton (for the projectile velocities $v \geq 0.5$ a.u. or $E_{proj}^{kin} \geq 6.2$ keV). This wake charge distribution becomes more elongated as the projectile velocity increases.

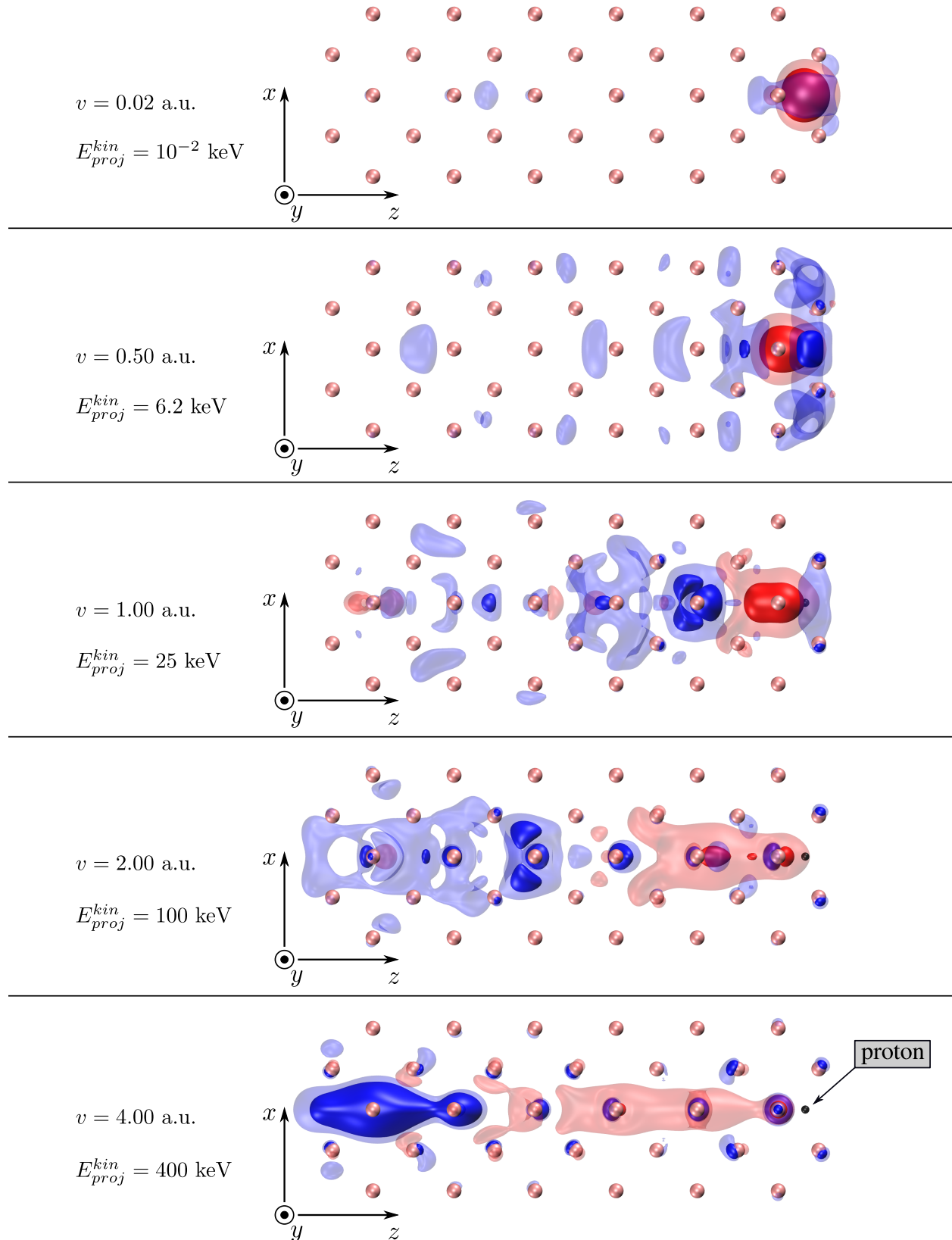


Figure 3.2 : Electronic density differences produced by a proton projectile in lithium cluster for 5 projectile velocities (indicated on the left-hand side as well as the projectile kinetic energies E_{proj}^{kin}). Red surfaces correspond to electron accumulation, while blue to electron depletion.

Average slope

Now we would like to discuss the method to extract the average slope, which corresponds to $S_e^{traj}(v)$, from the energy-penetration depth curves. One can easily calculate the *instantaneous* electronic stopping power $S_e(z, v, \mathbf{p})$ from $E(z)$ curves as a derivative of the total energy over the penetration depth z (equation 1.128). However, in order to calculate the electronic stopping power for a single trajectory $S_e^{traj}(v, \mathbf{p})$ one needs to calculate the average slope of the energy as a function of z . This procedure should be done for different impact parameters. It is seen from Fig. 3.1 (d) that the calculation of the average slope for small impact parameters could be quite challenging even though it is seen that the dependence is periodic. Ullah and coworkers propose to deal with this problem by subtracting the adiabatic energy $E(z, v = 0)$ from the non-adiabatic energy $E(z, v)$ in order to get rid of large but periodic peaks of $E(z)$ [94]. However, the calculation of the adiabatic curve is more computationally expensive (around 30 times) than the RT-TDDFT simulations themselves because DFT requires to perform the self-consistent loop for every z point. Therefore, we propose a 3-step procedure to obtain a stable average slope for any impact parameter.

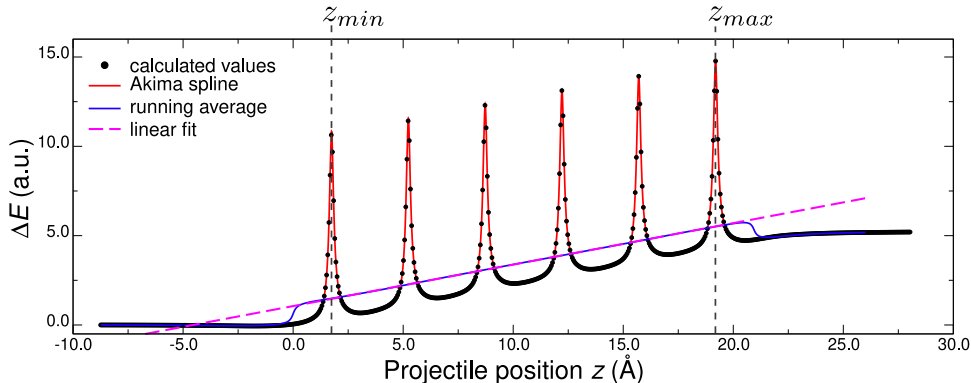


Figure 3.3 : The procedure of the electronic stopping power calculation from the total electronic energy as a function of the penetration depth z . The order in the legend corresponds to the order of the stopping power calculation described in the text: 0) energy values from the RT-TDDFT simulation \rightarrow 1) Akima spline \rightarrow 2) running average \rightarrow 3) linear regression.

First, we apply the Akima spline [125] to the total energy curve. We select the grid of z points for the interpolation so as to include precisely the positions of the B atomic layers, which correspond to the peaks of the energy curve. One can build such grid fixing the distance between two adjacent points of the grid, Δz , in the following way

$$\Delta z = \frac{z_{max} - z_{min}}{N_{interval} - 1}, \quad (3.2)$$

where z_{min} and z_{max} are the positions of the first and the last B layers respectively (see Fig. 3.1 (a)), $N_{interval}$ is the number of points in the interpolation grid between these layers

(including the boundaries). Then, the position of points in the grid z_n (starting from $z = 0$) is simply $z_n = n\Delta z$.

We use a sufficiently large number of interpolation points (around 12 000 for the case presented in Fig. 3.1). This is done in order to have a smooth energy dependence around the target atoms for small impact parameters ($p < 0.3 \text{ \AA}$). For larger impact parameters the energy curve is already smooth enough even without the spline, however, we apply this procedure to every impact parameter anyway.

Second, we apply a running average to the interpolated data. In order to calculate the averaged value of the energy \bar{E} at the position z_n , one uses the following expression

$$\bar{E}(z_n) = \frac{1}{N_p} \sum_{k=-\frac{N_p-1}{2}}^{\frac{N_p-1}{2}} E(z_{n+k}), \quad (3.3)$$

where N_p is the so-called ‘‘average window’’ - the number of points around z_n which are taken into account for the average calculation at z_n . We select N_p to be commensurate with the periodicity of the energy curve, i.e.,

$$N_p = \frac{z_{period}}{\Delta z} + 1, \quad (3.4)$$

where z_{period} is the period of $E(z)$ due to the cluster symmetry (see Fig. 3.1). For the [001] cluster orientation, z_{period} is just equal to the lattice parameter a_{lat} , however, for other orientations it is not necessarily the case. Choosing the interval of the running average equal to the distance of the period of $E(z)$, we cancel the contributions of the energy terms that are purely functions of the nuclei coordinates.

Third, we apply the linear regression to the averaged energy $\bar{E}(z)$ in the region between z_{min} and z_{max} . In this way, we remove the transient regions $[0; z_{min}]$ and $[z_{max}; L]$ so to minimize the surface effect. Finally, the electronic stopping power for a single projectile trajectory S_e^{traj} can be found from the slope of the linear fitting curve.

We have found that such a postprocessing of each trajectory is robust and accurate whatever the impact parameter or the cluster geometry (cluster must contain at least one periodic repetition though). All the steps are exemplified in Fig. 3.3 for the lowest impact parameter used in our calculations $p = 0.1 \text{ \AA}$ since it is the most difficult case to analyze.

3.1.2 Cluster geometry

In order to reproduce the bulk stopping power values for a crystalline material, the cluster used in *ab initio* simulations must be large enough so to minimize the influence of the surface effects. On the other hand, the computational time increases with the number of target atoms as N_{atoms}^3 . Therefore, one needs to find a compromise between the accuracy of the stopping power calculations and the computational cost. It has been reported [39, 126] that the convergence of the stopping power with respect to the cluster size is fast.

We have performed the convergence calculations of the electronic stopping power averaged over the projectile trajectory S_e^{traj} as a function of the cluster length (Fig. 3.4 (a)) and the cluster diameter (Fig. 3.4 (b)).

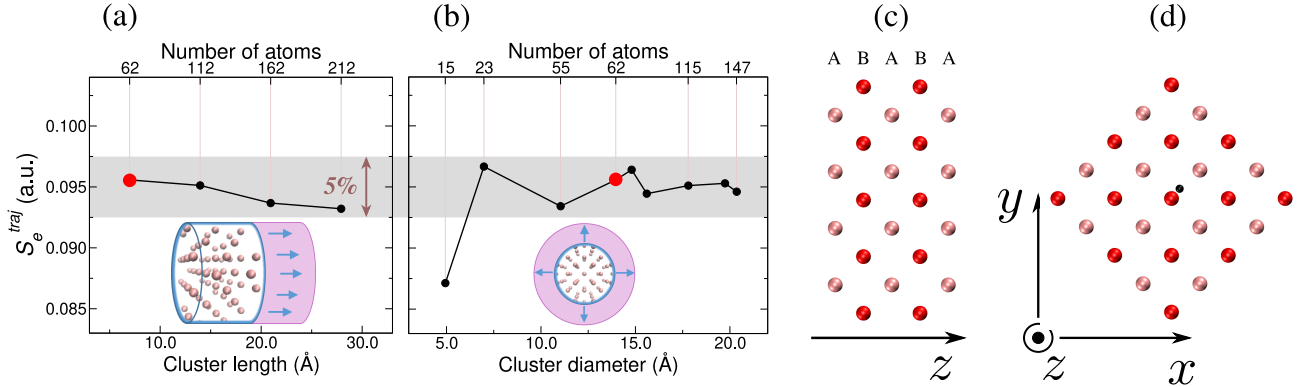


Figure 3.4 : (a), (b) Electronic stopping power averaged over projectile trajectory S_e^{traj} of proton in lithium cluster ([001] cluster orientation). (a) S_e^{traj} as a function of the cluster length for the fixed diameter of 14 Å. (b) S_e^{traj} as a function of the cluster diameter for the fixed length of 7 Å. Red circles specify the selected cluster geometry parameters. (c), (d) Profile and front views of the 62-atom lithium cluster retained in this work. The projectile position in the XY plane is depicted with a black sphere on the panel (d).

In order to select the longitudinal geometry of the cluster (of [001] orientation), we have been guided by the following considerations: We select the impact parameters in a way that the closest atoms along the projectile path are always the central atoms of B atomic layers (see Fig. 3.1 (c)). Therefore, we select such cluster configurations to have the electronic density around these atoms close to the bulk one. To do so, we always put the A layers as the first and the last layers in the cluster. Hence, the clusters used in the convergence tests have the following configurations: A(BA) n . With the cluster geometry selected in this way, the stopping power S_e^{traj} does not have significant variations as a function of the cluster length (Fig. 3.4 (a)).

Concerning the cluster diameter, we do not have any limitations regarding the choice of this parameter. It is seen (Fig. 3.4 (a) and (b)) that the stopping power is less sensitive to the cluster length than to the cluster diameter.

The results presented in Fig 3.4 have been produced with the projectile velocity $v = 1.0$ a.u. ($E_{proj}^{kin} \approx 25$ keV) and the projectile impact parameter $p_x = 0.5$ Å, $p_y = 0.6$ Å (see Fig. 3.4 (d)). For different velocities and different impact parameters we have observed similar behavior.

Finally, we have retained the 62-atom cluster represented in Fig. 3.4 (c) and (d), which permits one to evaluate the bulk limit within 5%. This cluster is approximately 7 Å long (having ABABA configuration) and 14 Å wide.

3.1.3 Random stopping power

In this section, we will describe the method we employ to calculate the random stopping power. First, we will consider the ensemble average technique (section 1.5.2) performed on fine grids for different crystal orientations. Then, we will discuss the polar symmetry approximation for the random stopping power calculations, and finally, we will describe our efficient working scheme to obtain the random stopping power. In addition, the correlation between the stopping power and the electronic density will be discussed.

Crystalline orientations

We have calculated the random electronic stopping power (RESP) in lithium for three orientations of the lattice: [001], [110], [111]. The cluster geometries for [110], [111] orientations (Fig. 3.5 (a) and (b)) were selected using similar reasoning as it was done for the [001] orientation. As a convention, for each orientation, we select the z -axis to be along the projectile path and the XY plane to be orthogonal to the projectile passage trajectory.

First, let us analyze the crystalline symmetry for each direction. Fig. 3.5 (b) shows in green the elementary surfaces \mathcal{A} for each orientation. The elementary surfaces are found using the crystalline symmetry considerations: For a given crystal orientation, one finds the smallest surface which can completely pave the entire surface in the XY plane. In our truncated clusters we focus on the most central elementary surface that would best mimic the infinite solid.

Impact parameter grid

Since in the ensemble average RESP calculations every value of $S_e^{traj}(\mathbf{p})$ is obtained by running a separate simulation for a given \mathbf{p} , we cannot average the stopping power over a *continuous* $\mathbf{p} \in \mathcal{A}$ (like in linear response approach [33]), but rather on a finite *discrete* grid of impact parameters $\{\mathbf{p}_i\}_{i=1}^{N_{grid}} \in \mathcal{A}$, where N_{grid} is the number of grid points.

To select the impact parameter grid, we break the elementary surface \mathcal{A} on subelements \mathcal{A}'_i . Then for a given \mathcal{A}'_i we select one point \mathbf{p}_i and assume that the stopping power $S_e^{traj}(\mathbf{p}_i)$ represents the average over \mathcal{A}'_i . Following the idea of the centroid path approximation (section 1.5.2), we select \mathbf{p}_i as the geometric center of \mathcal{A}'_i . One can say that doing so we perform the centroid path approximation, but applying it to every small \mathcal{A}'_i instead of to the entire \mathcal{A} .

Finally, we calculate RESP on the impact parameter grid as follows

$$\langle S_e(v) \rangle = \frac{1}{\mathcal{A}} \int d\mathbf{p} S_e^{traj}(v, \mathbf{p}) = \frac{\sum_{i=1}^{N_{grid}} S_e^{traj}(v, \mathbf{p}_i) w_i}{\sum_{i=1}^{N_{grid}} w_i}, \quad (3.5)$$

where w_i stands for a weight of an impact parameter point \mathbf{p}_i . This weight is proportional to the intersection between \mathcal{A} and \mathcal{A}_i : If \mathcal{A}_i is completely inside \mathcal{A} (which is the case of a large majority of the grid points), the weight is equal to 1. If \mathcal{A}_i is halfway inside \mathcal{A}

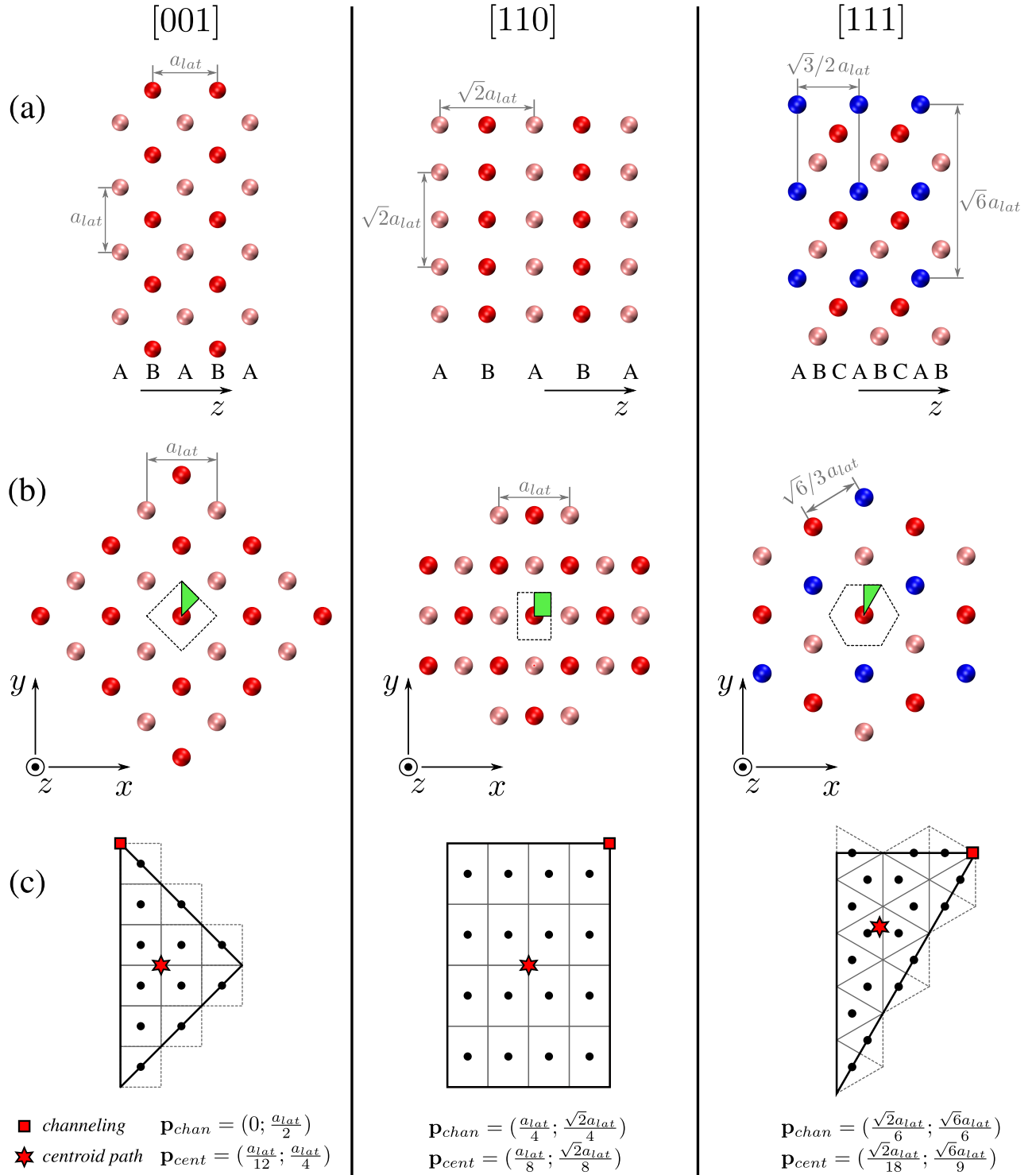


Figure 3.5 : (a) Profile and (b) front views of three lithium clusters used for the RESP calculations. For each crystal orientation we select z -axis along the projectile path. The elementary surfaces are presented in green and the Wigner-Seitz cells in 2D are depicted with black dashed lines in the panel (b). (c) Impact parameter grid for 3 orientations. Every impact point is enclosed in the subsurface \mathcal{A}_i , which can be entirely or partially included in \mathcal{A} . For the sake of clarity, the grids are presented for a small number of grid points N_{grid} . The positions of the channeling and centroid path impact points are indicated at the bottom of the figure.

(which is the case for \mathbf{p}_i on the borders for the orientations [001],[111], Fig. 3.5 (c)), then the weight is equal to 1/2, etc.

In order to perform a reliable comparison of the RESP values in different directions and to make valuable conclusions for the following calculations, we have used a large number of grid points. To make an equitable sampling, we have selected the number of grid points more or less proportional to the elementary surface area in a given direction: $N_{grid}^{[001]} = 72$, $N_{grid}^{[110]} = 88$, $N_{grid}^{[111]} = 45$ (one cannot choose any number of grid points because of the grid symmetry constraints). We have done the calculations for 5 projectile velocities. This amounts approximatively to 1000 calculations of $S_e^{traj}(v, \mathbf{p})$. We would like to emphasize that such an extensive study is possible due to the low computational cost of the calculations in the localized Gaussian basis set.

RESP in 3 crystalline directions

Fig. 3.6 presents a colormap of the stopping power $S_e^{traj}(v, \mathbf{p})$ calculated on the impact parameter grids for 3 crystalline orientations and the 3 most representative projectile velocities. Calculations were performed within the elementary surfaces and then replicated to larger surfaces thanks to the crystal symmetries. One can note the following features of the stopping power common to all the orientations:

- The stopping power becomes more polar-symmetric around the atoms when the projectile velocity increases.
- The stopping power is less homogeneous at larger velocities: The difference between the largest (around the atoms) and the lowest (far from atoms) stopping power is about 0.03 a.u. (≈ 0.015 keV/nm) for $v = 0.5$ a.u. and about 0.06 a.u. (≈ 0.03 keV/nm) for $v = 4.0$ a.u.. This is due to the core electron excitations. As we will see later, localized core electron excitations take place at high projectile velocities (higher than $v = 1.0$ a.u.), whereas delocalized valence electrons get excited at all the range of studied velocities. Therefore, at low v the stopping power is almost flat around the atoms whereas at high v one can see the peaks centered at the atomic positions.
- Different crystal orientations are more or less symmetric. Let us consider the [110] orientation. In this case, the distance between the projections of the atomic positions on the XY plane is different in x and y directions: the projections are closer in the x -direction than in the y -direction. Therefore, the variation of the stopping power along x -direction is considerably different from the one along y -direction. On the contrary, in the case of [111] orientation, the atomic projections are equidistant and, hence, the stopping power has the most symmetric behavior with respect to the polar angle among the 3 orientations.

Fig. 3.7 presents RESP as a function of the proton velocity for the 3 crystal orientations. One can see that despite the different behavior of $S_e^{traj}(v, \mathbf{p})$ in different crystalline

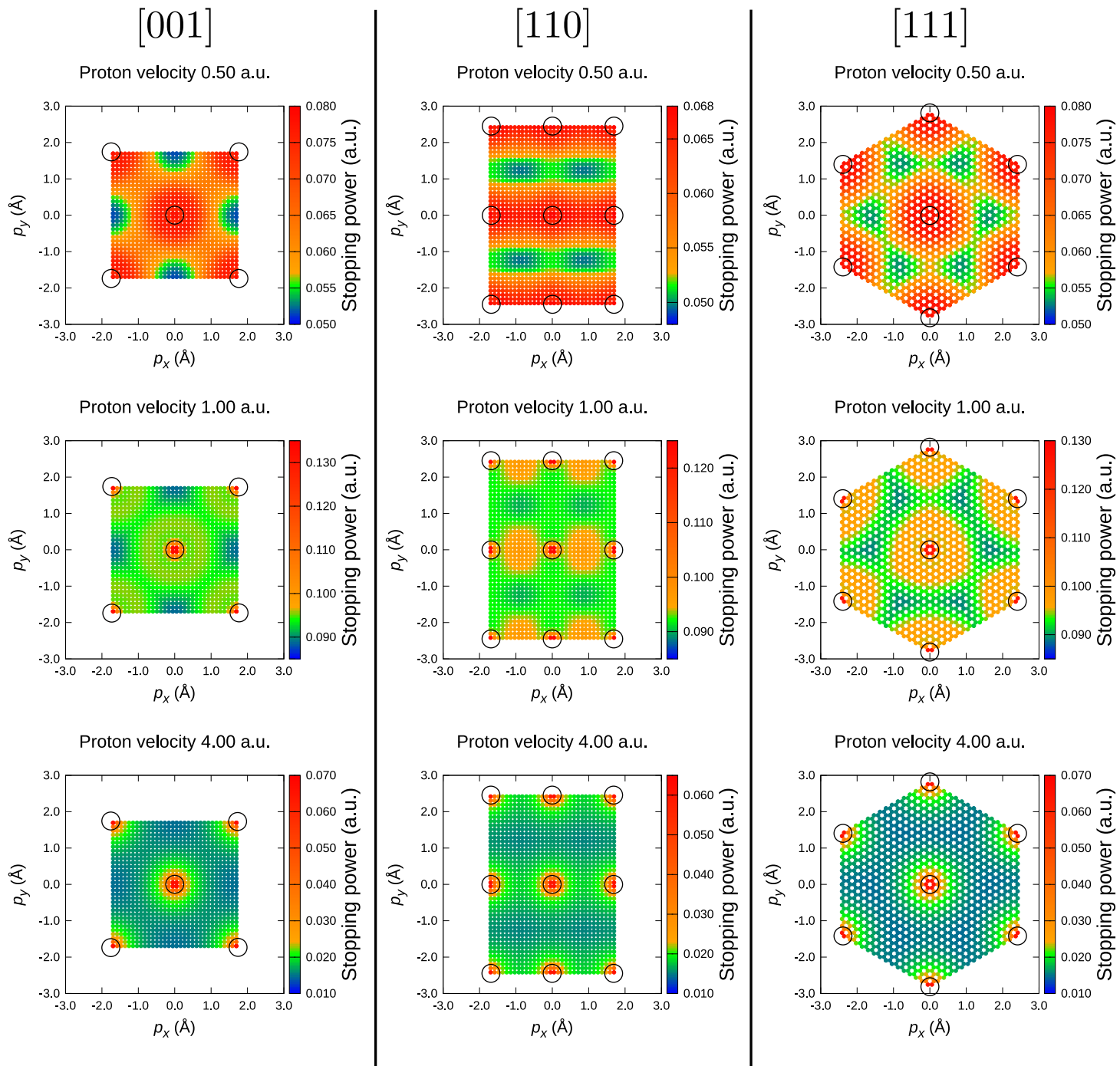


Figure 3.6 : $S_e^{traj}(v, \mathbf{p})$ for 3 Li crystal orientations and 3 velocities. Every colored point corresponds to a stopping power value. Black circles indicate the atomic positions. Calculations were performed using the cc-pVDZ Gaussian basis.

orientations, their *averaged* values are the same (except for minor discrepancies before the stopping power peak at $v = 0.5$ a.u. or $E_{proj}^{kin} = 6.2$ keV). Therefore, we select only one, [001], crystal orientation for the following studies of the *random* stopping power assuming that the average in this orientation represents the average in *any* other orientation and, therefore, it represents the random electronic stopping power for a polycrystalline material.

The necessary condition for such irrelevance with respect to the crystalline orientation is the cubic structure of the crystal. In anisotropic systems, like, for example, graphite, one does not have such property [34, 127].

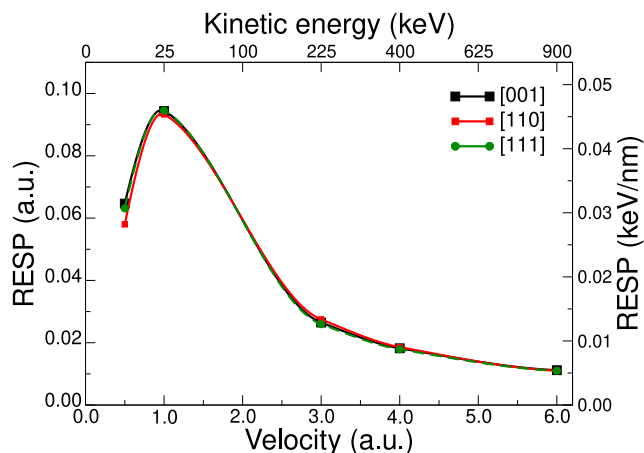


Figure 3.7 : Random electronic stopping power (RESP) of a proton in lithium as a function of the projectile velocity for 3 crystalline orientations. Calculations were performed using the cc-pVDZ Gaussian basis. The actual velocity points are marked with the squares. The lines are simple guides to the eye.

Correlation between stopping power and electronic density

In earlier models for the stopping power calculations [128, 129], it was assumed that the electronic stopping is directly related to the local electronic density of the target. Using our *ab initio* calculations we can check whether the electronic stopping power can be presented as a function of the ground state electronic density.

In order to identify a relation between the stopping power and the electronic density, we introduce a suitable quantity - normalized electronic density along the projectile path $\rho_{\perp}(\mathbf{p})$. For a given impact parameter $\mathbf{p} = (p_x, p_y)$, the value of $\rho_{\perp}(\mathbf{p})$ is calculated as follows

$$\rho_{\perp}(\mathbf{p}) = \frac{1}{L} \int dz \rho(p_x, p_y, z), \quad (3.6)$$

where L is the length of the projectile trajectory.

Fig. 3.8 presents the values of $\rho_{\perp}(\mathbf{p})$ for three crystalline orientations. This figure presents the total electronic density as well as the separate contributions from 1s and 2s

electrons. One can see that 1s electronic density is localized around the nuclei whereas 2s electrons are almost equally spread and also have a peak at the nuclei positions.

In order to evaluate the possible correlation between the stopping power and $\rho_{\perp}(\mathbf{p})$, we plot in Fig. 3.9 the stopping power as a function of the total electronic density along the path. To do so, we took the values of $S_e^{traj}(v, \mathbf{p})$ and $\rho_{\perp}(\mathbf{p})$ at the same grid points \mathbf{p}_i as previously described.

One can see that for any crystalline orientation (see Fig. 3.9 (a)) there is no correlation between the quantities for small densities: for one value of ρ_{\perp} one finds several values of S_e^{traj} corresponding to this ρ_{\perp} . In contrast, at large electronic densities, the stopping power is a normal single-valued function of the electronic density along the path. But this function is slightly different for different crystalline orientations.

Concerning the correlation at different projectile velocities (Fig. 3.9 (b)), one can mention that for all the projectile velocities except $v = 0.5$ a.u. the stopping power has a rapid growth when the electronic density approaches its maximal value. The absence of such behavior at $v = 0.5$ a.u. can be explained by the fact that large electronic densities along the path are associated mostly with 1s core electrons. The core electrons do not get excited at low velocities (this statement will be shown in detail later in section 3.2.2), therefore, the stopping power at $v = 0.5$ a.u. remains almost constant in the region where the core electron density has the largest variation.

The observed correlation behavior is more complicated than the one derived from the scattering theory in a non-uniform electron gas [128, 129], where the electronic stopping is a pure function of the electronic density at any projectile velocity.

Polar symmetry of the stopping power

In the following sections, we will consider the *random* stopping power calculations in the [001] crystal orientation, as we have shown, it can represent any direction.

As one can visually conclude from Fig. 3.6, the electronic stopping power has a polar symmetry, meaning that S_e^{traj} remains almost unchanged with respect to the polar angle α in the XY plane (we fix the origin at the central atom of the cluster). In order to present this fact in a more evident manner, we plot in Fig. 3.10 (a) and (b) the stopping power as a function of the absolute value of the impact parameter p . The polar angle α is encoded by the color of the points: blue points correspond to $\alpha = 0^\circ$ and red points to $\alpha = 45^\circ$, which is the direction along the y -axis. One can see that the stopping power becomes sensitive to the polar angle when one approaches the border of the elementary surface ($p \geq 1.0$ Å). This effect is more important at low velocities (see Fig. 3.10 (a) and (b)).

Taking into account the polar symmetry, one could save a lot of computational time: If only $S_e^{traj}(v, p)$ values (instead of $S_e^{traj}(v, \mathbf{p})$) are needed to calculate the random stopping, one can perform the stopping power calculations along only one direction in the XY plane and not on the grid. In order to quantify the error of the polar symmetry assumption, we keep the same grid as was used for previous RESP calculations (as in Fig. 3.7 for example) but for every grid point \mathbf{p}_i we assign the stopping power value corresponding to $p = |\mathbf{p}_i|$ and $\alpha = 45^\circ$ (see Fig. 3.10 (c)). Then we calculate the difference between RESP evaluated

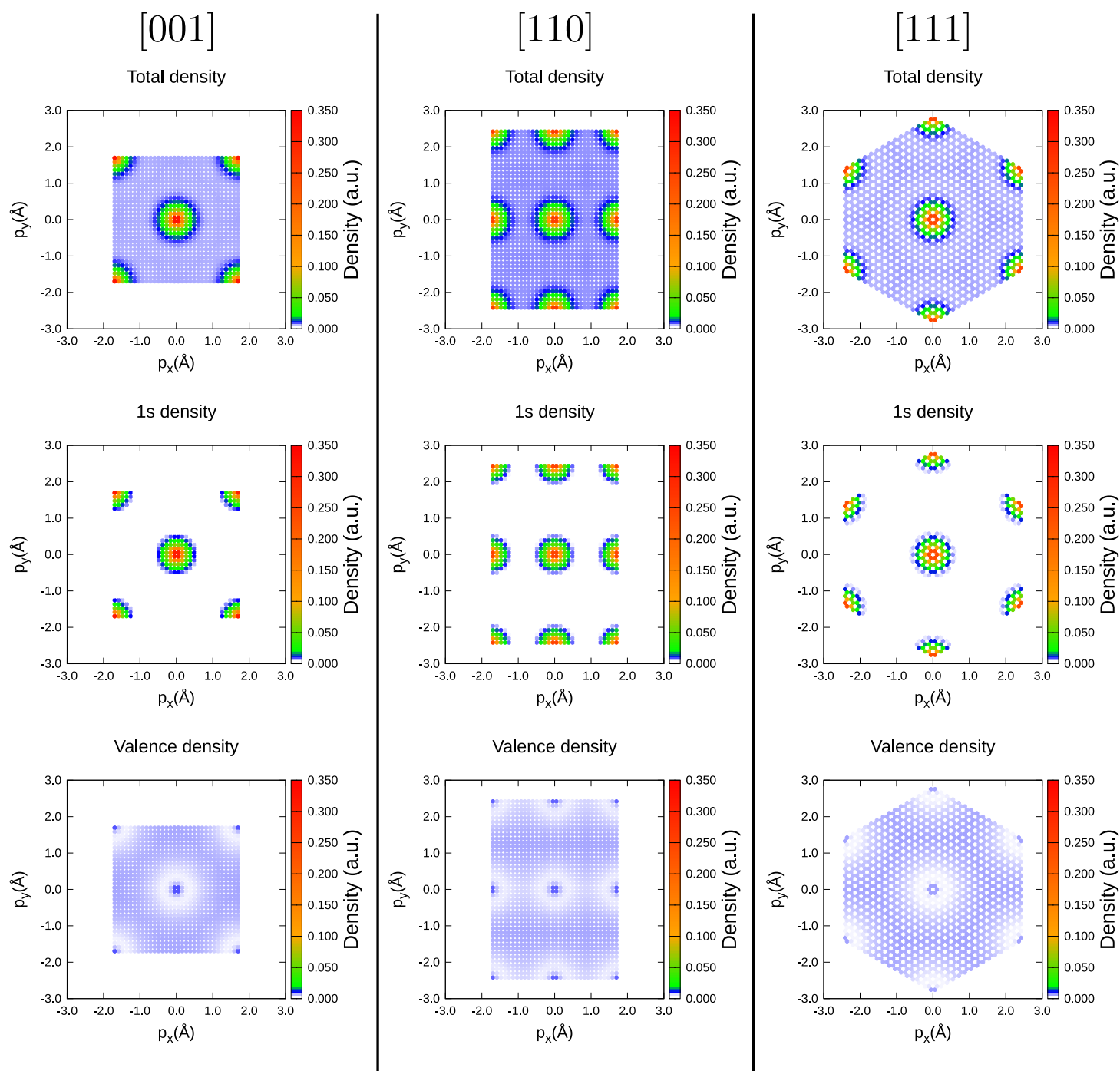


Figure 3.8 : Electronic density of lithium along the proton path for the 3 crystalline orientations. The first row of plots presents the total density. The second row - the localized $1s$ and the third - the valence densities.

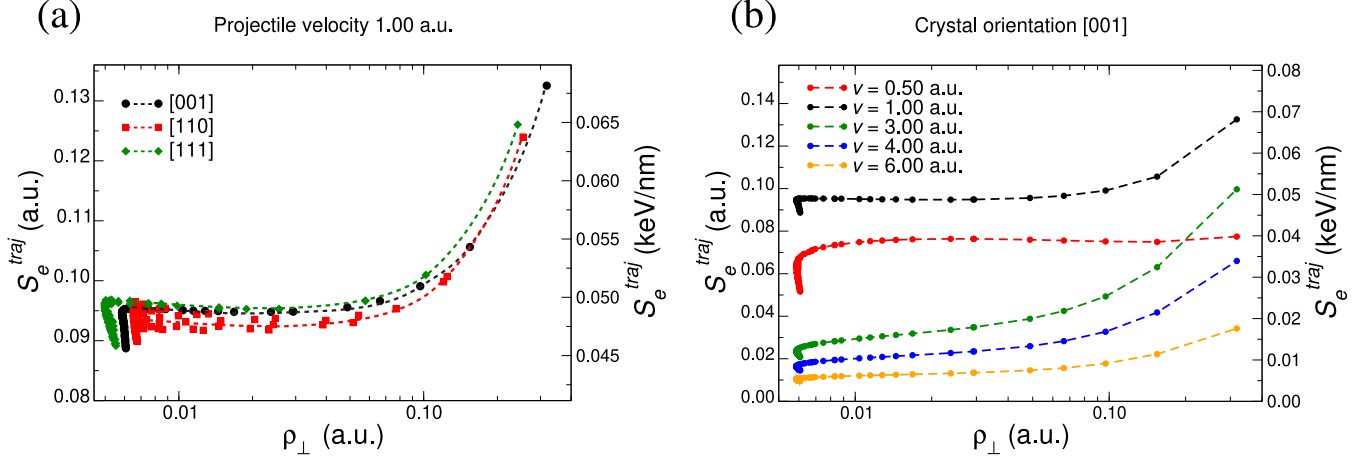


Figure 3.9 : Electronic stopping power as a function of the electronic density along the projectile path for: (a) the 3 crystalline orientations and one proton velocity $v = 1.0$ a.u.; (b) One crystalline orientation [001] and several projectile velocities.

in this way and RESP calculated on a real grid. This error (presented in Fig. 3.10 (d)) has the largest value at low v . The error is negative, it means that the stopping power along the direction $\alpha = 0^\circ$ is slightly larger than along $\alpha = 45^\circ$ (as one can see from Fig. 3.10 (a) and (b)). The absolute value of the error is lower than 2% which indicates that the polar symmetry approximation is good enough for the case of lithium. It is true though that lithium is a simple metal with non-directional bonds and that this statement is not completely unexpected.

Simplified RESP calculation scheme

For the whole rest of the work, we assume the polar symmetry of the stopping power and restrict the calculations of $S_e^{traj}(v, \mathbf{p})$ to the direction of y -axis $S_e^{traj}(v, p = (0, p_y))$. Therefore, in order to calculate the random stopping power, one can transform the 2D integration over \mathbf{p} to 1D integration over the absolute value p

$$\langle S_e(v) \rangle = \frac{1}{\mathcal{A}} \int d\mathbf{p} S_e^{traj}(v, \mathbf{p}) = \frac{1}{\mathcal{A}} \int_0^{a_{lat}/2} dp p \Delta\alpha(p) S_e^{traj}(v, p), \quad (3.7)$$

where $\Delta\alpha(p)$ is the angular range of the arc contained in the elementary tile at each distance p (Fig. 3.11 (a)). The integration is performed over the limits of the elementary surface along the y -axis (see Fig. 3.5). In this way, $p\Delta\alpha(p)$ is the weight of the stopping power $S_e^{traj}(v, p)$ that takes into account the crystal geometry. For the bcc [001] orientation, $\Delta\alpha(p)$ has the following expression

$$\Delta\alpha(p) = \begin{cases} \pi/4, & \text{if } 0 \leq p \leq \sqrt{2}a_{lat}/4 \\ 1/2 \arcsin(a_{lat}^2/4p^2 - 1), & \text{if } \sqrt{2}a_{lat}/4 < p \leq a_{lat}/2. \end{cases} \quad (3.8)$$

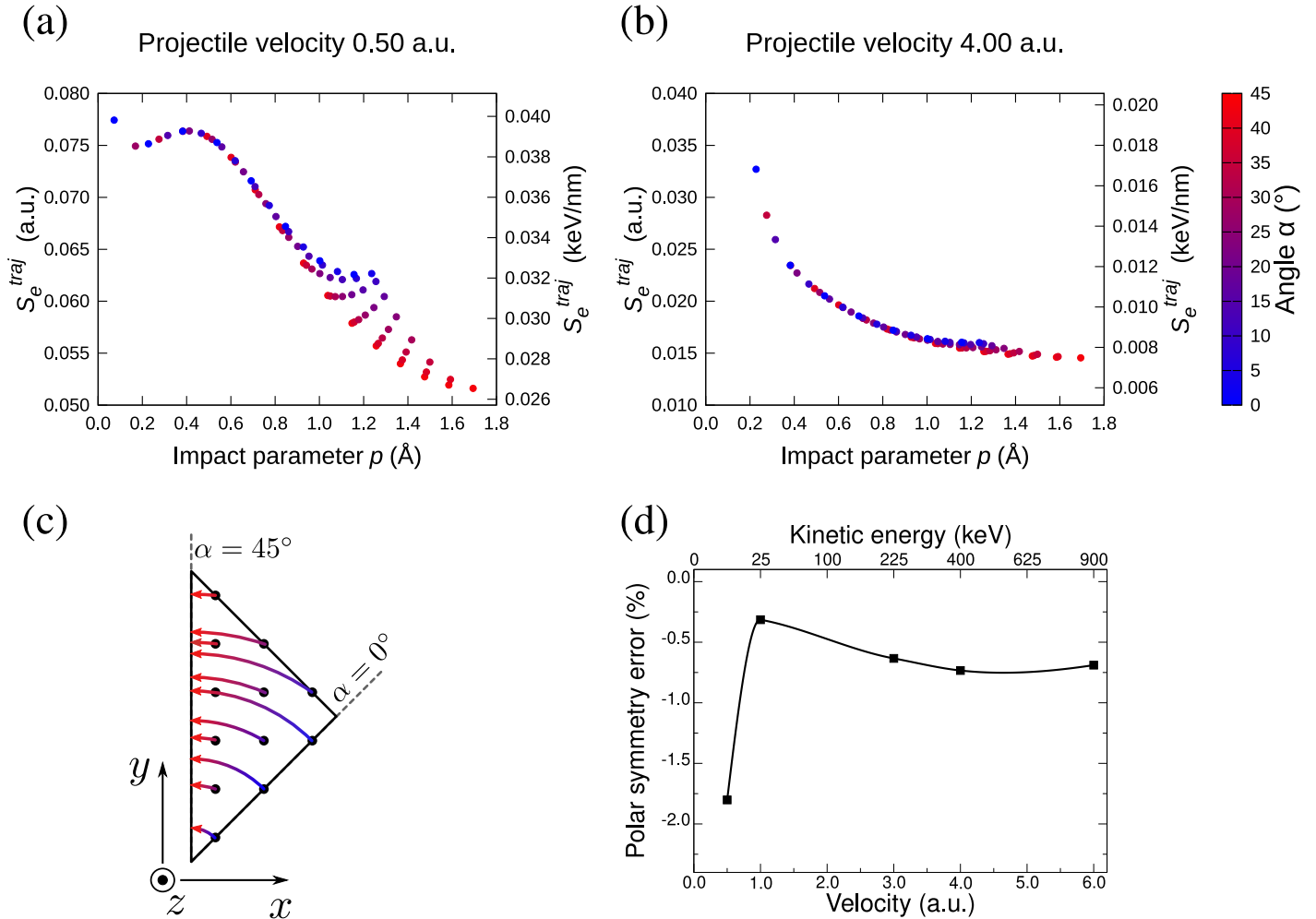


Figure 3.10 : (a) and (b) Electronic stopping power of lithium at proton velocity of 0.5 a.u. and 4.0 a.u. respectively as a function of the absolute value of the impact parameter p . The origin is placed on the central lithium atom. The coloring scheme encodes the polar angle. (c) Schematic illustration of the polar symmetry error evaluation. One assigns to each point of the grid the value of the stopping power corresponding to the same p , but along the y -direction. (d) Polar symmetry error as a function of the projectile velocity.

The factor $p\Delta\alpha(p)$ can be also interpreted as a probability to impinge the crystal (at [001] orientation) at the impact parameter p . For example, the probability for the projectile to impinge the surface of the target at precisely $p = 0.0$ as well as at $\mathbf{p} = (a_{lat}/2; 0)$ is zero (see Fig. 3.11 (b)). The impact point of the maximal probability is situated at $p = \sqrt{2}a_{lat}/4$.

For the case of lithium, we have found that 6 sampling points is sufficient to numerically perform the integral in equation 3.7. This scheme significantly reduces the number of calculations (from 72 points to only 6) needed to accurately evaluate the RESP values.

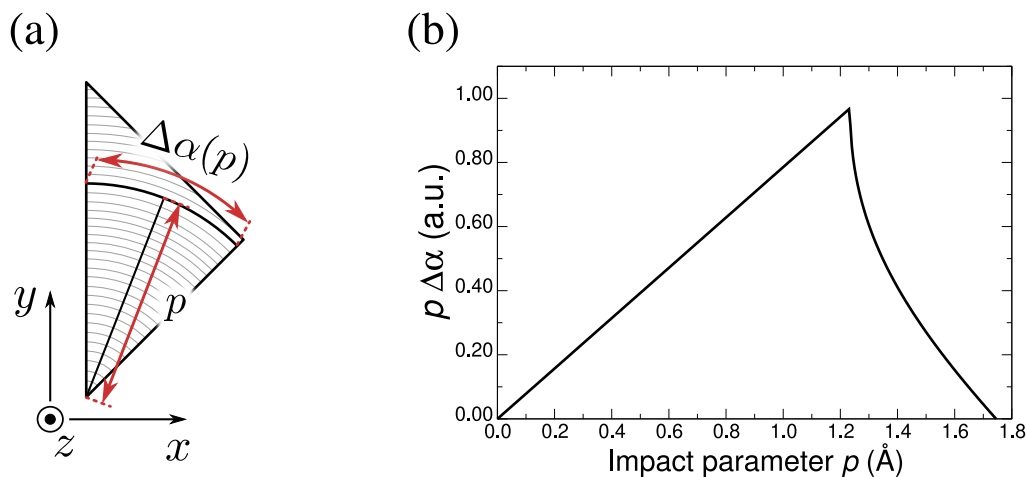


Figure 3.11 : (a) Illustration to the stopping power integration under the polar symmetry approximation. One assumes that the stopping power depends only on the module of the impact parameter p . Then, in the integration one needs to take into account the length of the arc $\Delta\alpha(p)$ as a function p ; (b) Weight function under the integral (equation 3.7).

3.2 Basis set influence on the stopping power

As was already mentioned in section 2.1, the particularity of the stopping power calculations is the strong effect of (almost) all-electron excitations due to the highly-energetic projectile. Therefore, a proper description of the unoccupied electronic states, provided by a localized basis set, is crucial for this problem.

We have considered in general terms the localized Gaussian basis sets in section 2.1.2. In this section, we will consider in detail the specifics of the basis sets as applied to the electronic stopping power calculations.

In general words, there are three different mechanisms (or “degrees of freedom”) that influence the Gaussian basis set of a given target:

- The cluster geometry. One of the advantages of the localized basis sets is their tunable accuracy as a function of space. Therefore, for a given system, one can identify “more important” atoms (when it is possible) and assign to them a larger number of basis functions than for the rest of the system. In this way, the electronic density (the ground state and the time-dependent) will be better described around the selected atoms.
- The order of the basis set X . As was discussed in section 2.1.2, increasing the order X of the standard Dunning basis sets $cc\text{-}pVXZ$, one increases the highest orbital momentum l and as well as the number of the basis functions for lower orbital momenta. It is expected that adding basis functions, one improves the description of the excited electronic states. Therefore, the X influence on the electronic stopping power will be studied here.

- The standard Dunning bases **cc-pVXZ** can be improved by inclusion of the tight-core **cc-pCVXZ** or diffuse **aug-cc-pVXZ** functions (or, even, both at the same time). However, the computational time, of course, will be also larger. Hence, the justification for such possible improvements should be carefully studied.

To make an analogy with the plane-wave codes, these parameters would correspond to tuning of the plane-wave cutoff and to choosing the number of electrons hidden in the pseudopotential [35, 88].

In this section, first, using the example of proton in lithium irradiation, we will introduce our technique of the position-dependent basis that allows us to save the computational time while keeping high accuracy. Then we will switch to the proton in aluminum system in order to study the basis set convergence problem. And finally we will describe a proposed scheme for the basis set generation specifically for the stopping power calculations.

3.2.1 Mixed basis technique

First, we would like to illustrate the importance of the unoccupied states description. Fig. 3.12 (a) presents the random electronic stopping power (RESP) for the following basis sets: **cc-pVDZ** (black curve, 14 basis functions per Li atom) and **cc-pVQZ** (red curve, 55 functions per Li). It is seen that for the projectile velocities $v < 0.7$ a.u. ($E_{proj}^{kin} < 12.2$ keV) both bases give almost the same result. However, for larger projectile velocities, the **cc-pVDZ** basis underestimates much the electronic stopping in comparison to the larger basis **cc-pVQZ**: The **cc-pVDZ** basis does not provide a proper description of the target electron excitations.

We found that the quality of the electronic states description is especially important for the atoms that are close to the projectile track. With Gaussian basis sets, it is possible to tune the quality of the basis set on each atom of the target individually. Therefore, we can assign more precise basis functions to the atoms that are closer to the projectile trajectory. Fig. 3.12 (b) demonstrates this idea: A larger basis set **cc-pVQZ** is assigned to the closest atoms to the projectile trajectory, depicted in red. Then, a less complete basis **cc-pVTZ** is assigned to the atoms that are more distant from the track, painted cyan. All the remaining atoms (presented in gray color) are described with the **cc-pVDZ** basis set quality. Such a basis set configuration allows one to produce almost the same results (green curve in Fig. 3.12 (a)) as for the system where *all* the target atoms are described in the **cc-pVQZ** basis set (red curve in 3.12 (a)). The tunable basis allows for a drastic reduction of the number of basis functions: In this example there are 3410 basis functions for the whole cluster described within the **cc-pVQZ** basis, whereas there is only 1570 of them with the mixed basis.

Therefore, for further basis set studies we will consider only the central region of the cluster (depicted in red): For every calculation we will keep the atoms in the “cyan region” described in the **cc-pVTZ** basis and in the “gray region” with **cc-pVDZ** basis, while changing the basis set of the central, “red”, region. The statement that such configuration is equivalent to a system where all atoms are described with the highest quality basis was verified

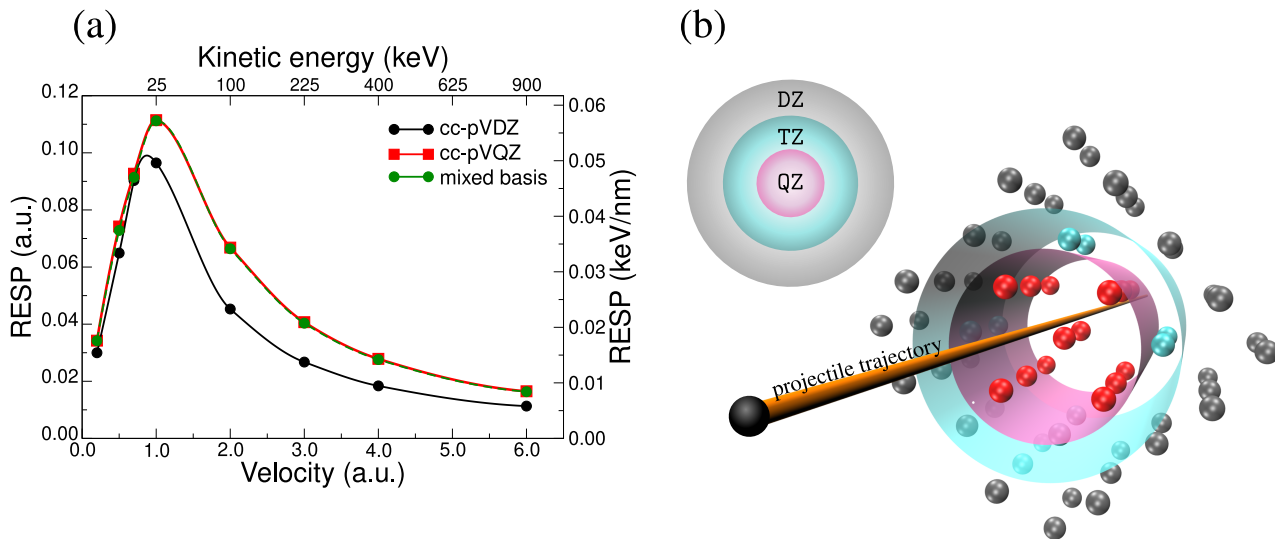


Figure 3.12 : (a) Random electronic stopping power of proton in lithium as a function of the proton velocity obtained with different basis sets. (b) The lithium cluster represented with a coloring scheme that encodes the basis quality on each atom for the mixed basis technique. Red atoms are described with cc-pVQZ (abbreviated as QZ in the figure) basis, cyan atoms with cc-pVTZ (TZ) and gray atoms with cc-pVDZ (DZ).

for different kinds of basis sets (including diffuse aug-cc-pVXZ).

One should mention that the mixed basis technique is well adapted for the ensemble average random stopping calculation since the projectile trajectories are known in advance and they have the impact parameters within the elementary surface which is small compared to the cluster size.

3.2.2 Dunning basis series comparison

As we have seen in Fig. 3.12 (a), increasing the basis set order X in the set cc-pVXZ improves the description of the electronic states and hence provides larger stopping power values, especially for high projectile velocities. In this section, we would like to compare different families of the Dunning basis sets for a fixed value of X . We would like to examine the standard correlation-consistent sets cc-pVXZ as compared with the diffuse aug-cc-pVXZ and the tight core cc-pCVXZ basis sets. The highest value of X for which all these bases exist for lithium is $X=Q$ (quadruple). The corresponding bases have the following number of basis functions per one Li atom: 55 for cc-pVQZ, 80 for aug-cc-pVQZ and 84 for cc-pCVQZ.

As the first criterion of the comparison, we can analyze the spatial extent and spatial density of the basis functions for each of the sets. As was explained in section 2.1.2, the square root of the inverse of a Gaussian exponent $1/\sqrt{\alpha_b}$ provides an approximate distance $|\mathbf{r} - \mathbf{R}_a|$ at which the corresponding Gaussian function $e^{-\alpha_b(\mathbf{r} - \mathbf{R}_a)^2}$ describes the electronic wave function around a target nucleus a . Fig. 3.13 presents these effective distances for

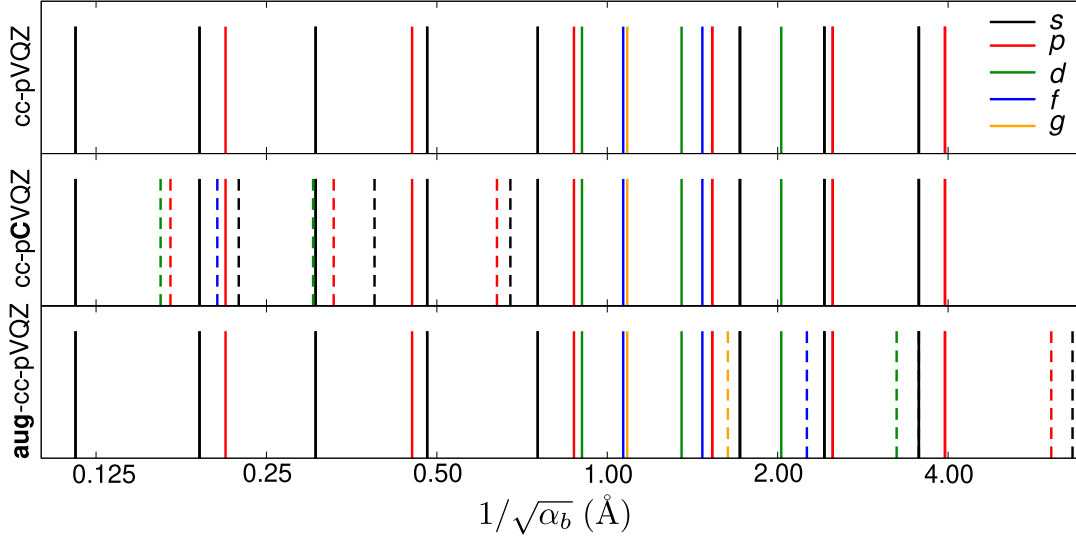


Figure 3.13 : Length scale of Gaussian basis functions for three basis sets of the basis order $X=Q$ for lithium. The color encodes the orbital momentum l of the basis functions. Four s basis functions with the effective distances lower than 0.1 \AA which are included in all considered basis sets are not presented.

each basis set. It is seen that **cc-pCVQZ** has more basis functions in comparison to **cc-pVQZ** in the region close to nuclei ($0.15 \text{ \AA} < |\mathbf{r} - \mathbf{R}_a| < 0.7 \text{ \AA}$). Whereas the basis set **aug-cc-pVQZ** describes better a region farther from the nuclei ($1.5 \text{ \AA} < |\mathbf{r} - \mathbf{R}_a| < 7.0 \text{ \AA}$). The basis set which includes both core and diffuse states, **aug-cc-pCVQZ** (109 basis functions per Li, not presented), incorporates all the functions shown in Fig. 3.13.

After having analyzed the spatial extension of the basis functions, we can compare them based on the electronic stopping power calculations. Fig. 3.14 (a) shows the random electronic stopping power of proton in lithium calculated with the three studied bases. The behavior of the basis functions is somewhat similar to the **cc-pVDZ/cc-pVQZ** comparison (Fig. 3.12 (a)): For small velocities all the three basis sets produce almost the same results, while for $v > 1.0 \text{ a.u.}$ ($E_{proj}^{kin} > 25 \text{ keV}$) the **cc-pCVQZ** basis set gives considerably larger stopping power values.

One can explain this effect by looking at the impact parameter dependence of the weighted stopping power $p\Delta\alpha S_e^{traj}(p)$ for different velocities (Fig. 3.14 (b) and (c)). We have taken two projectile velocities at which the stopping power impact parameter dependence is clearly different: $v = 0.5 \text{ a.u.}$ ($E_{proj}^{kin} \approx 6.2 \text{ keV}$) and $v = 4.0 \text{ a.u.}$ ($E_{proj}^{kin} \approx 400 \text{ keV}$). In the low-velocity case (Fig. 3.14 (b)), one can see that, as compared to the standard **cc-pVQZ** basis set, the weighted stopping power $p\Delta\alpha S_e^{traj}$ is slightly larger for the larger impact parameters p ($p > 0.6 \text{ \AA}$) for the diffuse **aug-cc-pVQZ** basis set. The tight core basis set provides slightly larger stopping power values for smaller p ($p < 0.6 \text{ \AA}$). This

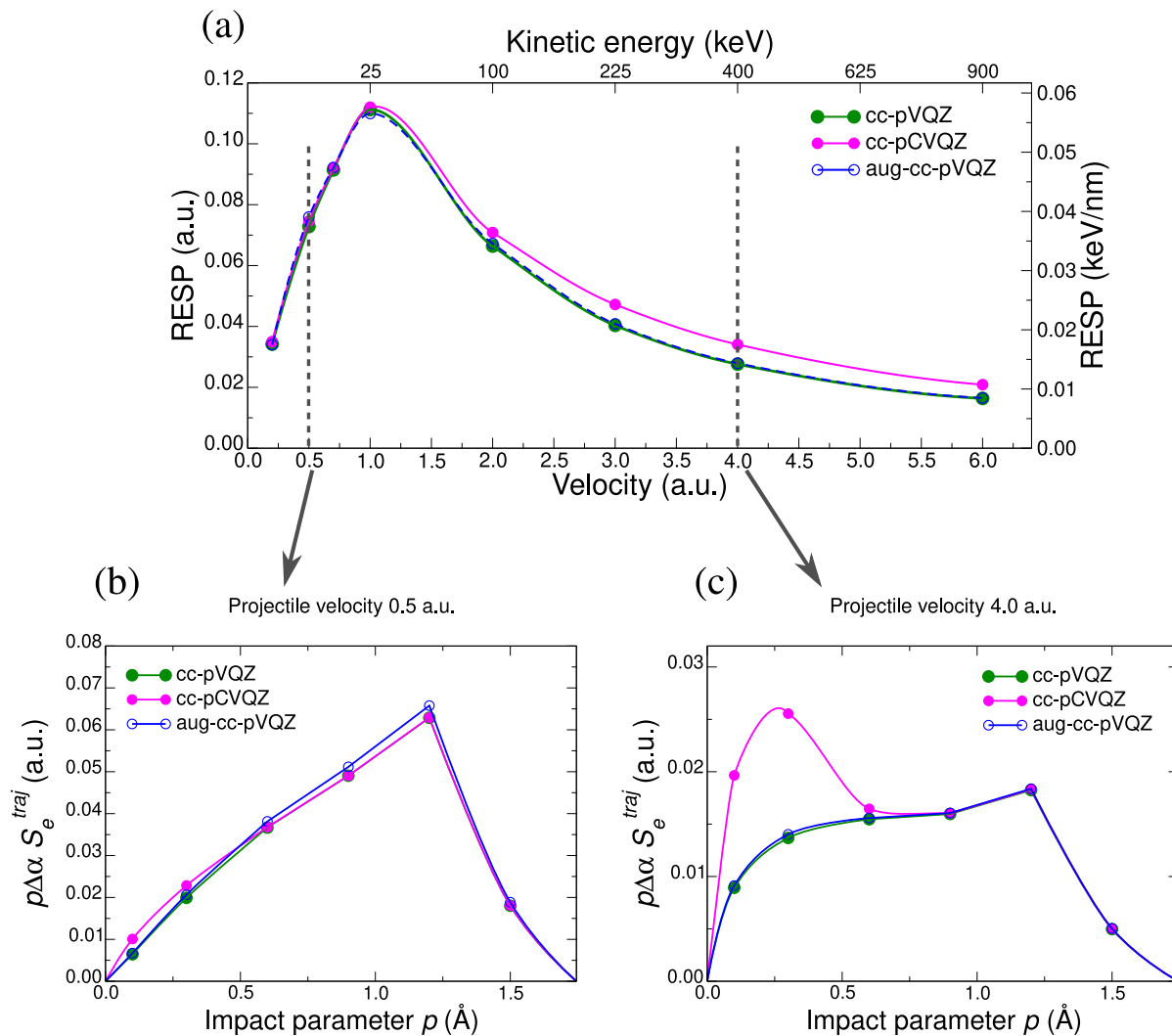


Figure 3.14 : (a) Random electronic stopping power as a function of the projectile velocity of proton in lithium for three Gaussian basis sets: standard cc-pVQZ, tight core cc-pCVQZ, and diffuse aug-cc-pVQZ; (b), (c) Weighted stopping power as a function of impact parameter for projectile velocities $v = 0.5$ a.u. ($E_{proj}^{kin.} \approx 6.2$ keV) and $v = 4.0$ a.u. ($E_{proj}^{kin.} \approx 400$ keV) respectively for the same three bases.

effect is due to different spatial extensions of the bases (see Fig. 3.13).

However, for the high velocity (Fig. 3.14 (c)), the difference between the bases becomes crucial: One can note a large peak at small p for the **cc-pCVQZ** basis, that is absent for the two other bases. For larger impact parameters, the difference between the bases at high velocities is minor. These results are resumed in Table 3.1 that presents the stopping power difference for these two distinct velocity regimes. One obtains the same qualitative results for other basis order X values. Therefore, we generalize our conclusions to the corresponding basis set families (standard, diffuse and tight core).

	$(\langle S_e \rangle^{\text{CQZ}} - \langle S_e \rangle^{\text{QZ}}) / \langle S_e \rangle^{\text{QZ}}$	$(\langle S_e \rangle^{\text{aug-QZ}} - \langle S_e \rangle^{\text{QZ}}) / \langle S_e \rangle^{\text{QZ}}$
$v = 0.5$ a.u.	2.4 %	4.2 %
$v = 4.0$ a.u.	23.4 %	0.9 %

Table 3.1 : Difference of the random electronic stopping power for two projectile velocities. **cc-pVQZ** basis (abbreviated as **QZ**) is taken as a reference. The first column presents the difference for the **cc-pCVQZ** (**CQZ**) basis and the second for the **aug-cc-pVQZ** (**aug-QZ**) basis set.

In conclusion, based on the stopping power calculations of proton in lithium, we consider that the tight core basis set family **cc-pCVXZ** is necessary because of the proper description of core electron excitations. The diffuse basis sets **aug-cc-pVXZ** bring the corrections to the random stopping power at low velocities. However, since these corrections are minor, we assume that taking into account the diffuse functions is needless in the case of lithium target. In the next section, we will see the difference in conclusions in the case of aluminum.

Correlation of weighted stopping power with the core electron density

Having identified the importance of the description of the core electron excitations that can be provided by including the tight core basis functions, we can re-examine the question of the stopping power correlation with the electronic density discussed in section 3.1.3. Since for the random stopping power calculation within the polar symmetry approximation (equation 3.7), the stopping power S_e^{traj} is integrated together with the weight function $p\Delta\alpha$, let us consider now the complete function under the integral for different velocities and compare it with the electronic density weighted in the same way (Fig. 3.15).

At low velocity (Fig. 3.15 (a)), the variation of the stopping power as a function of the impact parameter is rather limited and the shape of $p\Delta\alpha(p)S_e^{\text{traj}}$ is mostly dictated by the integration weight $p\Delta\alpha(p)$ (compare Fig. 3.11 (b) and Fig. 3.15 (a)). Since the valence electron density $\rho_{\perp}^{\text{val}}$ is almost flat with respect to p , the quantity $p\Delta\alpha(p)\rho_{\perp}^{\text{val}}$ also repeats the form of the weight function.

At large velocity (Fig. 3.15 (b)) the stopping power is strongly dependent on p and $p\Delta\alpha(p)S_e^{\text{traj}}$ is much flatter. Interestingly, the position of a peak in the weighted stopping power coincides with the position of the peak of the Li 1s electrons. This fact demonstrates that the core electrons participate much when the proton kinetic energy is large.

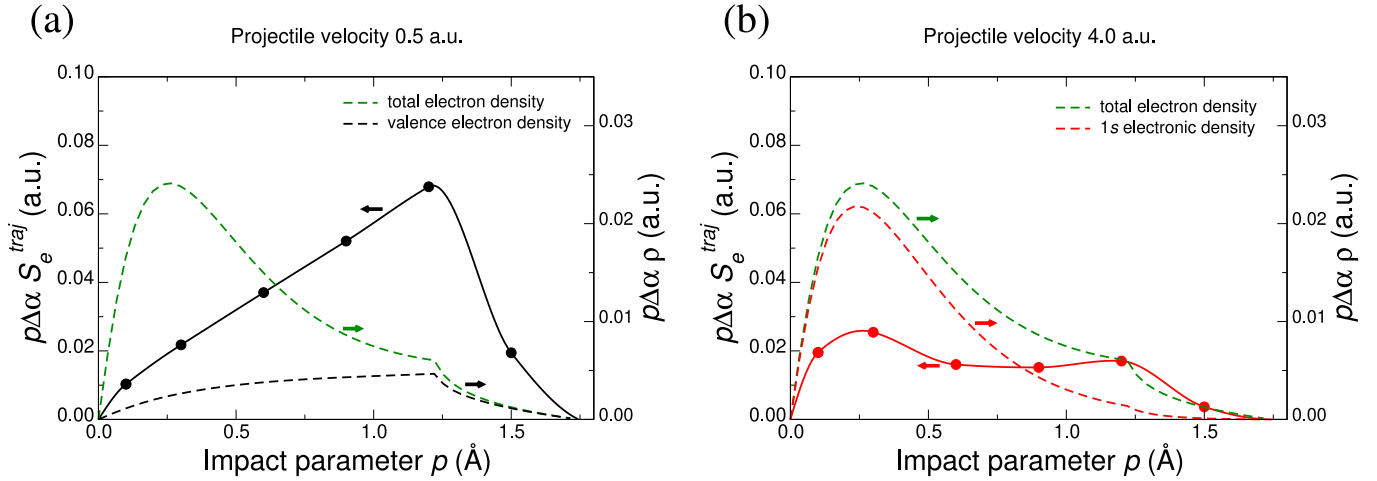


Figure 3.15 : (a) Weighted stopping power (solid black line), total weighted electron density (dashed green line) and weighted *valence* electron density (dashed line) as a function of the impact parameter p at the projectile velocity $v = 0.5$ a.u.. (b) Weighted stopping power (solid red line), total weighted electron density (dashed green line) and weighted *core* 1s electron density (dashed line) as a function of the impact parameter p at the projectile velocity $v = 4.0$ a.u..

3.3 Basis set convergence in aluminum

In this section, we will study in detail the electronic stopping power convergence with respect to the Gaussian basis set. For this problem, we have chosen the aluminum fcc [001] target because in this case, the convergence is more complicated than in the case of lithium. At first, we will examine the core electron excitations contribution to the convergence behavior. Then, we will re-examine the comparison of two larger basis families - tight core and diffuse basis sets. Finally, we will describe the stopping power extrapolation with respect to the basis set in order to obtain converged values.

Proton in aluminum irradiation: simulation setup

Switching from a simpler case of lithium to aluminum target did not affect significantly the numerical scheme of the stopping power calculations described in section 3.1. Here we briefly summarize the most important characteristics of the random electronic stopping power calculations in aluminum:

- The cluster size convergence has a similar behavior compared to the Li case. 8 Å-long and 9 Å-wide 54-atom cluster is retained for the calculations: It has 5 layers in z -direction, similarly to Li, of *ABABA* configuration.
- For aluminum, we also find the polar symmetry of the stopping power which allows us to switch from a surface average to a weighted average along one line.

- The geometry of the fcc [001] target is different from the case of lithium (bcc), however, the weight function for the $S_e^{traj}(p)$ integration derived for the lithium case is very similar: actually one just needs to substitute a_{lat} with $a_{lat}/\sqrt{2}$ in equation 3.8.
- The mixed basis technique is also successfully tested for Al and we will keep the same position-dependent basis configuration as for Li. In all further basis set convergence tests, the atomic basis for second and third layers (cyan and grey atoms in Fig. 3.12) will be always set to cc-pVTZ and cc-pVDZ respectively.
- The dependence of $S_e^{traj}(p)$ on the impact parameter p is more variable in Al than in Li, therefore, we perform calculations with a finer impact parameter grid: $\Delta p = 0.1 \text{ \AA}$, which amounts to 13 impact point calculations per velocity.
- In Al target we treat all the 13 electrons explicitly. The $1s2s2p$ electronic states, considered as core states, are much deeper in energy compared to the $1s$ core electrons of lithium. Therefore, the excitation dynamics of Al core electrons is faster than in the case of Li. In order to properly capture the core electrons excitation dynamics, we decrease the spatial step to $\Delta z = 0.04 \text{ \AA}$ for the impact parameters $p \leq 0.6 \text{ \AA}$. Such impact parameters correspond to the case when the projectile impinges the regions of core electrons. For impact parameters $p > 0.6 \text{ \AA}$ we keep the spatial step $\Delta z = 0.1 \text{ \AA}$ as in the case of Li target.
- For the same basis (for example, within cc-pCVQZ for both targets), the computational time for aluminum is approximatively two times larger than for lithium because of the larger number of basis functions (84 function for Li and 109 functions for Al in cc-pCVQZ basis set) and the larger number of electrons (3 for Li and 13 for Al).

3.3.1 Convergence of cc-pCVXZ basis sets: comparison with the frozen core dynamics

As was concluded for the Li target, the tight core cc-pCVXZ basis sets are necessary for the stopping power calculations. Therefore, we have started the convergence tests with this basis set family.

Fig. 3.16 (solid lines) shows the random stopping power as a function of projectile velocity for cc-pCVXZ basis sets. One can note that the stopping power has a convergent behavior for all velocities. Though, the convergence is not completely reached for any of projectile velocities: The difference between the most precise basis set cc-pCV6Z and the previous one cc-pCV5Z is about 6 %. In addition, the convergence is quite slow, especially for the larger basis sets (X=Q,5,6): For example, the difference between the previous pair of bases, cc-pVC5Z, and cc-pVCQZ, is about 7 %.

In order to get a better understanding of the nature of the convergence problem, we have performed the same series of calculations with the frozen core electron dynamics: We prohibit the electronic excitations from the localized $1s$, $2s$ and $2p$ electronic states of

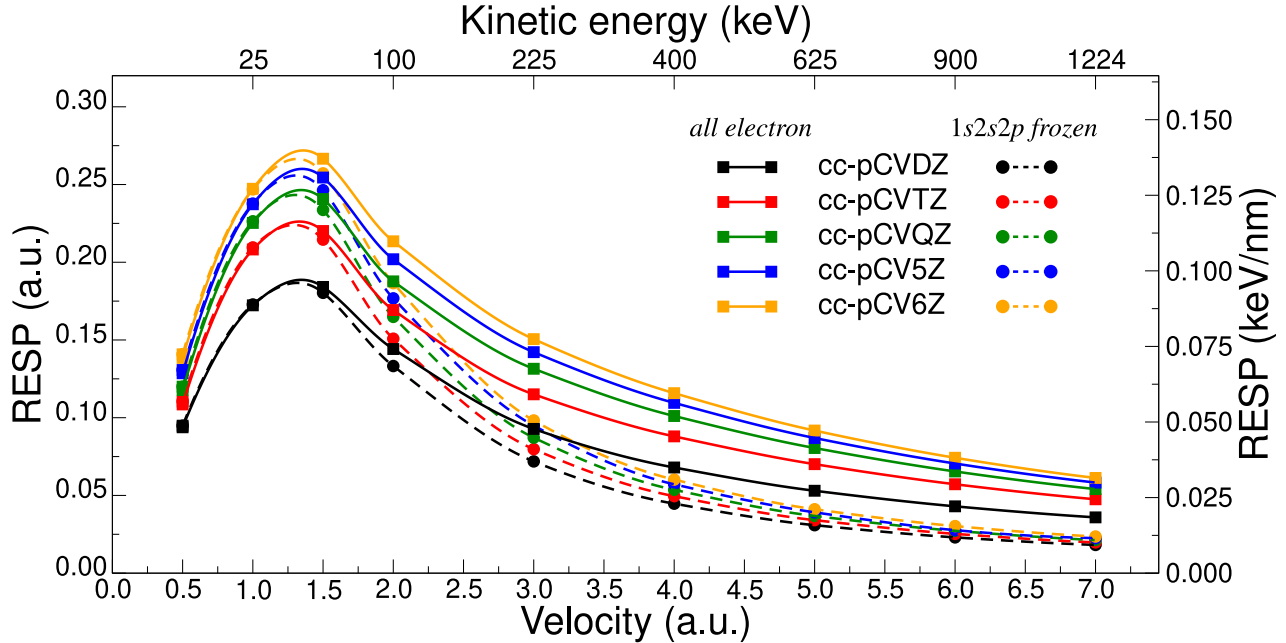


Figure 3.16 : Random electronic stopping power for proton in aluminum as a function of proton velocity within the cc-pCVXZ ($X=D, T, \dots, 6$) basis sets. The calculations are performed in all-electron (solid lines) and frozen core (dashed lines) dynamics.

aluminum target. The implementation of the frozen core dynamics in MOLGW code was described in section 2.2.7. It is seen that for high projectile velocities ($v > 3.0$ a.u. or $E_{proj}^{kin} > 225$ keV) in the case of frozen core states (Fig. 3.16, dashed lines), the stopping power has lower but converging values. While at lower velocities, especially at $v < 1.0$ a.u. ($E_{proj}^{kin} < 25$ keV), the stopping power with the frozen core is the same as in the case of the all-electron dynamics. These results lead to the following conclusion: The random stopping power convergence problem at high projectile velocities is due to the core electrons, whereas at low velocities it is due to the valence electrons.

As we have seen in the lithium case (Fig. 3.14), the addition of the diffuse functions to the basis set somewhat influences the stopping power at low projectile velocities. Even though, this effect was limited in the case of Li target, since Al contains more valence electrons, let us re-examine this effect.

3.3.2 Most complete aug-cc-pCVXZ basis set family

The tight core basis functions are necessary for the full convergence problem investigation (including all the range of studied projectile velocities). Therefore, in order to study the influence of diffuse functions on the stopping power, we do not consider the diffuse-only basis sets, i.e. aug-cc-pVXZ, but rather the most complete aug-cc-pCVXZ basis set family that includes both diffuse and localized basis functions.

Fig. 3.17 (a) shows the comparison between cc-pCVXZ and aug-cc-pCVXZ for the

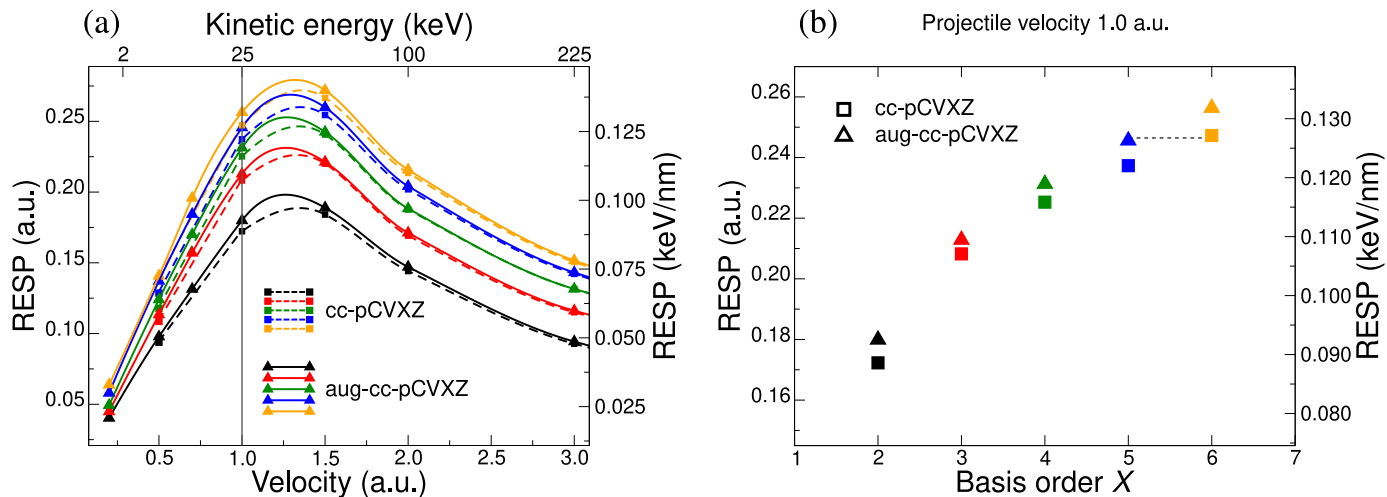


Figure 3.17 : (a) Random electronic stopping power of proton in aluminum as a function of projectile velocity for the tight core basis sets *cc-pCVXZ* (dashed lines) and the complete diffuse and tight core *aug-cc-pCVXZ* (solid lines). The basis order X varies for both sets from $X=D$ to $X=6$. (b) Random electronic stopping power for the same system and the same basis sets as a function of the basis order X for the proton velocity $v = 1.0$ a.u. ($E_{proj}^{kin} = 25$ keV). The colors of the symbols correspond to the basis set order and are consistent with (a) panel. The stopping power obtained with *aug-cc-pCV5Z* (blue triangle) is almost the same as the value obtained with *cc-pCV6Z* (yellow square).

projectile velocities ranging from 0.2 a.u. to 3.0 a.u. It is seen that the *aug-cc-pCVXZ* basis sets yield larger values of the stopping power for low velocities. In particular, at the projectile velocity $v = 1.0$ a.u. ($E_{proj}^{kin} = 25$ keV), the stopping power value within the *aug-cc-pV5Z* almost reaches the value obtained with the *cc-pCV6Z* basis set (see Fig. 3.17 (b)). Then, at $v > 3.0$ a.u. ($E_{proj}^{kin} > 225$ keV), the stopping power values obtained with both basis sets become similar. Hence, adding the diffuse basis set functions improves the convergence of the stopping power of proton in aluminum at the projectile velocities $v < 3.0$ a.u. The effect of adding the diffuse functions is more important in the case of aluminum target than of lithium one.

Finally, one could have a good description of the electronic excitations with the diffuse-only basis functions *aug-cc-pVXZ* at low velocities and tight core-only basis *cc-pCVXZ* at high velocities. However, in order to obtain a complete curve of the random stopping power including the transient regime, which incorporates both types of valence and core electron excitations, in the next section, we use the most complete basis set family, i.e. *aug-cc-pCVXZ*.

3.3.3 Stopping power extrapolation

Having determined the final basis set for the convergence calculations, we will study an extrapolation procedure of the stopping power as a function of the basis order X that would

allow us to find the asymptotic values.

We have tested two methods for the stopping power extrapolation:

- 1) Extrapolate the weighted stopping $p\Delta\alpha S_e^{traj}(p)$ for each impact parameter p separately (Fig. 3.18 (a)) and then integrate the extrapolated curve to obtain the random stopping power.
- 2) Extrapolate already integrated random stopping power $\langle S_e \rangle$ as a function of X (Fig. 3.18 (b)).

For both methods we have selected the extrapolation formula of the following form:

$$\langle S_e(\mathbf{X}) \rangle = A_0 - A_1 \exp \left\{ - A_2 \cdot \mathbf{X} \right\}, \quad (3.9)$$

where A_0 , A_1 , and A_2 are the fitting coefficients. We have tried to use different forms of the extrapolation curves (various polynomial and exponential-like functions). With the presented one (equation 3.9), we could achieve a good fitting quality of the stopping power for all ranges of impact parameters and velocities used in this work. A similar function was used by Yao and coworkers for the extrapolation of the stopping power as a function of the plane-wave cutoff in order to describe the K-shell excitations of water [130].

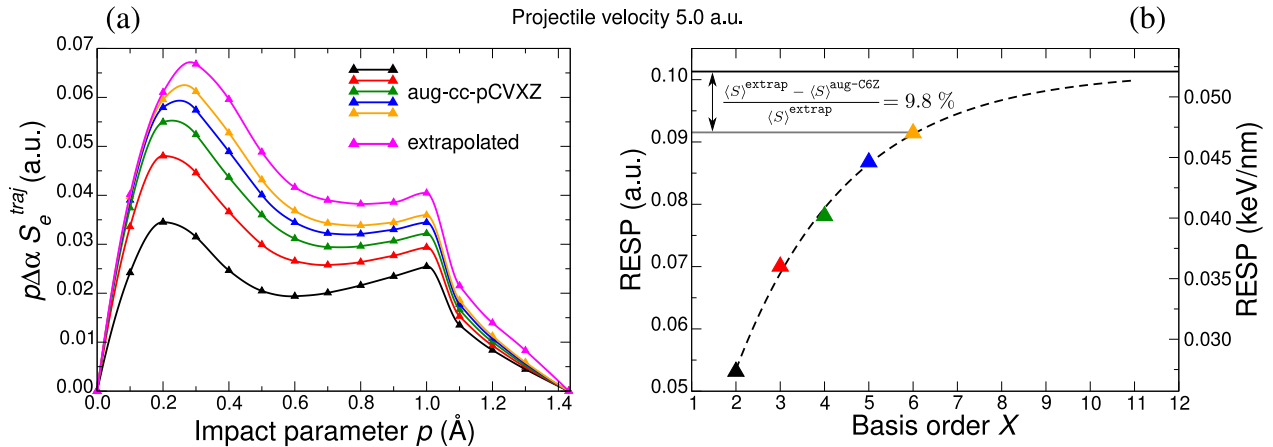


Figure 3.18 : Illustration of two possible methods for the stopping power extrapolation as a function of the basis order X for the projectile velocity $v = 5.0$ a.u. ($E_{proj}^{kin} \approx 625$ keV). (a) Extrapolation of weighted stopping power: each point on the extrapolated curve (pink line) is obtained as a separate extrapolation procedure. Then, to obtain the asymptotic value of the random stopping power, one needs to integrate the extrapolated curve. (b) Direct extrapolation of the random stopping power. The extrapolate value ($\langle S_e \rangle^{\text{extrap}} = 0.101$ a.u. = 0.052 keV/nm) is reported with the horizontal black line. The relative deviation of the asymptotic value with respect to the value obtained with the largest basis `aug-cc-pCV6Z` is also presented on the figure.

In order to select the method of the extrapolation we have used the following criteria: We extrapolate the stopping power with two methods using not complete data, namely, $X=D, T, Q, 5$ (without $X=6$). Then we compare the obtained values with ones obtain with

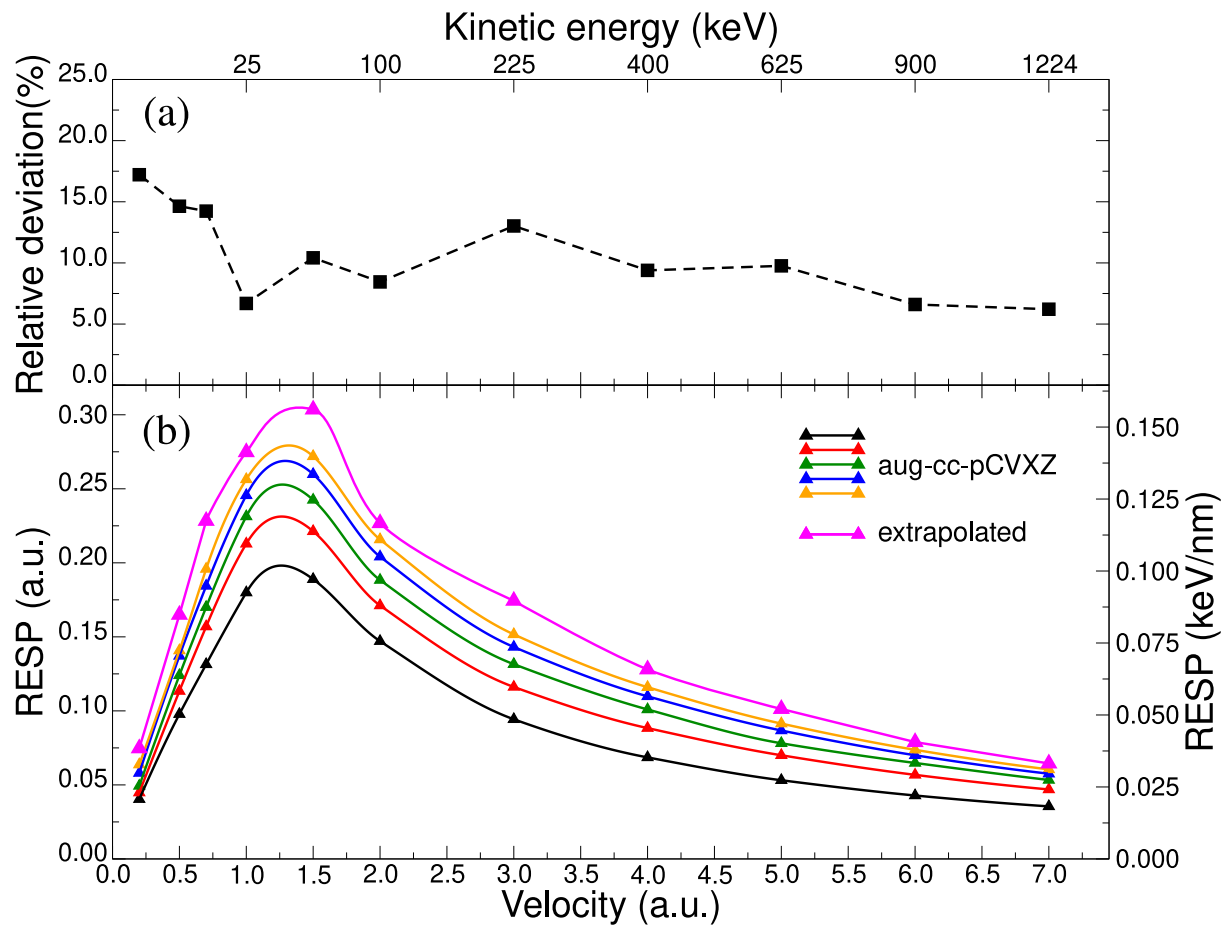


Figure 3.19 : Extrapolation of the random electronic stopping power using the direct $\langle S_e \rangle$ extrapolation method: (a) The standard deviation of the asymptotic values with respect to the values obtained with the largest basis aug-cc-pCV6Z; (b) Stopping power for the series of aug-cc-pCVXZ basis sets (black: X=D, red: X=T, ... , yellow: X=6) and the extrapolated values (in pink).

the full basis set basis data ($X=D, T, Q, 5, 6$). Finally, we found the random stopping extrapolation method (Fig. 3.18 (b)) more stable and precise than the weighted stopping extrapolation.

The final result of the electronic stopping power calculations using the largest Dunning basis sets family and the extrapolation scheme is presented in Fig. 3.19 (a). The relative deviation between the asymptotic stopping power values and the values obtained with the largest basis `aug-cc-pCV6Z` (Fig. 3.19 (a)) is at most 17 %. The best convergence is achieved at high projectile velocities: the relative deviation is only about 6 %. Nevertheless, the results of the relative deviation show that one needs to perform the calculations up to the highest basis order X to obtain the asymptotic values within the highest possible precision.

We have also tried to perform the extrapolation of the stopping power based on the `cc-pCVXZ` basis sets calculations (which is less computationally expensive). However, at low proton velocities ($v < 1.0$ a.u. or $E_{proj}^{kin} < 25$ keV) we could not achieve convergence: the stopping power growth with the basis order X was almost linear in this case. This fact proves again the necessity of the most complete basis sets (`aug-cc-pCVXZ`) usage for the accurate stopping power calculation of proton in aluminum.

3.4 Basis set generation

3.4.1 Motivation

As we have seen in the previous section, the basis set is crucial for the accuracy of the stopping power calculations. Among all simulation parameters (cluster size, polar symmetry assumption, number of impact parameter points, etc.), the stopping power is most sensitive to the basis set completeness. Note that without the extrapolation over the basis set order X we would get the stopping power errors up to 17 %. In addition, the convergence is very slow, which forces one to perform the calculations with the largest basis set that exists for each element. Though, slow convergence with respect to the basis set order X is a common problem for other physical quantities [131, 132]. Recently, Luppi and coworkers [133, 134] have proposed the methods of the Gaussian basis optimization for the high-harmonic generation spectroscopy.

Although Dunning Gaussian basis sets are the handiest bases commonly used in the quantum chemistry community for a variety of atomic systems, they are constructed in a way to reproduce, above all, the electronic correlation energy. Hence, these basis sets are not necessarily optimal for the electronic stopping power calculations. In order to examine this question, we have performed the following calculation: We have selected the `cc-pCVQZ` basis set, which has already a large number of basis functions in the case of aluminum ($N_{AO} = 109$). Then, in order to evaluate the ‘‘importance’’ of a given basis function presented in the set, we performed the random stopping power calculation of proton in aluminum within the `cc-pCVQZ` basis but *without* this function. Next, we calculated the deviation of the stopping power calculated without the basis function with respect to the

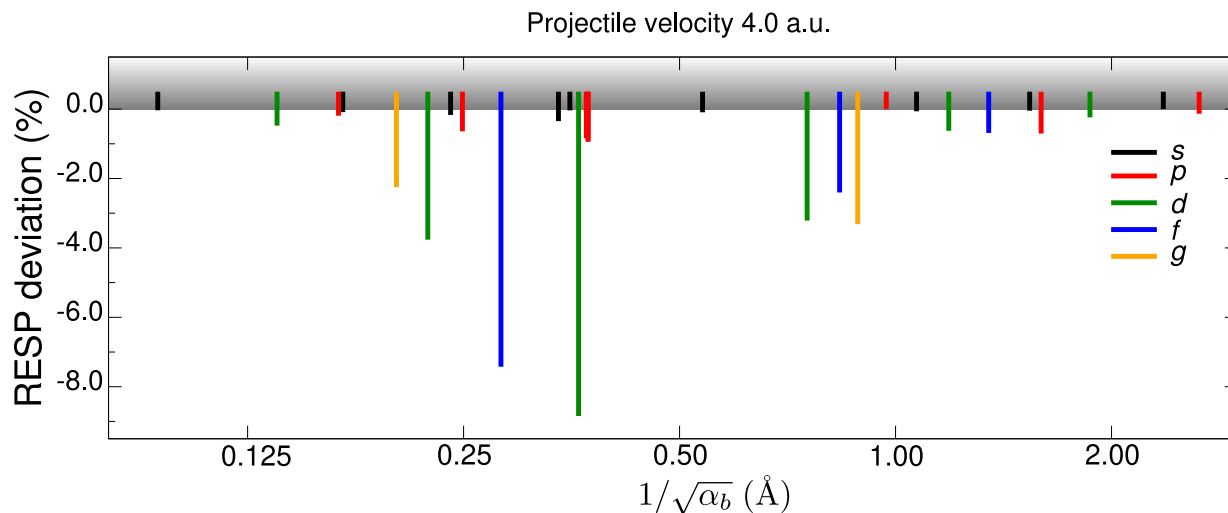


Figure 3.20 : Contribution of different basis functions of the set cc-pCVQZ to the random stopping power of proton in aluminum: Each line corresponds to the random stopping power deviation calculated without the basis function of a given Gaussian exponent α_b with respect to the value calculated with the complete basis. Some basis functions have very small contributions (lower than 0.2 %). Therefore, in order to make them visible in the diagram, every line begins in the grey region of the graph, which does not have any numerical significance.

one calculated with the complete basis set. In this way, we estimate a contribution of the given basis function to the random stopping power value. We have selected the proton velocity $v = 4.0$ a.u. ($E_{proj}^{kin} = 400$ keV) because at this velocity both core and valence electrons are excited by the projectile (see Fig. 3.16).

Fig. 3.20 presents the results of such analysis. Systematically, the stopping power calculated without a given basis function decreases. However, for many basis functions, it decreases by less than 1 %. Only some basis functions have strong importance on the stopping power leading to 4 % or more of stopping power reduction. Of course, the presence of basis functions that have a small contribution to the stopping power is also a consequence of a large total number of basis functions in the cc-pCVQZ set: Absence of one basis function can be more or less compensated by a linear combination of some other functions. However, taking into consideration that there are some other basis functions that are much more significant for the stopping power value, it is clear that one could have placed the basis function in another, more optimal, way that would have led to a more converged (larger) stopping power for the same number of basis functions.

There already exist some works that propose the “all-purpose” solutions for the basis set generation. For example, Lehtola and coworkers [135, 136] propose an approach for the basis set optimization within some finite region in space around a nucleus $[r_{min}, r_{max}]$. One assumes that the physical quantity of interest is sensitive to the electronic density in this range. The $[r_{min}, r_{max}]$ spatial interval corresponds to a range of Gaussian exponents $[\alpha_{b\ min}, \alpha_{b\ max}]$ such that $\alpha_{b\ min} = 1/r_{max}^2$ and $\alpha_{b\ max} = 1/r_{min}^2$. With the proposed algorithm one will retain as many Gaussian exponents in this range of α_b as needed to ensure

the completeness of the basis set within some specified accuracy.

Such a basis completeness-optimization approach is hard to apply to the stopping power problem for the following reason: Let us consider one atom of a target. During the irradiation process, the projectile-target distance varies from ∞ to p , where p is the projectile impact parameter with respect to the considered atom. Hence, strictly speaking, the region for the basis completeness optimization should be $[p, \infty]$ for which this algorithm, of course, would not be practical. Certainly, there exists some effective maximal distance of the interaction between the projectile and the target atom. However, this distance depends on a given atomic structure of the target, projectile energy, etc. Therefore, we have decided to develop the basis set optimization not with respect to some spatial range, but directly with respect to the quantity of interest - random electronic stopping power.

3.4.2 Basis set optimization algorithm

The idea underlying our algorithm is quite simple and is based on the following consideration: According to the variational principle, adding a basis function (to some existing basis set) with *any* Gaussian exponent α_b assigned to *any* atom of the target would improve the quality of the electronic states description, intuitively, this would *increase* the stopping power value. As an illustration of this idea, one can look at the stopping power convergence with respect to the Dunning basis sets (Fig. 3.18,3.19): An increase of the basis set order X leads for the increase of the stopping power for any impact parameter and any projectile velocity. One can mention also an example from the plane-wave codes: it has been reported [130] that the stopping power systematically increases with the increasing of the plane-wave cutoff energy (the data presented in [130] concerns a high projectile velocity). Therefore, our basis optimization procedure consists in the *maximization* of the random stopping power.

Here we present the detailed description of the basis set optimization algorithm (the steps of the description match the steps indicated on the diagram 3.21):

- (0) We start with the initial basis, called `opt0`. This basis must contain at least the minimal set of functions needed to describe the occupied electronic states. For the proton in aluminum system, to obtain `opt0`, we take the `cc-pCVQZ` basis and keep only s and p orbitals. Even though these retained orbitals might be not optimized, the computational cost of them is low (due to low $2l+1$ value). We start our optimization with the value of orbital momentum $l = 0$. The optimization scheme is designed for a fixed projectile velocity v_0 .
- (1) We perform the optimization progressively for the orbital momentum values from $l = 0$ to $l = l_{max}$. At steps (2)-(5) the value of l is fixed.
- (2) We define a candidate list of Gaussian exponents $\{\alpha_b^{(i)}\}_{i=1}^n$, that includes a large range of $\alpha_b^{(i)}$ values (typically, from $\alpha_b = 10^{-3}$ to $\alpha_b = 20$). If needed, this range can be extended on the fly of the optimization.

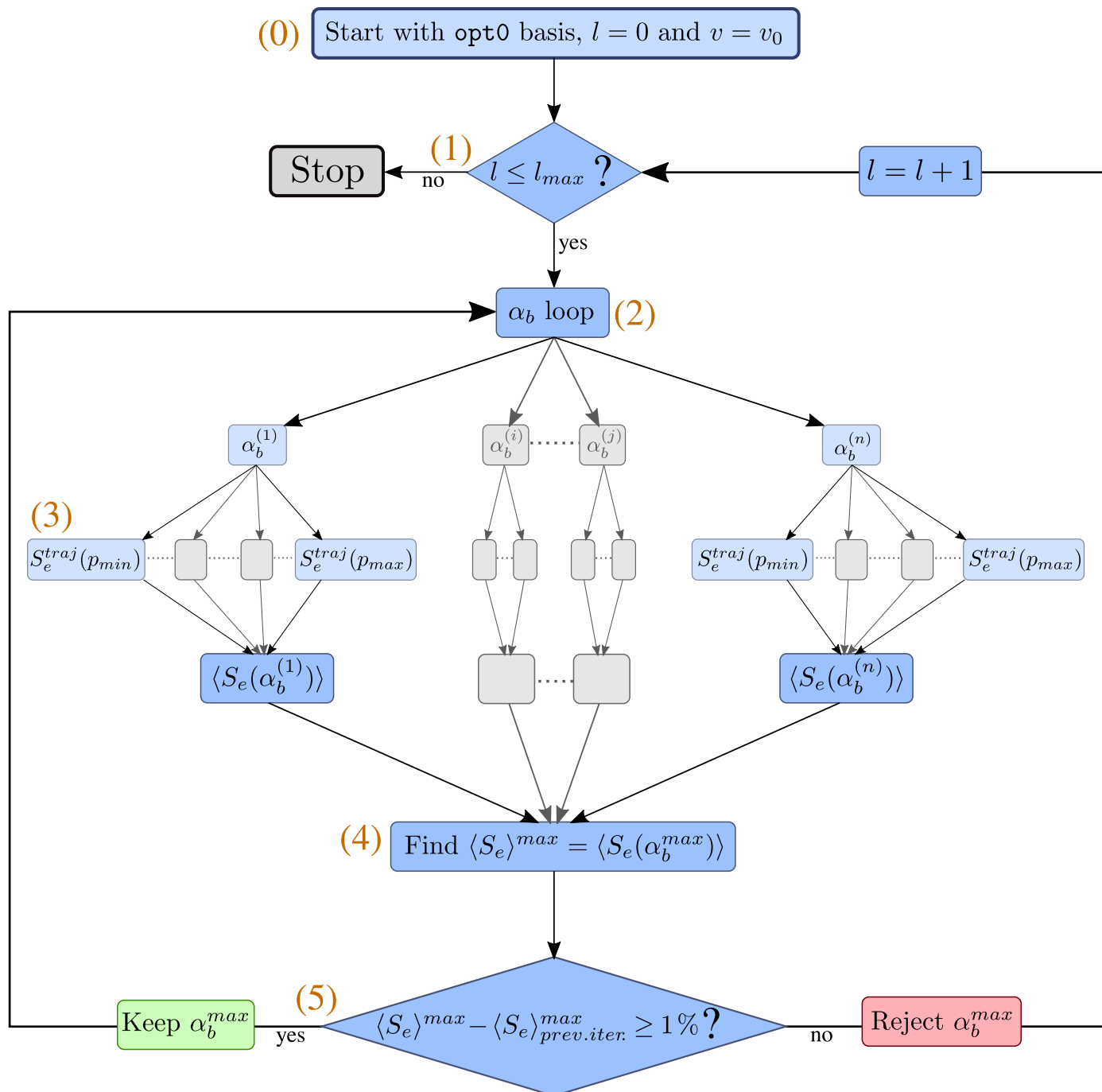


Figure 3.21 : Algorithm for the basis set optimization with respect to the electronic stopping power.

- (3) For each $\alpha_b^{(i)}$, we add this exponent to the basis set. Then, we calculate the random stopping power with the basis containing the additional function, $\langle S_e(\alpha_b^{(i)}) \rangle$ (the projectile velocity being equal to v_0). To do this, we proceed by the usual scheme: we calculate $S_e^{traj}(p)$ for a set of impact parameters and then we integrate $S_e^{traj}(p)$ with the weight function (equation 3.7).
- (4) Among all values of $\langle S_e(\alpha_b^{(i)}) \rangle$ we select the value of α_b (called α_b^{max}) that maximizes the random stopping power.
- (5) If the relative deviation of the stopping power calculated with the Gaussian function with exponent α_b^{max} , $\langle S_e \rangle^{max}$, with respect to the stopping power calculated without this function (in the previous iteration), $\langle S_e \rangle_{prev.iter}^{max}$, is larger than the threshold (fixed to 1 %), we keep this function and continue the optimization for a given orbital momentum l . Otherwise, we reject this function and increment the orbital momentum l .

Since the optimization procedure contains a large number of steps, we perform the stopping power calculations using a cluster of a small size, containing only the atoms of the central region (red atoms in Fig. 3.12). The optimization is designed for the basis set finding in the central region of the cluster, keeping the position-dependent basis set for the atoms that are outside the region, the same as in the previous sections (see Fig. 3.12).

In order to obtain a basis set that can be used for the stopping power calculations at the complete projectile velocity range, we perform the optimization procedure for two projectile velocities: We start with $v = 4.0$ a.u. ($E_{proj}^{kin} = 400$ keV). At this step, we optimize the basis mostly with respect to the core electrons. Then, we use the obtained basis set as the starting basis (`opt0`) for $v = 0.5$ a.u. ($E_{proj}^{kin} \approx 6.2$ keV). The optimization at low velocity adds the more diffuse functions that describe the valence electron excitations. After the second optimization run (at $v = 0.5$ a.u.) we obtain around 40 % of additional basis functions. In the case of aluminum, we run the optimization up to the orbital momentum $l = 7$ (k) and we call the final optimized basis `opt-k`.

Now, let us discuss the main optimization steps. Here, we will consider the first part of optimization, for the proton velocity $v = 4.0$ a.u. ($E_{proj}^{kin} = 400$ keV). First, we focus on the α_b loop (steps (2)-(4) on the optimization diagram 3.21). As an example, we take the first iteration for the orbital momentum $l = 2$ (d). Fig. 3.22 (a) presents the weighted stopping power dependence on the impact parameter for different Gaussian exponents α_b ($0.5 \text{ bohr}^{-2} \leq \alpha_b \leq 12.0 \text{ bohr}^{-2}$). For the sake of simplicity, we do not present the whole range of α_b used in optimization. One can see that at low α_b values ($\alpha_b < 3.0 \text{ bohr}^{-2}$) the stopping power has larger values at larger impact parameters ($p > 0.8 \text{ \AA}$) and vice versa. Then, according to the step (4), the algorithm will select the α_b parameter at which the random stopping is maximal. The stopping power deviation is shown in Fig. 3.22 (b) and the selected α_b value ($\alpha_b^{max} = 2.0 \text{ bohr}^{-2}$) is highlighted with the green circle. At the given example, as it is the first iteration for $l = 2$, the selected exponent leads to the increase of both the values of S_e^{traj} for core and valence electrons. In the next iterations, the exponents maximizing only core and only valence regions will be also retained.

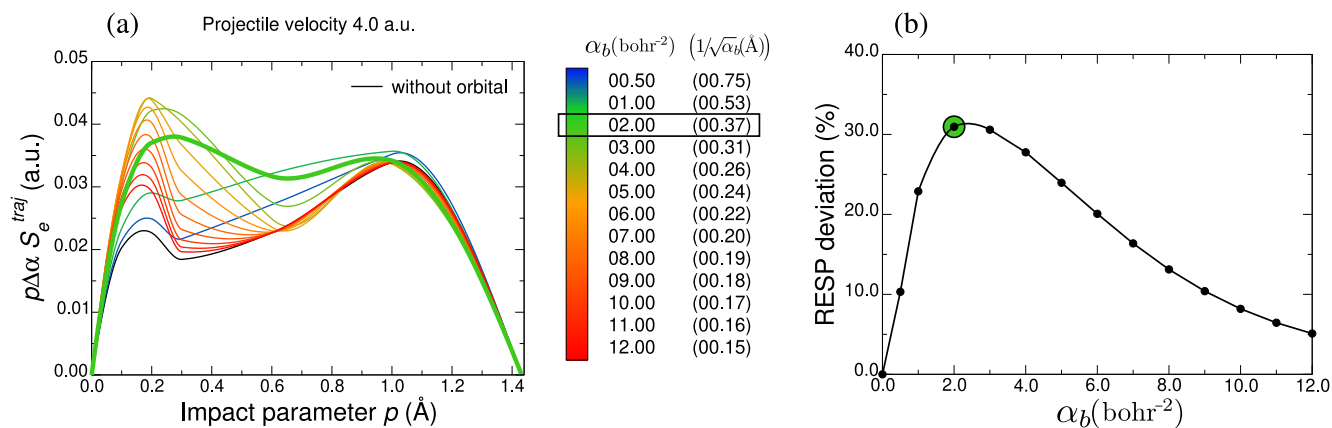


Figure 3.22 : Basis optimization procedure for the first iteration corresponding to the orbital momentum $l = 2$ (*d*). (a) Weighted stopping power of proton ($v = 4$ a.u.) in aluminum as a function of the impact parameter for a set of Gaussian exponents α_b of the additional basis function. The color of the curves encodes the α_b value. The selected curve for this iteration (in green), that provides the highest random stopping value, has a larger width as compared to others. (b) The deviation of the random stopping power calculated with a given α_b with respect to the stopping power calculated without the additional basis function. The selected maximal value is highlighted with a green circle.

Next, let us consider only the results of each α_b loop for different iterations at fixed l and for different l values. Fig. 3.23 (a) presents the resulting weighted stopping power for all orbital momenta l and all iterations within one l . In other words, in Fig. 3.22 (a) we have presented the curves for each α_b (fixed l), then Fig. 3.23 shows only the curves corresponding to the *selected* α_b^{max} . In the same manner, we present the random stopping deviation: for the set of α_b (Fig. 3.22 (b)) and only the selected values for different l (Fig. 3.23 (b)).

It is seen that the stopping power corresponding to both core and valence regions increases with each subsequent iteration and with the value of l . A large change in S_e^{traj} is seen for the transition from the orbital momentum p to d . Then, the difference decreases at each subsequent l . At the last orbital momentum used in optimization, k ($l = 7$), the weighted stopping power curve almost coincides at all impact parameters with the curve obtained at $l = 6$, which demonstrates the stopping power convergence. Fig. 3.23 (b) presents the random stopping power deviations at each step of the optimization procedure. Each colored sector corresponds to a given value of orbital momentum l , and the points within a sector correspond to iteration for a fixed value of l . In agreement with 3.23 (a), the largest deviation is observed at $l = 2$ (*d*), and for higher orbital momenta the value decreases. Low deviations for s and p are due to the fact that the initial basis `opt0` contained already the functions taken from the `cc-pCVQZ` basis with these orbital momenta.

Now, let us examine the spatial extension of the optimized basis exponents. On Fig. 3.24 we compare the values of α_b between the optimized basis `opt-k` (obtained after two runs, for $v = 4.0$ a.u. and $v = 0.5$ a.u.) and the most complete Dunning basis set

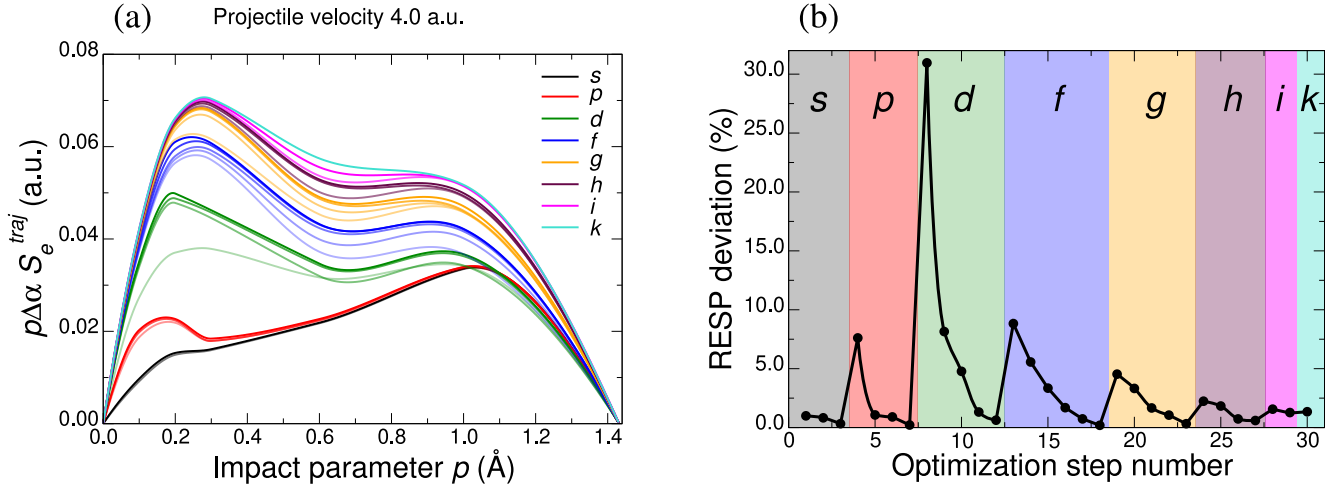


Figure 3.23 : Basis optimization presented for all orbital momenta l and all iterations with each l , projectile velocity is $v = 4.0$ a.u. (a) The weighted stopping power as a function of the impact parameter. Colors of the curves correspond to different orbital momenta. Curves corresponding to earlier iterations have dimmer shades. (b) Stopping power deviations as a function of the optimization step number divided into sectors corresponding to different orbital momenta l . The color scheme of sectors matches the one from the panel (a).

for aluminum, `aug-cc-pCV6Z`. Since both bases contain quite a large number of basis functions, we compare their exponents for each orbital momentum separately. We start the comparison with $l = 2$ (d) because lower s and p momenta do not have a large importance in the optimization. One can see that the spreading of the optimized basis exponents is smaller than in the case of Dunning basis. The values of $1/\sqrt{\alpha_b}$ of `opt-k` are mostly concentrated in the region $[0.25 \text{ \AA}; 1.0 \text{ \AA}]$. This region corresponds to the projectile impact parameters at which the stopping power weight has the largest values. In this region, the density of optimized exponents is noticeably larger than in the case of `aug-cc-pCV6Z` basis.

Even though the Gaussian exponents of the optimized basis are somewhat closely-grouped in the highest impact parameter weight region, different orbital momenta l have different corresponding spatial regions. For example, f and i orbitals contain some exponents that correspond to $1/\sqrt{\alpha_b} > 2.0 \text{ \AA}$. Therefore, one cannot simply define a spatial region common for all l . Hence, we suppose that the completeness-optimization procedure [135, 136] would not be the best basis optimization choice for the stopping power calculations.

Concerning the number of basis functions per orbital momentum, the optimized functions follow approximately the “pyramid” form similarly to the standard basis sets: the number of basis functions decreases with respect to l (see Fig. 3.24).

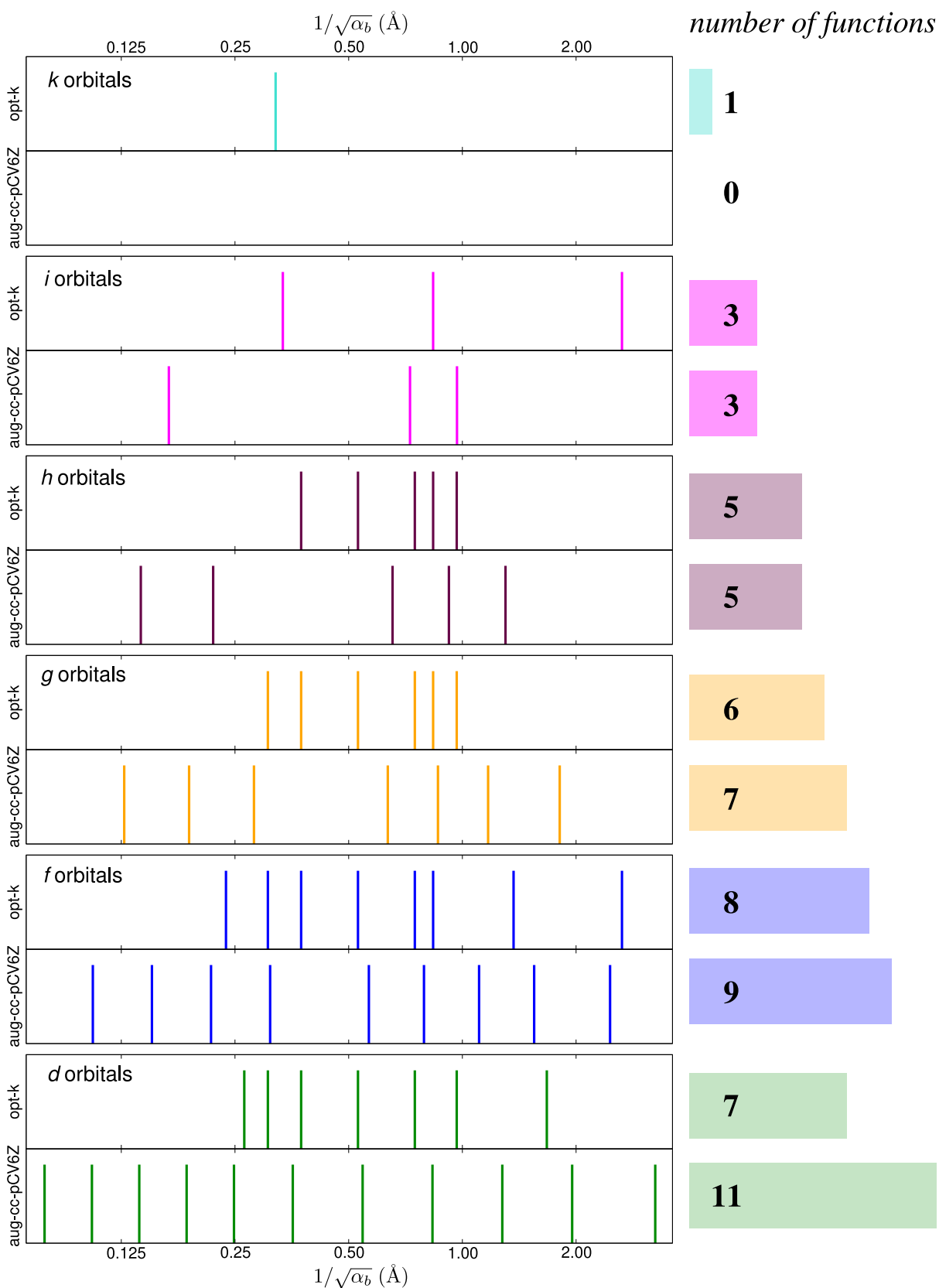


Figure 3.24 : Comparison of spatial extensions of the optimized basis opt-k with the standard aug-cc-pCV6Z for each orbital momentum l (starting at 2) separately. The numbers and rectangles on the right-hand side indicate the number of basis functions per l .

3.4.3 Stopping power calculated with the optimized basis

Velocity dependence

Fig. 3.25 shows the random stopping power of proton in aluminum calculated with the optimized basis `opt-k` compared with the largest standard basis set `aug-cc-pCV6Z` and with the extrapolated values obtained from the `aug-cc-pCVXZ` series. For the proton velocities $v \leq 0.5$ a.u. ($E_{proj}^{kin} \leq 6.2$ keV) the stopping power values obtained with the `opt-k` basis almost coincide with the extrapolated ones. For the velocity range 0.7 a.u. $\leq v \leq 5.0$ a.u. (12.2 keV $\leq E_{proj}^{kin} \leq 0.6$ MeV), $\langle S_e \rangle$ values for the `opt-k` basis are lower than the extrapolated ones and only slightly larger than the values calculated with the `aug-cc-pCV6Z` basis set. Finally, for $v > 6.0$ a.u. ($E_{proj}^{kin} > 0.9$ MeV) `opt-k` basis gives the values slightly lower than `aug-cc-pCV6Z`.

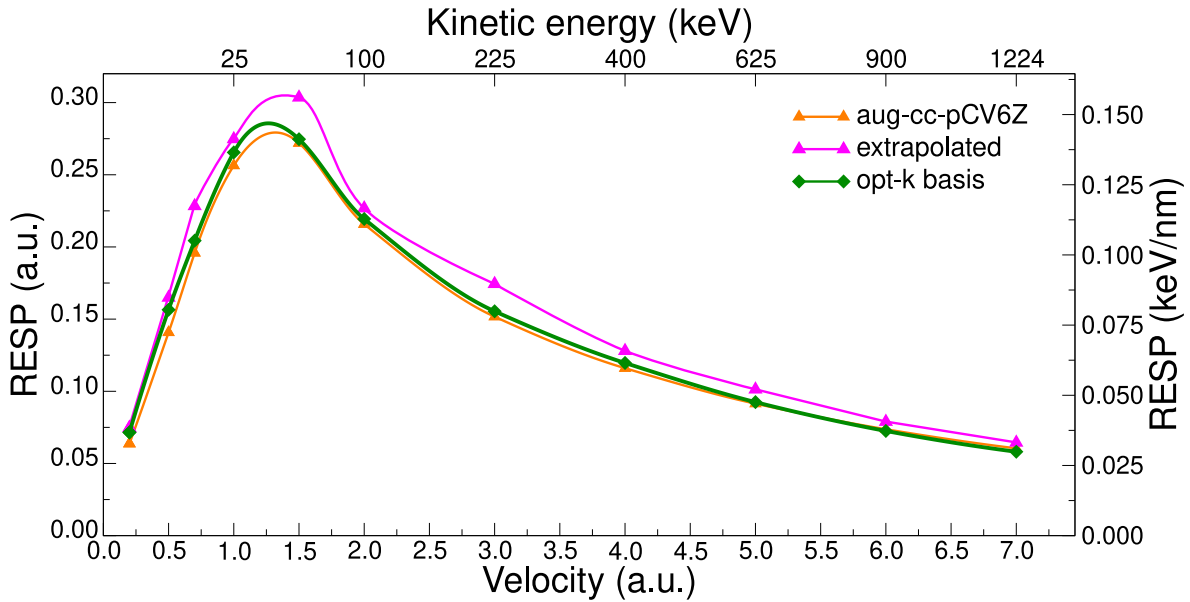


Figure 3.25 : Random electronic stopping power of proton in aluminum calculated using the most complete standard `aug-cc-pCV6Z`, optimized `opt-k` basis sets and obtained from the extrapolation of the `aug-cc-pCVXZ` bases.

These results indicate that for small projectile velocities, the basis set functions with the orbital momenta $0 \leq l \leq 7$ are sufficient to describe the stopping power without the extrapolation. This is not the case for larger v . For $l \leq 7$ the `opt-k` basis contains as many basis functions as needed to ensure the stopping power convergence within 1%. Therefore, the difference between `opt-k` stopping power and the extrapolated values for $v \geq 0.7$ a.u. shows that the missing basis functions necessarily have the orbital momenta larger than $l = 7$. The underestimation of the stopping power calculated with `opt-k` basis at $v > 6.0$ a.u. is minor and can be neglected.

Optimized basis set convergence

Similarly to the standard Dunning basis set series, one can use the optimized basis sets for the extrapolation of the random stopping power. In the case of Dunning bases `aug-cc-pCVXZ`, the extrapolation argument is the basis set order X , whereas in the case of optimized bases, the argument is the orbital momentum l . Fig. 3.26 presents the random stopping power for the proton velocity $v = 4.0$ a.u. as a function of the basis set order X in the case of `aug-cc-pCVXZ` bases and of the orbital momentum l in the case of optimized bases `opt-1`. For the stopping power extrapolation, we have used the same function as in the previous section (equation 3.9) for both data sets. One can see that the optimized bases converge faster than the Dunning bases. Noticeably, both curves converge towards the same stopping power value (within 3 %). It is also seen that at high orbital momenta ($l > 6$) the convergence of the stopping power with respect to the `opt-1` basis sets becomes extremely slow. Therefore, using the orbital momenta $l > 7$ would not significantly change the stopping power value, however, would be much more computationally expensive.

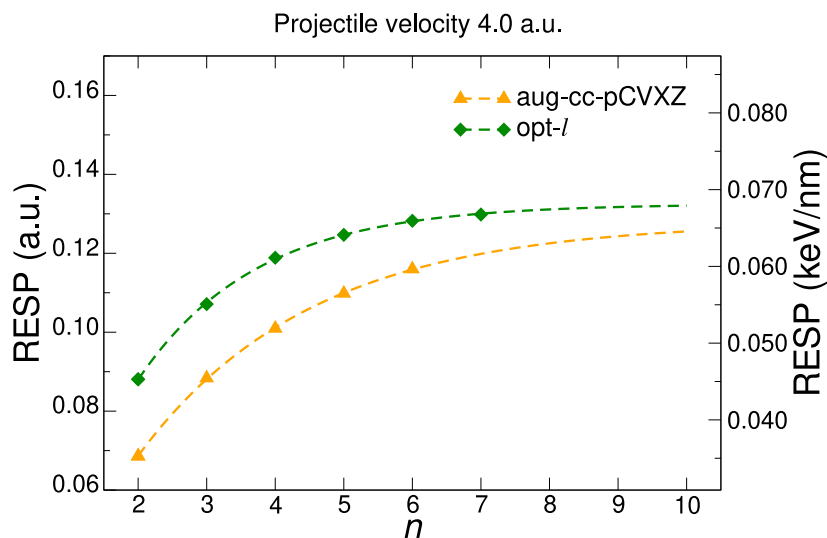


Figure 3.26 : Random stopping power as a function of the basis set parameter n . The value of n stands for the basis set order X in the case of Dunning basis sets (orange points) and for the orbital momentum l in the case of the optimized bases `opt-1` (green points). Dashed lines represent the extrapolation curves.

Though, the stopping power extrapolation as a function of l for the optimized basis sets `opt-1` could be a good option, the full study including different projectile velocities and different target materials stays in a perspective and is out of the scope of this work. In this work, we use the stopping power obtained only at the *highest* orbital momentum $l = 7$, `opt-k`.

Computational time

The optimized `opt-k` basis contains $N_{AO} = 293$ basis functions, whereas for the largest Dunning basis `aug-cc-pCV6Z`, $N_{AO} = 324$. Even though the difference is only in 31 basis functions, because of the cubic dependence of the computational time on N_{AO} , the cost of calculations using `opt-k` is 1.5 lower than for the `aug-cc-pCV6Z` basis (Fig. 3.27). Moreover, the `opt-k` basis provides more converged random stopping power values.

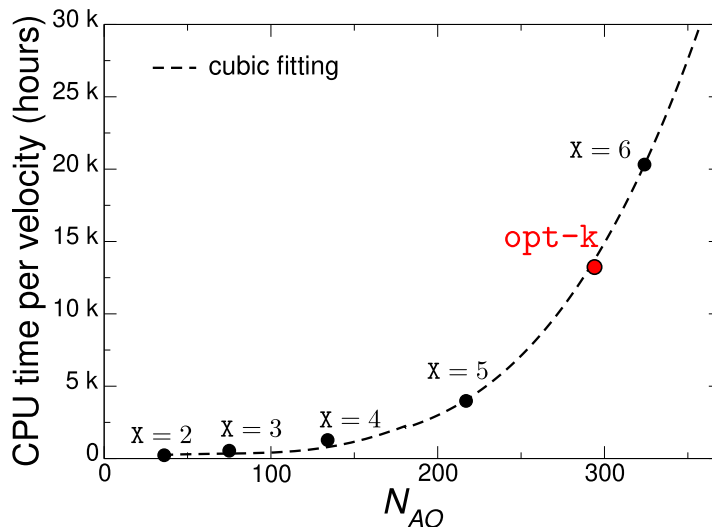


Figure 3.27 : Computational time of the random stopping power of proton in aluminum as a function of the number of basis functions. The timing is presented for one projectile velocity (13 impact parameter points). Black points present the data for the Dunning `aug-cc-pCVXZ` basis sets and red point - for the optimized `opt-k` basis. The calculations were performed on a Haswell CPU supercomputer.

Conclusions

To summarize, we have studied three approaches for the random stopping power calculations with respect to the Gaussian basis set:

1. Calculation with the highest basis of the Dunning basis set series `aug-cc-pCVXZ` or `cc-pCVXZ`.
2. Extrapolation of the stopping power based on the calculations using all the basis sets of a given Dunning basis set family.
3. Calculation within the optimized basis `opt-1` created for a given target with the highest orbital momentum l_{max} .

As we have seen in Fig. 3.19, the first method can lead to the stopping power errors up to 17 % (for small velocities). The second method is the most accurate. However, it

is quite expensive since it requires the calculations within all the basis sets of one family. Moreover, one still has the error due to the extrapolation function, because the choice of the function is arbitrary. The third method provides less converged values than the second one, however, it avoids the extrapolation error. In addition, often the existing Dunning basis set families do not contain the basis sets including X values high enough. For example, for lithium, the maximal basis set order X for the basis sets containing the tight core functions (`cc-pCVXZ` and `aug-cc-pCVXZ`) is $X=4$ (see Fig. 3.28). Therefore, with the basis set optimization procedure, one can generate the basis sets with higher orbital momenta and obtain more converged stopping power values.

Finally, we find the optimized basis approach to be a good compromise between the computational cost and the high stopping power accuracy. Therefore, we will use this method in the following stopping power calculations for different target materials and different projectiles (chapter 4).

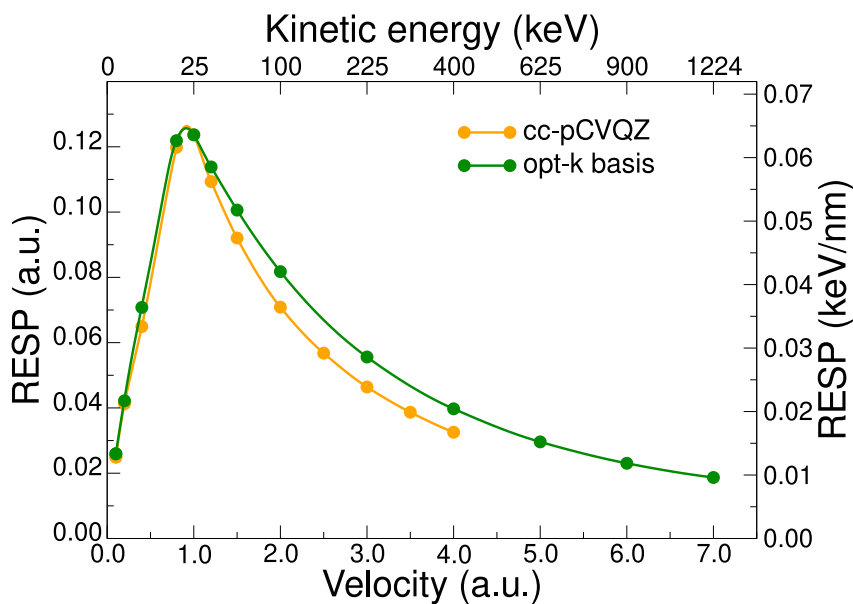


Figure 3.28 : Random electronic stopping power of proton in lithium target. The calculations were performed using the largest available Dunning basis set (`cc-pCVQZ`) and the basis set created in this work (`opt-k`).

3.5 Validity of fixed trajectory approximation

As discussed in sections 1.5.1 and 3.1.1, in our *ab initio* simulations we restrict the projectile to move along a straight line with a constant velocity. In this section, we will discuss the validity of this approximation and the stopping power errors it leads to. Having calculated the electronic stopping power (per trajectory $S_e^{traj}(p, v)$ and random $\langle S_e(v) \rangle$), we can estimate these errors applied to the systems that are studied in this work.

We will characterize the validity of the fixed trajectory approximation using the following criteria: 1) relative slowing down of the projectile along a straight trajectory and 2) deviation of the projectile from the straight line within the two-body scattering theory. Since the atomic number of aluminum and the electronic stopping power of proton in aluminum are larger than the corresponding values in the case of lithium target, the approximation errors are also larger in aluminum. Therefore, in this section we will consider the proton irradiation in aluminum target for the error estimations.

3.5.1 Projectile slowing down

To estimate the proton velocity change during the path, we will use the continuous slowing down approximation (CSDA). Within this approximation, the projectile energy loss in every point of its trajectory (equation 1.134) is calculated using the average stopping power ($S_e^{traj}(p, v)$ or $\langle S_e(v) \rangle$) rather than instantaneous one ($S_e(p, v, z)$).

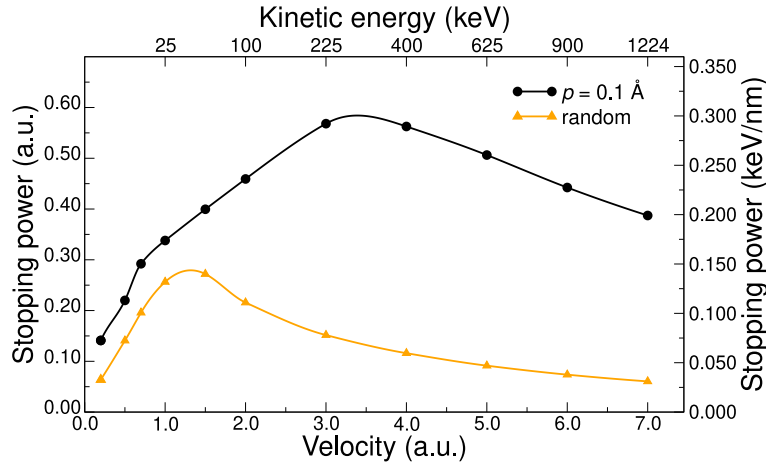


Figure 3.29 : Comparison between the stopping power averaged over the proton trajectory at $p_{min} = 0.1 \text{ \AA}$ (black line) and the random stopping power (yellow line) of proton in aluminum. The calculations were performed in `aug-cc-pCV6Z` basis.

In this section, our objective is to examine the extreme cases of the deviations from the fixed trajectory and fixed velocity approximation. Therefore, we will consider the highest stopping power $S_e^{traj}(p, v)$ values we encounter in our simulations that correspond to the smallest impact parameter $p_{min} = 0.1 \text{ \AA}$. For the trajectories corresponding to $p = p_{min}$,

the slowing down is maximal. The stopping power $S_e^{traj}(p_{min}, v)$ as a function of velocity compared with the random stopping power is shown in Fig. 3.29.

The loss of the projectile kinetic energy in this case is given by the equation

$$\frac{dE_{proj}^{kin}}{dz} = -S_e^{traj}(p_{min}, v). \quad (3.10)$$

We assume that the projectile enters the target with the initial energy E_0 (velocity $v = v_0$, see Fig. 3.30). Within CSDA the projectile kinetic energy is a monotonically decreasing function, hence, one can find the penetration depth $z(t)$ as a function of time by integrating equation 3.10

$$z(t) = - \int_{E_0}^{E(t)} \frac{dE}{S_e^{traj}(v)} = - \int_{v_0}^{v(t)} \frac{mv dv}{S_e^{traj}(v)}, \quad (3.11)$$

where m is the mass of the projectile. We are interested in the projectile slowing down at the scales corresponding to our *ab initio* simulations. Therefore, we will take the penetration depth approximatively equal to our cluster length L , say 10 Å. Suppose that at a time t_1 the projectile reaches this distance, then

$$z(t_1) = L = \int_{v(t_1)}^{v_0} \frac{mv dv}{S_e^{traj}(v)}. \quad (3.12)$$

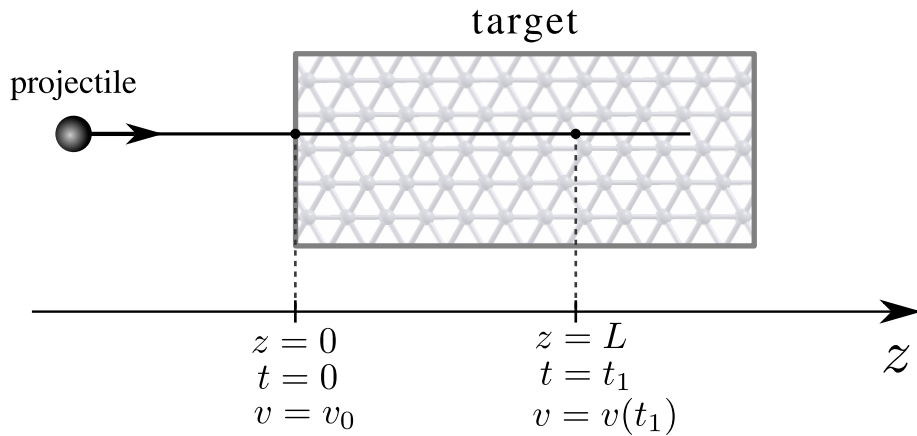


Figure 3.30 : Illustration of the projectile passage in a target within the fixed trajectory and the continuous slowing down (CSDA) approximations.

From this equation we, cannot get an explicit expression for the projectile slowing down. However, we can solve it numerically: One should find such velocity v ($v < v_0$), at which the integration between v and v_0 in equation 3.12 would give precisely the penetration depth L .

Fig. 3.31 presents the relative slowing down ($\Delta v/v$) of proton in aluminum target for the smallest impact parameter p_{min} . It is seen that the largest value is at the lowest projectile velocity $v = 0.2$ a.u. and is equal to 3.7 %. Therefore, we can neglect the effect of

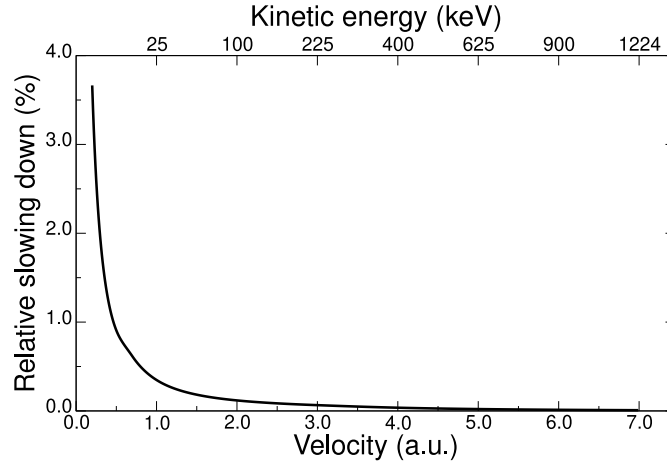


Figure 3.31 : Relative slowing down of proton in aluminum at the impact parameter $p_{min} = 0.1 \text{ \AA}$ as a function of proton velocity. The lowest presented velocity is $v_{min} = 0.2 \text{ a.u.}$ ($E_{proj}^{kin} = 1 \text{ keV}$).

projectile slowing down in our calculations. In addition, this impact point has a low weight in the random stopping power integration (see Fig. 3.11). For other impact parameters, the slowing down is lower. For example, for the channeling trajectory, the largest relative slowing down is only about 1 % (for the projectile velocity $v = 0.2 \text{ a.u.}$).

3.5.2 Deviation from straight path due to ballistic losses

In this section, we will consider the deviation of the projectile trajectory from the straight path for different projectile impact parameters p and velocities v . Obviously, the most significant deviations occur for projectile trajectories at which the projectile approaches the target nuclei. Therefore, to study the errors of the random stopping power calculations due to this effect, the binary collision approximation (BCA) is sufficient. In this approximation, one considers a two-body scattering problem [20, 77]: the scattering of the projectile ion on a target atom (Fig. 3.32).

We will characterize the scattering trajectory using three quantities: the impact parameter p , the distance of closest approach r_{min} and the deflection angle in the laboratory coordinate system φ . In order to calculate r_{min} and φ for a given p , one needs to know the scattering potential $V(r)$. Instead of using the semi-empirical models for the potential which include in some way the complex electronic screening of two nuclei [20], we calculated this potential for the proton-aluminum case from DFT using the MOLGW code: for each distance r we performed a separate DFT calculation in order to find the ground-state energy. Obtained in this way potential $V(r)$ corresponds to the adiabatic motion of the projectile (see section 3.1.1), which approaches the real projectile-target potential for small velocities. As we will see, the largest deviations take place at small velocities regime, therefore, this level of description - two-body scattering theory with the adiabatic potential - is well suited for the largest errors estimations.

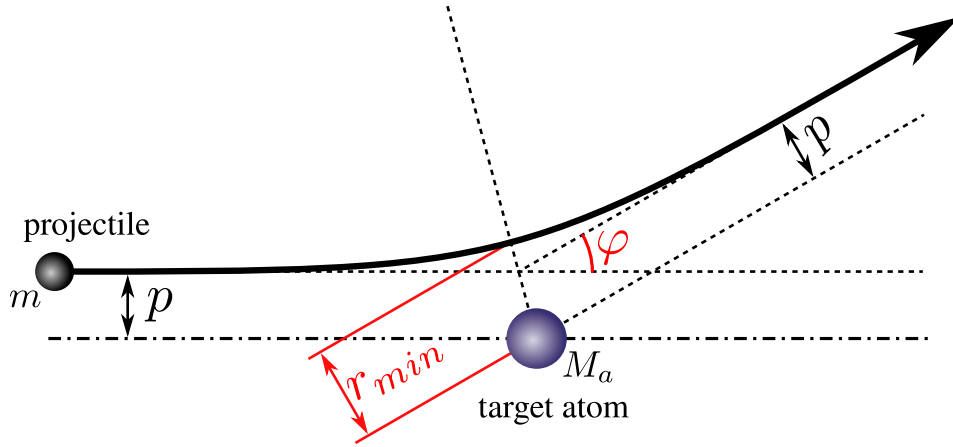


Figure 3.32 : Scattering of projectile on a target atom in the laboratory system of coordinates. The main quantities for our calculations are the projectile impact parameter p , the closest approach distance r_{min} , and the projectile deflection angle φ .

Closest approach distance

We will start to characterize the deviation with the distance of the closest approach of the projectile to the target atom r_{min} . From the two-body scattering theory, there is no explicit expression for this quantity. Though, it can be found from the numerical solution of the following equation (see reference [77], chapter 1, equation 1.77)

$$\eta E_{proj\ i}^{kin} = \frac{V(r_{min})}{1 - \frac{p^2}{r_{min}^2}}, \quad (3.13)$$

where $E_{proj\ i}^{kin}$ is the initial kinetic energy of the projectile and η is

$$\eta = \frac{M_a}{m + M_a}, \quad (3.14)$$

where m and M_a are the masses of the projectile and the target atom respectively.

Fig. 3.33 (a) shows r_{min} as a function of projectile impact parameter p for a range of projectile velocities. We also characterize the relative deviation of r_{min} with respect to p : $(r_{min} - p)/p \times 100\%$ (Fig. 3.33 (b)). It is seen that r_{min} approaches to p for higher p and for higher velocities. For the projectile velocities $v > 1.0$ a.u. ($E_{proj}^{kin} > 25$ keV), the absolute value of r_{min} is almost the same as p for any impact parameter p .

In our simulations we do not take into account the deflection of the projectile: the distance of the closest approach is just equal to the impact parameter p for any value of p within the fixed trajectory approximation. Therefore, in order to calculate the error in the random stopping power calculation due to this effect, we can assume that the value of the stopping power that we obtain, S_e^{traj} , corresponds not to the impact parameter p , but rather to r_{min} . Hence, we propose the following r_{min} -correction scheme: We use the

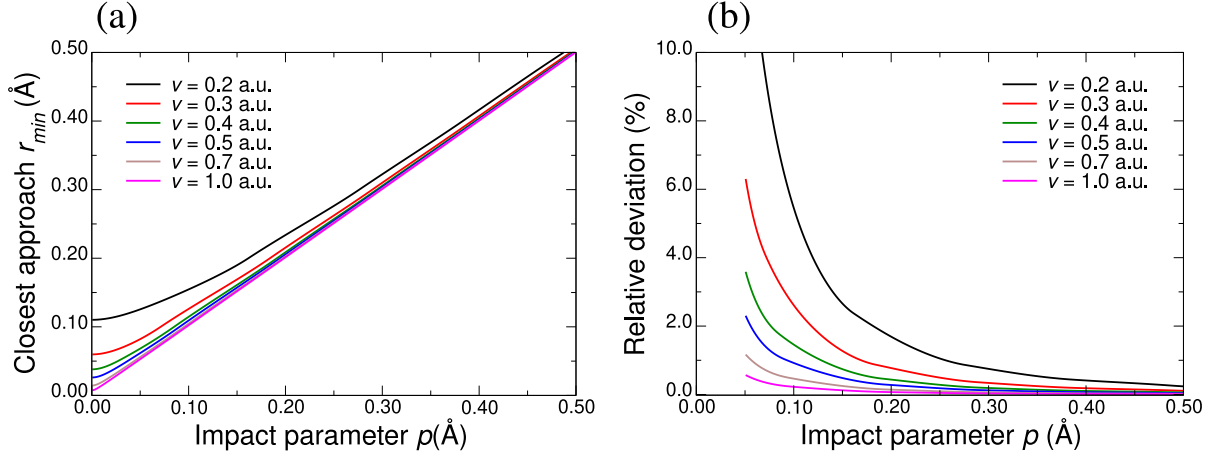


Figure 3.33 : (a) Closest approach value as a function of the impact parameter for several velocities in the case of proton projectile and aluminum target atom. (b) The same information, but in terms of the relative deviation of r_{min} from p . The colors of lines designate the projectile velocities in the same way in both panels.

same sampling of the impact parameter p with the weight function $p\Delta\alpha(p)$ (equation 3.8). However, the stopping power $S_e^{traj}(p)$ in equation 3.7 should be changed to $S_e^{traj}(r_{min}(p))$

$$S_e^{traj}(p) \rightarrow S_e^{traj}(r_{min}(p)) \quad (3.15a)$$

$$\langle S \rangle = \int_0^{a_{lat}/2} dp p\Delta\alpha(p) S_e^{traj}(p) \rightarrow \int_0^{a_{lat}/2} dp p\Delta\alpha(p) S_e^{traj}(r_{min}(p)). \quad (3.15b)$$

The stopping power S_e^{traj} is calculated for a proton in an aluminum cluster, whereas $r_{min}(p)$ is obtained from the two-body scattering theory. The weight function $p\Delta\alpha(p)$ takes into account the surface geometry and should not be changed due to the projectile deflection.

This idea is illustrated in Fig. 3.34: We “send” a beam of projectiles with the impact parameters which are equally distributed. Due to the deflection of the projectile, we assign to each value of p the closest approach distance $r_{min}(p)$ and then we integrate $S_e^{traj}(r_{min}(p))$ using the weight function that corresponds to the initial impact parameters grid. We obtain the $S_e^{traj}(r_{min}(p))$ values from the interpolation of the stopping power calculated on the p grid for each projectile velocity.

This r_{min} correction leads to a region of impact parameters, at which the projectile never enters (red region in Fig. 3.34). This region is limited by r_{min0} - the distance of the closest approach at the head-on collision. The value of r_{min0} can be obtained from the limit $p \rightarrow 0$ in equation 3.13

$$\eta E_{proj}^{kin} = V(r_{min0}). \quad (3.16)$$

It is seen that r_{min0} depends on the initial projectile energy.

We would like to mention, that within the proposed correction scheme, we still assume the rectilinear motion of the projectiles, but with a $r_{min}(p)$ impact parameter instead of p .

Therefore, it can be used only for the random stopping power errors estimations and not as a method for the improvement of the stopping power values.

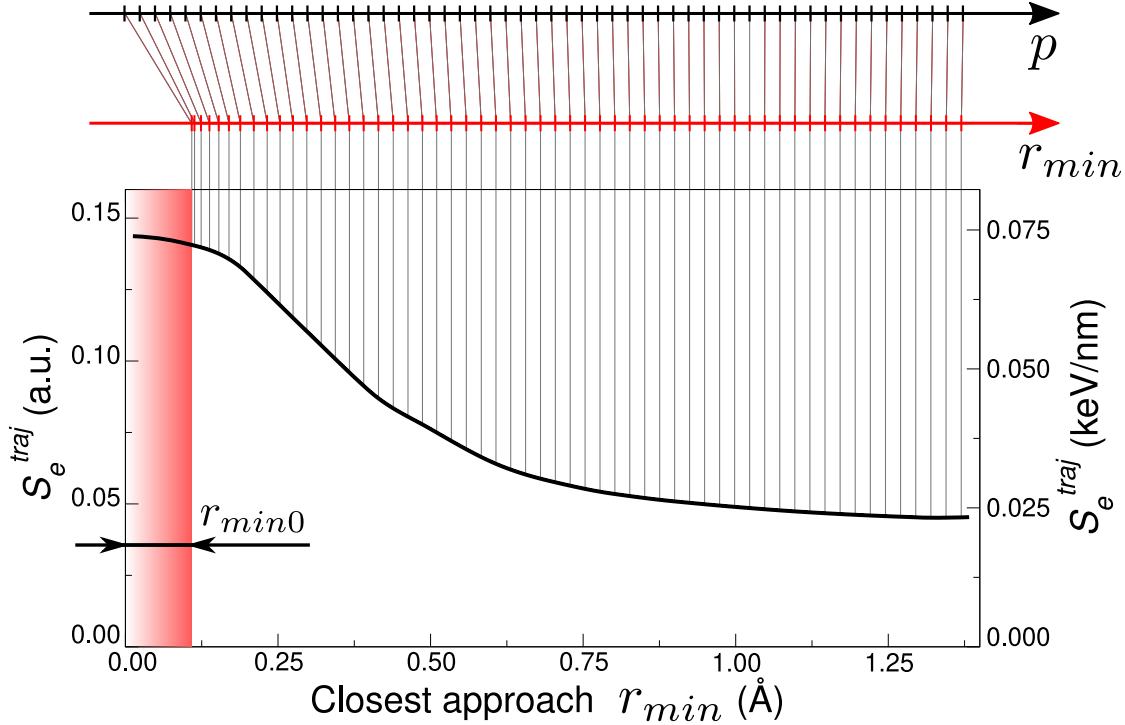


Figure 3.34 : Stopping power integration within the r_{min} -correction scheme. The first axis at the top of the figure represents the equidistant impact parameter grid. Then one can obtain the $r_{min}(p)$ grid (in red) used for the integration. The stopping power S_e^{traj} obtained within the fixed trajectory technique from our simulations can be associated with $S_e^{traj}(r_{min})$, presented on the graph.

The results of the r_{min} -correction scheme for proton projectile in aluminum are presented in Fig. 3.35. Fig. 3.35 (a) shows the weighted stopping power calculated with (red line) and without (black line) the correction. We have selected the lowest projectile velocity we use in our calculation since the difference is the most significant. One can see that even at the extreme velocity, taking into account the deviation of the closest approach distance from the impact parameter leads to errors not larger than 1.5 % (Fig. 3.35 (b)). Even if this deviation becomes significant at very small impact parameters ($p < 0.1$ Å), due to the weight function, the difference is still almost zero.

Deflection angle

To find the projectile deflection angle in the *center of mass* coordinate system, θ , one can use the following expression (see reference [77], chapter 1, equation 1.76)

$$\theta = \pi - 2 \int_0^{1/r_{min}} dx \left[\frac{1}{p^2} \left(1 - \frac{V(1/x)}{\eta E_{proj i}^{kin}} \right) - x^2 \right]^{-1/2}. \quad (3.17)$$

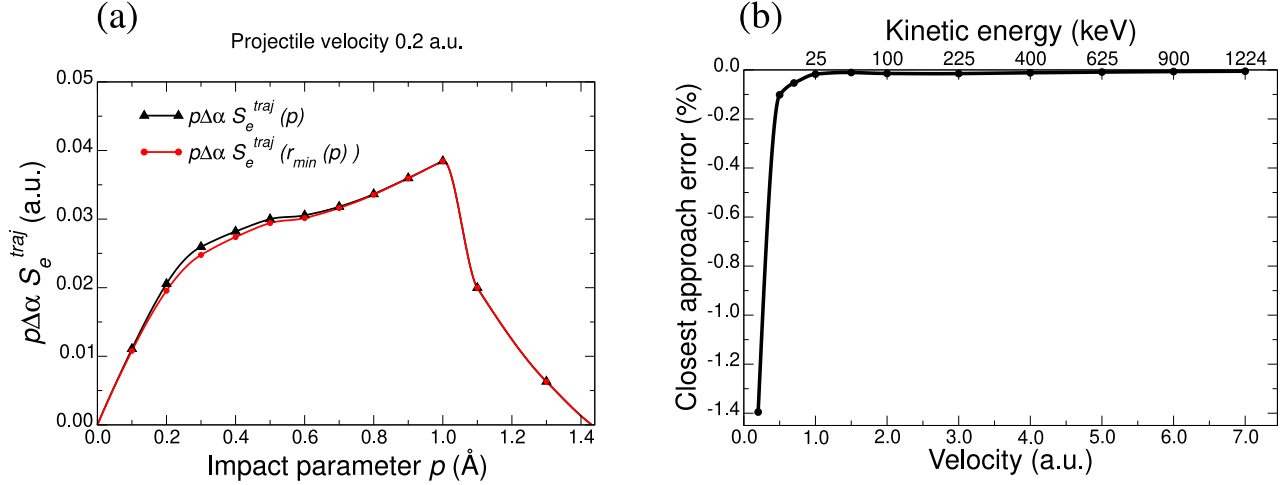


Figure 3.35 : (a) Weighted stopping power of proton in aluminum. The black line is the stopping power without the r_{min} -correction, the red line is the stopping power with the correction, as a function of $r_{min}(p)$. (b) The error of the random stopping power due to the closest approach distance deviation from the projectile impact parameter.

Then, the deflection angle in the *laboratory* system of coordinates, φ , can be obtained from θ as

$$\tan^2 \varphi = \frac{\sin^2 \theta}{\left(\cos \theta + \frac{m}{M_a} \right)^2}. \quad (3.18)$$

Fig. 3.36 (a) shows the deflection angle φ in the case of the proton projectile and aluminum target atom. We can see that the deflection is quite large. It follows the same behavior as the closest approach distance: it decreases for larger impact parameters and larger projectile velocities. However, the values of the angle φ are non-negligible even for large impact parameters. In order to evaluate the importance of a given deflection angle, we also calculate the deviation of the projectile y -position at the penetration depth z , corresponding to the next atomic layer of aluminum, z_{a2} (see Fig. 3.36 (b) for the results and 3.36 (c) for the schematic explanation). For example, at projectile velocity $v = 0.2$ a.u. ($E_{proj}^{kin} = 1$ keV) and impact parameter $p = 0.3$ Å, the deflection angle is $\varphi = 12.8^\circ$ and the projectile deviation $\Delta p = 0.9$ Å, which is three times larger than the impact parameter p . The projectile deviation Δp can be neglected only starting at $v = 2.0$ a.u. ($E_{proj}^{kin} = 100$ keV).

We think that in order to calculate the random stopping power using the ensemble average technique, one *has* to fix the projectile y -position because of the following reasons: The random stopping power is obtained by means of the sampling of the projectile impact parameters p . Therefore, for each trajectory we need to know the value of $S_e^{traj}(p)$ for a *fixed* impact parameter. If we allow for the projectile to deflect, we then would obtain the impact parameter that changes from one atomic layer to another and we would not

be able to perform a proper sampling over the impact parameters. Similar considerations are taken into account in the SRIM ion implantation profile calculations [20]: For each independent collision, one randomly selects an impact parameter, then one calculates the energy transfer from the projectile to a target atom and the projectile deflection. For the scattering calculation at the next iteration, the knowledge of the previous deflection angle is not needed: the impact parameter is selected randomly using the same distribution law as at the previous step. In such a way, during one projectile trajectory one will perform an impact parameter sampling which takes into account the target *density*, but not its *structure*. The deflection angle can be then useful only to reproduce the projectile implantation profile.

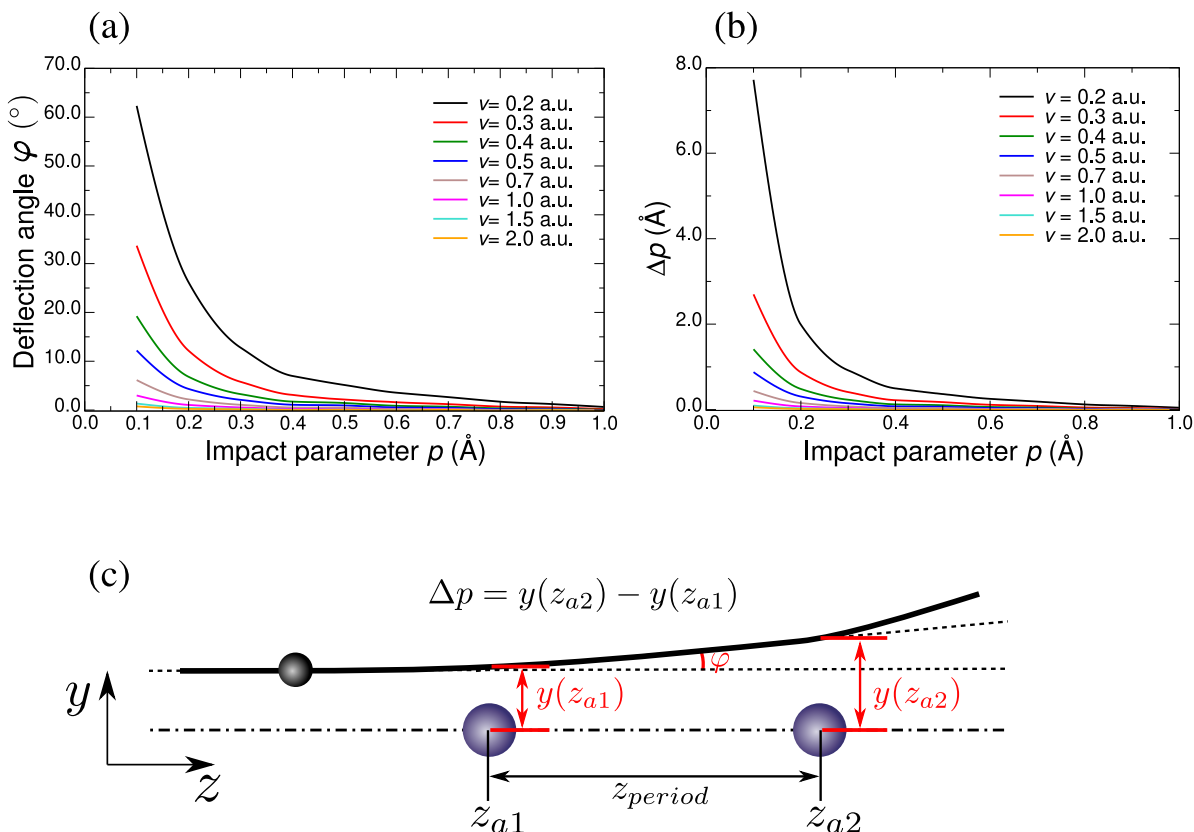


Figure 3.36 : (a) Proton deflection angle of the scattering on aluminum atom as a function of the impact parameter for a set of proton velocities. (b) Deviation of the distance to the target atom Δp from one atomic plane to another as a function of the impact parameter. The set and the color scheme for the projectile velocities are the same as in panel (a). (c) Illustration of the impact parameter deviation Δp because of the deflection of the projectile. To simplify the representation, we assume that the closest approach distance is approximatively equal to the impact parameter $r_{min} \approx p$.

Conclusive remarks

In this section, we have estimated the main quantities that characterize the deviation of the projectile from the uniform motion along a straight line. As a general rule, the largest deviations of all the studied quantities (slowing down, closest approach, deflection angle) occur for small projectile velocities and for the projectile trajectories that correspond to small impact parameters. At the same time, these trajectories contribute to the random stopping with low weights (equations 3.7, 3.8). In other words, thinking about the beam of many projectiles, such trajectories are less probable than the trajectories that correspond to larger impact parameters. Therefore, one can neglect the slowing down and deviation of the closest approach distance r_{min} from the impact parameter p . In contrast, the deflection angles are significant even for large impact parameters. However, from our point of view, taking into account the projectile deflection would bring an excessive structure dependence into the averaging procedure. Our goal is to calculate a proper average over the impact parameters. Even if the separate projectile trajectories (in particular those having small impact parameters) do not correspond to the real ones, the *average* over the trajectories yields the correct random stopping power.

The projectile deflection considerations do not apply to the simulations of the channeling trajectories. Under the channeling conditions, the projectile moves along a straight line without any assumption. On the other hand, the projectile slowing down, treated in section 3.5.1, can be applied for the channeling case. To do that, one needs to take the stopping power value at the channeling impact parameter $S_e^{traj}(p_{chan})$. The relative slowing down along the cluster length is negligible, however, using the presented approach one can calculate the total penetration depth in a target (will be considered in chapter 4).

3.6 Summary

In this chapter, we have developed a methodology for the random electronic stopping power calculations in the localized Gaussian basis code.

First, we have described our method to deduce the stopping power from a single projectile trajectory (with fixed velocity and fixed impact parameter). Then, we have performed the convergence tests of the electronic stopping as a function of the cluster size. As expected, relatively small clusters (50-60 atoms) are enough to reproduce the stopping power of the crystalline material. Though we have found that the transverse size (with respect to the projectile path) has greater importance on the stopping power than the longitudinal one, therefore, the retained clusters are approximatively two times larger in width than in length.

Then, we have focused on the *random* stopping power calculation methodology. In order to study the direction dependence, we have taken three orientations of the Li cluster ([001], [110] and [111]). For all the chosen orientations we have calculated an accurate average over the impact parameter (using very fine grids). We have found that the *random* stopping power in all the directions is the same (except for small deviation at low projectile

velocities). This conclusion allowed us to consider only one cluster orientation for further random stopping power studies.

Even, dealing with only one cluster orientation, the calculation of the stopping power average over the impact parameter can be still a challenging task in terms of the number of calculations. Therefore, we have studied the polar symmetry of the stopping power in order to attempt to reduce the calculation time. Indeed, the average calculated along one line (in XY plane, selected as y -axis) differs from the average calculated on the grid not more than by 2 %. At the same time, the variation of S with the module of the impact parameter p is significant and should be taken into account. Neglecting the p dependence and taking only one p_{cent} for the RESP calculations would be the centroid path approximation. We will discuss the validity of this approximation in chapter 4.

In the following sections, we have studied in detail the Gaussian basis set problem in relation to the stopping power calculations. We have started with the standard Dunning basis sets. We have shown that in the case of the aluminum target, the inclusion of both tight-core and diffuse basis functions is necessary to obtain the full range of projectile velocities we are interested in. In the lithium target case, only the tight core additional basis functions are important. We have also seen that with increasing of the basis set order X , the stopping power significantly increases. Therefore, the stopping power extrapolation can be employed in order to obtain more accurate values.

Then, we have proposed our algorithm for the Gaussian basis sets generation specific to the stopping power problem. Having empirically observed that the stopping power increases with the increase of X , we have elaborated the basis generation scheme based on the stopping power maximization. With those basis sets we can obtain the stopping power values more converged than the highest available standard bases and with a lower computational time. Therefore, for all the rest of the calculations, we will use the optimized basis sets.

CHAPTER 4

Stopping power of light projectiles in lithium and aluminum

In this chapter, we present the final results of the random stopping power calculations. Here we take into account all the conclusions obtained in the previous chapter (cluster size, random stopping calculation technique, Gaussian basis set, etc.) in order to obtain the most accurate values of the electronic stopping power.

In this work, we have performed the calculations in two crystalline targets: lithium and aluminum with [001] orientation for three types of projectiles: protons H^+ , antiprotons $\bar{\text{H}}^-$, and α -particles He^{2+} . Therefore, in order to systemize the results, most of the times, we will present the calculations for both targets side by side.

First, we will discuss the calculations of the stopping power of the proton in lithium and aluminum targets. Using this system as an example, we will estimate the influence of the exchange-correlation functional on the stopping power values. Then, will focus on the core electrons contribution to the stopping power using the frozen core technique and the occupation analysis (the method will be presented in this chapter). We will also evaluate the accuracy of the centroid path approximation for the proton in the aluminum system.

After that, we will present the random stopping power calculated for the α -particle. Next, we will discuss the penetration depth obtained from the electronic stopping power within the continuous stopping down approximation (CSDA).

Then, the stopping power of the antiproton will be discussed. And finally, we will provide the effective charge of the antiproton and α -particle projectiles calculated as a scaling factor between RT-TDDFT and the linear response theories.

4.1 RESP of proton

Fig. 4.1 presents the results of the RT-TDDFT stopping power calculations of proton in lithium (Fig. 4.1 (a)) and aluminum (Fig. 4.1 (b)) targets. We compare our results with the linear response theory (LR-TDDFT) [33], the empirical code SRIM [20] and the experimental data. We remind the main parameters used for our RT-TDDFT calculations:

- The calculations are performed in the optimized Gaussian basis sets (obtained in this work).
- The target orientations are [001].
- The exchange-correlation functional is LDA.
- We have used the 62-atom and the 54-atom clusters for Li and Al targets respectively.

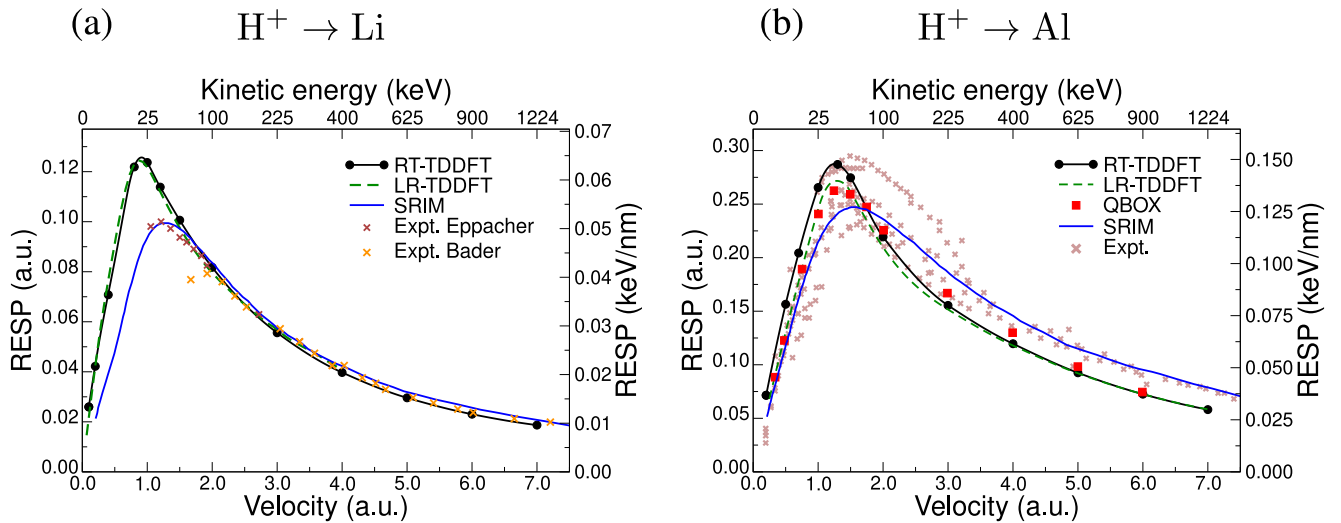


Figure 4.1 : Random electronic stopping power of proton in lithium (panel (a)) and aluminum (panel (b)) as a function of the projectile velocity. The target orientation is [001], the exchange-correlation functional is LDA. RT-TDDFT results obtained in this work are in black. LR-TDDFT curves (dashed green lines) come from reference [33]. Experimental points for the proton in lithium irradiation are from references [137, 138]. In the case of aluminum target, 18 different experiments have been performed, therefore we do not cite them separately. SRIM interpolation curves are depicted in blue. For the aluminum target, the QBOX *ab initio* code results are presented in red.

4.1.1 Lithium target

In the case of the lithium target, we can note an excellent agreement between RT-TDDFT and LR-TDDFT for the whole range of velocities available for the linear response results

($v \leq 4.0$ a.u. or $E_{proj}^{kin} \leq 400$ keV). Concerning the comparison with SRIM, there is a very good agreement for high velocities ($v \geq 2.0$ a.u. or $E_{proj}^{kin} \geq 100$ keV). However, for low velocities, the disagreement is compelling: the *ab initio* results are larger than the SRIM values. We argue that SRIM is extrapolated from experimental data that are missing for the proton in lithium at low velocities. Furthermore, between two experiments performed by Bader [137] and Eppacher [138] there is a disagreement on the proton velocity at which the stopping power has the maximal value as well as on the absolute value of the peak. Hence, due to the absence of the experimental data at low v and the disagreement around the peak velocities, we conclude that SRIM results are certainly not reliable for $v \leq 2.0$ a.u. ($E_{proj}^{kin} \leq 100$ keV).

4.1.2 Aluminum target

For the proton irradiation in aluminum target, there are much more experimental data including small projectile velocities. The dispersion of experimental points around the maximum of the stopping power is significant, however, at large velocities, the points follow more or less the same line. For this system, the real-time *ab initio* calculations of a plane-wave code QBOX [35] are also available.

One can see that in the low-velocity regime, all the *ab initio* results are in agreement with the experimental data and with SRIM. However, the MOLGW RT-TDDFT calculations yield slightly larger values. Then, around the peak, the results of *ab initio* codes provide larger values than SRIM. It is difficult to judge the agreement with the experiment since the discrepancy of experimental data is large in this region (around 35 %). However, for larger projectile velocities ($v \geq 4.0$ a.u. or $E_{proj}^{kin} \geq 400$ keV) it is clearly seen that all the *ab initio* results are lower than both SRIM and the experimental data. In addition, such behavior is quite common for the comparison between the *ab initio* and the experimental results [79, 82, 87, 88].

We have tried to identify the possible causes of the disagreement between the experimental data and the *ab initio* results at large proton velocities. Having tested all the convergence parameters in our MOLGW code (cluster size, averaging procedure, Gaussian basis, etc.), there is only the exchange-correlation functional that still needs to be tested. Moreover, to our knowledge, the *ab initio* calculations (based on TDDFT) have never been performed using a hybrid exchange-correlation functional for the proton irradiation simulations in aluminum. All the theoretical results presented in Fig. 4.1 are performed with the LDA functional.

Another possible source of the difference between the *ab initio* results and the experimental data concerns the QBOX plane-wave code: In the work of Schleife et coworkers [35], a pseudopotential that treats $2s2p3s3p$ electrons explicitly was used. This means that the $1s$ electron excitations were not taken into account in these calculations.

Therefore, in the following sections, we will separately consider these possible sources of errors: First, we will analyze the stopping power calculations performed with a hybrid exchange-correlation functional and then we will evaluate the role of the $1s$ electrons in the proton stopping in aluminum. Finally, in order to perform a more complete study, we

will discuss the electronic contributions to RESP from other electronic levels.

Exchange-correlation functional dependence

Fig. 4.2 shows the random electronic stopping power calculated in RT-TDDFT with the MOLGW code using the LDA functional and PBE0 hybrid functional. With the purpose of comparison and a more complete study, we present the results not only for the aluminum, but also for the lithium targets.

It is seen that the change of the exchange-correlation functional leads to a minor difference in the electronic stopping power: The largest change for aluminum is for $v = 1.0$ a.u. ($E_{proj}^{kin} = 25$ keV) and is equal to 3.5 %. For the lithium target the maximal difference of 4.5 % is for $v = 0.7$ a.u. ($E_{proj}^{kin} = 12.2$ keV).

For the lithium target, we have also tested other exchange-correlation functionals: HSE06, B3LYP, PBE (not presented). The conclusions are similar to those obtained for the LDA/PBE0 comparison: the largest change is around the stopping power peak and is lower than 5 %.

Hence, we conclude that for the studied target materials, there is no significant importance of the exchange-correlation functional. Therefore, the usage of the less expensive LDA functional is justified.

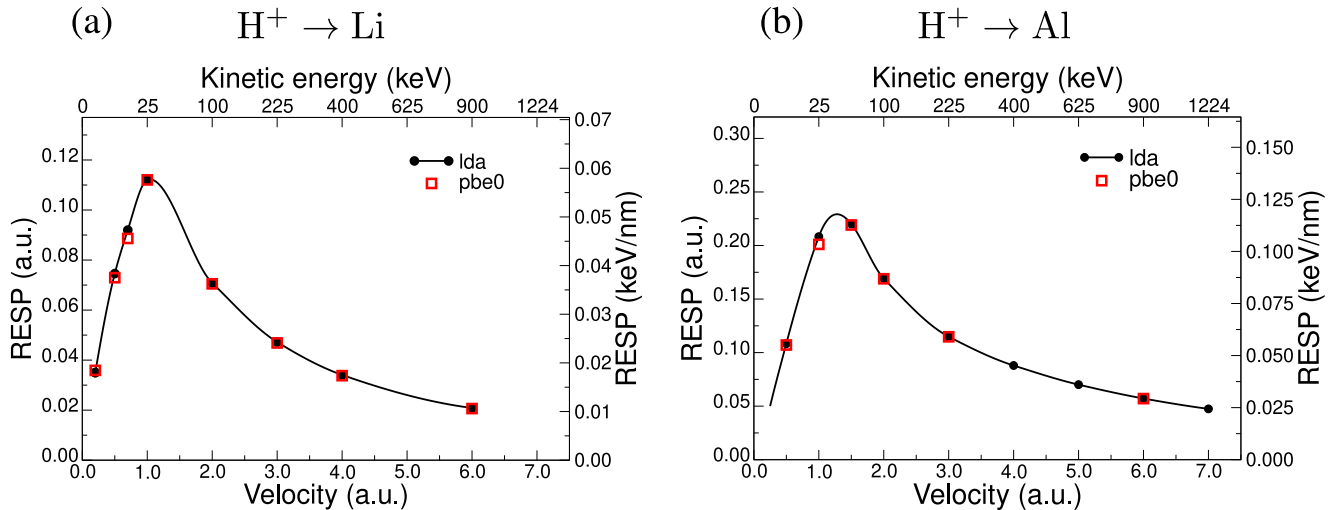


Figure 4.2 : Random electronic stopping power of proton in lithium, (a), and proton in aluminum, (b), obtained in this work as a function of the projectile velocity. Calculations performed with the LDA functional are presented in black, with the PBE0 functional is in red.

Core states contribution to the stopping power in aluminum

Here, our goal is to tackle the second point: the role of the 1s electron excitations in the stopping power of proton in aluminum, which can be a source of the error for the plane-wave approaches. With our localized basis all-electron code, we deal with it by simply

	$E - E_F$ (eV)
1s	[-1498.5, -1496.7]
2s	[-104.1, -102.2]
2p	[-67.2, -65.0]
valence	[-10.1, 0.0]
excited	> 0.0

Table 4.1 : Energy ranges with respect to the Fermi level of different electronic states of the aluminum cluster. We remind the aluminum electronic configuration: $1s^2 2s^2 2p^6 3s^2 3p^1$.

freezing the 1s states in the simulation and taking the difference between the all-electron and the frozen 1s stopping power values. In addition, we will evaluate the contributions to the stopping power from other states (2s, 2p, and valence) in the same manner. The numerical approach that we use to perform the frozen states RT-TDDFT propagation is described in section 2.2.7.

Fig. 4.3 (a) shows the stopping power as a function of the projectile velocity calculated with the all-electron response as well as with 1s, 1s2s, and 1s2s2p frozen electrons. It is seen that the results with the 1s frozen electrons (red squares) are almost the same as in the all-electron case: The largest difference is at the highest projectile velocity used in our calculations, $v = 7.0$ a.u. ($E_{proj}^{kin} = 1.2$ MeV), and it is equal to 0.2 %.

Fig. 4.3 (b) presents the weighted stopping power dependence on the projectile impact parameter for the projectile velocity $v = 4.0$ a.u. ($E_{proj}^{kin} = 400$ keV). The frozen states coloring scheme is the same as in Fig. 4.3 (a). One can see that the weighted stopping power values for the 1s frozen electrons coincide with the all-electron results for all the impact parameters.

The absence of the 1s excitations can be explained by their very low energies: around 1500 eV below the Fermi level. In comparison, 2p electrons have energy around -65 eV (see Table 4.1).

Hence, in the case of the proton irradiation in aluminum target, the reason of the underestimation of the *ab initio* calculations (LR-TDDFT and RT-TDDFT performed in MOLGW and QBOX) with respect to the experimental results and SRIM at high projectile velocities (presented in Fig. 4.1) remains to be determined.

In the following, we will evaluate the contribution to the stopping power of the 2s, 2p and valence electronic levels in the aluminum target. It is seen from Fig. 4.3 that the contribution of 2s and 2p levels is significant for the projectile velocities $v \geq 2.0$ a.u. ($E_{proj}^{kin} \geq 100$ keV): The random stopping power calculated with the frozen 1s2s and 1s2s2p electrons is considerably lower than the values obtained with the all-electron dynamics. From the impact parameter dependence (Fig. 4.3), one can note that the characteristic peak of the weighted stopping power around $p = 0.3$ Å disappears when all the core electrons are frozen. This demonstrates the core electron contribution.

Having calculated the stopping power with the different number of frozen states, we can now calculate separately the contributions from each shell. We can arbitrarily define

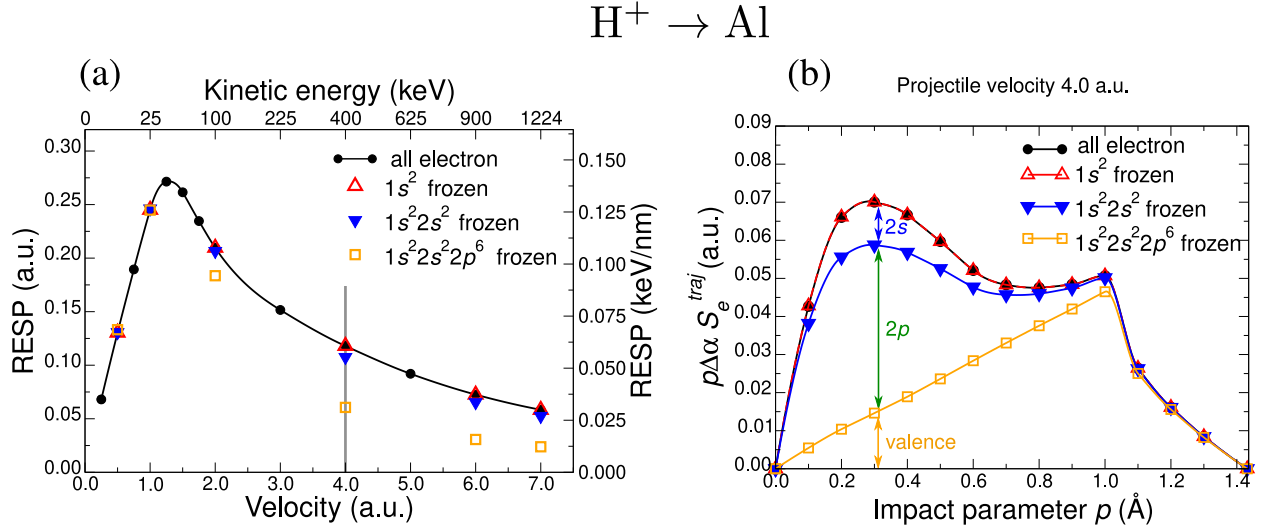


Figure 4.3 : (a) Random electronic stopping power of proton in aluminum as a function of the projectile velocity performed with the all-electron dynamics (black solid line) as well as with $1s$ (red points), $1s2s$ (blue points) and $1s2s2p$ (orange points) frozen electronic states; (b) Weighted stopping power as a function of the proton impact parameter for the projectile velocity $v = 4.0$ a.u. ($E_{proj}^{kin} = 400$ keV). The frozen state color scheme is the same as in panel (a).

the valence electron contribution, S^{val} , as the stopping power calculated with all the core electrons ($1s2s2p$) frozen

$$S^{val} = S^{frozen\ 1s\ 2s\ 2p}. \quad (4.1)$$

The contribution from $1s$ electrons can be defined as the difference between the total all-electron stopping power and the stopping power calculated with $1s$ electrons frozen (this difference, as we have seen, is negligible)

$$S^{1s} = S^{total} - S^{frozen\ 1s}. \quad (4.2)$$

Then, one can find the $2s$ contribution, S^{2s} , as the difference between the all-electron stopping power calculated with $1s$ and $1s2s$ frozen electrons, i.e.,

$$S^{2s} = S^{frozen\ 1s} - S^{frozen\ 1s\ 2s}. \quad (4.3)$$

Finally, the $2p$ contribution can be defined as the difference between $1s2s$ and $1s2s2p$ frozen electrons,

$$S^{2p} = S^{frozen\ 1s\ 2s} - S^{frozen\ 1s\ 2s\ 2p}. \quad (4.4)$$

See also the vertical arrows that indicate the $2s$, $2p$ and the valence electron contributions in Fig. 4.3. Using these definitions, we satisfy the total stopping power, namely,

$$S^{total} = S^{1s} + S^{2s} + S^{2p} + S^{val}. \quad (4.5)$$

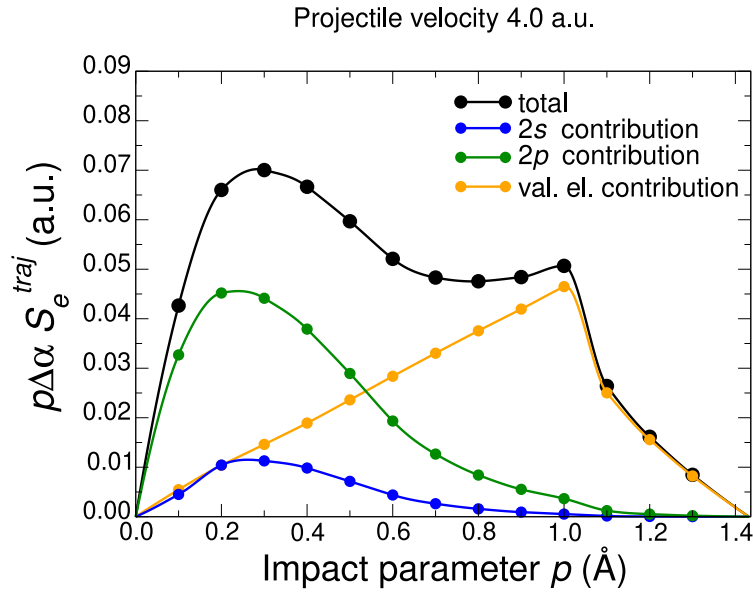


Figure 4.4 : Weighted stopping power of proton in aluminum as a function of the proton impact parameter for the projectile velocity $v = 4.0$ a.u. ($E_{proj}^{kin} = 400$ keV). The total stopping power (black line) is divided on the $2s$ (blue), $2p$ (green) and the valence (orange) contributions. Being negligible, the $1s$ contribution is not presented.

We apply this separation to the weighted as well as to the random stopping power. The electron contributions as a function of the impact parameter for the projectile velocity $v = 4.0$ a.u. ($E_{proj}^{kin} = 400$ keV) are presented in Fig. 4.4.

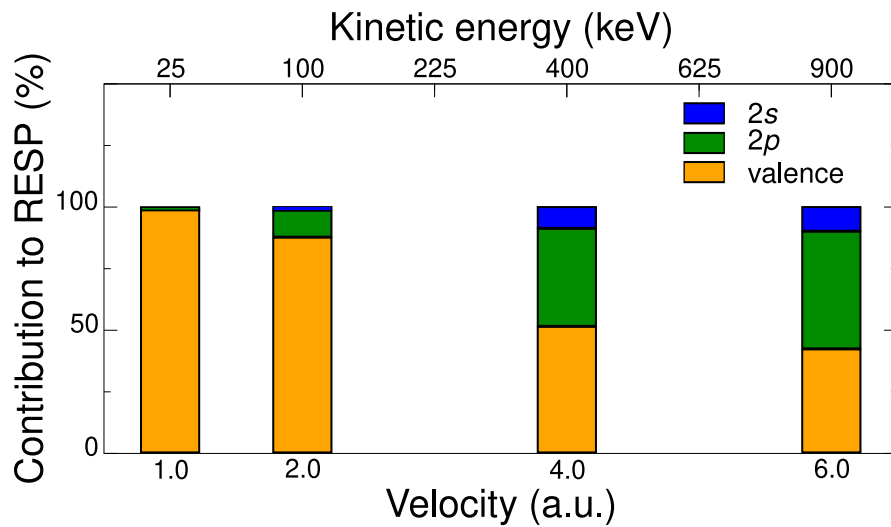


Figure 4.5 : The relative contributions to the random electronic stopping power of the proton in aluminum of $2s$ (blue), $2p$ (green) and valence (orange) electrons as a function of the projectile velocity.

Fig. 4.5 presents the electron contributions to the random stopping power as a function of the projectile velocity. It is seen that at the stopping power peak velocity (around $v = 1.0$ a.u. or $E_{proj}^{kin} = 25$ keV) the contribution of the core electrons ($2s2p$) is very limited (lower than 1 %), however, for $v \geq 4.0$ a.u. ($E_{proj}^{kin} \geq 400$ keV) the core electron contribution is 50 % or larger. This shows the necessity of a proper core electron excitation description, especially, for large projectile velocities.

4.2 Occupation analysis

In this section, we aim to get a deeper insight into the excitation dynamics, in particular, of the core electrons. In the previous section, we have evaluated the contributions of the different electronic levels using the frozen core technique. Here, we will analyze the electronic excitations by looking directly at the electronic levels occupations. This analysis is quite similar for the lithium and aluminum targets, except that it is richer for Al since it contains more electrons than Li. Therefore, in this section, we will focus only on the Al target.

4.2.1 Single-trajectory occupation dynamics

In section 2.2.5 we have presented how to calculate the occupation of the electronic levels, called q , in the localized basis code. In brief, we obtain an occupation of a given electronic level from the projection of the time-dependent wave function on the ground state wave function corresponding to this level. During our RT-TDDFT simulation trace the occupations of the electronic levels. We divide the levels into 5 groups according to their energies (see Table 4.1): $1s$, $2s$, $2p$, valence and excited.

Fig. 4.6 shows the change in the occupations during the projectile irradiation. This graph looks like the total energy of the system as a function of the penetration depth (Fig. 3.1). However, here, in addition, we have a decomposition of the occupation dynamics on different energy levels. Naturally, the electronic levels that were initially occupied ($1s$, $2s$, $2p$, and valence), lose some part of electrons, while the excited levels become populated. For example, as seen from Fig. 4.6, after the passage of the proton projectile along the 8 \AA aluminum cluster, the excited levels of the target acquire approximately 1.5 electrons from the initially occupied levels.

Concerning the $1s$ electronic excitations, the largest occupation change, which occurs at the largest projectile velocity used in our calculations, $v = 7.0$ a.u. ($E_{proj}^{kin} = 1.2$ MeV) is only about 2.4×10^{-3} . The absence of the $1s$ electron excitations is consistent with the conclusions drawn in the previous section. Therefore, we will not consider this level in the following.

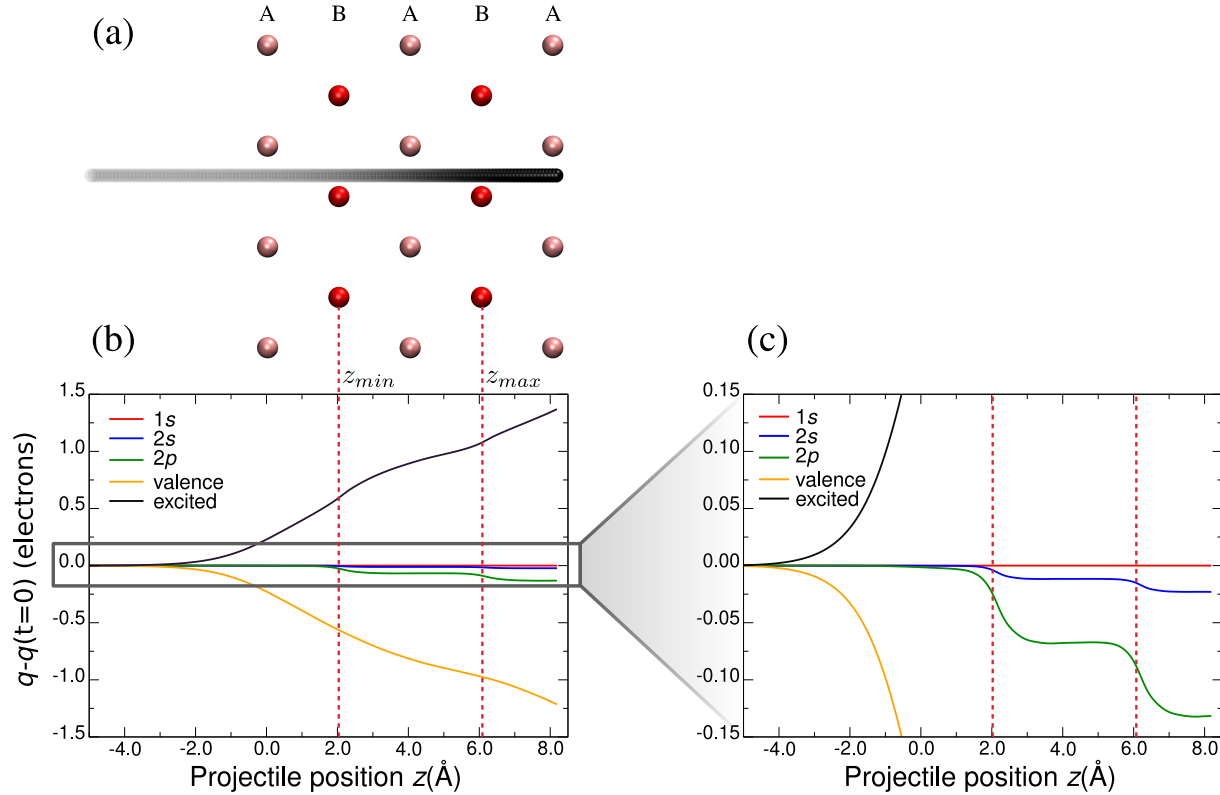


Figure 4.6 : (a) Illustration of the proton penetration (black trace) in the aluminum cluster. The target atoms belonging to the A (odd) atomic levels are in pink, those that belong to the B (even) atomic layers are in red. z -positions of even atomic levels are depicted in red dashed lines in panels (b) and (c). (b) Change of the occupation with respect to the initial state as a function of the proton penetration depth. Proton velocity is $v = 4.0$ a.u. ($E_{proj}^{kin} = 400$ keV) and the impact parameter is $p_x = 0.0$ Å; $p_y = 0.6$ Å. (c) The same as panel (b), but in a lower scale in order to better visualize the 2s and 2p occupation changes.

4.2.2 Weighted occupations: correlation with weighted stopping power

Similarly to the stopping power definition, a reasonable quantity to characterize the occupation dynamics can be the occupation change per penetration distance, $\frac{dq}{dz}$ (in electrons/bohr). In order to get valuable results based on the occupation analysis, we proceed with the same numerical scheme as for the random stopping power calculations that was introduced in chapter 3: We calculate the average occupations change rate per trajectory, $\left(\frac{dq}{dz}\right)^{traj}$, using our 3-step procedure (described in section 3.1.1). Then, in order to calculate the averaged (or, one can say, random) occupation change, $\left\langle\frac{dq}{dz}\right\rangle$, we use the same as for the stopping power assumption of the polar symmetry and, using the geometrical con-

siderations, integrate $\left(\frac{dq}{dz}\right)^{traj}$ as a function of the impact parameter along one direction in the XY plane, multiplied by the weight function (for the details, see section 3.1.3).

Fig. 4.7 shows the weighted occupations as a function of the projectile impact parameter. We have taken the projectile velocity ($v = 4.0$ a.u. or $E_{proj}^{kin} = 400$ keV) at which the core electrons contribution is significant. As in the case of the single-trajectory occupations (Fig. 4.6 (b)), excited state occupation change is always positive, while the occupation changes of all initially occupied levels are negative.

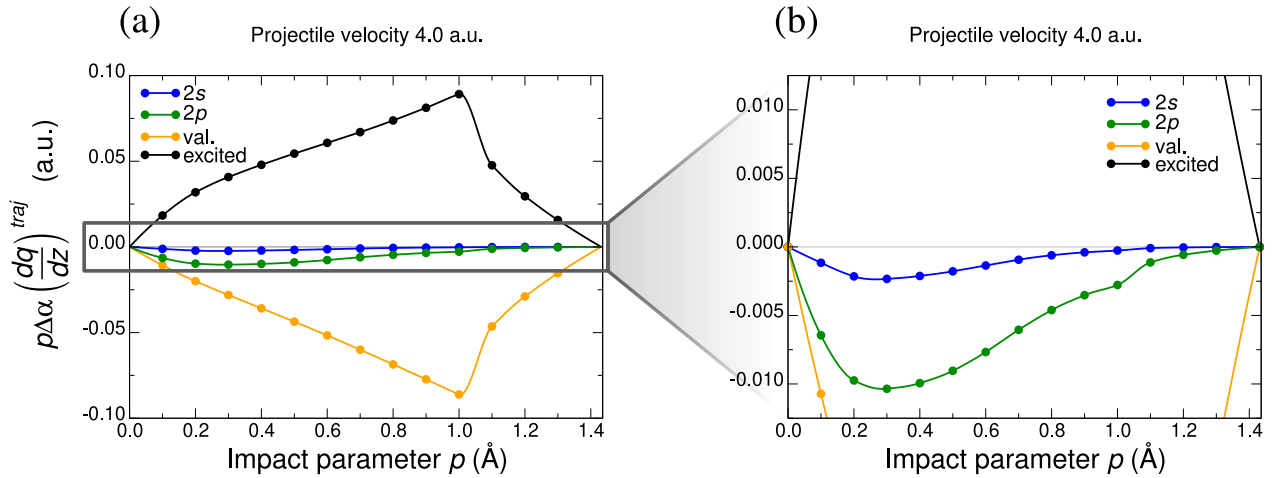


Figure 4.7 : Weighted value of $\left(\frac{dq}{dz}\right)^{traj}$ for the proton in aluminum as a function of the projectile impact parameter. The projectile velocity is $v = 4.0$ a.u. ($E_{proj}^{kin} = 400$ keV). Panel (b) presents a magnification of (a)-panel.

Comparing the positions of the peaks of the weighted occupations of different levels and the position of peaks of the different contributions to the stopping power (Fig. 4.4) one can see a perfect match: The maximum of 2s and 2p electrons corresponds to the impact parameter $p \approx 0.3$ Å, while the valence contribution mainly repeats the weight function form and has a maximum at $p \approx 1.0$ Å. However, the relative contribution of the core state occupations to the excited state occupation is not the same as the contribution of the core stopping power to the total one: The peak of the excited state occupations corresponding to the core states depopulation (at $p = 0.3$ Å) is much less pronounced than in the case of the weighted stopping power. One can explain this observation by the fact that the valence electrons are much easier to excite. Therefore, the contribution to the stopping power of valence $\frac{dq_{val}}{dz}$ and core $\frac{dq_{2s, 2p}}{dz}$ occupation changes have to be taken into account in different ways. In other words, the promotion of one 2s electron to the conduction band due to the projectile passage would contribute more to the stopping power than the promotion of one valence electron. Hence, the direct comparison of the absolute values of the occupation changes from different levels cannot be translated into a conclusion on the stopping power. Therefore, in this section, we concentrate rather on the

velocity dependence of the occupations and on the comparison of the occupations of the same levels under different conditions (frozen core simulations, channeling conditions).

4.2.3 Valence electron occupations in frozen core dynamics

Having adapted the methodology of the average occupation change calculation from the stopping power, we would like first to verify whether the separation of the total stopping power S^{tot} into the core S^{2s} , S^{2p} and the valence S^{val} contributions (equations 4.1-4.4) is reasonable for the proton in aluminum system (we do not consider here the 1s contribution because it is negligible).

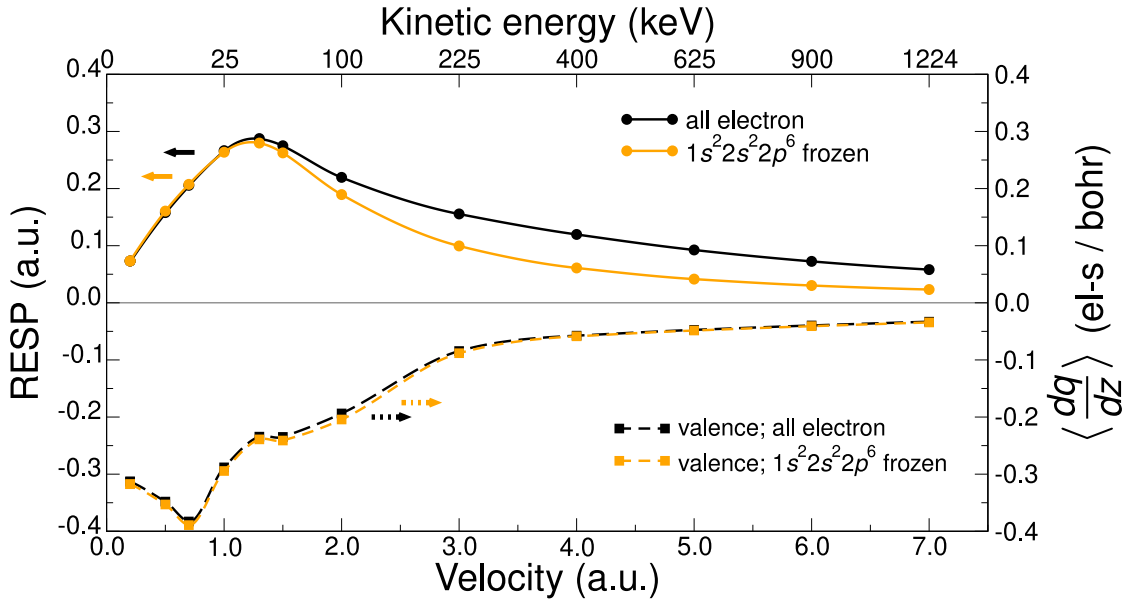


Figure 4.8 : Proton in aluminum simulation within the all-electron (black curves) and the frozen core (orange curves) dynamics. Random electronic stopping power is presented in solid and random valence state occupations change in dashed lines.

Fig. 4.8 shows the stopping power of proton in aluminum performed in the all-electron and the frozen core dynamics. As well, on the same graph we present the calculations of the occupation change of the valence electrons $\langle \frac{dq_{val}}{dz} \rangle$, similarly, for the all-electron response and the frozen core case. One can see that while the stopping power has considerably lower values starting from $v = 2.0$ a.u. ($E_{proj}^{kin} = 100$ keV) in the case of the frozen core, the dependence of the valence state occupations is almost the same for both the all-electron and the frozen core dynamics. This demonstrates that, in the case of the proton irradiation in aluminum, the core and the valence states excitation dynamics can be decoupled: Regardless of the fact that the core excitations are allowed or not, during the irradiation simulation, the valence electrons excitation dynamics is almost the same. Hence, we justify the separation of the stopping power into the core and valence contributions

done is the previous chapter. For the proton in lithium target case (not presented) we have obtained the same conclusion.

Concerning the correlation between RESP and the valence state occupations, one can note the overall similarity of the curves. However, the peak of the valence occupations is shifted to the left: $v \approx 0.7$ a.u. ($E_{proj}^{kin} \approx 12.2$ keV), while RESP has the maximum at $v \approx 1.3$ a.u. ($E_{proj}^{kin} \approx 42.2$ keV). One can also note that the valence electrons are well excited even at small projectile velocities: For the lowest projectile velocity that was used in our calculations ($v = 0.2$ a.u. or $E_{proj}^{kin} = 1$ keV), the valence state occupation change is still large (80 % of the peak value), while the stopping power is already quite low (25 % of the peak value) and goes linearly to zero.

4.2.4 Core electron occupations velocity dependence

Now, we will focus on the $2s$ and $2p$ core occupations change dynamics. Fig. 4.9 presents the contribution of the core electrons (sum of $2s$ and $2p$) to the random stopping power as a function of proton velocity, calculated as follows

$$\langle S_e \rangle^{core} = \langle S_e \rangle^{total} - \langle S_e \rangle^{frozen\ 1s2s2p}. \quad (4.6)$$

In the same plot we present the random occupation change of $2s$ and $2p$ levels separately. We observe that the proton velocity at which the core electrons are the most excited is about $v = 3.0$ a.u. ($E_{proj}^{kin} = 22.5$ keV). This velocity is different from the peak velocity of the total stopping power.

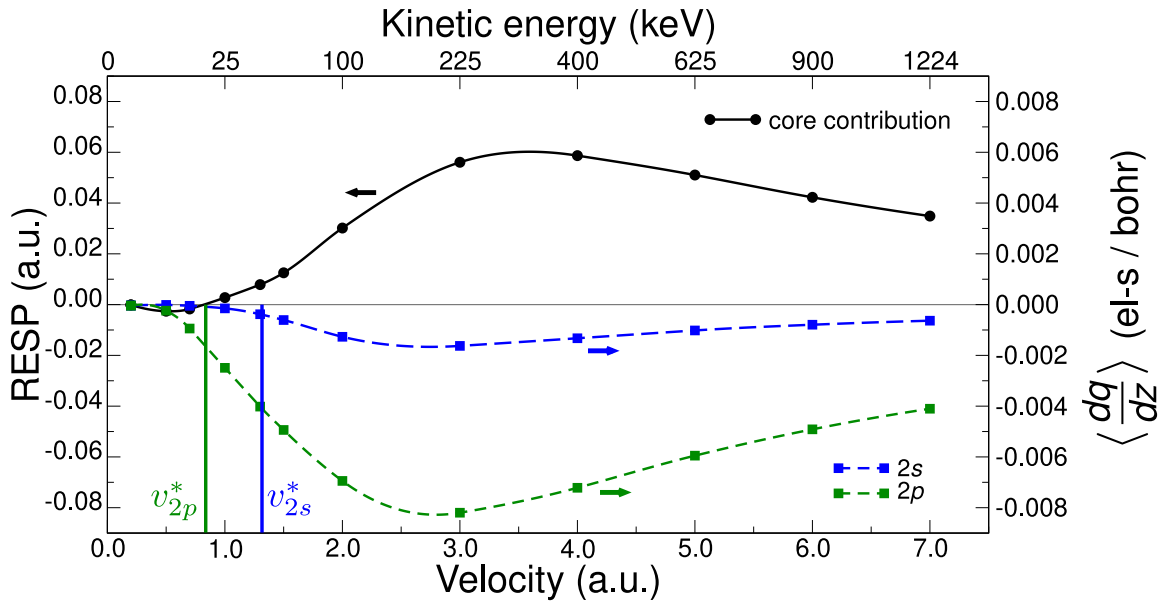


Figure 4.9 : Proton velocity dependence of the core ($2s + 2p$) contribution to the random electronic stopping power (black curve), $2s$ (dashed blue) and $2p$ (dashed green) random occupation changes.

One can also note a threshold behavior at low velocities of all the curves: after some projectile velocity, the core contribution to the stopping power as well as the occupation changes start to increase. Such behavior is inherent to semiconductors, where the stopping power is strictly equal to zero for the projectile velocities lower than the threshold velocity v^* , that has the following expression (in SI units) [16]

$$v^* = \frac{E_g}{2k_F\hbar}, \quad (4.7)$$

where E_g is the bandgap energy (in the case of semiconductors) and k_F is the Fermi wave number. k_F can be expressed from the Fermi velocity v_F as follows

$$\hbar k_F = m_e v_F. \quad (4.8)$$

In turn, one can find the Fermi velocity of a homogeneous electron gas from the electron density n in the following way

$$v_F = \frac{(3\pi^2 n)^{1/3} \hbar}{m_e}. \quad (4.9)$$

The final expression for the threshold velocity is then

$$v^* = \frac{E_g}{2\hbar(3\pi^2 n)^{1/3}}. \quad (4.10)$$

We can apply this formalism to the $2s$ and $2p$ electrons of aluminum assuming their effective bandgap energy equal to the energy difference of the level with respect to the Fermi level: -102.2 eV for $2s$ and -65.0 eV for $2p$ (see Table 4.1). Usually, one takes the density for the Fermi velocity calculations equal to the valence electron density. However, since we consider here $2s$ and $2p$ electrons, we will include them into the electronic density n . One should note that such treatment is approximate.

Finally, we get the following threshold velocities for $2s$ and $2p$ electrons: $v_{2s}^* = 1.32$ a.u. ($E_{2s}^* = 43.5$ keV), $v_{2p}^* = 0.84$ a.u. ($E_{2p}^* = 17.6$ keV). These values are indicated in Fig. 4.9 as vertical lines. We can see that, even this treatment that uses the effective bandgap is approximate, the values of the threshold velocities are in a very good agreement with the *ab initio* RT-TDDFT simulations results.

One can add that the threshold velocity for the $1s$ electrons (according to their energy ≈ -1500 eV) is very large and is equal to $v_{1s}^* = 19.3$ a.u. ($E_{1s}^* = 10.0$ MeV). At these projectile velocities, the electronic stopping power of proton is already very low.

4.2.5 Channeling conditions

Here we would like to analyze the difference between the random and channeling conditions for both the stopping power and the electronic occupations as a function of the proton velocity presented in Fig. 4.10. The channeling stopping power is lower than the random

one for all the projectile velocities. Thanks to the occupation analysis we have a clue about the contributions of different electronic levels to the difference in the stopping power.

First, while the $2s$ excitations do contribute to the random stopping for $v > 1.0$ a.u. ($E_{proj}^{kin} > 25$ keV), their contribution in the case of the channeling trajectory is negligible (compare solid and dashed blue lines in Fig. 4.10 (c)).

Concerning the $2p$ core electrons, we can see small excitations in the channeling case starting from $v > 2.0$ a.u. ($E_{proj}^{kin} > 100$ keV) that increase with the projectile velocity (compare solid and dashed green curves in Fig. 4.10 (c)).

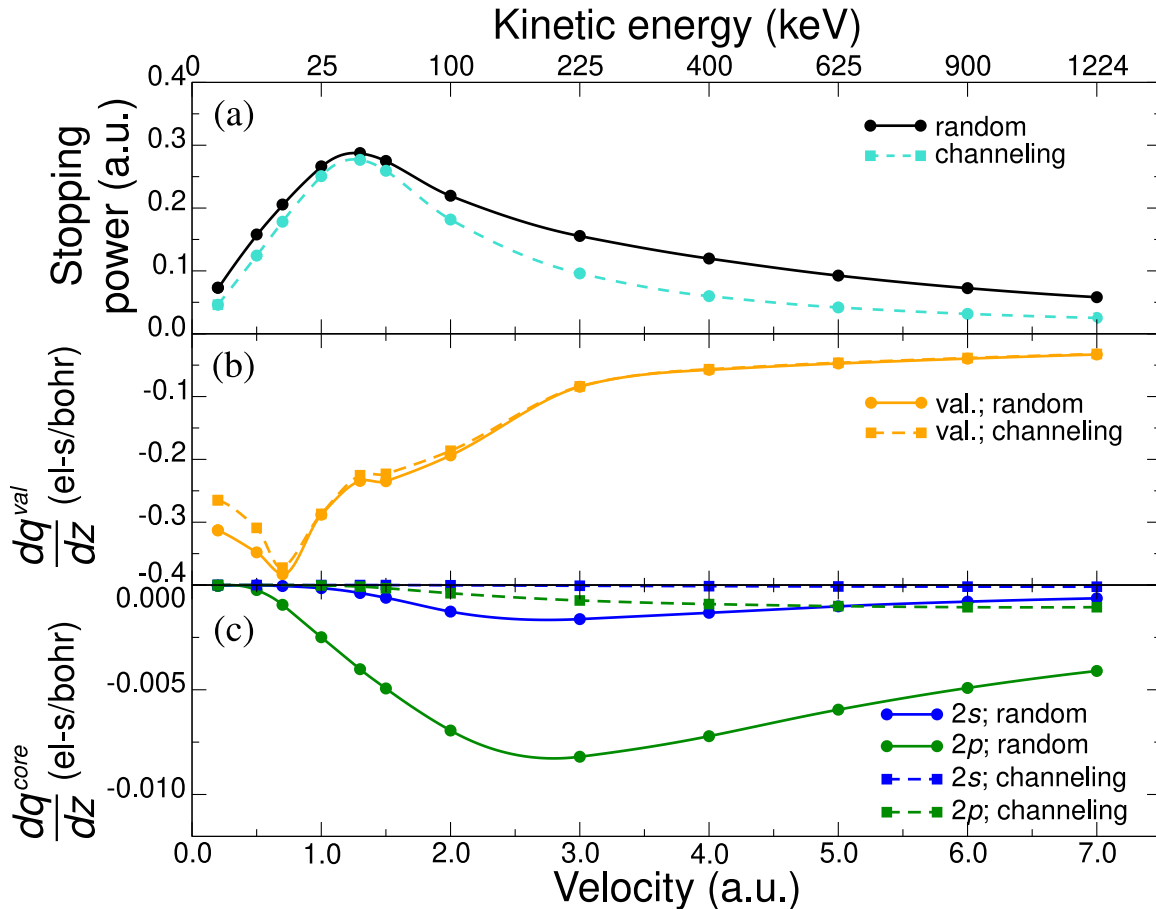


Figure 4.10 : (a) Random (black solid line) and channeling (turquoise dashed line) electronic stopping power of proton in aluminum. (b), (c) Random (solid lines) and channeling (dashed lines) occupation change as a function of the proton velocity. (b)-panel presents the valence electron and (c)-panel shows the core ($2s$ and $2p$) occupation changes. The aluminum cluster orientation is $[001]$.

Random and channeling valence electron occupations changes are the same for large projectile velocities ($v \geq 3.0$ a.u. or $E_{proj}^{kin} \geq 225$ keV). However, we can see a difference in the occupation dynamics of the valence levels for lower velocities (solid and dashed orange lines in Fig. 4.10 (b)).

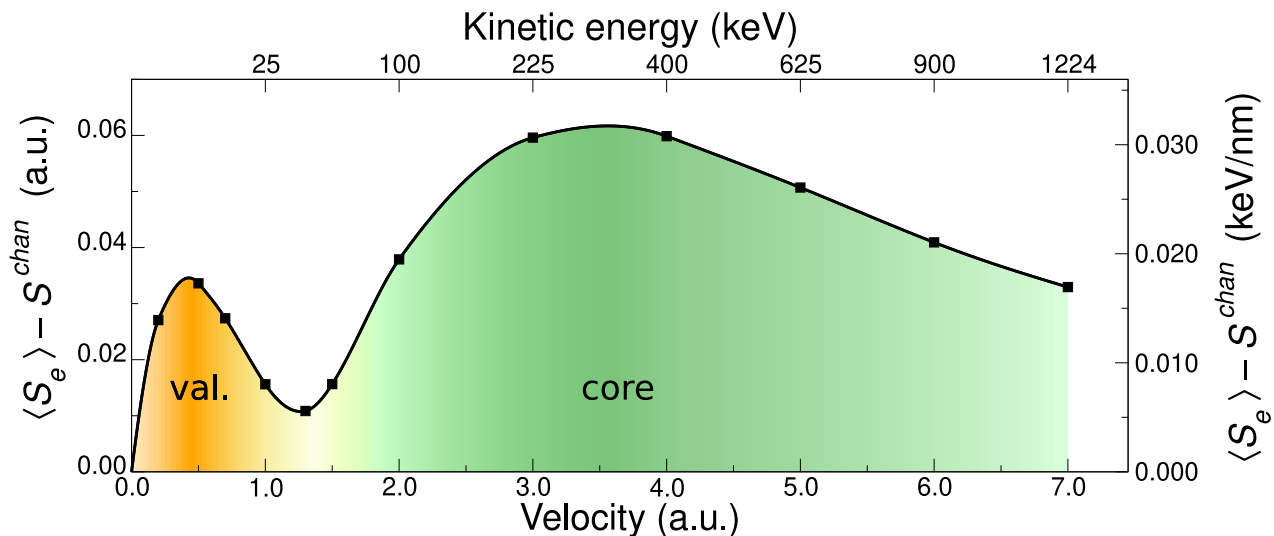


Figure 4.11 : Difference between the random electronic stopping power and the channeling stopping power of the proton in the aluminum target. Orange fill of the curve corresponds to the *valence* occupation dynamics difference in the random and channeling cases and green fill corresponds to the *core* occupations dynamics difference.

Therefore, we can conclude, that for the small projectile velocities, the channeling stopping power is lower than the random one because of lower valence electrons excitations (core excitations being negligible at small v). While for large projectile velocities, the difference in the stopping power is mostly due to lower core electron excitations in the channeling case. This conclusion is illustrated in Fig. 4.11 that presents the difference between the random and the channeling stopping power. The curve has two peaks. The maximum of the random - channeling stopping at low velocities is due to the difference in the valence excitation dynamics, while the peak at high velocities is due to the difference in the core electron excitations in the random and channeling simulations.

Conclusive remarks

As we have seen in this section, the frozen core technique and the occupation analysis provide useful pieces of information about different electronic level excitations during the RT-TDDFT simulations. Both techniques give quite similar information: We have seen a good agreement between the contributions of different electrons to the stopping power calculated using the frozen core simulations and the occupation change. There is a good correlation for both the impact parameter and the velocity dependencies. However, using the frozen core technique, we have information about the relative contributions of the electrons from different shells to the *stopping power*. Whereas we do not have this piece of information from the occupation analysis, where we can compare only the absolute values of occupation changes within the same electronic levels (bands). On the plus side of the occupation analysis technique, using this method we were able to demonstrate that the

valence and the core excitations are decoupled, while it is not possible to show within the frozen core simulations.

Hence, we conclude that the occupation analysis can be a complementary tool to the frozen core technique. One should also mention that the calculation of the occupation dynamics during the RT-TDDFT simulations is performed on-the-fly and adds less than 0.5 % of the overall computational time, whereas, for the frozen core technique, one needs to run separate simulations.

4.3 Centroid path approximation accuracy

In this section, we would like to discuss the accuracy of the centroid path approximation in the random stopping power calculations. This approach was presented in section 1.5.2 and it is used in some RT-TDDFT stopping power calculations, for example, in this reference [88].

We have performed the calculations of the stopping power for the centroid trajectories $S_e^{traj}(p_{cent})$ for proton in lithium and proton in aluminum targets having the [001] orientation. For lithium, the impact parameter corresponding to the centroid path is $p_{cent}^{Li} = (\frac{a_{lat}^{Li}}{12}; \frac{a_{lat}^{Li}}{4})$ and for aluminum $p_{cent}^{Al} = (\frac{a_{lat}^{Al}}{12\sqrt{2}}; \frac{a_{lat}^{Al}}{4\sqrt{2}})$, where a_{lat}^{Li} and a_{lat}^{Al} are the lattice constants of lithium (bcc structure) and aluminum (fcc structure) respectively.

We compare the random stopping power calculated within the centroid path approximation with the random stopping obtained using our averaging approach that has only the polar symmetry approximation and leads to errors not larger than 2 % (see section 3.1.3). Fig. 4.12 shows this comparison. It is seen that the centroid path approximation works well at low projectile velocities ($v < 1.0$ a.u. or $E_{proj}^{kin} < 25$ keV). However, for large velocities, it leads to significant errors (up to 35 %) in $\langle S_e \rangle$ for both targets.

Based on our calculations of the stopping power along the y -axis, $S_e^{traj}(\mathbf{p} = (0; p_y))$, we have found the impact point p'_y at which the stopping power $S_e^{traj}(\mathbf{p} = (0; p'_y))$ is equal to the random stopping $\langle S_e \rangle$ (see Fig. 4.13). As one can see, this point changes as a function of the proton velocity: At low velocities, the stopping power dependence on the impact parameter is quite flat, therefore, any impact parameter point in some large interval would yield almost the same value of S_e^{traj} as the random $\langle S_e \rangle$. Concerning the high-velocity limit, the core excitations become significant, therefore the p'_y value shifts towards the nucleus.

In order to demonstrate that the centroid path error at high velocity comes from the core electrons, we have performed the same centroid path/ensemble average comparison as in Fig. 4.12 but with the frozen core.

The results are presented in Fig. 4.14. One can see that in this case, the stopping power obtained within the centroid path approximation agrees very well (less than 3 % of difference) with the $\langle S_e \rangle$ values obtained using the ensemble average. It is important to mention that our results shed new light on those obtained by Yost and coworkers [87] for the α -particle stopping power calculations in SiC. Indeed, in that work, a pseudopotential

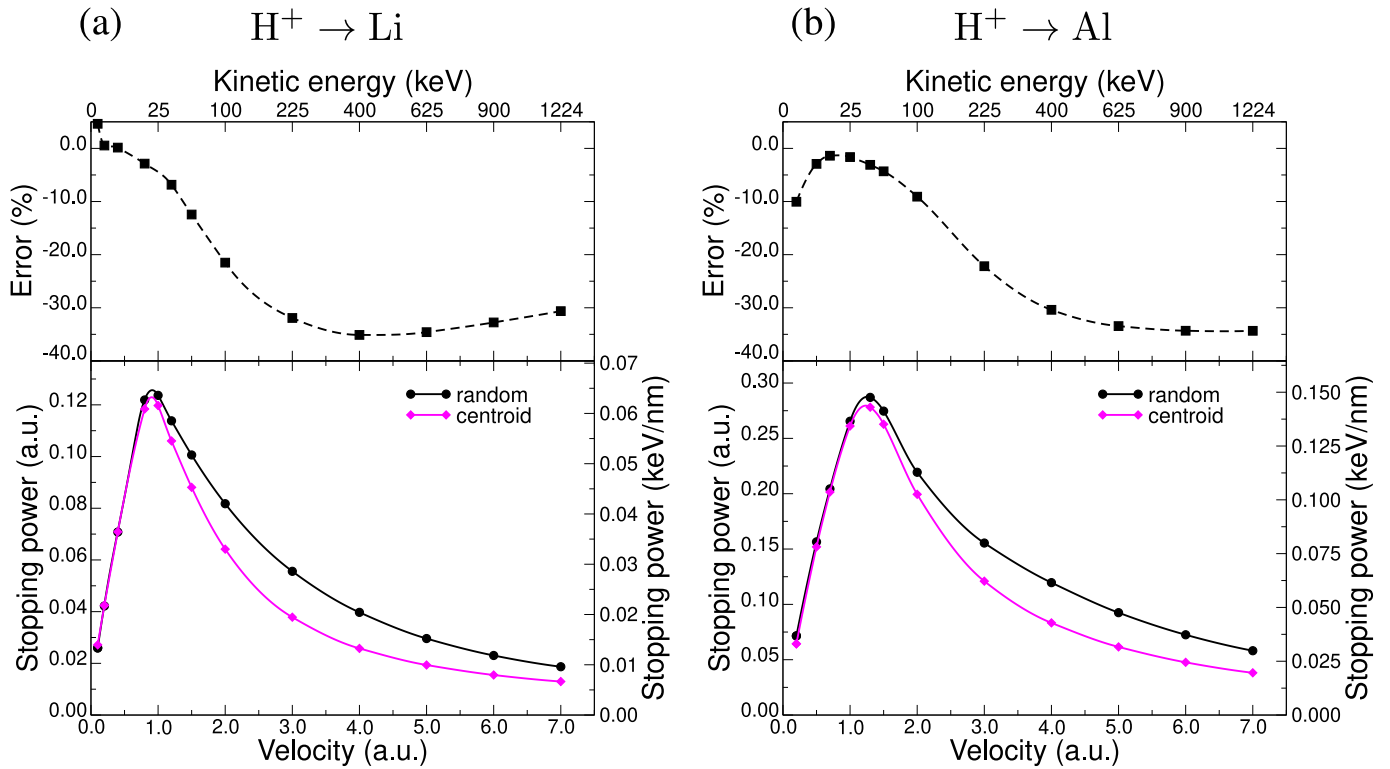


Figure 4.12 : Random electronic stopping power calculated within the impact parameter averaging (black curves) and the centroid path approximation (pink curves) of proton in lithium (a), and proton in aluminum (b). The relative error of the centroid path approach with respect to the impact parameter averaging is shown on the top plots in black dashed lines.

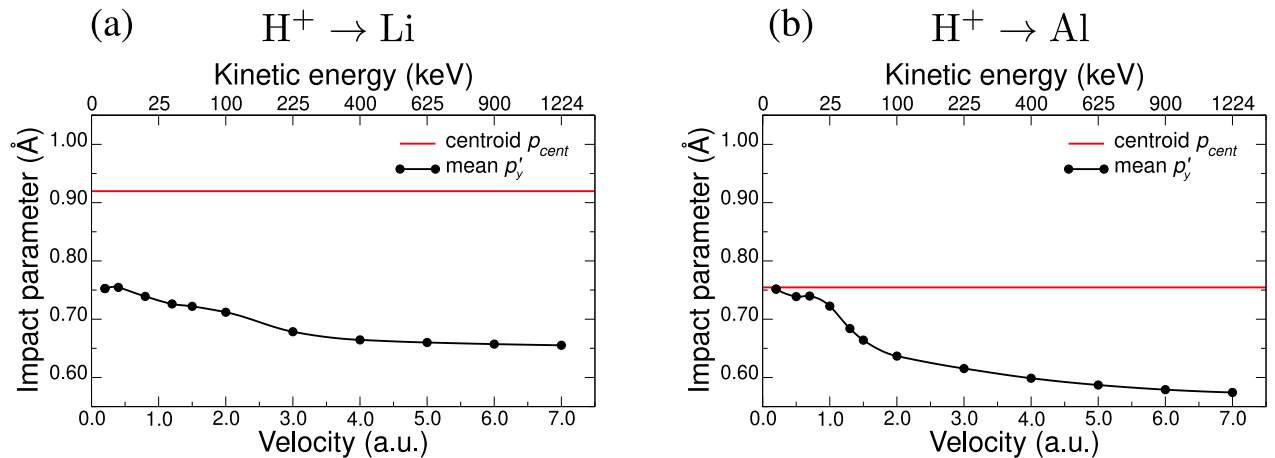


Figure 4.13 : The impact parameter along y -axis p'_y at which the stopping power is equal to the random one. The norm of the centroid impact parameter p_{cent} is presented as the red line. (a) Proton in lithium. (b) Proton in aluminum.

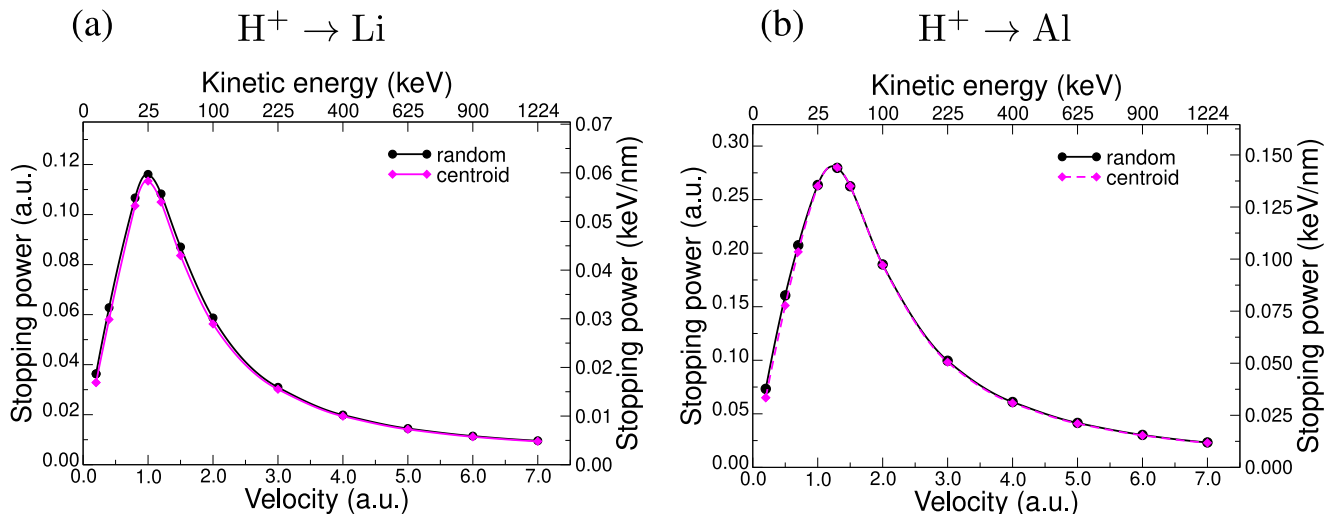


Figure 4.14 : Random electronic stopping power calculated within the impact parameter averaging and the centroid path approximation within the frozen core ($1s2s2p$) dynamics for: (a) Proton in lithium irradiation; (b) Proton in aluminum.

that does not include the core states was used and, hence, the centroid path approximation compared well with the ensemble average results. This fact shows that the centroid path approximation can yield a reasonable estimate of the average *only* in the case of the frozen core electron dynamics.

Finally, we conclude that, in the case of the all-electron calculations, the centroid path approach yields significant errors in the random stopping power for proton in lithium and aluminum systems. Therefore, the average over the impact parameter (described in section 3.1.3) should be carefully performed for each projectile velocity.

4.4 RESP of α -particle

Having analyzed in detail different aspects of the stopping power using the proton projectile as an example, we will now mostly concentrate on the random stopping and on the comparison of the stopping power of different ionic projectiles. We start with the α -particle irradiation simulations.

Fig. 4.15 presents the stopping power of α -particle in lithium and aluminum targets. As was done for the proton case (Fig. 4.1), we compare our *ab initio* results with SRIM, experimental data, and the linear response theory results. For both targets, one can note similar trends that we have seen in the case of the proton projectile: overestimation of the RT-TDDFT stopping power with respect to SRIM around the peak and underestimation at high projectile velocities. The disagreement between SRIM and RT-TDDFT is larger in the case of the lithium target for low v . One can note that in this case, SRIM code had only one experimental point in its database at large α -particle velocity ($v = 9.3$ a.u. or $E_{proj}^{kin} = 8.6$ MeV). Remarkably, this experimental point is not far from RT-TDDFT values.

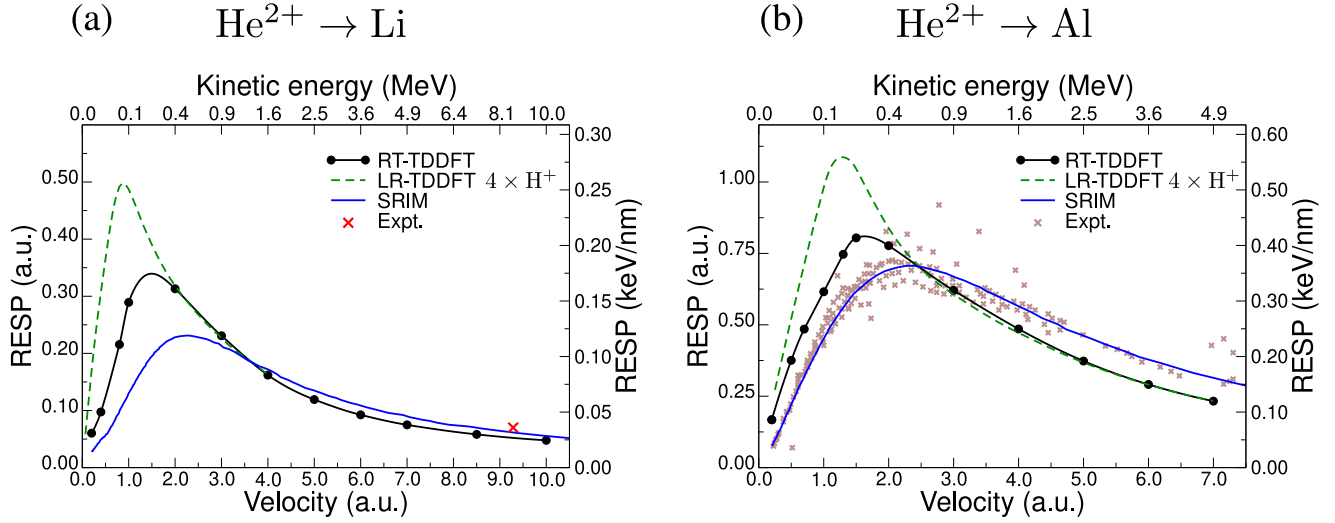


Figure 4.15 : Random electronic stopping power of α -particle in lithium, (a), and aluminum, (b). The RT-TDDFT results obtained in this work are in black. Data from the SRIM code (in blue) as well as the experimental points (crosses) are taken from the reference [20].

However, in the region of the stopping power peak and of the low velocities, similarly to proton in Li case, we argue that SRIM data is not reliable because of the absence of the experimental data.

Concerning the linear response results, within this theory, the random stopping power of an ion having the charge Z , S^Z , can be found from the proton stopping power, S^{H^+} , in the following way [34]

$$S^Z = Z^2 S^{\text{H}^+}. \quad (4.11)$$

Hence, within the linear response, the stopping power of the α -particle is simply $4 \times S^{\text{H}^+}$. It is seen from Fig. 4.15 that for the α -particle velocities $v > 3.0$ a.u. ($E_{proj}^{kin} > 0.9$ MeV) the linear response results are in a very good agreement with the RT-TDDFT results. However, LR-TDDFT overestimates much the RT-TDDFT and SRIM values for the projectile velocities around the stopping power peak and for lower v . Indeed, the linear response theory does not include the charge transfer for the projectile irradiation simulations. This becomes a significant problem for low projectile velocities and the projectile charges larger than $Z = 1$.

4.5 Penetration depth of H⁺ and He²⁺ within CSDA

Having calculated the stopping power of proton and α -particle in lithium and aluminum targets, we can now evaluate the penetration depths of the projectiles using the continuous slowing down approximation (CSDA). This approximation was introduced in section 3.5.1. We have used the CSDA approach to evaluate the projectile slowing down during its passage

along the cluster length. Here, we would like to calculate the penetration depth at which the projectile will be completely stopped. Therefore, the penetration depth Δz_{CSDA} has the following expression

$$\Delta z_{CSDA} = \int_0^{E_0} \frac{dE}{S(E)} = \int_0^{v_0} \frac{mv dv}{S(v)}, \quad (4.12)$$

where E_0 and v_0 are the initial projectile energy and velocity before entering the material. In order to find the penetration depths corresponding to the channeling conditions as well as to the random trajectories, we will substitute the stopping power in equation 4.12 with the channeling or the random stopping calculated in RT-TDDFT.

The CSDA approach assumes the projectile penetration trajectory along a straight line. However, as we have seen in section 3.5, the deflection of a projectile from the straight-line path can be significant at low projectile velocities. Therefore, in the case of the random stopping power, the CSDA approach that we use here, can provide only the maximal penetration depth corresponding to the straight trajectory. The complete penetration depth profile based on the electronic stopping power can be obtained using the Monte Carlo simulations within the binary collision approximation. This approach is implemented, for example, in SRIM [20] or Iradina [139] codes.

In contrast, in the case of the channeling propagation, the projectile indeed moves along a straight-line trajectory (see section 1.5.3). Hence, the penetration depth profile in this case should be very narrow and the CSDA approach has to provide the value corresponding to the position of the profile peak.

Fig. 4.16 presents the stopping power (RT-TDDFT random, RT-TDDFT channeling and the data from the SRIM stopping power) as well as the penetration depths for proton and α -particle in lithium and aluminum targets calculated from these stopping power curves. For the projectile energy range studied in this work, the penetration depth varies in a wide range (from 10^{-1} μm to 10^2 μm). Therefore, we present the data in the logarithmic scale.

In order to compare the numerical values of the penetration depths, we present the Δz_{CSDA} values in Table 4.1 for the initial projectile energy $E_0 = 1$ MeV ($v_0 = 6.3$ a.u. for H^+ and $v_0 = 3.2$ for He^{2+}).

	Li			Al		
	random	channeling	SRIM	random	channeling	SRIM
H^+	55.5	107.2	51.7	18.3	37.8	14.9
He^{2+}	14.0	26.5	13.6	4.7	9.2	4.1

Table 4.2 : Penetration depths in μm for the proton and α -particle irradiation in lithium and aluminum targets calculated within the CSDA approach. The values are calculated using the random and channeling stopping power calculated in this work as well as from the SRIM stopping power. The initial projectile kinetic energy is taken as $E_0 = 1$ MeV.

Despite the discrepancies between the SRIM data and RT-TDDFT random stopping power calculations, the penetration depths of H^+ and He^{2+} projectiles in both targets are in

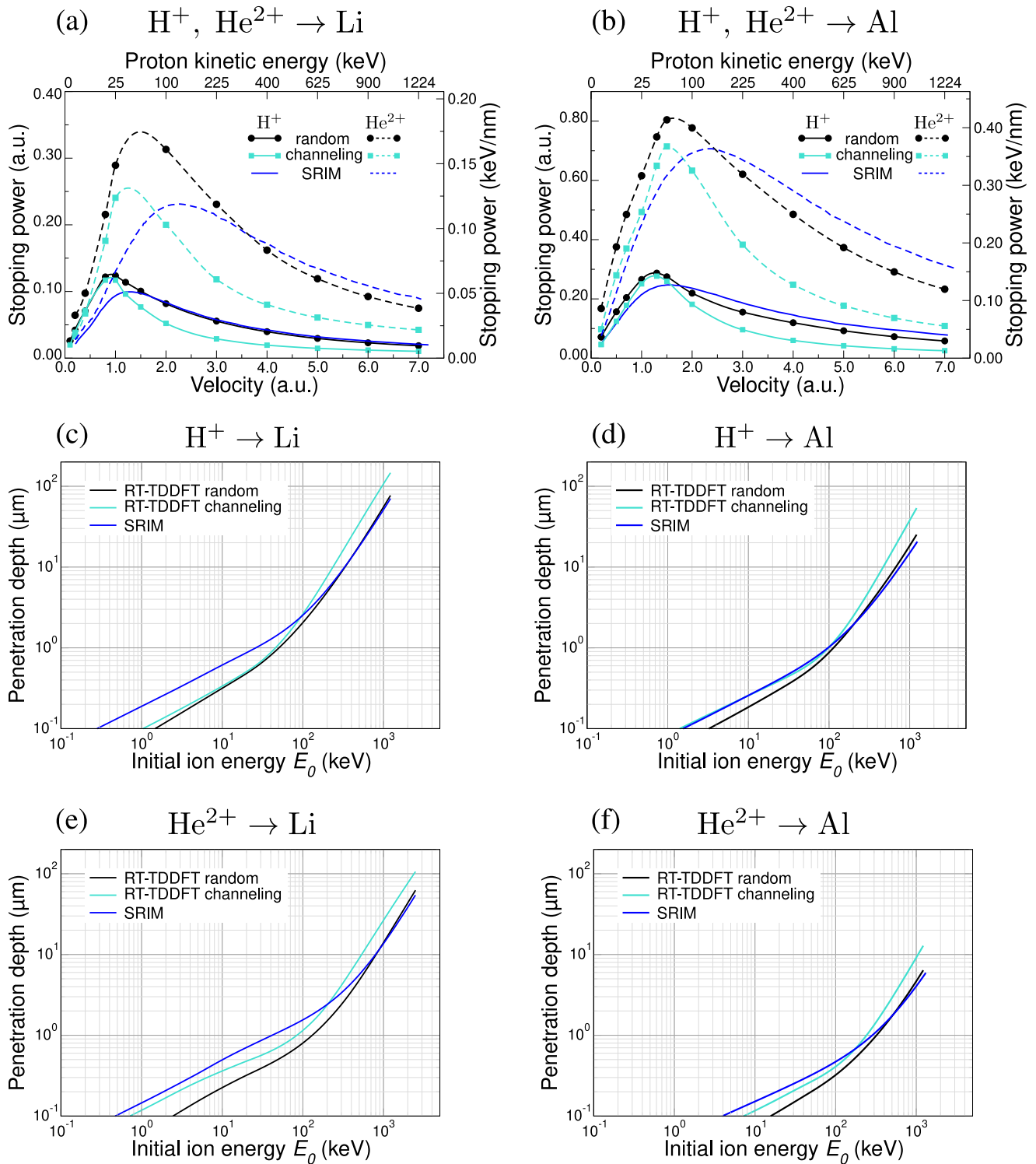


Figure 4.16 : (a), (b) Electronic stopping power of proton (solid lines) and α -particle (dashed lines) in lithium, (a), and aluminum (b) as a function of the projectile velocity. The penetration depth as a function of the projectile initial energy is presented for proton in lithium (c), proton in aluminum (d), α -particle in lithium (e) and α -particle in aluminum (f). The curves corresponding to the random trajectory obtained from RT-TDDFT are in black, from SRIM in blue and the curves corresponding to the channeling conditions obtained from RT-TDDFT are in turquoise.

a good agreement. This is due to the fact that the random stopping power calculated in RT-TDDFT is more or less in agreement with SRIM for quite a large range of projectile velocities after the stopping power peaks. On the other hand, there is a compensation of errors: SRIM is larger than RT-TDDFT for high v and lower for small v . In the case of lower initial projectile energies E_0 , especially, before the peaks, the discrepancies are larger.

Concerning the channeling penetration depth, one can note that it is approximately 2 times lower than in the case of the random trajectory for both projectiles and both targets. We would like to mention that the SRIM database does not contain information about the channeling projectiles. In our *ab initio* RT-TDDFT calculations, it is easier to obtain the channeling stopping power because to do that, one needs to calculate S^{straj} at only one impact point (instead of 13).

4.6 RESP of antiproton

Having analyzed the “usual” types of projectiles, H^+ and He^{2+} , we now switch to a more “exotic” case: antiproton. In our code, the implementation of the antiproton irradiation just means a change of the sign of the perturbation potential from $Z = 1$ (proton case) to $Z = -1$ in equation 3.1.

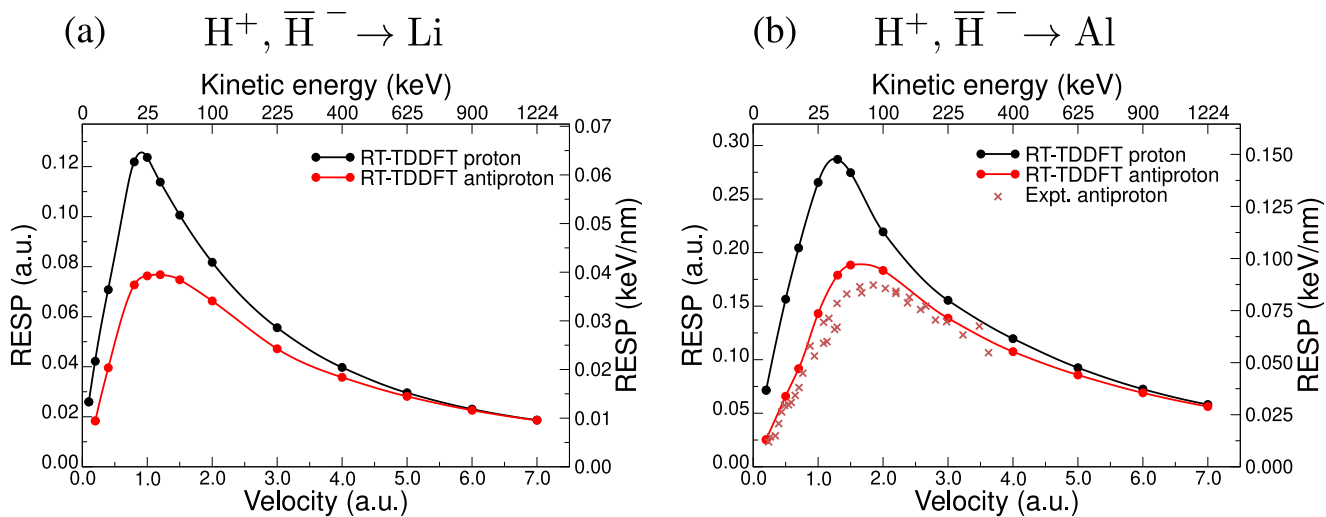


Figure 4.17 : Random electronic stopping power of proton (black) and antiproton (red) irradiation in lithium, (a), and aluminum, (b). Experimental points (for \bar{H}^- in Al) are depicted in crosses and are taken from references [140–142].

Fig. 4.17 presents the comparison of the random stopping power for proton and antiproton in lithium and aluminum targets. One can note that the random stopping power of antiproton is lower than that of proton, known as the so-called Barkas effect [143]. This shows that the electron screening for proton and antiproton is different [144]. Though,

at large projectile velocities, the random stopping power of both projectiles is almost the same.

Since the linear response results are simply proportional to Z^2 , within this theory one obtains the very same result as for proton projectile. Indeed, the Barkas effect is proportional to Z^3 [145] and cannot be captured by LR-TDDFT.

Concerning the comparison with the experimental data (available for antiproton in aluminum), we see a good agreement with our *ab initio* results, though, RT-TDDFT slightly overestimates the experiment around the peak (around 12 %).

4.7 Effective charge of projectile

In this section, we will study in more detail the discrepancies between RT-TDDFT and the linear response results (obtained in reference [33]). While the agreement between LR-TDDFT and RT-TDDFT is strikingly good for the proton irradiation simulations in lithium and aluminum targets, the disagreement for $\bar{\text{H}}^-$ and He^{2+} projectiles is compelling, especially for the projectile velocities around the stopping power peaks (see Fig. 4.15 and 4.17). Having the stopping power values obtained from both methods, we can introduce an idea of an effective projectile charge: For the stopping power within LR-TDDFT of a projectile of charge Z , S^Z , instead of using the nominal projectile charge Z (as in equation 4.11), we substitute it with Z_{eff}

$$S^Z = Z^2 S^{\text{H}^+} \quad \rightarrow \quad S^Z = Z_{eff}^2 S^{\text{H}^+}. \quad (4.13)$$

Then, we select this effective charge in a way to reproduce the stopping power values calculated within RT-TDDFT. Finally, we can find Z_{eff} simply from the ratio of the stopping power S^Z , calculated in RT-TDDFT, and the stopping power of proton

$$Z_{eff} = (S^Z / S^{\text{H}^+})^{1/2}. \quad (4.14)$$

One can also interpret Z_{eff} as a scaling factor between LR-TDDFT and RT-TDDFT.

Fig. 4.18 presents the effective charge calculated in this way for $\bar{\text{H}}^-$ and He^{2+} projectiles in lithium and aluminum targets. The value of Z_{eff} varies as a function of the projectile velocity. This shows that for these projectiles additional higher-orders in Z perturbation terms are necessary to obtain an adequate stopping power. Though, one can see from Fig. 4.18 that at large v , the effective charge reaches the values given by the linear response theory: $|Z_{eff}| = 1$ for antiproton and $Z_{eff} = 2$ for α -particle, meaning that this level of theory is enough for a proper description of the electronic response at high v .

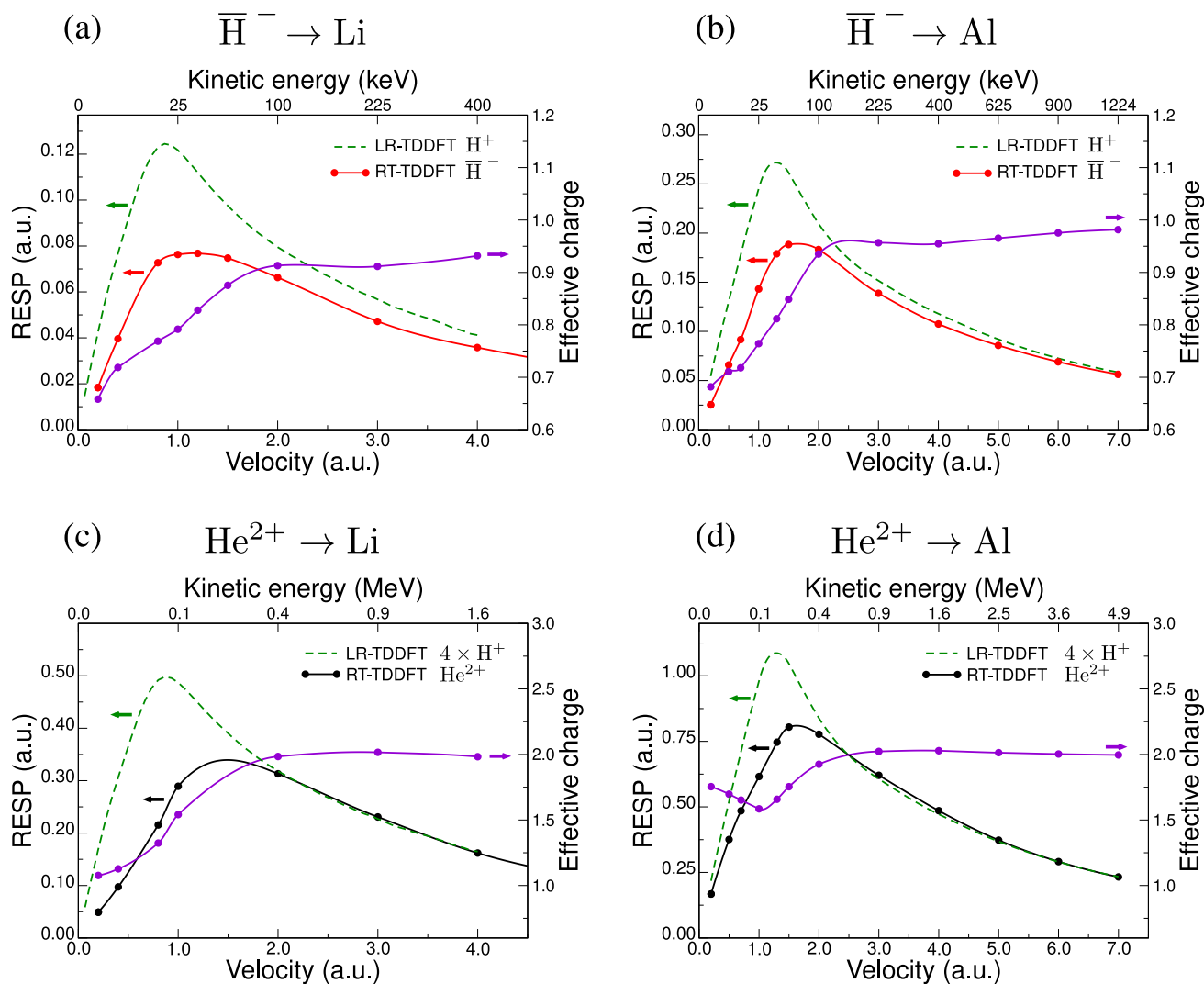


Figure 4.18: Effective charge (in violet) of antiproton ((a) and (b)) and α -particle ((c) and (d)) irradiation in lithium and aluminum targets. Random electronic stopping power obtained from the linear response theory is presented in green dashed lines, the one obtained from RT-TDDFT is presented in red (for antiproton) and in black (for α -particle).

4.8 Summary

In this chapter, we have present the random electronic stopping power calculated with our RT-TDDFT localized basis code. The calculations were performed for proton, antiproton and α -particle irradiation in lithium and aluminum targets.

Concerning the proton irradiation in lithium, for large projectile velocities, we note a good agreement between our RT-TDDFT results, SRIM and experimental points. For the velocities lower than the peak, the experimental data are absent and the disagreement with SRIM is significant. We think that since in this velocity range there is no experimental data, the SRIM results are simply a reckless extrapolation. For the aluminum target, the experimental database is considerably larger for all the velocities and the agreement between SRIM is better. However, we note an underestimation of RT-TDDFT with respect to SRIM around the peak and an overestimation for larger velocities. Such behavior is common to other *ab initio* codes though. Even if the disagreements are not significant, we have tried to identify their possible origins: we have analyzed the exchange-correlation functional importance and the contribution of $1s$ electrons to the stopping power. None of those can lead to the observed difference between the *ab initio* codes and the experimental data. Then, using the proton in Al system, we have studied in detail the contribution from different electronic levels to the stopping power using the frozen core technique and the occupation analysis. We have also seen the spatial extension and the velocity dependence for each level separately.

For the case of α -particles in Li and Al, one can draw a similar conclusion as in the proton case. For the lithium target, the comparison with SRIM is good for the velocities where one has experimental points (only one odd data point available in this case though). For aluminum, one has a large number of measurements and the overall comparison is better than in lithium case.

Then, using the stopping power values obtained from our RT-TDDFT code for the above-mentioned projectiles and target, we have calculated the penetration depths within the CSDA approach. The calculations were done for the random electronic stopping power and for the channeling one. We have seen that in the channeling conditions the projectiles travel around 2 times deeper in targets before the complete stopping.

For the antiproton irradiation, we have shown that the proton stopping power is larger than in the antiproton case for the projectile velocities around the stopping power peak. However, in the regime of high velocities, the stopping power values corresponding to both projectiles become very similar.

Concerning the LR-TDDFT results, we have seen a very good agreement between LR-TDDFT and RT-TDDFT for the proton irradiation, while this approach fails for the other projectiles. From the stopping power obtained from RT- and LR- TDDFT methods, we have evaluated the effective charge of antiproton and α -particle.

Conclusions and perspectives

Conclusions

In the present work, we have developed a real-time TDDFT approach based on the Gaussian basis set code MOLGW for the electronic stopping power calculations. This development involved the following steps:

- The derivation of the time-dependent Kohn-Sham equations in the localized basis set.
- The implementation of different time propagation algorithms that consist in a propagator and a predictor-corrector scheme.
- The benchmarking of the implementation using the optical absorption spectra calculations.
- The optimization of different parameters for the stopping power calculations (cluster size, time step, impact parameter grid, basis set, etc.).
- The development of the post-processing scripts that allow us to manipulate a large amount of data (for example, one stopping power curve includes around 200 separate RT-TDDFT trajectories, for each trajectory one needs to apply the 3-step averaging procedure, described in section 3.1, in order to deduce the stopping power).

The developed methodology, in particular, equations 2.70 - 2.107, can be easily applied to any localized basis code that contains a standard ground-state DFT part in order to extend it to RT-TDDFT.

At the present moment, within this code, one can perform the non-perturbative absorption spectra calculations and, more importantly, the random electronic stopping power calculations of ionic projectiles. In the code, we have implemented the time propagation of Kohn-Sham equations, which is general to any time-dependent problem that one would need to solve numerically. Hence, our code is easy to generalize to any other perturbation type.

The overall computational performance of the code is very good (around 14 000 CPU hours for the random stopping power calculation for one projectile velocity within LDA exchange-correlation functional). For the moment, the target nuclei are fixed and the projectile is naked (without Gaussian basis functions around the impinging ion). Indeed, implementation of the moving basis functions around the projectile is quite a challenging task because of the following reasons: 1) The two-electron integrals, which are presently calculated once at the beginning of a calculation, would change in time because of the changing basis set; 2) The time propagation in an evolving Hilbert space would lead to additional complicated terms in equations 2.70 - 2.107 [146].

We expected benefits from the localized basis implementation, therefore, here, we would like to reevaluate the pros and cons of the localized basis implementation based on the accomplished calculations:

- As was anticipated, one of the main advantages of the localized basis codes with respect to the stopping power calculations is the cheap account of core electrons that we prove to be very important in this problem. In plane-wave codes, the explicit treatment of core electrons can come at a prohibitive computational expense because of very high cutoff energies required in this case [88].
- The calculations with the hybrid exchange-correlation functionals (tested B3LYP, PBE0, HSE08) are about 7 times heavier than in the case of LDA, however, this timing stays still lower than a plane-wave calculation even within the LDA functional [91].
- Even if the ionic projectile is naked in our simulations, the basis functions centered around the nuclei are enough for light projectiles (H^+ , \bar{H}^- , He^{2+}) irradiation simulations.
- As an unexpected advantage, the tunable position-dependent basis set (described in section 3.2.1) is very useful together with the fixed projectile trajectory approximation (section 1.5.1) and the ensemble average technique (section 3.1.3). This technique allows one to save a large amount of computational time: The calculations with the mixed basis are around 4 times faster than in the case where the highest precision basis is assigned to all atoms of the cluster.
- In the case of highly energetic excitations (like one we have in the stopping power calculations), the basis set has a crucial importance (especially for the atoms that are close to the projectile trajectory): The stopping power variation with the basis set is almost one magnitude larger than the variation with any other simulation parameter (cluster size, impact parameter grid, exchange-correlation functional, time step, etc.). Therefore, one should pay special attention to the basis set problem when the excitation energy is large. In this work we have proposed two solutions related to this problem:

- 1) Extrapolation of the stopping power based on standard Dunning basis sets (described in section 3.3). The extrapolation is quite slow, therefore one needs to include the largest bases available for a given material. In addition to its computational expense, the problem of this approach is the fact that for some atoms (like Li), basis sets at high enough order are not available in the literature. We have shown that the incorporation of both diffuse and tight core basis functions is necessary for the extrapolation over the whole projectile velocity range.
- 2) Basis set generation (presented in section 3.4). The proposed approach is based on the maximization of the stopping power. The obtained in this work optimized bases for Li and Al targets, allow one to perform the RESP calculations with better accuracy than provided by the highest Dunning basis sets and with a lower computational time. The optimization procedure is quite simple to implement and parallelize. However, some additional algorithmic optimization and the parameters space exploration remains to be done.

The elaborated solutions to the basis set problem could be useful for other fields, where the localized basis codes are applied (for example, in the case of strong optical excitations). The possibility of use of the ghost atoms around the real target atoms in order to improve the basis set accuracy (like, for example, in reference [133]) for stopping power simulations will be considered in the future.

Concerning the random electronic stopping power calculations, we would like to point out the most important and general conclusions. Throughout this work, we have used the ensemble average technique (presented in section 1.5.2). We have seen that this technique is well adapted for the localized basis: It provides accurate random stopping power values and, at the same time, it allows one the dummy parallelization over different impact parameters. We have also shown that the centroid path approximation works well *only* in the case when the core excitations are forbidden (within the frozen core technique in our code or with a pseudopotential within plane-wave codes). Hence, for the RESP calculations, one should properly calculate the impact parameter average for each projectile velocity.

Using the ensemble average technique and very fine impact parameter grids, we have shown that the random stopping power is the same for different cubic target orientations (see section 3.1.3). Thank to this fact, for the RESP calculations we have considered only the [001] crystalline orientation of targets. Although, the correlation between the stopping power and the electronic density along the projectile path is different for different target orientations. In addition, the correlation vanishes at low projectile velocities.

Throughout this work, we have proven the importance of the core electron excitations in the stopping power simulations using different approaches: Basis set tuning (section 3.2.2), frozen core technique (section 4.1) and the occupation analysis (section 4.2). We have also evaluated the contribution of the core electrons in RESP as a function of the projectile impact parameter. As well, the velocity behavior of the contributions from different electronic levels to RESP was analyzed.

Concerning the exchange-correlations functionals dependence, we have found that it does not have significant importance in the case of the studied targets (Li and Al). However, since the relatively moderate cost of the exchange-correlation functionals is an advantage of our code, we are looking for a projectile/target system, where the exchange-correlation functional would be an important parameter.

Comparing the RT-TDDFT *ab initio* results with SRIM, we would like to summarize that there is an overall good agreement between our theoretical results and the empirical code SRIM in the cases when the SRIM database contains enough experimental points. There are some systematic discrepancies though between the RT-TDDFT results and experiment common for different *ab initio* codes and different targets: the RT-TDDFT results are usually larger than the experimental points around the stopping power peak, whereas at high projectile velocities, the *ab initio* results slightly underestimate the experiment. In addition, using our code, we can calculate the channeling stopping power (even more easily, than RESP), which is absent in the SRIM database.

Regarding the linear response theory, LR-TDDFT produces the same results as RT-TDDFT for proton projectile. In the case of antiproton and α -particle, one notes a good agreement only at high projectile velocities. This fact allowed us to determine the effective velocity-dependent projectile charge such that with this charge, LR-TDDFT would yield the same results as RT-TDDFT. The effective charge reaches the nominal projectiles' charge values only at high projectile velocities.

Perspectives

This work could be extended in several directions. Using the current state of the code, we would like to continue the stopping power calculations of light projectiles (H^+ , \bar{H}^- , He^{2+}) in other materials. In particular, we are interested in the iron target that is of paramount importance for the nuclear industry.

In this work, we have spent a lot of effort to calculate the electronic stopping power of crystalline materials because this was our initial goal. However, our localized basis implementation is very well adapted for the stopping power calculations of finite systems. Therefore, we would like to investigate the electronic stopping of gases (a work that we have already started but did not report in this thesis), polymers, 2D materials, and other nanostructures. The localized basis has even more advantages than the plane-wave codes in the case of these systems. For example, to simulate a graphene layer in a plane-wave code, one needs to use a large simulation box in order to ensure a separation between the periodic images of the system in the direction perpendicular to the layer. Furthermore, the vacuum between the images would “cost” as much as the most important region of space around the graphene layer. On the other hand, within the localized basis code, firstly, one does not need to deal with the unwanted periodic repetitions of the atomic system and, secondly, since the basis functions are centered around the atoms, the “vacuum” part (necessary for the stopping power setup) would in no case increase the computational time.

Moreover, we are going to analyze in more detail the Barkas effect using the frozen core technique and the occupation analysis (some calculations being already performed). Even-

tually, we would like to finalize the calculations of the wake electronic density distribution of different projectiles (in relation to the Barkas effect).

In the long term perspectives, it would be useful to implement the moving Gaussian basis functions around the projectiles, which would allow one to calculate the stopping power of heavy ions. One would be able to simulate systems such as Fe projectile in Fe target. Such projectile/target system would be important in the cases of the iron target irradiation with any nature of the irradiating beam (any ionic projectile or, even, photons): because of the interaction with the external beam, some Fe target atoms become secondary projectiles themselves and interact with the target. Hence, in order to simulate this effect, the electronic stopping power of Fe projectile in Fe target is required. A similar simulation setup of nickel projectile in nickel target was studied very recently by Ullah, Artacho, and Correa [91]. Concerning the medical applications, the stopping power of carbon ions in organic matter is of particular interest in the hadron therapy of cancer [78, 147].

In addition, the implementation of the forces in the code (between the target nuclei and between the target and the projectile) would give an *ab initio* access to the systems where both nuclear and electronic stopping are important (slow heavy ion irradiation, for example) and one would be able to describe the dissociation of molecules under the irradiation.

Bibliography

- [1] Professor E. Rutherford F.R.S. Lxxix. the scattering of α particles by matter and the structure of the atom. *The London, Edinburgh, and Dublin Philosophical Magazine and Journal of Science*, 21(125):669–688, 1911. (Cited on page 9).
- [2] W. P. Levin, H. Kooy, J. S. Loeffler, and T. F. DeLaney. Proton beam therapy. *British Journal of Cancer*, 93(8):849–854, 2005. (Cited on page 10).
- [3] Kenneth R Hogstrom and Peter R Almond. Review of electron beam therapy physics. *Physics in Medicine and Biology*, 51(13):R455–R489, jun 2006. (Cited on page 10).
- [4] Radhe Mohan and David Grosshans. Proton therapy – present and future. *Advanced Drug Delivery Reviews*, 109:26 – 44, 2017. Radiotherapy for cancer: present and future. (Cited on page 9).
- [5] Sophie Duzellier. Radiation effects on electronic devices in space. *Aerospace Science and Technology*, 9(1):93 – 99, 2005. (Cited on page 9).
- [6] Sidney Yip. *Handbook of materials modeling*. Springer Science & Business Media, 2007. (Cited on page 10).
- [7] H. Kraus, D. Simin, C. Kasper, Y. Suda, S. Kawabata, W. Kada, T. Honda, Y. Hijikata, T. Ohshima, V. Dyakonov, and G. V. Astakhov. Three-dimensional proton beam writing of optically active coherent vacancy spins in silicon carbide. *Nano Letters*, 17(5):2865–2870, May 2017. (Cited on page 10).
- [8] C. A. Volkert and A. M. Minor. Focused ion beam microscopy and micromachining. *MRS Bulletin*, 32(5):389–399, 2007. (Cited on page 10).
- [9] BW Ward, John A Notte, and NP Economou. Helium ion microscope: A new tool for nanoscale microscopy and metrology. *Journal of Vacuum Science & Technology B: Microelectronics and Nanometer Structures Processing, Measurement, and Phenomena*, 24(6):2871–2874, 2006. (Cited on page 10).

- [10] M. J. Berger, M. Inokuti, H. H. Andersen, H. Bichsel, D. Powers, S. M. Seltzer, D. Thwaites, and D. E. Watt. Report 49. *Journal of the International Commission on Radiation Units and Measurements*, os25(2):NP–NP, 04 2016. (Cited on pages 11 and 13).
- [11] Steven P. Ahlen. Theoretical and experimental aspects of the energy loss of relativistic heavily ionizing particles. *Rev. Mod. Phys.*, 52:121–173, Jan 1980. (Cited on page 11).
- [12] Jens Lindhard and Allan H. Sorensen. Relativistic theory of stopping for heavy ions. *Phys. Rev. A*, 53:2443–2456, Apr 1996. (Cited on page 11).
- [13] Jorge Kohanoff. *Electronic structure calculations for solids and molecules: theory and computational methods*. Cambridge University Press, 2006. (Cited on page 11).
- [14] S Pellegrino, P Trocellier, S Miro, Y Serruys, É Bordas, H Martin, N Chaâbane, S Vaubaillon, JP Gallien, and L Beck. The jannus saclay facility: A new platform for materials irradiation, implantation and ion beam analysis. *Nuclear Instruments and Methods in Physics Research Section B: Beam Interactions with Materials and Atoms*, 273:213–217, 2012. (Cited on page 12).
- [15] Lucile Beck, Yves Serruys, Sandrine Miro, Patrick Trocellier, Eric Bordas, Frédéric Leprêtre, Daniel Brimbal, Thomas Loussouarn, Hervé Martin, Sylvain Vaubaillon, et al. Ion irradiation and radiation effect characterization at the jannus-saclay triple beam facility. *Journal of Materials Research*, 30(9):1183–1194, 2015. (Cited on page 12).
- [16] Alfredo A. Correa. Calculating electronic stopping power in materials from first principles. *Computational Materials Science*, 150(March):291–303, 2018. (Cited on pages 12, 13, 50, 52, 55, and 159).
- [17] Peter Sigmund. Particle penetration and radiation effects volume 2. In *Springer series in solid-state sciences*, volume 179. Springer, 2014. (Cited on page 12).
- [18] Hans Bethe. Zur theorie des durchgangs schneller korpuskularstrahlen durch materie. *Annalen der Physik*, 397(3):325–400, 1930. (Cited on page 12).
- [19] Enrico Fermi and Edward Teller. The capture of negative mesotrons in matter. *Physical Review*, 72(5):399, 1947. (Cited on page 12).
- [20] J. F. Zielger, J. P. Biersack, and M. D. Ziegler. *SRIM The Stopping and Range of Ions in Matter*. (Cited on pages 13, 138, 143, 148, 165, and 166).
- [21] Lech Nowicki, Andrzej Turos, Renata Ratajczak, Anna Stonert, and Frederico Garrido. Modern analysis of ion channeling data by monte carlo simulations. *Nuclear Instruments and Methods in Physics Research Section B: Beam Interactions with*

- Materials and Atoms*, 240(1):277 – 282, 2005. Accelerators in Applied Research and Technology. (Cited on page 13).
- [22] Catherine Sabathier, Laetitia Vincent, Philippe Garcia, Frederico Garrido, Gaëlle Carlot, Lionel Thome, P. Martin, and Carole Valot. In situ tem study of temperature-induced fission product precipitation in uo2. *Nuclear Instruments and Methods in Physics Research Section B: Beam Interactions with Materials and Atoms*, 266(12):3027 – 3032, 2008. Radiation Effects in Insulators. (Cited on page 13).
- [23] Aurélien Debelle, Alexandre Boulle, Frédéric Garrido, and Lionel Thomé. Strain and stress build-up in he-implanted uo2 single crystals: an x-ray diffraction study. *Journal of Materials Science*, 46(13):4683–4689, Jul 2011. (Cited on page 13).
- [24] Jens Lindhard, Morten Scharff, and Hans E Schiøtt. *Range concepts and heavy ion ranges*. Munksgaard Copenhagen, 1963. (Cited on page 13).
- [25] PM Echenique, RM Nieminen, JC Ashley, and RH Ritchie. Nonlinear stopping power of an electron gas for slow ions. *Physical Review A*, 33(2):897, 1986. (Cited on page 13).
- [26] P. Hohenberg and W. Kohn. Inhomogeneous electron gas. *Phys. Rev.*, 136:B864–B871, Nov 1964. (Cited on pages 13 and 21).
- [27] A. Arnau, M. Pealba, P. M. Echenique, F. Flores, and R. H. Ritchie. Stopping power for helium in aluminum. *Phys. Rev. Lett.*, 65:1024–1027, Aug 1990. (Cited on page 13).
- [28] Erich Runge and E. K. U. Gross. Density-functional theory for time-dependent systems. *Phys. Rev. Lett.*, 52:997–1000, Mar 1984. (Cited on pages 14 and 39).
- [29] M. Petersilka, U. J. Gossmann, and E. K. U. Gross. Excitation energies from time-dependent density-functional theory. *Phys. Rev. Lett.*, 76:1212–1215, Feb 1996. (Cited on pages 14 and 44).
- [30] I. Campillo, J. M. Pitarke, and A. G. Eguiluz. Electronic stopping power of aluminum crystal. *Phys. Rev. B*, 58:10307–10314, Oct 1998. (Cited on pages 14 and 53).
- [31] I Campillo, J.M Pitarke, A.G Eguiluz, and Alberto García'. Electronic stopping power of periodic crystals. 135(1-4):103 – 106, 1998. (Cited on page 14).
- [32] J.M. Pitarke and I. Campillo. Band structure effects on the interaction of charged particles with solids. 164-165(0):147 – 160, 2000. (Cited on page 14).
- [33] Abdullah Atef Shukri, Fabien Bruneval, and Lucia Reining. *Ab initio* electronic stopping power of protons in bulk materials. *Phys. Rev. B*, 93:035128, Jan 2016. (Cited on pages 14, 53, 96, 103, 148, and 169).

- [34] Abdullah Atef Shukri. *Ab initio electronic stopping power in materials*. PhD thesis, Ecole Polytechnique, November 2015. (Cited on pages 14, 53, 107, and 165).
- [35] André Schleife, Yosuke Kanai, and Alfredo A Correa. Accurate atomistic first-principles calculations of electronic stopping. *Physical Review B*, 91(1):014306, 2015. (Cited on pages 15, 50, 52, 53, 113, and 149).
- [36] André Schleife, Erik W Draeger, Yosuke Kanai, and Alfredo A Correa. Plane-wave pseudopotential implementation of explicit integrators for time-dependent kohn-sham equations in large-scale simulations. *The Journal of chemical physics*, 137(22):22A546, 2012. (Cited on page 15).
- [37] Alberto Castro, Heiko Appel, Micael Oliveira, Carlo A Rozzi, Xavier Andrade, Florian Lorenzen, Miguel AL Marques, EKV Gross, and Angel Rubio. octopus: a tool for the application of time-dependent density functional theory. *physica status solidi (b)*, 243(11):2465–2488, 2006. (Cited on page 15).
- [38] Miguel A.L. Marques, Alberto Castro, George F. Bertsch, and Angel Rubio. octopus: a first-principles tool for excited electron–ion dynamicse-mail: octopus@tddft.org. *Computer Physics Communications*, 151(1):60 – 78, 2003. (Cited on page 15).
- [39] J. M. Pruneda, D. Sánchez-Portal, A. Arnau, J. I. Juaristi, and Emilio Artacho. Electronic stopping power in LiF from first principles. *Physical Review Letters*, 99(23):1–4, 2007. (Cited on pages 15, 50, and 101).
- [40] M. Valiev, E.J. Bylaska, N. Govind, K. Kowalski, T.P. Straatsma, H.J.J. Van Dam, D. Wang, J. Nieplocha, E. Apra, T.L. Windus, and W.A. de Jong. Nwchem: A comprehensive and scalable open-source solution for large scale molecular simulations. 181(9):1477 – 1489, 2010. (Cited on page 15).
- [41] Jürg Hutter, Marcella Iannuzzi, Florian Schiffmann, and Joost VandeVondele. Cp2k: atomistic simulations of condensed matter systems. *Wiley Interdisciplinary Reviews: Computational Molecular Science*, 4(1):15–25, 2014. (Cited on page 15).
- [42] Fabien Bruneval, Tonatiuh Rangel, Samia M. Hamed, Meiyue Shao, Chao Yang, and Jeffrey B. Neaton. molgw 1: Many-body perturbation theory software for atoms, molecules, and clusters. *Computer Physics Communications*, 208:149 – 161, 2016. (Cited on pages 15, 57, and 68).
- [43] Gordon Drake. *Springer Handbook of Atomic, Molecular, and Optical Physics*. 01 2006. (Cited on page 18).
- [44] Tosio Kato. On the eigenfunctions of many-particle systems in quantum mechanics. *Communications on Pure and Applied Mathematics*, 10(2):151–177, 1957. (Cited on page 22).

- [45] Robert G. Parr and Weitao Yang. *Density-functional theory of atoms and molecules*. Oxford University Press, New York, 1989. (Cited on page 22).
- [46] W. Kohn and L. J. Sham. Self-consistent equations including exchange and correlation effects. *Phys. Rev.*, 140:A1133–A1138, Nov 1965. (Cited on pages 23 and 34).
- [47] J Cramer Christopher. Essentials of computational chemistry. *Theories and Models*, pages 191 – 232, 2002. (Cited on page 27).
- [48] F. Sasaki and M. Yoshimine. Configuration-interaction study of atoms. i. correlation energies of b, c, n, o, f, and ne. *Phys. Rev. A*, 9:17–25, Jan 1974. (Cited on page 27).
- [49] L. H. Thomas. The calculation of atomic fields. *Mathematical Proceedings of the Cambridge Philosophical Society*, 23(5):542–548, 1927. (Cited on page 27).
- [50] Attila Szabó and Neil S. Ostlund. *Modern quantum chemistry : introduction to advanced electronic structure theory*. Dover Publications, Mineola (N.Y.), 1996. (Cited on pages 30, 32, 37, and 65).
- [51] U von Barth and L Hedin. A local exchange-correlation potential for the spin polarized case. i. *Journal of Physics C: Solid State Physics*, 5(13):1629–1642, jul 1972. (Cited on page 33).
- [52] J. P. Perdew and Alex Zunger. Self-interaction correction to density-functional approximations for many-electron systems. *Phys. Rev. B*, 23:5048–5079, May 1981. (Cited on page 33).
- [53] G. L. Oliver and J. P. Perdew. Spin-density gradient expansion for the kinetic energy. *Phys. Rev. A*, 20:397–403, Aug 1979. (Cited on page 33).
- [54] Kieron Burke. Perspective on density functional theory. *The Journal of Chemical Physics*, 136(15):150901, 2012. (Cited on page 34).
- [55] Jianwei Sun, Adrienn Ruzsinszky, and John P. Perdew. Strongly constrained and appropriately normed semilocal density functional. *Phys. Rev. Lett.*, 115:036402, Jul 2015. (Cited on pages 34 and 36).
- [56] D. M. Ceperley and B. J. Alder. Ground state of the electron gas by a stochastic method. *Phys. Rev. Lett.*, 45:566–569, Aug 1980. (Cited on page 35).
- [57] S. H. Vosko, L. Wilk, and M. Nusair. Accurate spin-dependent electron liquid correlation energies for local spin density calculations: a critical analysis. *Canadian Journal of Physics*, 58(8):1200–1211, 1980. (Cited on page 35).
- [58] John P. Perdew and Yue Wang. Accurate and simple analytic representation of the electron-gas correlation energy. *Phys. Rev. B*, 45:13244–13249, Jun 1992. (Cited on page 35).

- [59] Pierre-François Loos and Peter M. W. Gill. The uniform electron gas. *Wiley Interdisciplinary Reviews: Computational Molecular Science*, 6(4):410–429, 2016. (Cited on page 35).
- [60] A. D. Becke. Density-functional exchange-energy approximation with correct asymptotic behavior. *Phys. Rev. A*, 38:3098–3100, Sep 1988. (Cited on page 36).
- [61] Chengteh Lee, Weitao Yang, and Robert G. Parr. Development of the colle-salvetti correlation-energy formula into a functional of the electron density. *Phys. Rev. B*, 37:785–789, Jan 1988. (Cited on page 36).
- [62] Renato Colle and Oriano Salvetti. Approximate calculation of the correlation energy for the closed shells. *Theoretica chimica acta*, 37(4):329–334, Dec 1975. (Cited on page 36).
- [63] John P. Perdew, Kieron Burke, and Matthias Ernzerhof. Generalized gradient approximation made simple. *Phys. Rev. Lett.*, 77:3865–3868, Oct 1996. (Cited on page 36).
- [64] John P Perdew. Electronic structure of solids’ 91 ed p ziesche and h eschrig (berlin: Akademie) perdew jp, chevary ja, vosko sh, jackson ka, pederson mr, singh dj and fiolhais c 1992. *Phys. Rev. B*, 46:6671, 1991. (Cited on page 36).
- [65] Jianmin Tao, John P. Perdew, Viktor N. Staroverov, and Gustavo E. Scuseria. Climbing the density functional ladder: Nonempirical meta-generalized gradient approximation designed for molecules and solids. *Phys. Rev. Lett.*, 91:146401, Sep 2003. (Cited on page 36).
- [66] A. Seidl, A. Görling, P. Vogl, J. A. Majewski, and M. Levy. Generalized kohn-sham schemes and the band-gap problem. *Phys. Rev. B*, 53:3764–3774, Feb 1996. (Cited on page 37).
- [67] PJ Stephens, FJ Devlin, CFN Chabalowski, and Michael J Frisch. Ab initio calculation of vibrational absorption and circular dichroism spectra using density functional force fields. *The Journal of Physical Chemistry*, 98(45):11623–11627, 1994. (Cited on page 37).
- [68] Matthias Ernzerhof and Gustavo E Scuseria. Assessment of the perdew–burke–ernzerhof exchange–correlation functional. *The Journal of chemical physics*, 110(11):5029–5036, 1999. (Cited on page 38).
- [69] Marco Bernardi. On the physical origin of the 1/4 exact exchange in density functional theory. *arXiv preprint arXiv:1810.02446*, 2018. (Cited on page 38).
- [70] Carsten A. Ullrich. *Time-Dependent Density-Functional Theory: Concepts and Applications*, volume 569. 2012. (Cited on pages 39 and 48).

- [71] Giovanni Vignale. Real-time resolution of the causality paradox of time-dependent density-functional theory. *Phys. Rev. A*, 77:062511, Jun 2008. (Cited on page 39).
- [72] Robert van Leeuwen. Mapping from densities to potentials in time-dependent density-functional theory. *Phys. Rev. Lett.*, 82:3863–3866, May 1999. (Cited on page 41).
- [73] Neepa T. Maitra and Kieron Burke. Demonstration of initial-state dependence in time-dependent density-functional theory. *Phys. Rev. A*, 63:042501, Mar 2001. (Cited on page 43).
- [74] Johanna I. Fuks, Angel Rubio, and Neepa T. Maitra. Charge transfer in time-dependent density-functional theory via spin-symmetry breaking. *Phys. Rev. A*, 83:042501, Apr 2011. (Cited on page 43).
- [75] J. I. Fuks and N. T. Maitra. Charge transfer in time-dependent density-functional theory: Insights from the asymmetric hubbard dimer. *Phys. Rev. A*, 89:062502, Jun 2014. (Cited on page 43).
- [76] Henrik Bruus and Karsten Flensberg. Many-body quantum theory in condensed matter physics: An Introduction (Oxford Graduate Texts). *Oxford University Press*, (August):336, 2002. (Cited on page 46).
- [77] Gary S. Was. *Fundamentals of Radiation Damage Materials Science*. 2007. (Cited on pages 49, 138, 139, and 141).
- [78] Jorge Kohanoff and Emilio Artacho. Water radiolysis by low-energy carbon projectiles from first-principles molecular dynamics. *PLoS ONE*, 12(3):1–11, 2017. (Cited on pages 49 and 177).
- [79] Alfredo A. Correa, Jorge Kohanoff, Emilio Artacho, Daniel Sánchez-Portal, and Alfredo Caro. Nonadiabatic forces in ion-solid interactions: The initial stages of radiation damage. *Physical Review Letters*, 108(21):1–5, 2012. (Cited on pages 49 and 149).
- [80] M. Caro, A. A. Correa, E. Artacho, and A. Caro. Stopping power beyond the adiabatic approximation. *Scientific Reports*, 7(1):1–10, 2017. (Cited on page 49).
- [81] Edwin E. Quashie and Alfredo A. Correa. Electronic stopping power of protons and alpha particles in nickel. *Physical Review B*, 98(23):1–6, 2018. (Cited on pages 50 and 55).
- [82] Kyle G. Reeves, Yi Yao, and Yosuke Kanai. Electronic stopping power in liquid water for protons and α particles from first principles. *Physical Review B*, 94(4):1–6, 2016. (Cited on pages 50 and 149).

- [83] M. Ahsan Zeb, J. Kohanoff, D. Sánchez-Portal, A. Arnau, J. I. Juaristi, and Emilio Artacho. Electronic stopping power in gold: The role of d electrons and the H/He anomaly. *Physical Review Letters*, 108(22):1–5, 2012. (Cited on page 50).
- [84] M. Ahsan Zeb, J. Kohanoff, D. Sánchez-Portal, and Emilio Artacho. Electronic stopping power of H and He in Al and LiF from first principles. *Nuclear Instruments and Methods in Physics Research, Section B: Beam Interactions with Materials and Atoms*, 303:59–61, 2013. (Cited on page 50).
- [85] Chang Kai Li, Fei Mao, Feng Wang, Yan Long Fu, Xiao Ping Ouyang, and Feng Shou Zhang. Electronic stopping power of slow-light channeling ions in ZnTe from first principles. *Physical Review A*, 95(5), 2017. (Cited on page 50).
- [86] Ari Ojanpera, Arkady V. Krashennnikov, and Martti Puska. Electronic stopping power from first-principles calculations with account for core electron excitations and projectile ionization. *Physical Review B - Condensed Matter and Materials Physics*, 89(3):1–5, 2014. (Cited on pages 50, 53, and 55).
- [87] Dillon C. Yost and Yosuke Kanai. Electronic stopping for protons and α particles from first-principles electron dynamics: The case of silicon carbide. *Physical Review B*, 94(11):1–8, 2016. (Cited on pages 50, 53, 54, 149, and 162).
- [88] Dillon C. Yost, Yi Yao, and Yosuke Kanai. Examining real-time time-dependent density functional theory nonequilibrium simulations for the calculation of electronic stopping power. *Physical Review B*, 96(11):1–9, 2017. (Cited on pages 50, 113, 149, 162, and 174).
- [89] Kyle G. Reeves and Yosuke Kanai. Electronic Excitation Dynamics in Liquid Water under Proton Irradiation. *Scientific Reports*, 7(December 2016):1–8, 2017. (Cited on page 50).
- [90] R. J. Magyar, L. Shulenburger, and A. D. Baczewski. Stopping of Deuterium in Warm Dense Deuterium from Ehrenfest Time-Dependent Density Functional Theory. *Contributions to Plasma Physics*, 56(5):459–466, 2016. (Cited on page 50).
- [91] Rafi Ullah, Emilio Artacho, and Alfredo A. Correa. Core Electrons in the Electronic Stopping of Heavy Ions. *Physical Review Letters*, 121(11):116401, 2018. (Cited on pages 50, 174, and 177).
- [92] D. Roth, C. E. Celdon, D. Goebel, E. A. Sanchez, B. Bruckner, R. Steinberger, J. Guimpel, N. R. Arista, and P. Bauer. Systematic analysis of different experimental approaches to measure electronic stopping of very slow hydrogen ions. *Nuclear Instruments and Methods in Physics Research, Section B: Beam Interactions with Materials and Atoms*, 437(September):1–7, 2018. (Cited on page 50).

- [93] Gary Was. *Fundamentals of Radiation Materials Science*. Springer, 2015. (Cited on page 52).
- [94] Rafi Ullah, Fabiano Corsetti, Daniel Sánchez-Portal, and Emilio Artacho. Electronic stopping power in a narrow band gap semiconductor from first principles. *Physical Review B - Condensed Matter and Materials Physics*, 91(12), 2015. (Cited on pages 53 and 100).
- [95] E. A. Figueroa, E. D. Cantero, J. C. Eckardt, G. H. Lantschner, J. E. Valdés, and N. R. Arista. Threshold effect in the energy loss of slow protons and deuterons channeled in Au crystals. *Physical Review A - Atomic, Molecular, and Optical Physics*, 75(1):1–4, 2007. (Cited on page 55).
- [96] Jiaming Wang, Symphony H. Y. Huang, Christoph Herrmann, Shelley A. Scott, François Schiettekatte, and Karen L. Kavanagh. Focussed helium ion channeling through Si nanomembranes. *Journal of Vacuum Science & Technology B, Nanotechnology and Microelectronics: Materials, Processing, Measurement, and Phenomena*, 36(2), 2018. (Cited on page 55).
- [97] Ma Zhongquan, Liu Jiarui, and Zhu Peiran. Stopping power of proton in monocrystalline, polycrystalline and amorphous silicon. *Chinese Physics Letters*, 7(5):226–229, may 1990. (Cited on page 55).
- [98] Donald S. Gemmell. Channeling and related effects in the motion of charged particles through crystals. *Reviews of Modern Physics*, 46(1):129–227, 1974. (Cited on page 55).
- [99] Jens Lindhard. Influence of Crystal Lattice on Motion of Energetic Charged Particles. *Matematisk-Fysiske Meddelelser Kongelige Danske Videnskabernes Selskab*, 34(14):1–64, 1965. (Cited on page 55).
- [100] Erik Holm Mortensen, Jens Oddershede, and John R. Sabin. Polarization propagator calculations of generalized oscillator strengths and stopping cross sections of he. *Nuclear Instruments and Methods in Physics Research Section B: Beam Interactions with Materials and Atoms*, 69(1):24 – 32, 1992. (Cited on page 60).
- [101] J.A. Nobel, S.B. Trickey, John R. Sabin, and Jens Oddershede. Basis set limitations on the ab initio calculation of stopping cross-sections via generalized oscillator strengths. *Chemical Physics*, 309(1):89 – 94, 2005. Electronic Structure Calculations for Understanding Surfaces and Molecules. In Honor of Notker Roesch. (Cited on page 60).
- [102] Thom H Dunning Jr. Gaussian basis sets for use in correlated molecular calculations. i. the atoms boron neon and hydrogen. *The Journal of chemical physics*, 90(2):1007–1023, 1989. (Cited on page 60).

- [103] Rick A Kendall, Thom H Dunning Jr, and Robert J Harrison. Electron affinities of the first-row atoms revisited. systematic basis sets and wave functions. *The Journal of chemical physics*, 96(9):6796–6806, 1992. (Cited on page 60).
- [104] David E Woon and Thom H Dunning Jr. Gaussian basis sets for use in correlated molecular calculations. iii. the atoms aluminum through argon. *The Journal of chemical physics*, 98(2):1358–1371, 1993. (Cited on page 60).
- [105] Asger Halkier, Trygve Helgaker, Poul Jørgensen, Wim Klopper, and Jeppe Olsen. Basis-set convergence of the energy in molecular hartree–fock calculations. *Chemical Physics Letters*, 302(5):437 – 446, 1999. (Cited on page 60).
- [106] Kirk A Peterson, Rick A Kendall, and Thom H Dunning Jr. Benchmark calculations with correlated molecular wave functions. ii. configuration interaction calculations on first row diatomic hydrides. *The Journal of chemical physics*, 99(3):1930–1944, 1993. (Cited on page 60).
- [107] Asger Halkier, Wim Klopper, Trygve Helgaker, and Poul Jo/rgensen. Basis-set convergence of the molecular electric dipole moment. *The Journal of chemical physics*, 111(10):4424–4430, 1999. (Cited on page 60).
- [108] Peter Pulay. Improved scf convergence acceleration. *Journal of Computational Chemistry*, 3(4):556–560, 1982. (Cited on page 67).
- [109] S. Obara and A. Saika. Efficient recursive computation of molecular integrals over cartesian gaussian functions. *The Journal of Chemical Physics*, 84(7):3963–3974, 1986. (Cited on page 69).
- [110] EF Valeev. Libint: A library for the evaluation of molecular integrals of many-body operators over gaussian functions. 2017. (Cited on page 69).
- [111] Miguel AL Marques, Micael JT Oliveira, and Tobias Burnus. Libxc: A library of exchange and correlation functionals for density functional theory. *Computer Physics Communications*, 183(10):2272–2281, 2012. (Cited on page 69).
- [112] Florian Weigend. A fully direct ri-hf algorithm: Implementation, optimised auxiliary basis sets, demonstration of accuracy and efficiency. *Physical Chemistry Chemical Physics*, 4(18):4285–4291, 2002. (Cited on page 69).
- [113] Kenneth Lopata and Niranjana Govind. Modeling fast electron dynamics with real-time time-dependent density functional theory: application to small molecules and chromophores. *Journal of chemical theory and computation*, 7(5):1344–1355, 2011. (Cited on pages 70 and 89).
- [114] Wilhelm Magnus. On the exponential solution of differential equations for a linear operator. *Communications on pure and applied mathematics*, 7(4):649–673, 1954. (Cited on page 73).

- [115] S. Blanes, F. Casas, and J. Ros. Improved high order integrators based on the magnus expansion. *BIT Numerical Mathematics*, 40(3):434–450, Sep 2000. (Cited on page 73).
- [116] Chiao-Lun Cheng, Jeremy S Evans, and Troy Van Voorhis. Simulating molecular conductance using real-time density functional theory. *Physical Review B*, 74(15):155112, 2006. (Cited on pages 73, 82, and 92).
- [117] Alberto Castro, Miguel AL Marques, and Angel Rubio. Propagators for the time-dependent kohn–sham equations. *The Journal of chemical physics*, 121(8):3425–3433, 2004. (Cited on page 75).
- [118] Conn O’Rourke and David R Bowler. Linear scaling density matrix real time tddft: Propagator unitarity and matrix truncation. *The Journal of chemical physics*, 143(10):102801, 2015. (Cited on page 76).
- [119] Xavier Andrade, David Strubbe, Umberto De Giovannini, Ask Hjorth Larsen, Micael J. T. Oliveira, Joseba Alberdi-Rodriguez, Alejandro Varas, Iris Theophilou, Nicole Helbig, Matthieu J. Verstraete, Lorenzo Stella, Fernando Nogueira, Alan Aspuru-Guzik, Alberto Castro, Miguel A. L. Marques, and Angel Rubio. Real-space grids and the octopus code as tools for the development of new simulation approaches for electronic systems. *Phys. Chem. Chem. Phys.*, 17:31371–31396, 2015. (Cited on page 84).
- [120] Fabien Bruneval, Samia M. Hamed, and Jeffrey B. Neaton. A systematic benchmark of the ab initio bethe-salpeter equation approach for low-lying optical excitations of small organic molecules. 142(24):244101, 2015. (Cited on page 86).
- [121] Nicolas O Foglia, Uriel N Morzan, Dario A Estrin, Damian A Scherlis, and Mariano C Gonzalez Lebrero. Role of core electrons in quantum dynamics using tddft. *Journal of chemical theory and computation*, 13(1):77–85, 2016. (Cited on page 89).
- [122] K Lopata, Benjamin E Van Kuiken, Munira Khalil, and Niranjana Govind. Linear-response and real-time time-dependent density functional theory studies of core-level near-edge x-ray absorption. *Journal of chemical theory and computation*, 8(9):3284–3292, 2012. (Cited on page 89).
- [123] K. Yabana and G. F. Bertsch. Time-dependent local-density approximation in real time. *Phys. Rev. B*, 54:4484–4487, Aug 1996. (Cited on page 89).
- [124] Argyrios Tsolakidis, Daniel Sánchez-Portal, and Richard M Martin. Calculation of the optical response of atomic clusters using time-dependent density functional theory and local orbitals. *Physical Review B*, 66(23):235416, 2002. (Cited on page 90).
- [125] Hiroshi Akima. A method of smooth curve fitting. Technical report, Institute for Telecommunication Sciences Boulder CO, 1969. (Cited on page 100).

- [126] M. Quijada, A. G. Borisov, I. Nagy, R. Díez Muiño, and P. M. Echenique. Time-dependent density-functional calculation of the stopping power for protons and antiprotons in metals. *Physical Review A - Atomic, Molecular, and Optical Physics*, 75(4):1–4, 2007. (Cited on page 101).
- [127] Jessica Halliday and Emilio Artacho. Anisotropy of electronic stopping power in graphite. pages 1–8, 2019. (Cited on page 107).
- [128] G. J. Iafrate, J. F. Ziegler, and M. J. Nass. Application of lindhard’s dielectric theory to the stopping of ions in solids. *Journal of Applied Physics*, 51(2):984–987, 1980. (Cited on pages 107 and 108).
- [129] H. Winter, J. I. Juaristi, I. Nagy, A. Arnau, and P. M. Echenique. Energy loss of slow ions in a nonuniform electron gas. *Phys. Rev. B*, 67:245401, Jun 2003. (Cited on pages 107 and 108).
- [130] Yi Yao, Dillon C Yost, and Yosuke Kanai. K-shell Core Electron Excitations in the Electronic Stopping of Protons in Water. (Cited on pages 122 and 126).
- [131] David E. Woon and Thom H. Dunning. Gaussian basis sets for use in correlated molecular calculations. iv. calculation of static electrical response properties. *The Journal of Chemical Physics*, 100(4):2975–2988, 1994. (Cited on page 124).
- [132] Pekka Manninen and Juha Vaara. Systematic Gaussian basis-set limit using completeness-optimized primitive sets. A case for magnetic properties. *Journal of Computational Chemistry*, 27(4):434–445, 2006. (Cited on page 124).
- [133] Emanuele Coccia and Eleonora Luppi. Optimal-continuum and multicentered gaussian basis sets for high-harmonic generation spectroscopy. *Theoretical Chemistry Accounts*, 135(2):43, Feb 2016. (Cited on pages 124 and 175).
- [134] Marie Labeye, Felipe Zapata, Emanuele Coccia, Valérie Vénier, Julien Toulouse, Jérémie Caillat, Richard Taïeb, and Eleonora Luppi. Optimal basis set for electron dynamics in strong laser fields: The case of molecular ion h2+. *Journal of Chemical Theory and Computation*, 14(11):5846–5858, Nov 2018. (Cited on page 124).
- [135] Susi Lehtola, Pekka Manninen, Mikko Hakala, and Keijo Hämäläinen. Contraction of completeness-optimized basis sets: Application to ground-state electron momentum densities. *Journal of Chemical Physics*, 138(4), 2013. (Cited on pages 125 and 130).
- [136] Susi Lehtola. Automatic algorithms for completeness-optimization of Gaussian basis sets. *Journal of Computational Chemistry*, 36(5):335–347, 2015. (Cited on pages 125 and 130).
- [137] M. Bader, R. E. Pixley, F. S. Mozer, and W. Whaling. Stopping cross section of solids for protons, 50-600 kev. *Phys. Rev.*, 103:32–38, Jul 1956. (Cited on pages 148 and 149).

- [138] Ch. Eppacher, R. Díez Muiño, D. Semrad, and A. Arnau. Stopping power of lithium for hydrogen projectiles. 96(3):639 – 642, 1995. *The Interaction of Swift Particles and Electromagnetic Fields with Matter*. (Cited on pages 148 and 149).
- [139] C. Borschel and C. Ronning. Ion beam irradiation of nanostructures – a 3d monte carlo simulation code. *Nuclear Instruments and Methods in Physics Research Section B: Beam Interactions with Materials and Atoms*, 269(19):2133 – 2138, 2011. (Cited on page 166).
- [140] S. P. Møller, E. Uggerhøj, H. Bluhme, H. Knudsen, U. Mikkelsen, K. Paludan, and E. Morenzoni. Direct measurements of the stopping power for antiprotons of light and heavy targets. *Physical Review A - Atomic, Molecular, and Optical Physics*, 56(4):2930–2939, 1997. (Cited on page 168).
- [141] S. P. Møller, A. Csete, T. Ichioka, H. Knudsen, U. I. Uggerhøj, and H. H. Andersen. Antiproton Stopping at Low Energies: Confirmation of Velocity-Proportional Stopping Power. *Physical Review Letters*, 88(19):4, 2002. (Cited on page 168).
- [142] S. P. Møller, A. Csete, T. Ichioka, H. Knudsen, U. I. Uggerhøj, and H. H. Andersen. Stopping power in insulators and metals without charge exchange. *Phys. Rev. Lett.*, 93:042502, Jul 2004. (Cited on page 168).
- [143] Walter H. Barkas, John N. Dyer, and Harry H. Heckman. Resolution of the Σ^- -mass anomaly. *Phys. Rev. Lett.*, 11:26–28, Jul 1963. (Cited on page 168).
- [144] R. Vincent, J. I. Juaristi, and I. Nagy. Transport cross sections based on a screened interaction potential: Comparison of classical and quantum-mechanical results. *Physical Review A - Atomic, Molecular, and Optical Physics*, 71(6):1–5, 2005. (Cited on page 168).
- [145] Henning Esbensen and Peter Sigmund. Barkas effect in a dense medium: Stopping power and wake field. *Annals of Physics*, 201(1):152–192, 1990. (Cited on page 169).
- [146] Emilio Artacho and David D. O’Regan. Quantum mechanics in an evolving hilbert space. *Phys. Rev. B*, 95:115155, Mar 2017. (Cited on page 174).
- [147] Koji Noda, Takuji Furukawa, Takashi Fujisawa, Yoshiyuki Iwata, Tatsuaki Kanai, Mitsutaka Kanazawa, Atsushi Kitagawa, Masataka Komori, Shinichi Minohara, Takeshi Murakami, Masayuki Muramatsu, Shinji Sato, Yuka Takei, Mutsumi Tashiro, Masami Torikoshi, Satoru Yamada, and Ken Yusa. New Accelerator Facility for Carbon-Ion Cancer-Therapy. *Journal of Radiation Research*, 48(Suppl_A) : A43 – A54, 032007. (Cited on page 177).

Synthèse

1. Introduction

Le dommage d'irradiation dans la matière condensée est un phénomène important pour de nombreux domaines : les matériaux pour le nucléaire bien sûr, mais aussi l'électronique embarquée dans les satellites sujets aux rayonnements cosmiques, ou encore la matière vivante soumise au traitement des tumeurs par radiothérapie. Une connaissance précise de l'interaction entre la particule irradiante et le matériau cible est par conséquent fondamentale. L'interaction entre un projectile ionique et une cible peut être décrite par le biais du pouvoir d'arrêt, S . Il est défini comme étant le transfert d'énergie du projectile au matériau divisé par la profondeur d'implantation. La perte d'énergie d'un ion est induite majoritairement par les excitations électroniques de la cible. Le pouvoir d'arrêt électronique, S_e , est alors la grandeur principale dans ce domaine. L'arrivée de la théorie de la fonctionnel de la densité dépendante du temps (TDDFT) a permis de largement améliorer la description de ce phénomène.

Donc, l'objectif de cette thèse était de développer une approche basée sur TDDFT et l'utiliser pour les calculs du pouvoir d'arrêt électronique dans le cas d'irradiation aux projectiles ioniques pour des matériaux cristallins.

2. Approche

2.1 Implémentation

Au cours de cette thèse, nous j'ai développé un code *ab initio* basé sur la TDDFT en temps réel (RT-TDDFT) dans les bases gaussiennes. Cette implémentation a des avantages considérables comme le traitement direct des électrons de cœurs, la rapidité de calculs des fonctionnelles hybrides et la flexibilité de la base. Nous avons basé l'implémentation sur le code MOLGW (implémenté également dans notre laboratoire).

Pour calculer l'évaluation du système électronique soumis à une perturbation, nous calculons la fonction d'onde électronique dépendante du temps, $\Psi(t)$, avec la technique du propagateur. Pour calculer la fonction d'onde à un instant $t + \Delta t$, $\Psi(t + \Delta t)$, Δt étant le pas de temps, à partir de $\Psi(t)$, nous appliquons l'opérateur de propagation \hat{U} : $\psi(t+\Delta t) = \hat{U}(t+\Delta t, t)\psi(t)$. Cet opérateur a une expression suivante : $\hat{U} = \hat{T} \exp \left\{ -i \int_t^{t+\Delta t} d\tau \hat{H}(\tau) \right\}$, où \hat{T} est le « time-ordering operator ». En fait, l'expression de cet opérateur est juste la reformulation de l'équation temporelle de Schrödinger, mais qui permet de mieux contrôler la stabilité et la précision de la propagation. Dans un cas général, afin d'implémenter cette technique, nous devons appliquer deux approximations : une pour l'intégral d'Hamiltonien en temps et une autre pour l'exponentielle. Cependant, dans les bases gaussiennes localisées, la dimension typique de la matrice d'Hamiltonien permet d'évaluer l'exponentielle directement, sans aucune approximation. La seule approximation qui reste à faire, c'est celle de l'intégrale. Cela peut être considéré comme un autre avantage d'implémentation dans les bases gaussiennes par rapport, par exemple, aux ondes planes. La stabilité numérique de la solution en temps a été ensuite améliorée grâce à une technique de prédicteur-correcteur, développée dans cette thèse spécialement pour ce problème.

Finalement, une simulation typique de RT-TDDFT implémentée dans le code MOLGW est la suivante. Nous calculons l'état électronique fondamental d'un système donné avec la DFT statique. Ensuite nous appliquons une perturbation et nous calculons l'évaluation du système électronique avec la méthode de RT-TDDFT. Le calcul d'état fondamental de DFT a été implémenté en MOLGW avant cette thèse, tandis que la partie de la propagation en temps a été implémenté dans ce travail.

2.2 Validation

Une fois que le code de RT-TDDFT a été implémenté, nous avons tout d'abord calculé un cas de figure permettant le test de la qualité du code écrit. Nous avons donc effectué un calcul de RT-TDDFT en temps réel pour une situation que nous pouvions calculer par ailleurs avec une approche déjà existante dans MOLGW, la réponse linéaire.

Nous avons évalué le spectre d'absorption optique d'une petite molécule, le benzène C_6H_6 . Pour ces deux méthodes, nous avons utilisé les mêmes positions atomiques et la même base localisée, dans l'approximation de la densité locale (LDA) pour l'échange corrélation.

Le spectre d'absorption optique est obtenu tout d'abord de façon classique dans le cadre de la réponse linéaire grâce à la solution de la TDDFT dans l'espace des fréquences : ce sont les équations de Casida. Puis nous avons entrepris une simulation en temps réel avec RT-TDDFT. Pour exciter le système nous avons introduit une impulsion de champ électrique homogène dans l'espace et de forme gaussienne dans le temps à instant $t = 0$. Cette impulsion gaussienne est une excitation quasiment « blanche » qui active tous les modes du benzène.

L'intensité de l'impulsion est faible de façon à rester dans le régime de la réponse linéaire et pouvoir ainsi comparer avec notre calcul de référence.

Finalement, nous avons obtenu un très bon accord pour les résultats obtenus avec la réponse linéaire et RT-TDDFT ce qui certifie notre implémentation. Il faut remarquer que nous avons utilisé la limite des petites perturbations afin de comparer nos résultats avec la réponse linéaire. Cependant, après cette étape de vérification, notre code permet d'avoir des spectres d'absorption qui correspondent aux intensités d'excitations quelconques.

De plus, l'approche de l'évaluation du système électronique sous une perturbation en RT-TDDFT et en base localisée pourrait être appliquée pour des différents types d'excitations.

2.3 Méthode de simulations *ab initio* du pouvoir d'arrêt

Après la validation de l'implémentation, nous nous sommes tournés vers les simulations de pouvoir d'arrêt électronique aux ions. MOLGW n'a pas de conditions aux limites périodique, c'est pourquoi un système typique pour simuler le pouvoir d'arrêt se compose d'un projectile ionique et d'un agrégat qui représente la cible.

Pour calculer le pouvoir d'arrêt, dans un premier temps, nous calculons l'état fondamental du système. Ensuite, nous imposons une vitesse de projectile constante. Cela veut dire que nous appliquons un travail supplémentaire pour maintenir cette vitesse, ce qui implique une croissance de l'énergie totale du système projectile-agrégat. Le travail appliqué compense la perte de l'énergie cinétique du projectile. Par conséquent, la croissance de l'énergie, ΔE , divisé par la profondeur d'implantation, Δz , est exactement le pouvoir d'arrêt $S = \Delta E / \Delta z$. Dans nos

simulations nous fixons les positions atomiques de la cible, donc le pouvoir d'arrêt calculé avec cette approche est purement électronique, S_e .

Le but de cette thèse était de calculer le pouvoir d'arrêt pour des matériaux cristallins. Pour ce faire, il est nécessaire de simuler des agrégats assez grands pour représenter approximativement le solide. Nous avons vérifié la convergence du pouvoir d'arrêt vis-à-vis de la taille de la cible et nous avons retrouvé des conditions d'irradiation de matériaux cristallins.

Ensuite, pour comparer nos résultats avec l'expérience, il est nécessaire d'effectuer une moyenne sur les différentes trajectoires du projectile. Nous avons simulé de nombreuses trajectoires pour considérer cette moyenne et nous avons établi une stratégie pour obtenir les moyennes à un coût contrôlé et avec une bonne précision.

2.4 Optimisation de la base Gaussienne

Une des particularités du phénomène d'irradiation aux ions est le fait que ce phénomène est très énergétique : un projectile ionique rapide excite tous les électrons de la cible en les promouvant sur des états énergétiques très loin d'équilibre. C'est pourquoi la base utilisée pour décrire correctement les états électroniques de la cible joue le rôle principal dans ce problème.

Au cours de ce travail, j'ai montré que le pouvoir d'arrêt électronique est très sensible à la base et que les bases standards de la chimie quantique ne sont pas adaptées pour le problème du pouvoir d'arrêt. Cela s'explique par le fait que dans la plupart de problèmes de la chimie quantique, l'excitation du système électronique est relativement faible ce qui n'est pas le cas dans ce travail.

Pour faire face à ce problème, nous avons proposé deux stratégies :

- 1) L'extrapolation du pouvoir d'arrêt en fonction de la base. Nous avons remarqué que le pouvoir d'arrêt devient plus grand quand on augmente la précision de la base de la cible. Cela est dû au fait qu'en augmentant la taille de la base, on améliore la qualité de la description des états occupés et, par conséquent, on ouvre plus de canaux de la dissipation de l'énergie du projectile. Donc, on peut arriver à la limite de la base complète en extrapolant le pouvoir d'arrêt en fonction de la base. Cependant, nous avons trouvé que la convergence est assez lente ce qui demande à mener des calculs avec des bases très grandes. Cela conduit à un autre problème : pour certains éléments (comme, par exemple le lithium), on ne dispose pas de bases standards disponibles assez grands.

En prenant en compte les problèmes de l'extrapolation du pouvoir d'arrêt en utilisant des bases standards, nous avons proposé une autre solution :

- 2) La génération des bases spécialement pour le problème du pouvoir d'arrêt. Le fait que le pouvoir d'arrêt électronique croît avec la précision de la base, permet d'établir une procédure de génération de bases qui s'appuie sur la *maximisation* du pouvoir d'arrêt. Pour ce faire, j'ai créé des scripts qui permettent de générer les bases de façon automatique pour des cibles différentes.

Les bases obtenues dans ce travail pour lithium et aluminium ont permis de calculer le pouvoir d'arrêt électronique avec une meilleure précision et avec un coût de calculs modéré. La procédure élaborée pour le pouvoir d'arrêt pourrait être appliquée aux autres problèmes physiques où il y a des fortes excitations électroniques.

3. Résultats

Dans ce travail, j'ai effectué les calculs du pouvoir d'arrêt électronique en RT-TDDFT du lithium et de l'aluminium dans le cas d'irradiation aux protons, aux antiprotons ainsi qu'aux particules alpha. J'ai comparé les résultats directement aux données expérimentales et aux données générées par le code empirique SRIM, largement utilisé par les expérimentateurs. On obtient un bon accord avec SRIM lorsque celui-ci contient une base de données expérimentales suffisamment riche.

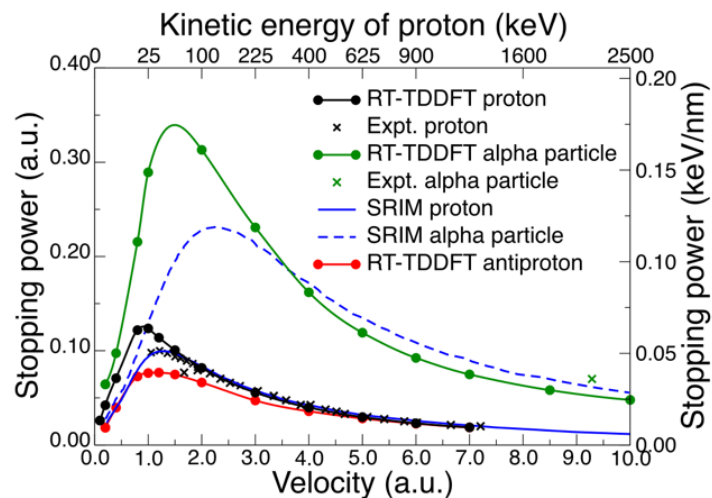


Fig. S1: Pouvoir d'arrêt électronique (en unités atomiques, a.u., ou en keV/nm) calculé à partir de simulations en RT-TDDFT pour l'irradiation aux protons (noir continu), antiprotons (rouge continu) et aux particules alpha (vert continu) dans lithium en fonction de la vitesse des projectiles (en unités atomiques, a.u.) ou de l'énergie cinétique du proton (en keV). Les données de SRIM pour le proton sont en bleu. Les points expérimentaux sont présentés pour l'irradiation aux protons (croix noires) et aux particules alpha (croix vertes). Les résultats de RT-TDDFT sont obtenues avec les bases optimisées, en utilisant LDA comme le fonctionnelle d'échange corrélation.

Dans le cas d'irradiation de lithium aux protons (Fig. S1, une courbe et des points en noir), la base de données de SRIM ne dispose pas de points expérimentaux pour des petites vitesses ($v < 1.0$ unités atomiques, a.u.). Remarquablement, seulement dans cette région il y a un désaccord entre les données de SRIM et de RT-TDDFT. Pour des vitesses plus grandes, on voit un excellent accord entre les résultats *ab initio*, SRIM et les points expérimentaux. C'est pourquoi, nous pouvons conclure que les données de SRIM ne sont pas fiables dans la région de petites vitesses. Pour l'irradiation aux particules alpha, la situation est encore plus inquiétante : dans la base de données de SRIM il n'y a qu'un seul point expérimental datant de 1928 (Fig. S1, la croix en vert). Finalement, pour l'irradiation aux antiprotons, il n'y a aucune donnée expérimentale. Ces exemples montrent l'importance de calculs *ab initio* qui peuvent enrichir la base de données du pouvoir d'arrêt.

Dans le cas l'irradiation d'aluminium aux protons (Fig. S2 (a)), la base de données de SRIM est assez large pour toutes les vitesses et nous observons un meilleur accord entre SRIM et les calculs *ab initio*. Pour les antiprotons (Fig. S2 (b)), on observe un bon accord avec l'expérience, le code SRIM ne fournit pas de résultats pour des antiprotons.

Concernant la dynamique électronique pendant l'irradiation, nous avons montré l'importance des excitations des électrons de cœurs : leur contribution dans le pouvoir d'arrêt est supérieure à 50 % pour des grandes vitesses des projectiles ($v > 2.0$ a.u.).

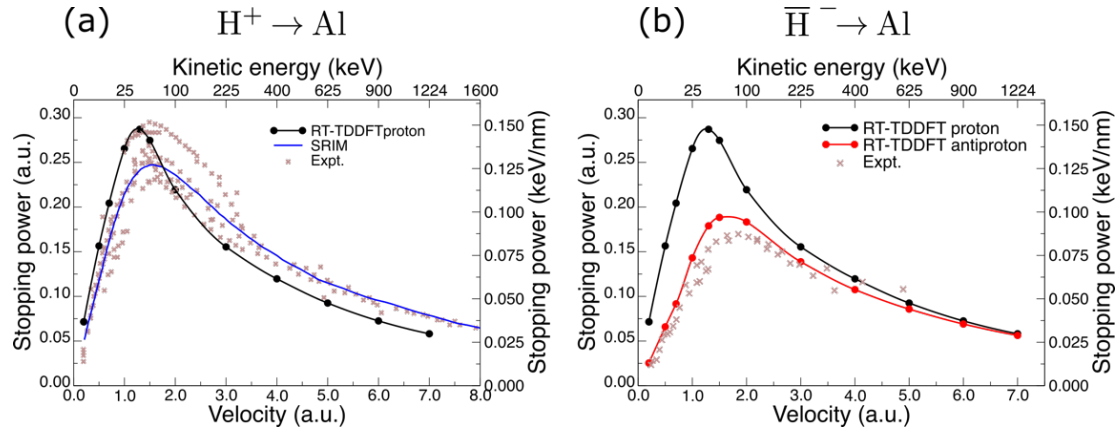


Fig. S2 : Pouvoir d'arrêt électronique pour l'irradiation aux protons (a) et aux antiprotons (b) dans l'aluminium. Les calculs de RT-TDDFT sont faits avec LDA et la base optimisée.

Nous avons aussi montré qu'il est très important d'avoir un nombre de trajectoires assez grand pour échantillonner correctement la cible. La méthode du « centroid path » qui propose d'utiliser qu'une seule trajectoire et qui est souvent utilisé, ne peut être précis que dans le cas de petites vitesses de projectiles ($v < 1.0$ a.u.) quand les excitations des électrons de cœurs sont négligeables. Pour calculer le pouvoir d'arrêt avec une bonne précision pour toute la gamme de vitesses, les calculs de la moyenne sur les trajectoires pour *chaque vitesse* de projectile est nécessaire.

MOLGW permet d'effectuer des calculs avec les fonctionnelles d'échange corrélation hybrides avec un coût de calculs modéré. Nous avons trouvé que l'influence de la fonctionnelle d'échange corrélation sur le pouvoir d'arrêt est très limitée (au moins, dans le cas des cibles métalliques).

De plus, nous avons retrouvé l'effet de Barkas, c'est à dire l'observation du pouvoir d'arrêt d'antiprotons inférieur à celui de protons (Fig. S2 (b) pour aluminium, les résultats pour lithium ne sont pas montrés ici). Cet effet n'est pas reproduit dans les cas de théories plus simples telle que la théorie de la réponse linéaire.

Liste de publications

1. I. Maliyov, J.-P. Crocombette, and F. Bruneval, "Quantitative electronic stopping power from localized basis set", *Physical Review B* **101**, 035136 (2020).
2. I. Maliyov, J.-P. Crocombette, and F. Bruneval, "Electronic stopping power from time-dependent density-functional theory in Gaussian basis", *European Physics Journal B* **172**, 91 (2018).
3. D. Li, R. Banerjee, S. Mondal, I. Maliyov, M. Romanova, Y.-J. Dappe, and A. Smogunov, "Symmetry aspects of spin filtering in molecular junctions: Hybridization and quantum interference effects", *Physical Review B* **99**, 115403 (2019).
4. M. Girych, G. Gorbenko, I. Maliyov, V. Trusova, C. Mizuguchi, H. Saito, and P. Kinnunen, "Combined Thioflavin T - Congo Red fluorescence assay for amyloid fibril detection", *Methods and Applications in Fluorescence* **4**, 100126 (2016).

Titre : Irradiation ionique des matériaux : dynamique des excitations électroniques en temps réel

Mots clés : DFT, RT-TDDFT, excitations électroniques, irradiation, pouvoir d'arrêt

Résumé : Le dommage d'irradiation dans la matière condensée est un phénomène important pour de nombreux domaines : les matériaux pour le nucléaire bien sûr, mais aussi l'électronique embarquée dans les satellites sujets aux rayonnements cosmiques, ou encore la matière vivante lors du traitement d'une tumeur par radiothérapie. Une connaissance précise de l'interaction entre la particule irradiante et le matériau cible est par conséquent fondamentale. L'interaction entre un projectile ionique et une cible peut être décrite par le biais du pouvoir d'arrêt. Il est défini comme étant le transfert d'énergie du projectile au matériau divisé par la profondeur d'implantation. La perte d'énergie d'un ion est induite majoritairement par les excitations électroniques de la cible. Le pouvoir d'arrêt électronique est alors la grandeur principale dans ce domaine. L'arrivée de la théorie de la fonctionnelle de la densité dépendante du temps (TDDFT) a permis d'améliorer largement la description de ce phénomène.

Au cours de cette thèse, nous avons développé un code *ab initio* basé sur la TDDFT en temps réel (RT-TDDFT) dans les bases gaussiennes. Cette implémentation a des avantages considérables comme le traitement direct des électrons de cœurs, la rapidité de calculs des fonctionnelles hybrides et la flexibilité spatiale de la base. Avec notre code, nous avons vérifié la

convergence du pouvoir d'arrêt vis-à-vis de la taille de la cible afin de tendre vers les matériaux cristallins. Nous avons analysé la dépendance du pouvoir d'arrêt en fonction du paramètre d'impact afin d'obtenir un pouvoir d'arrêt moyenné, correspondant aux conditions expérimentales. L'importance des excitations des électrons de cœurs dans l'irradiation ionique a été démontrée. Nous avons également étudié l'effet de la base gaussienne sur le pouvoir d'arrêt. Cette étude nous a permis de définir deux stratégies pour obtenir une bonne précision du pouvoir d'arrêt : l'extrapolation du pouvoir d'arrêt à partir des bases standards ou la génération de nouvelles bases.

Finalement, nous avons calculé le pouvoir d'arrêt du lithium et de l'aluminium dans le cas de l'irradiation aux protons, aux antiprotons ainsi qu'aux particules alpha. Nous avons comparé nos résultats directement aux données expérimentales et aux données générées par le code empirique SRIM, largement utilisé par les expérimentateurs. Nous obtenons un bon accord avec SRIM lorsque celui-ci contient une base de données expérimentales suffisamment riche. De plus, nous avons observé l'effet de Barkas : le pouvoir d'arrêt des antiprotons est inférieur à celui des protons. Cet effet n'est pas reproduit dans les cas de théories plus simples telle que la théorie de la réponse linéaire.

Title : Ionic irradiation of materials: real-time dynamics of electronic excitations

Keywords : DFT, RT-TDDFT, electronic excitations, irradiation, stopping power

Abstract : Ionic irradiation damage in condensed matter is central to many technological applications : materials in nuclear plants of course, but also electronics and solar panels in space that are subjected to the cosmic irradiation, living matter treated by radiotherapy to eliminate tumors, etc. For all these subjects, an accurate knowledge of the interaction between the irradiating projectile and the target is crucial. The interaction between the irradiating ion and the target material can be described by a stopping power, defined as the energy transfer from projectile to material per penetration distance. The most important ionic energy loss channels in irradiation process are the electronic excitations. Therefore, the electronic stopping power is the central quantity in this field. With the advent of time-dependent density-functional theory (TDDFT), it is nowadays possible to provide a complete and realistic quantum-mechanical description of the phenomenon.

In this thesis, we have developed a fully *ab initio* real-time TDDFT (RT-TDDFT) approach in the localized Gaussian basis. This implementation has several appealing advantages, such as the cheap account of core electrons, the ease of using the modern hybrid functionals, the flexibility of the basis set and overall low computational cost. With our tool, we explored the bulk limit,

the validity of the projectile impact parameter averaging to obtain the experimental random electronic stopping power. We have proven the importance of core electron excitations in the ionic irradiations. A great care was also taken about the Gaussian basis set convergence: the extrapolation of the stopping power based on standard basis sets and the basis set generation scheme were proposed.

Finally, we have computed the random electronic stopping power in lithium and aluminum targets for three types of projectiles: protons, antiprotons and α -particles. We have compared our results directly to the experiment as well as to the empirical code SRIM, that is a widely-used database of stopping powers and a *de facto* standard for experimentalists. The agreement with SRIM is good when the SRIM database contains enough experimental points, whereas we show that the SRIM extrapolation can be hazardous when the underlying experimental data points are too few. Concerning the antiproton irradiation, our RT-TDDFT calculations show that the antiproton stopping power is lower than the proton one, which is in agreement with the general experimental observation (the so-called Barkas effect). This effect is out of reach of simpler theories, such as the linear response approximation.

